C.1

APPLICATION OF THE HF PRECISION-VELOCITY TECHNIQUE TO THE STUDY OF δ SCUTI VARIABLES

by

STEPHENSON YANG

M.Sc., University of British Columbia, 1980

B.Sc., University of British Columbia, 1976

A THESIS SUBMITTED IN PARTIAL FULFILMENT OF

THE REQUIREMENTS FOR THE DEGREE OF

DOCTOR OF PHILOSOPHY

in

THE FACULTY OF GRADUATE STUDIES

Department of Geophysics and Astronomy

We accept this thesis as conforming

to the required standard

THE UNIVERSITY OF BRITISH COLUMBIA

October 1985

In presenting this thesis in partial fulfilment of the requirements for an advanced degree at the University of British Columbia, I agree that the Library shall make it freely available for reference and study. I further agree that permission for extensive copying of this thesis for scholarly purposes may be granted by the head of my department or by his or her representatives. It is understood that copying or publication of this thesis for financial gain shall not be allowed without my written permission.

Department of Geophysics & Astronomy

The University of British Columbia
1956 Main Mall
Vancouver, Canada
V6T 1Y3

Date 19th March, 1986

ABSTRACT

In conventional radial-velocity techniques, wavelength calibration in stellar spectra is limited by collimation and guiding errors. These errors can be largely eliminated by imposing absorption lines of known wavelengths on the spectra. The most suitable natural absorption lines belong to the R-branch (3-0) vibration-rotation band of HF. The calibration is achieved by placing an absorption cell filled with HF gas into the stellar beam. The monel cell and the sapphire windows are maintained at 100°C in order to avoid polymerisation of the HF molecules. Connected to the cell is a reservoir of liquid HF maintained at 0°C and this would then maintain a constant pressure inside the cell. Meanwhile, the Reticon detector is utilised to provide the necessary high s/n spectra.

In reducing the stellar spectra with the imposed HF lines, the effect of line blending between the two sets of lines can be minimised by performing numerical line cancellations using standard stellar or HF spectra. The relative positions of spectral lines are measured by means of the Fahlman-Glaspey difference technique. A modified Fahlman-Glaspey difference function can also be used to minimise the effect of small offset and scale differences between the line profiles. Simulation studies with artificial spectra have confirmed that the accuracy of line-position measurement would increase linearly with both s/n of the spectra and depth of the line profiles. Furthermore, the accuracy was found to decrease with

increasing linewidths when the equivalent widths were held constant.

A method has been devised to measure the HF gas temperature directly from the observed HF lines. This involves calculating the ratios between the observed HF line strengths. Theoretical line strengths for the (3-0) HF lines have also been calculated in order to study their dependence on the gas temperature. These theoretical values can also be used with the observed HF line strengths to calculate the relative gas pressure. A cutoff-free ATC theory on collisional line broadening was used to calculate HF linewidths and line shifts. Good agreement has been achieved between the calculated and published (1-0), (2-0), and (3-0) linewidths. This also enables a study on the temperature dependence of the (3-0) HF collisional self-broadened linewidths. Poor agreement was obtained between the published and calculated line shifts. Nevertheless, pressure-shift corrected wavelengths of the reference (3-0) lines have been derived.

The δ Scuti stars are distinguished by pulsation periods of less than 0.3^{d} and spectral type A or F. The small-amplitude δ Scuti stars typically have a light amplitude Δm_v of 0.05^{m} and a velocity 2K amplitude of less than $10 kms^{-1}$. Since the $2K/\Delta m_v$ value is about $92 kms^{-1}mag^{-1}$ for most δ Scuti stars, a velocity precision of just $\pm 0.1 kms^{-1}$ would already be equivalent to a precision of about $\pm 0.001^{m}$ in the light curve. Hence one can improve the study of δ Scuti pulsations with the use of precision

radial-velocity techniques. The HF technique would also enable the study of individual spectral lines for profile variations.

The star 20 CVn is a 0.122^d δ Del type δ Scuti variable observed using the HF technique at CFHT. A 2K value of $1.4 kms^{-1}$ was obtained for the Ca II λ8662 line while a value of $1.2 kms^{-1}$ was obtained for the other lines. These give a $2K/\Delta m_v$ of about $40 kms^{-1} mag^{-1}$ for 20 CVn which could imply nonradial pulsation.

The star ρ Pup is a 0.141^d δ Del type δ Scuti variable observed at CFHT. The line intensities of the stellar lines have been found to vary in phase with the light curve. These variations are at levels between 0.5% and 1% of the continuum. The lines are strongest near maximum light and weakest near minimum light. The variations can be considered as spectral-type variations caused by the variations of the effective temperature of the star over the pulsation cycle.

The star o^1 Eri is a 0.082^d broad-line δ Scuti variable observed at CFHT. A 2K amplitude of $4.3 kms^{-1}$ was measured for the Ca II λ8662 and H I λ8750 lines. Line-profile variations which are at a level of about 2% of the continuum, have been observed in the Ca II line. The variations can be characterised as the temporal movement of "features" across the broadened line profile. This would suggest the existence of nonradial pulsation in the star.

The star β Cas is a 0.104^d broad-line δ Scuti variable observed at CFHT. The Ca II λ8662 line has a 2K value of about $7 kms^{-1}$ while the value for the H I λ8750 and the other

metallic lines is about 4.5kms^{-1}. The H I velocity curve was found to lag the other velocity curves by about 2% in phase. Line-profile variations which are at a level of 1% of the continuum, have been observed in the Ca II line. The variations can be characterised as linewidth variations. The broad-line phase coincides with the velocity minimum while the narrow-line phase coincides with the velocity maximum.

Table of Contents

List of Tables

List of Figures

Acknowledgements

I would like to thank my supervisor Dr. Gordon Walker for his assistance, guidance, support, and patience. He is involved in every part of the HF project. His participation ranges from his design of the DAO HF system to performing most if not all the image guiding at the telescope for the data discussed in this thesis.

I would also like to thank Dr. Bruce Campbell for his assistance. He and Dr. Walker are responsible for the whole HF project. Dr. Campbell designed, built, and operated the CFHT HF system with which the data discussed in this thesis was based. Dr. Campbell also discovered and solved many of the problems associated with the data reduction of the spectra.

I would also like to thank Mr. John Amor and Mr. Dieter Screiber for their assistance. Mr. John Amor has been responsible some of the data-reduction techniques discussed in this thesis while Mr. Dieter Scrieber built the DAO HF absorption cell and the current gas-handling systems for both DAO and CFHT. I would also like to express my appreciation to Mr. Ron Johnson for his technical support of the instrumentations.

I would like to thank Dr. Friedhelm Aubke and his graduate students for their help with the DAO HF system. Dr. Aubke has made available, on many occasions, his laboratory and performed some of the dangerous tasks of replacing or removing HF from the absorption-cell system.

I would like to express my appreciation to Drs. Anne Underhill, Greg Fahlman, Anthony Merer, Michael Ovenden, Jason Auman, and Harvey Richer for their guidance and helpful discussion on this thesis. All the faculty, graduate students, and staffs in the department have offered their help and encouragement to the HF project and this thesis. I would especially like to thank Zoran Ninkov, Chris Millward, Garry Joslin, John Nicol, Daniel Thibault, Phil Bennett, Grant Hill, Enrico Kindl, Peter Whaite, Dennis Crabtree, and Gerry Grieve. Many of them have assisted with the observing at DAO. Once, Zoran Ninkov carried the HF lecture bottle from Vancouver to Victoria in his own car. Unfortunately, the bottle was empty by the time we received it. I would like to express my sympathy to John Nicol who has been losing one beer for every week that I have been working on this thesis. I would like to acknowledge the work of Phil Bennett on the theory of spectral-type variations. I would also like to thank Mr. Bill Siep who let us borrow some of his equipment to go on observing trips. I would like to thank Dr. Tad Ulrych and Colin Walker for the use of their power-spectrum-analysis program. I would also like to thank the technical staffs in the Physics department who, on many occasions, leak-tested our equipment.

I would like to thank the Dominion Astrophysical Observatory in Victoria and the Canada-France-Hawaii Telescope Corporation in Mauna Kea for extensive use of their facilities. I would also like to thank the staffs at both DAO and CFHT for their support. Murray Fletcher has

been very helpful to our observing at DAO. On numerous occasions, he has to re-coat the red coude train before our observing run. He has also provided very helpful discussion on the project. Dr. Allan Batten of DAO has also provided the literature references for the star β Cas. I would also like to acknowledge the work of Dr. Michael De Robertis on the barycentric-correction program.

I would like to acknowledge my late parents for their support and patience over the years. I would like to dedicate this thesis to the memory of them.

In memory of my parents

Chapter 1

INTRODUCTION

1.1 THE MEASUREMENT OF STELLAR RADIAL VELOCITIES

In 1842, Christian Doppler derived formulae relating the ocean wave frequency that is seen by a stationary observer who is on shore and that seen by an observer who is on a moving ship. He noted that the difference in the observed frequencies depends on the velocity of the ship. This phenomenon has been commonly known as the Doppler effect. If one considers the difference in the light frequency as emitted by a star from that actually observed on Earth, the Doppler effect gives:

$$f = f_0 \left(1 - v/c \right) \qquad (1.1)$$

The term f is the observed frequency, and f_0 is the emitted or rest frequency. The velocity of light is c, and v is the relative velocity in the line of sight or radial direction between the observer and the star. This is generally called the observed radial velocity of the star. If v is negative, the frequency is blue shifted and the star would be moving towards the observer. If v is positive, the frequency is red shifted and the star would be moving away from the observer.

As an application of the principle given by Doppler [1842], Fizeau [1870] outlined the method to measure the motions of celestial bodies. There were many unsuccessful attempts between 1863 and 1887 to produce a single trustworthy velocity measurement of any star. The low dispersion instruments available then would introduce errors

many times larger than the velocities to be measured. It was not until 1890 that the first reliable visually determined stellar velocities were obtained. Based on the displacements of the stellar sodium D lines, the first stellar velocity measurement was made on April 10th 1890 on the bright star α Bootis (Keeler [1894]).

In 1905, Albert Einstein postulated that the velocity of light is the same in all velocity frames of reference and derived the Doppler effect of special relativity:

$$f = f_0 \left(1 - (v/c)\cos\phi \right) / \sqrt{\left(1 - (v^2/c^2) \right)} \qquad (1.2)$$

The velocity of the star is v while ϕ is the angle between the velocity and the observer's line of sight direction to the star. Equation 1.2 will give a non-zero Doppler shift even when ϕ is 90°.

The radial velocity of a star can be estimated by comparing the observed frequency of a stellar spectral line against its corresponding laboratory rest frequency. Generally, the transverse component of a stellar velocity could contribute the equivalence of a few tens of metres per second to the observed Doppler shift. Therefore, the velocity inferred directly from the observed Doppler shift does not represent the true radial velocity of the star. Correction for this transverse Doppler effect would have to be made if the particular application requires the precise value of the true radial stellar motion. In most applications, one is only interested in the relative change in the radial velocities; therefore, the second-order Doppler effect would be unimportant.

The radial velocity of a star has traditionally used the centre of the Sun as the velocity frame of reference. Hence the observed value has to be corrected for the relative motion between the observer and the solar centre. Moreover, the value for f_0 used in Equations 1.1 and 1.2 is generally not the rest laboratory value. An effective f_0 value which takes into account many minor technical and physical effects is normally used. These include spectral line blending effects, stellar gravitational redshift, and detailed stellar photospheric conditions (Dravins [1982]). Minor zero-point corrections may still need to be applied to the measured velocities in order to place them on the same system with the radial-velocity standard stars. There are several systems of radial-velocity standard stars. In addition to the I.A.U. system (Pearce [1955]), there are the earlier Lick system and the various recent photoelectric systems (Fletcher et al. [1982], Beavers et al. [1979], Neese et al. [1985]). The observed radial-velocity estimate of a star is essentially defined by the Doppler effect displayed by its spectral lines. But it may not necessarily imply a physical motion of the star's centre of gravity relative to the observer by the implied velocity. The Doppler effect as experienced by the stellar lines in variable stars may, in part, be the result of stellar atmospheric motions caused by stellar pulsation.

1.2 CONVENTIONAL RADIAL-VELOCITY TECHNIQUES

The conventional determination of radial velocities involves simply the measurement of spectral line positions as well as the dispersion relation which translates these positions into wavelengths. The dispersion relation is generally derived from the positions of reference spectral lines e.g. hollow cathode atomic emission lines. The accuracy of a derived dispersion relation depends on how well the reference spectral lines can be used to remove the various systematic yet unpredictable effects which can also alter spectral line positions. The most serious of these is the effect of guiding error in terms of uneven illumination across the entrance slit of the spectrograph. Inconsistent guiding can be caused by tracking problems of the telescope and unavoidably by the changing atmospheric refraction and seeing. A slightly out-of-focus stellar image on the spectrograph's slit will cause nonuniform illumination of the collimator. This with focus error in the camera will also cause spectral line displacements (Petrie and Fletcher [1967]). Other problems include variations in the dispersion and focus of the spectrograph, miscollimation in the telescope and spectrograph, as well as instabilities in the spectrograph and detector. In conventional Coudé spectroscopy, the stellar and comparision beams may follow slightly different optical paths and the collimator will be illuminated differently. Zonal imperfections in the spectrograph camera mirror will cause variable spectral shifts (Tull [1969]). The use of emission reference line

spectra will also suffer from severe intensity dependent displacement of the spectral lines if the instrumental profile of the spectrograph exhibits some degree of asymmetry (Griffin and Griffin [1973]). Reviews of the problems in accurate conventional determination of radial velocities are discussed by Prevot [1967], Petrie and Fletcher [1967], Griffin and Griffin [1973], Serkowski [1976,1978], Campbell et al [1981], Campbell [1983], and Campbell and Walker [1985].

The highest precision ever attained in the measurement of stellar radial velocity by the conventional photographic method is about $\pm 100 ms^{-1}$ as reported by Petrie and Fletcher [1967]. This was achieved by narrowing the spectrograph's slit and hence reducing the guiding-induced external error per plate of about $\pm 0.3 kms^{-1}$ to the same value as the internal error of about $\pm 0.07 kms^{-1}$. Higher precision can be achieved using a Reticon detector as in Gray [1983]. Photoelectric methods using a cross-correlation technique between the spectrum and a spectral mask at the focal plane of the spectrograph have achieved a precision of about $\pm 100 ms^{-1}$. Reviews of these photoelectric cross-correlation techniques can be found in van Citters [1974], Griffin and Gunn [1974], Baranne et al. [1979], Beavers and Eitter [1977], and Fletcher et al. [1982]. The objective of various precision radial velocity methods is to achieve better than $\pm 100 ms^{-1}$ in precision. In fact, most methods aim to achieve about $\pm 10 ms^{-1}$, or in some cases, $\pm 1 ms^{-1}$ in precision.

1.3 MODERN PRECISION RADIAL-VELOCITY TECHNIQUES

Non-conventional radial-velocity methods can be classified into roughly two main categories depending on whether a spectrograph is utilised or not. Most of the precision radial-velocity techniques involve imposing wavelength calibration marks on the stellar light itself while many others rely on the stability of the instruments over a short time scale. In almost all of these techniques, the objective is to measure accurate relative velocities. Dravins [1975] has pointed out that small scale inhomogeneities in the stellar line formation region would limit the the measurement of absolute velocities to about $\pm 500 ms^{-1}$. Convective motions would especially cause line asymmetries and wavelength shifts (Dravins [1982]).

1.3.1 COUDE OPTICAL FIBRE FEED

Heacox [1983,1984] eliminated the guiding and collimation errors by scrambling the image of the stellar input to the spectrograph. This was accomplished by feeding the Coudé spectrograph with an optical fibre. The comparison lamp is also used at the telescope end of the fibre. The goal of this technique is to achieve a precision of about $\pm 50 ms^{-1}$.

1.3.2 INFRARED HETERODYNE TECHNIQUE

The wind velocities in the atmosphere of Venus have been measured by infrared heterodyne measurement of the CO_2 emission lines at about $950 cm^{-1}$ (Betz et al. [1976]). A

review of infrared heterodyne detection can be found in Blaney [1975]. Basically, the infrared beam from the telescope is combined with a stablised CO_2 laser. The combined beam is then focused on a HgCdTe photodiode mixer which generates a difference frequency current over the radio frequency bandwidth. The radio frequency current is then amplified, and corrected for the Doppler shift caused by the relative motion between the observer and Venus. The signal is then analysed into 40 independent channels whose outputs are multiplexed into a computer. A precision of $6ms^{-1}$ can be achieved after correcting for various systematic errors e.g. frequency instability of the CO_2 laser. One of the main disadvantages of this method is the crowding by telluric lines in the spectral region such that unblended CO_2 lines are only visible at specific radial velocities which vary with the barycentric motion of the observer.

1.3.3 MEASUREMENT OF THE SOLAR OSCILLATIONS

Various methods have been used to measure the 160 minutes and the 5 minutes period pulsation of the Sun. These oscillations have velocity amplitudes of $1ms^{-1}$ and $2ms^{-1}$, respectively. Severny et al. [1976] observed a pole-to-pole strip across the Sun. A circular polariser is placed in the solar beam in front of the spectrograph such that only the light from the central portion of the Sun would become polarised while the light from the polar rim would remain unaffected. Two photomultipliers are set on the

wings of a magnetically insensitive line. Doppler shifts can then be measured by comparing the difference in the output of the photomultipliers at different polarisations. The internal accuracy of this technique to compare the inner circular half of the solar disk against its outer ring was reported to be about $0.5ms^{-1}$.

Brooks et al. [1976] used an optical, resonant-scattering method to measure the solar pulsation. Basically, an absorption line is first isolated with an interference filter. The solar light is then passed through a polariser and an electro-optical light modulator which produces left- or right-handed polarisation. The solar light is then passed through a temperature controlled metal vapour cell containing Sr, Na, or K. The vapour cell is placed in a longitudinal magnetic field which produces the σ^- and σ^+ Zeeman components. The solar light excites the optical resonance of the vapour and the light re-emitted by the vapour is measured by cooled photomultipliers. The intensity of scattered light is proportional to the incident light intensity at the wavelength of the particular shifted Zeeman component. By varying the magnetic field and hence the wavelength of the Zeeman components, one can sample the whole absorption line profile. However, if only the radial velocity is desired, one can simply apply a constant magnetic field that would place the two Zeeman components on the wings near the maximum slope of the solar line profile. The difference in the intensities of the scattered light as sampled by the σ^- and σ^+ i.e. the short and long wavelength

components, will give the radial velocity of the absorption line. A precision of better than $\pm 1 ms^{-1}$ can be achieved using this or a variant of this method. Further application of this method can be found in Blamont and Roddier [1961], Fossat and Roddier [1971], Grec et al. [1976], Snider [1970], Grec et al. [1980], and Brooks et al. [1978]. The main disadvantage of this method is that it cannot be applied to the 10^{11} times fainter stellar flux since the detectable scattered light would only be a very small fraction of the input flux.

1.3.4 INFRARED FOURIER TRANSFORM SPECTROMETER

Fourier Transform spectrometers have been used to measure precision radial velocities. Basically, the stellar beam is divided into two beams using a beam splitter or dual entrance apertures. The two beams are later recombined after the optical path of one of the beams has been varied. The path difference is generally varied continuously with a moving mirror and is monitored by a laser going through the same optical path as the starlight. The resultant interference pattern is essentially the Fourier transform of the stellar spectrum. The stellar spectrum itself can be recovered by numerically applying the inverse Fourier transform to the output. Many of these interference patterns can be added together to achieve the required signal-to-noise ratio (s/n). Reviews on Fourier spectroscopy have been given by Connes [1970] and Ridgway and Brault [1984]. Hall et al. [1979] used the Kitt Peak

Fourier spectrometer to observe the CO band (3900-4500cm^{-1}) in bright late type stars. Telluric lines of CH_4, CO_2, H_2O, and N_2O were used as wavelength standards. They obtained a radial-velocity precision of 20ms^{-1} for the K giant α Tauri. Hall and Hinkle [1981] introduced a N_2O absorption cell into the stellar beam to impose artificial reference absorption lines on the spectrum. They expected the precision to be better than 10ms^{-1}. Apparently, even for bright stars, the required s/n ($\simeq$400) can be achieved only after several hours of integration with a 4m telescope.

Peery [1978] has used Fourier spectroscopy to study the stellar atmospheric velocity gradient in 19 Psc. Velocities were measured fom the lines of CO, HF, Fe I, and Ti I. However, the effect of line blending has limited the precision to only about 0.4kms^{-1}.

1.3.5 MODIFIED MICHELSON INTERFEROMETER

Forrest [1983] and Forrest and Ring [1978] used a modified Michelson interferometer to search for small radial-velocity variations in bright stars. The temperature stablised interferometer has a fixed path difference; in fact, a reference laser beam is used in conjunction with a servo control unit to maintain the fixed path difference. A fibre optic feed is also used to scramble the input image. An absorption line isolated by an interference filter is the input signal for the interferometer. One detector is used to observe the output intensity of the fringe pattern while another is used to observe the intensity of the input. A

radial-velocity shift of the absorption line will produce a change in the output intensity as fringes move through the output. The intensity difference between the two detectors will then give the phase of the fringes and hence the radial velocity. The system was used on the 3.8m UKIRT telescope and the 1.5m Tenerife telescope in a program to search for stellar oscillations. A precision of about $2ms^{-1}$ was obtained for two stars while that of about $20ms^{-1}$ was obtained for twelve other stars. The stability of the system between nights and observing seasons has still to be tested.

Connes [1983,1984] proposed the use of a servo-controlled interferometer with a vacuum echelle spectrograph and an image scrambler. A tunable laser referenced to a stable laser by beat mixing would be used to monitor the interferometer.

1.3.6 FABRY-PEROT TECHNIQUES

The PEPSIOS spectrometer has also been used to search for stellar oscillations (Traub et al. [1978]) as well as to measure the retrograde wind velocities on Venus (Traub and Carleton [1979]). The PEPSIOS system has been described by Mack et al. [1963]. The spectrometer consists of three Fabry-Perot étalons of different spacings. The étalons are linked in a series to isolate a single order of transmittance by suppressing all the neighbouring parasite orders. The incident starlight is premonochromatised by an interference filter before entering the train of étalons. The scanning of the spectrum is accomplished by varying the

pressure of the N_2 gas in each étalon. A cooled GaAs photomultiplier is used as the detector. To detect short-term radial-velocity variations without scanning, the spectrometer is set at a half-intensity point of a line profile e.g. the Fe I λ6678 line. A change in the output intensity will imply a radial-velocity change. A precision of $3ms^{-1}$ was achieved for α Bootis while values larger than $10ms^{-1}$ were found for other bright stars.

Reay et al. [1983a,1983b], Atherton et al. [1978], and Wells et al. [1978] described a Fabry-Perot stellar radial-velocity spectrometer that has a precision of $10ms^{-1}$. The input to the system is fed by an optical fibre from the telescope. An interference filter is used to isolate an absorption line. The scanning of this étalon system is accomplished by a servo-controlled variation of the gap between the plates of the Fabry-Perot. In fact, the scanning in this case is used in rapid chopping mode between the two inflection points of the line profile. The change in the output intensity will be interpreted as a radial-velocity change. The stability of the system is supposed to be better than λ/1000 on time scale of days to weeks while better than λ/10000 can be expected on the shorter time scale of minutes to hours. The system was used on the 1.9m SAAO and the 1.5m IRFC telescope to search for rapid radial-velocity oscillations in Ap and δ Scuti stars. A precision of about $20ms^{-1}$ was achieved for the δ Scuti variable ρ Pup while about $4ms^{-1}$ was achieved for the bright star Canopus.

Serkowski [1972,1976] proposed a polarimetric method to measure radial velocities. The starlight is first linearly polarised by a Wollaston prism. It is then passed through a temperature stablised phase retarder which rotates the plane of polarisation. Upon emergence from the retarder, the stellar light has a steep change in the position angle of polarisation as a function of wavelength. Hence the wavelength of each resolution element in the spectrum is encoded with a unique position angle of polarisation. The starlight is then passed through a rotating half-wave plate and a calcite Wollaston prism. A Fabry-Perot étalon is used to isolate the individual spectral resolution element while a tilting echelle spectrograph is used to sort out the various étalon orders. The output is then scanned by a Digicon image tube detector. One of the main disadvantages of this method is that both the optical system and the data reductions are very complicated. The accuracy in the wavelength calibration ia also dependent on the stellar flux.

Serkowski [1977,1978] and Serkowski et al. [1979a,1979b] modified the polarimetric radial-velocity spectrometer into a Fabry-Perot radial-velocity spectrometer. The Fabry-Perot interferometer provides the wavelength calibration since the wavelengths of the transmitted maxima depend only on the specifications of the étalon. The starlight passes through a rotating reversion prism before reaching the Fabry-Perot. This eliminates the dependence of radial velocities on the position of the star

in the entrance aperture. A later version of the spectrometer uses an optical fibre image scrambler instead of the rotating reversion prism. The image scrambler will also provide identical illumination when light from a calibration lamp, rather than a star, is incident on the Fabry-Perot. The output from the Fabry-Perot is then dispersed by an echelle spectrograph such that the output spectrum consists of rows of bright spots. The scanning of the spectrum is realised by tilting the Fabry-Perot interferometer hereby changing the wavelength of the transmitted maxima. An Fe-Ar hollow cathode source was used in the earlier version of the spectrometer to calibrate the tilts of the Fabry-Perot. With the image scrambler in the later version of the system, an NO_2 absorption cell illuminated by a lamp is used instead. A Digicon image tube was originally used as the detector. An array of 42x342 pixels intensified charge-injection device (CID) was used instead in a later version of the spectrometer. It can record eight echelle orders simultaneously. The spectrum covers about 260Å and is centred at about λ4230. The spectrum is then reconstructed from the intensities of the wavelength-calibrated Fabry-Perot maxima. The most recent version of the spectrometer uses a charge-coupled device (CCD) of 512x320 pixels as the detector and can record eighteen echelle orders simultaneously (Smith et al. [1983], McMillan [1984]). A precision of $5ms^{-1}$ is expected for this latest version of the spectrometer. Initial test with disk integrated sunlight has achieved a precision of about $6ms^{-1}$

while short exposures of Arcturus with a small telescope gave a precision of $40ms^{-1}$.

1.3.7 USE OF TELLURIC LINES

Griffin and Griffin [1973] proposed to use telluric absorption lines as wavelength references. Since the telluric lines are imposed on the stellar spectrum before the starlight enters the spectrograph, most of the problems in conventional radial-velocity methods can be eliminated. The poor photometric characteristics of photographic emulsions have limited the precision of the result in Griffin and Griffin [1973]. Modern electronic detectors, e.g. the Reticons, have been used with the telluric-absorption-line technique to measure the wind velocities on Venus (Young et al. [1979], Barker et Cochrane [1980]), and to search for stellar oscillations in the bright stars α Tauri and α Bootis (Smith [1982a,1983]). The most common set of telluric lines used is the O_2 band at λ6300.

One disadvantage of the telluric-absorption-line technique is that the telluric spectrum (O_2, H_2O) is not stable enough as a wavelength calibrator if very high precision is required. Weak lines from other absorption bands and various isotopic species of the elements may overlap the reference absorption bands to produce a rather complicated spectrum. The wavelengths as well as the strengths of different telluric lines will also vary differently under different atmospheric conditions. O_2 lines

will grow with zenith distance while the H_2O lines will also grow with humidity. The blending of telluric lines with weak stellar lines and telluric lines as well as the blending of stellar lines with weak telluric lines cause fictitious line shifts depending on the topocentric velocity of the stars and atmospheric conditions. This effect has been demonstrated by Campbell [1983]. Changing atmospheric pressure will also affect the wavelength of the reference telluric lines. Campbell and Walker [1979] have reported pressure induced shifts of more than 10^{-2} angstrom for the A-band O_2 lines.

The blending problems caused by telluric lines can probably be reduced by numerically removing the telluric line spectrum with a telluric line spectrum obtained by observing, say, an early type star under the same observing conditions. Similarly, the blending problems caused by the stellar lines can be reduced by numerically removing the stellar lines with a 'cleaner' stellar spectrum. Nevertheless, the numerical removal of the blends is difficult and can never be perfect i.e. one can only reduce the effect but not eliminate the problem. The telluric absorption line technique should still be useful for short time scale calibration with an ultimate precision of about $10ms^{-1}$ under excellent atmospheric conditions.

1.3.8 IMPOSING ARTIFICIAL CALIBRATION LINES

Cochrane et al. [1982] and Cochrane [1984] described a method to impose artificial calibration lines on the

spectrum before the starlight enters the spectrograph. The artificial absorption lines, in this case, are formed by two temperature-stablised Fabry-Perot étalons in reflection. An optical fibre scrambler is again used here to completely scramble the input image. This eliminates the variations in the illumination caused by guiding or seeing variations. The scrambled starlight is first divided into two beams. Each beam falls on a separate Fabry-Perot étalon. Each Fabry-Perot transmits the interference maxima which are absorbed by a black background while reflecting back the rest of the beam. The spectrum in each reflected beam contains imposed absorption minima caused by the loss of the transmitted maxima. The two reflected beams are then recombined to form the output beam. Both Fabry-Perots are identical except that one is tilted such that the transmitted maxima are displaced in wavelength by half the free spectral range of the Fabry-Perot. Consequently, the output spectrum contains absorption minima separated from each other in wavelength by half the free spectral range of the Fabry-Perot while the depth of each absorption minimum is only 50% of the continuum. The detector to be used is an Octicon which is eight 1872-Reticons placed end-to-end. The spectrum covers about 1500Å and is centred at about λ6820. The availability of several hundred stellar and reference lines in the wide bandpass will increase the precision of the result if the error in each line measurement is randomly distributed. The expected precision of the technique is $1 ms^{-1}$.

An absorption cell filled with hydrogen fluoride (HF) gas has been used to impose artificial reference absorption lines on the spectrum before the starlight enters the spectrograph. The generated absorption lines at about λ8700 are stablised by controlling the temperature and pressure of the HF gas. Details of the HF absorption cell technique are described in later chapters of this thesis. Yang et al. [1982] and Yang and Walker [1983] used the technique to measure the relative radial-velocity variations of δ Scuti variables. Irwin and Campbell [1983] applied the technique to search for oscillations in bright stars. Campbell and Walker have also been applying the HF technique in the search for low-mass companions (extra-solar planets ?) to solar-type stars (Campbell [1983], Walker et al. [1984], Campbell and Walker [1985], Campbell et al. [1985]). The internal precision of the technique is about $\pm 6 ms^{-1}$ for data obtained on the same night (Irwin and Campbell [1983]). This value was obtained from the scatter in the measured velocities of a time series of α Boo spectra. The precision for data observed over nights and observing seasons is about $\pm 12 ms^{-1}$ (Campbell and Walker [1985]). This value was derived from the scatter in the measured relative radial-velocity curve of τ Ceti.

1.4 DELTA SCUTI VARIABLES

1.4.1 INTRODUCTION

The Delta Scuti or Ultrashort-Period Cepheid variables are one group of variable stars distinguished by pulsation periods of less than 0.3 day and spectral type A or F. The light amplitude for this group of variables ranges from several thousandths of a magnitude to 0.8 magnitude in V. The large-amplitude (>0.3 magnitude) variables are generally referred to as RRs stars, dwarf Cepheids, or AI Vel variables while the small-amplitude δ Scuti variables have a typical V amplitude of about 0.05 magnitude. The radial-velocity amplitude is generally less than 10 kms^{-1}. The δ Scuti instablity strip is a lower luminosity extension of the Cepheid instability strip. It ranges from just below the main sequence to about 2.5 magnitudes above it. The blue edge of the strip has been determined by Breger [1977] to be 8000K on the ZAMS and 8400K at absolute visual magnitude of 0.65. The red edge is at 7500K on the ZAMS and 6950K at absolute visual magnitude of 1.7. δ Scuti stars have been found in open star clusters e.g. the α Persei cluster (Slovak [1978]). About one-quarter to one-third of the stars inside the instability strip have been found to be variable with amplitude greater than 0.01 magnitude. This suggests that the δ Scuti pulsation is a common and normal phenomenon. In fact, after the white dwarf pulsators (ZZ Ceti stars), the δ Scuti stars are the most numerous type of pulsators in the Galaxy. δ Scuti variables are usually Population I objects. They are generally considered to be two-solar-mass Population I stars that are just

evolving off the main sequence. There is a subgroup of the variables led by SX Phe which resembles Population II stars in their kinematics and low metal abundances. In fact, several variables are probably members of the globular cluster ω Cen or are objects in the galactic halo (Frolov and Irkaev [1984a]).

1.4.2 MAIA SEQUENCE ?

Struve [1955] has proposed the existence of a sequence of Maia (20 Tau) variables which would fill the space in the HR diagram between the β Cep and δ Sct stars. The existence of nonradial pulsations as cool as B5 (Smith [1977]) has increased the speculation that nonradial pulsation may be quite common for all B and A stars. At the present time, the existence of the Maia variables is still not conclusive (Breger [1979]). Studies of variabilities have concentrated on 20 Tau (B7III), γ UMi (A3II-III), γ CrB (A0IV), τ Peg (A5IV), and o Ser (A2V). One of the difficulties lies in the fact that the stars may only occasionally show detectable photometric variations e.g. the case of γ CrB (Percy [1970], Tippets and Wilcken [1970], Veto and Kovacs [1981], Veto [1983]). This is also the situation with another probable candidate, α Lyr (A0V). A recent review on the variability of Vega has been given by Kholopov [1984].

1.4.3 δ DELPHINI ANOMALIES

Some δ Scuti variables also have δ Del type anomalies while not all δ Del stars are δ Scuti variables. Delta

Delphini stars are subgiant or giant stars of spectral type A or F. The degree of metallicism varies among the δ Delphini stars but generally, they are underabundant in Ca and Sc relative to Fe while Sr, Y, Zr, and the rare earths are overabundant. There may also be a marginal underabundance in Ti, V, and Cr relative to Fe.

Because of the similarities in metallicism and other properties, Eggen [1976] and Kurtz [1979] have suggested that the δ Del stars are evolved Am stars. The abnormal abundances in Am stars have generally been explained by the diffusion theory (Vauclair and Vauclair [1982]). In a quiescent and slowly rotating star, the helium in the He II ionisation zone may disappear due to its tendency to settle downward gravitationally. This destroys the He II convection which would normally produce the mixing of elements. Consequently, under the influence of downward gravitational settling and upward radiation pressure, some elements will rise while others will sink in the outer stellar photospheric layers. This explains the observed under- and overabundance of elements. Metallicism, in fact, can occur as soon as 10^3 years after the disappearance of the He II convection (Vauclair [1976]).

1.4.4 COEXISTENCE OF PULSATION AND METALLICISM

The depletion of helium from the He II ionisation zone however also implies that the star will not pulsate. This agrees very well with the observational fact that classical Am stars do not pulsate. Several marginal Am stars have been

found to pulsate (Kurtz [1978]); in fact, the marginal Am star HR3321 has been found to be a δ Scuti variable with a period of 55 minutes and an amplitude of 0.006 magnitude (Kurtz [1984]). Similarly, the existence of the pulsating Am-like δ Del stars poses a problem for the theoretical interpretation which has to explain the coexistence of both pulsation and metallicism. Valtier et al. [1979], Stellingwerf [1979], Cox et al. [1979b], and Saez et al. [1981] have suggested that metallicism and pulsation can coexist for the δ Del stars which are more evolved than the classical Am stars. With mild metallicism, there will be enough drive for pulsation to occur from enhanced H as well as residual He due to incomplete settling or recent upward mixing.

1.4.5 MODELS OF δ SCUTI STARS

δ Scuti pulsation is driven mainly by the He II ionisation zone at 5.2×10^4K and partly by the H ionisation zone at 1.2×10^4K. Stellingwerf [1979] pointed out that there is another minor driving zone at 1.5×10^5K caused by the coincidence of maximum photon flux with the frequency of the second helium ionisation edge. Pulsation amplitudes, period ratios, pulsation constants, and other observables are often computed from the theoretical models for comparision with the observed values. A wide range of models with stellar mass ranging from 0.2 to 3.0 solar masses and the composition Z (the content of elements heavier than He) ranging from 0.01 to 0.001 have been claimed to agree with

the observations. Nonlinear approaches in the theoretical models are often required for the δ Scuti stars. Current results, however, depend very much on the treatment of the opacities, the artificial viscosity parameters (i.e. the dissipation mechanisms), and other input physics (Stellingwerf [1980], Percy [1980]).

Some of the current theoretical problems involve finding the mechanisms which govern the pulsation amplitudes and the particular excited modes (radial and nonradial), as well as why some modes appear and disappear. For example, Fitch [1980] has suggested that multimode pulsation may be preferentially excited in stars where there is a resonance between radial and nonradial modes. One of the problems is to find out why some stars in the instability strip are not variables. Antonello [1982] has suggested that the stars in the lower part of the instability strip are pulsators if they have a sufficiently high rotational velocity or if they are in an appropriate binary system. Other problems include a better determination of the edges of the instability strips as well as the role of rotation and diffusion on the variabilities. Recent discussions on the theoretical aspects of δ Scuti stars can be found in Peterson [1975], Stellingwerf [1979], Cox et al. [1979a,1979b], Stellingwerf [1980], Cox and Hodson [1980], Fitch [1980], Dziembowski [1980], Kurtz[1980], Andreasen et al. [1980], Percy [1980], Fitch [1981], Tsvetkov [1982ab], Andreasen et al. [1983], and Cox [1984b]. The most recent effort to compare between the theoretical and observational properties of both

high-amplitude and low-amplitude δ Scuti variables can be found in Andreasen [1983]. It also includes a discussion on the high-amplitude metal-poor, metal-rich, and double-mode δ Scuti stars.

1.4.6 PERIOD-LUMINOSITY-COLOUR RELATION

There is a period-luminosity-colour relation (PLC) for the δ Scuti stars. Breger [1979] gives the following relation :

$$M_v = -3.052 \log P - 8.456 (b - y) - 3.121 \qquad (1.3)$$

Other determinations of the PLC relation include those by Breger and Bregman [1975], Antonello and Conconi [1982], and Frolov and Irkaev [1984b]. In fact, PLC relations are given for each radial pulsation mode by Gupta [1978] and Tsvetkov [1982b]. The corresponding relations between M_{bol} and $\log T_{eff}$ are also given. The period-gravity relation of the δ Scuti stars gives a slope between 0.030 day and 0.035 day. This agrees well with the expected radial fundamental mode pulsation constant Q_0 of 0.035 day (Breger [1980b]).

1.4.7 LIGHT AND VELOCITY AMPLITUDES

Antonello et al. [1981] have found a relationship between the visual light amplitude and the narrow band colours of the δ Scuti stars:

$$\log\Delta m_v = 2.06(\delta c_1)_0 M_v + 7.54(\delta c_1)_0 (b-y)_0 - 1.91 \qquad (1.4)$$

The term Δm_v is the peak-to-peak visual light amplitude. The above relation will be simplified if the colours are replaced by the period using the PLC relation.

There is also a linear relation between Δm_v and the velocity amplitude 2K. Breger [1969] has given a value of 92kms^{-1}mag^{-1} for $2K/\Delta m_v$. Smith [1982b] has shown that this is a typical value for the radial pulsators. For the nonradially pulsating δ Scuti stars, a more typical value is about 45kms^{-1}mag^{-1}. In fact, one may be able to use this large difference between the two values to distinguish between radial and nonradial pulsators.

The pulsation periods in almost all δ Scuti stars are believed to be stable in spite of the complex structures found in the light and radial-velocity curves. These are generally attributed to the beating effects from the various excited pulsation modes. There is still, however, a question about the stability of the pulsation amplitudes. Breger [1982] has proposed that stellar rotation is responsible for the small amplitudes in HR6434, an AI Vel -like δ Scuti star.

1.4.8 SYSTEMATICS OF δ SCUTI STARS

From the statistical distribution of the pulsation constant Q, Antonello and Pastori [1981] found that about 25% of the low-amplitude (i.e. < 0.3 magnitude) variables pulsate in the radial fundamental mode. Based upon all the available results on δ Scuti stars with determined pulsation modes from multiperiodic analyses, Breger [1980b] was able to draw some conclusion about their general pulsation properties. Several radial modes are simultaneously excited in many stars. For stars pulsating mainly in the higher

radial overtones, the fundamental and lower overtone modes may also be present. The radial fundamental mode is only dominant for stars in the cool part of the δ Scuti instability strip. Nonradial pulsation can be found in stars over the entire instability strip. Not all stars have nonradial modes although nonradial pulsation often coexists with radial modes. The AI Vel stars pulsate mainly in the radial fundamental and the first overtone mode. Recent reviews of the properties of the δ Scuti variables can be found in Leung [1970], Baglin et al. [1973], Frolov [1975], Fitch [1976], Eggen [1979], Breger [1979,1980a,1980b,1980c], Wolff [1983], and Breger and Stockenhuber [1983].

1.5 OSCILLATION MODES

1.5.1 MODE CLASSIFICATION

The eigenfunctions which characterise the normal modes of stellar pulsation in the spherical polar coordinates (r,θ,ϕ) are proportional to functions of radial distance r, the spherical harmonics $Y_m^l(\theta,\phi)$, and a temporal dependence $\exp(i\sigma t)$. The function $Y_m^l(\theta,\phi)$ is equal to $P_m^l(\cos\theta)\exp(im\phi)$ with the $P_m^l(\cos\theta)$ being the Associated Legendre Polynomials of the first kind. The terms σ are the eigenvalues which have for the real parts, the oscillation angular frequencies. The angular quantum numbers, $l=0,1,2,...,$ are the orders of the spherical harmonics while the azimuthal quantum numbers, $m=-l,...,0,...l$, are the azimuthal spherical harmonics indices. The $(2l+1)$-fold degeneracy of l

in m can be lifted by the rotation of the star. A review of m-splitting has been given by Cox [1984a]. The condition $m>0$ corresponds to waves travelling in the opposite direction to the stellar rotation while $m<0$ corresponds to waves travelling in the same direction. The $l=0$ mode corresponds to the special case of radial pulsation. The $l=1$ mode is the case of nonradial dipole oscillation while $l=2,3$ correspond to quadrupole and octupole oscillations, respectively. There are also the radial quantum numbers k, which distinguish the number of nodes in the displacement from the centre of the star. The $k=0$ mode corresponds to the fundamental pulsation while $k=1,2$ are the first and second overtone modes, respectively. Tidal effects on the variable in binary orbit, e.g. 14 Aur, may also cause hyperfine splittings of the pulsation modes (Fitch and Wisniewski [1979]).

There are four types of spheroidal nonradial oscillations (p,f,g^+,g^-). Each type of oscillation corresponds to an infinite discrete spectrum of the eigenvalues σ^2. The p-modes are the pressure (acoustic) modes with the restoring force due to pressure variations. The propagation zones of the p-modes are generally situated in the envelope of the star. The σ^2 values of these modes increase with increasing k (the number of radial nodes) and l values. The p-modes usually have mainly vertical motions as well as large pressure and density variations. The values of σ^2 are generally large for the p-modes in comparison with the g-modes. The g or gravity modes have gravity (buoyancy) as the restoring force. The propagation zones of the g-modes

are generally situated in the interior of the star. For a given l value, the σ^2 values of the g-modes approach 0 as k increases. The g-modes usually have mainly horizontal motions as well as small pressure and density variations. For the g^+-modes, σ^2 are positive while σ^2 are negative for the g^--modes. The condition $\sigma^2<0$ implies the modes are dynamically unstable. The eigenfunctions of the g^+-modes are oscillatory in the radiative regions of the star while the g^--modes can be oscillatory only in the convectively unstable regions. The f or Kelvin modes exist only with the lowest k value (i.e. no radial node) and for $l \geq 2$. The effects of the f-modes on the pressure and density variations as well as their σ^2 values are intermediate between those of the p- and g-modes. In simple homogeneous stellar models, the f-modes can be considered as surface waves on a fluid sphere. Toroidal modes may also be present for a rotating pulsator. Papaloizou and Pringle [1978] have given the r-modes designation to a class of toroidal modes in slowly rotating stars. They are Rossby-like waves driven by Coriolis forces. Their motions are horizontal (vortex-like) and carry no information from one atmospheric depth to another (Smith [1981], Saio [1982]).

The radial displacement $\xi(r,t)$ due to spheroidal nonradial oscillations can be expressed as :

$$\xi(r,t) = (\xi_r, \xi_\theta, \xi_\phi) \exp(i\sigma t) \qquad (1.5)$$

$$\xi_r = a(r)\, P_m^l(\cos\theta) \exp(im\phi) \qquad (1.6)$$

$$\xi_\theta = b(r)\, d(P_m^l(\cos\theta))/d\theta \exp(im\phi) \qquad (1.7)$$

$$\xi_\phi = imb(r)\, P_m^l(\cos\theta)\, \exp(im\phi) \,/\, \sin\theta \qquad (1.8)$$

$$a(r) = \psi(r)/r^2 \qquad (1.9)$$

$$b(r) = (d\chi/dr)/(l(l+1)r) \qquad (1.10)$$

In a rotating star with angular frequency Ω, $\sigma = \sigma_0 - m\Omega C$ where σ_0 is the eigenfrequency in the non-rotating case. The constant C is given in Cox [1980] and is a function of both the stellar structure and the pulsation mode. The functions $a(r)$ and $b(r)$ are the radial part of the displacement in the radial and horizontal direction, respectively. The functions $\psi(r)$ and $\chi(r)$ are given in Ledoux and Walraven [1958]. For the p- and f-modes, they can be approximated by power series e.g. $\psi(r) = r^{l+1}\Sigma a_k r^{2k}$ and $\chi(r) = r^{l+1}\Sigma b_k r^{2k}$ (Clement [1984]). In most models with a thin pulsating envelope e.g. Osaki [1971] and Kubiak [1978], they are treated as constants and with the ratio $b(r)/a(r) = (Q/0.116)^2$. The velocity change is then simply the time derivative of $\xi(r,t)$.

Recent discussions on the theories of stellar pulsation can be found in Ledoux and Walraven [1958], Christy [1966], Cox [1976], Papaloizou and Pringle [1978], Tassoul [1978], Dziewbowski [1979], Unno et al. [1979], Fitch and Wisniewski [1979], Cox [1980], Stothers [1981], Saio [1982], Barranco et al. [1982], Perdang and Blacher [1982], Buchler and Goupil [1984], Aikawa [1984], Clement [1984], and Cox [1984a].

1.5.2 MODE IDENTIFICATION TECHNIQUES

1.5.2.1 Period ratios

Mode identifications for δ Scuti stars can be accomplished by several methods. Usually, no single method can unambiguously identify all the different pulsation modes present in the star. The pulsation modes of several stars, however, have been determined using a combination of several methods. One of the simplest and most common methods is looking at period ratios. Theoretical period ratios have been computed for a variety of stellar models and pulsation modes (Peterson [1975], Stellingwerf [1979], Cox and Hodson [1980], Andreasen et al. [1980], Fitch [1980]). Observed periods of the variable can be checked for certain "magic" period ratios e.g. $P_1/P_0 = 0.76$ and $P_2/P_1 = 0.81$ for radial pulsation. Ambiguities may arise for higher overtone radial pulsations. From theoretical models, Andreasen et al. [1983] have found that as the star evolves with a downwards helium depletion from the stellar outer zones, the period ratio between the fundamental and first overtone pulsation increases. Cox [1984b] has pointed out that the large observed period ratio in VZ Cnc could be the result of such evolutionary effect.

No specific nonradial pulsation period ratio has been determined. Generally, any observed period ratio which does not agree with any of the specific radial mode period ratios would indicate the presence of nonradial modes. The existence of three almost equally-spaced frequencies in V474 Mon has suggested the presence of nonradial modes with

m-splitting due to stellar rotation (Shobbrook and Stobie [1979]). Detailed analysis by Balona and Stobie [1980b] has indicated that of the three frequencies, one is an overtone radial mode while the other two are nonradial dipole modes with rotational *m*-splitting.

1.5.2.2 Use of the pulsation constant Q

The observed pulsation constant Q of a variable can be used to distinguish between oscillation modes. With the narrow band uvbyβ photometry, and knowing the main pulsation period P, Q can be calculated using the following formula from Breger and Bregman [1975]:

$$\log Q = -6.454 + \log P + 0.5 \log g + 0.1 M_{bol} + \log T_{eff} \qquad (1.11)$$

The quantities M_{bol}, T_{eff}, and log g can be calculated with the uvbyβ indices from the calibrations of Harris [1963], Allen [1973], Crawford [1975,1979], Breger [1977], and Philip and Relyea [1979]. A Q value of 0.033 day will indicate fundamental radial pulsation. While it is not always the case, Q = 0.025 day may indicate first overtone radial pulsation and Q values of less than 0.025 day may imply nonradial modes. The Q values for various stellar models and pulsation modes have been computed by Stellingwerf [1979] and Fitch [1981]. This method cannot be applied to the SX Phe subgroup since the uvbyβ calibrations are valid only for normal stars.

1.5.2.3 Line profile analysis

Line profile analysis provides means to examine the instantaneous distribution of velocities across the pulsating stellar surface. A time series of line profiles can be used to identify pulsation modes e.g. radial pulsations cause large radial-velocity variations but only small linewidth variations while nonradial pulsations tend to show the opposite. The observed time series of line profiles is generally fitted by a time series of theoretically generated line profiles which have been distorted by a specified pulsation mode. This is more reliable than just fitting line-profile parameters like radial velocities, half widths, and equivalent widths.

The theoretical stellar disk is first divided into many grid points. The effect of radial-velocity changes due to pulsations is then imposed upon the unperturbed intrinsic line profile associated with each grid point. The unperturbed profile in each square grid is generally computed from stellar model atmospheres. The radial-velocity changes are calculated from the time derivative of $\xi(r,t)$ for a given set of the modal constants (l,m), frequency, and pulsation amplitude. The effect of superimposed modes can be linearly added. Each profile at each grid point is then corrected for the effect of stellar rotation, limb darkening, and other effects. Summation of all the perturbed profiles from all the grid points over the entire visible stellar disk will then provide a theoretical line profile. A time series of line profiles

can be generated by varying the ϕ values in the expression for $\xi(r,t)$. The time parameter t in this case is irrelevant. This method requires high s/n data as well as long time coverage for the time series. Due to the large number of available degrees of freedom in the fit, multiperiodic variables with two or more superimposed modes will pose a problem for this method, especially if there are not enough observational data. Campos and Smith [1980] and Smith [1982] used this method to model the line profiles of the δ Scuti variables. Generally, the identification of either radial or nonradial pulsation for the dominant mode was accomplished. However, the identification of the modal constants (l,m) as well as the secondary superimposed modes were not conclusive. The method also failed for the variable 20 CVn. In this case, the effect of the Doppler imaging on the line profile is reduced by the low projected rotational velocity of the star.

1.5.2.4 Use of simultaneously observed data

Dziembowski [1977], Balona and Stobie [1979a,1979b,1980a], Balona [1981], and Stamford and Watson [1981] have derived linearised expressions for the variations in light, colour, and radial velocity of a pulsating star. The major assumption is that the surface brightness variations are proportional to the colour variations. For radial pulsations, Balona and Stobie [1979b] obtained expressions for $\Delta L/L$, $\Delta F/F$, and ΔV_r which are the brightness, colour, and radial-velocity variations,

respectively. The expressions are:

$$\Delta L/L = \epsilon\sqrt{(f^2+4f\cos\psi+4)}\ \cos(\sigma t+\eta) \quad (1.12)$$

$$\Delta F/F = \epsilon f\ \cos(\sigma t+\psi) \quad (1.13)$$

$$\Delta V_r = 0.708\epsilon\sigma R_0\ \cos(\sigma t-\pi/2) \quad (1.14)$$

$$\tan\eta = f\sin\psi/(2+f\cos\psi) \quad (1.15)$$

where

σ = frequency

ϵ = semi-amplitude

ψ = phasing between colour and velocities

η = phasing between light and velocities

R_0 = equilibrium radius of the star

f = scaling factor for the amplitude

With simultaneous light, colour, and radial-velocity data, one can solve for the unknowns ϵ, f, ψ, R_0, and η in the four equations above. Balona and Stobie [1980b] applied the above equations to the data of V474 Mon which had been prewhitened to isolate only the radial mode i.e. removing the effects of the two nonradial modes from the data. They were able to obtain a value for the radius of the star.

Similarly, for nonradial pulsation, Balona and Stobie [1979a,1980a] and Balona [1981] have obtained expressions for ΔV, ΔC, and ΔV_r which are the light, colour, and radial-velocity variations, respectively. The expressions are:

$$\Delta V = 1.086\epsilon\ P_m^l(\cos i)F_V\ \cos(\sigma t+\phi_V) \quad (1.16)$$

$$\Delta C = (1.086\epsilon P_m^l(\cos i)F_C/A)\ \cos(\sigma t+\phi_C) \quad (1.17)$$

$$\Delta V_r = \sigma R_0\epsilon P_m^l(\cos i)F_{RV}\ \cos(\sigma t-\pi/2) \quad (1.18)$$

$$F_V \sin\phi_V = -(f b_l \sin\psi) \tag{1.19}$$

$$F_V \cos\phi_V = -(f b_l \cos\psi + (2+l)(l-1) b_l) \tag{1.20}$$

$$F_C \sin\phi_C = -(f b_l \sin\psi) \tag{1.21}$$

$$F_C \cos\phi_C = -(f b_l \cos\psi + (2+l)(l-1)(b_l - 2I_1)) \tag{1.22}$$

$$F_{RV} = (2-\beta) I_2 + 1.5 I_3 + 74.6 Q^2 (l(l+1)/2)((2-\beta) I_2 + \beta I_3) \tag{1.23}$$

$$b_l = (2-\beta) I_1 + 1.5 \beta I_2 \tag{1.24}$$

$$I_n = \int_0^1 \cos^n\theta \; P_l(\cos\theta) \; d\cos\theta \tag{1.25}$$

where

β = the limb-darkening coefficient

i = the inclination angle

ψ = phase lag of the flux relative to the radius

A = factor relating ΔC with surface brightness

P_l = Legendre Polynomial of order l

Simultaneous light, colour, and radial-velocity data can provide three amplitudes and two phase differences i.e. five quantities for the above equations which have six unknowns in l, f, ψ, ϵ, A, and R_0. Some constraints, however, can be placed on the value of l since it is an integer. For $\psi \simeq \pi/2$ (δ Scuti stars), one can identify a value for l from the position of the data on a plot between $(\phi_V - \phi_C)$ and $(\phi_V - \phi_{RV})$, which are the phase difference between light and colour variations and the phase difference between light and radial-velocity variations, respectively. Theoretical lines of constant f and ψ can be generated on the plot for each discrete value of l using

rough estimates of the other unknowns e.g. R_0. For odd values of l, however, the projected area variation of the pulsator is zero. The light variation is then determined only by the surface brightness variations i.e. $\phi_V-\phi_C=0$ for all odd values of l. Nevertheless, one can still get an estimate for l from the phase difference plot e.g. $\phi_V-\phi_C<0$ implies $l=0$ and $\phi_V-\phi_C>0$ implies $l\geq 2$. For $\psi\simeq\pi$, l can be identified from the position of the data on a plot between the quantities F_V/F_C and F_V/F_{RV} which is similar to a plot between the corresponding amplitude ratios. This is a refinement of the less reliable method of examining the ratio of the velocity and light amplitude for mode-typing. Balona et al. [1980b,1981] have successfully applied this extensive mode analysis technique to the variables V474 Mon and δ Scuti. Burki and Mayor [1981] also applied this mode-typing method to the variable HD37819. One of the main disadvantages of this method of mode-typing is the large amount of required data. Simultaneous data of light, colour, and radial velocities are normally difficult to obtain. The method is also best applied to only one particular pulsation mode at a time, hence the data have to be prewhitened to isolate each mode. This makes the data analysis rather tedious.

Stamford and Watson [1981] rederived all the above equations for nonradial pulsation but taking into account also the variations of the effective gravity as well as the wavelength dependence in the limb-darkening function. They found for nonradial pulsations, the assumption that the

variations of surface brightness are proportional to the variations of colour is invalid. Balona [1981] studied the effect of surface gravity variations on his mode-typing method and concluded that the effect is too small in most cases to affect the result. Nevertheless, he generated correction factors to be used in conjunction with his mode-typing method. In the new derivation by Stamford and Watson [1981], one can still identify l from the $(\phi_V-\phi_C)$ vs $(\phi_V-\phi_{RV})$ or the F_V/F_C vs F_V/F_{RV} plot, but the theoretical lines on the plots are distorted from those in Balona [1981]. Mode discrimination for odd values of l is also possible in the new derivation. Stamford and Watson [1981] re-analysed the data on V474 Mon using the new method but obtained almost the same result as Balona and Stobie [1980b]. They pointed out that, even with the new derivation, mode identification of $l>3$ will be rather insecure when the surface radial-velocity variations cannot be inferred simply from the variations of the mean wavelengths of the line profile. The limb-darkening function from current model atmospheres becomes inadequate for higher values of l. They also pointed out that the correction factor for the centre-to-limb effect of 1.31 between the observed radial velocity and pulsation velocity from Parsons [1972] can be used for $l<2$, provided that the rotational velocity field is less than the pulsational velocity field.

1.5.2.5 Use of polarisation measurements

Mode-typing by measuring the polarisation variations has not yet been applied to the δ Scuti stars. Stamford and Watson [1980] have shown that at visible wavelengths, the amplitude of the polarisation variations would be too small for detection in even most B stars except for BW Vul which has been mode-typed using this method by Odell and Tapia [1981]. Polarisation variations have been reported for the peculiar large-amplitude δ Scuti variable SX Phe (Haefner et al. [1976]).] A recent discussion of the method is given by Watson [1983].

1.6 SPECTROSCOPIC OBSERVATIONS OF DELTA SCUTI STARS

1.6.1 DIFFICULTIES WITH LOW-AMPLITUDE VARIABLES

Observation of the spectroscopic variations of the low-amplitude δ Scuti variables is usually difficult. The amplitude of the radial-velocity variations, 2K, is generally less than $10 kms^{-1}$ and can be less than $2 kms^{-1}$ for many of the variables. This implies the need of very-high-dispersion spectroscopy. The main pulsation period is generally very short and is of the order of three hours while many are of the order of just one hour. The exposure time in each spectrum is generally limited to at most 10% or 20% of the pulsation period in order to avoid significant phase-smearing effects on both the line profiles and the radial-velocity curve. The effect of exposure time upon the line profile has been studied by Huang and Struve [1955].

Except for β Cas and ρ Pup, however, all the other δ Scuti variables are not brighter than third magnitude. This certainly imposes a very stringent limitation on the attainable s/n in each spectrum. One method of improvement is to obtain an average radial-velocity curve over many periods. Not taking into account any systematic effect, the improvement is only by a factor of $\sqrt{n}$ where n is the number of observations in each phase bin. This implies many observations are required if one wants the error in each phase bin of the mean radial-velocity curve to be reduced for example from 1 kms^{-1} to 0.1 kms^{-1}. The actual improvement will be worse than $\sqrt{n}$ when other effects are considered. The correct phasing of the radial velocities will be very difficult without prior knowledge of the precise period and almost impossible if the variable is multiperiodic. Cycle-to-cycle variations may also be present.

The use of photoelectric radial-velocity scanner-type systems has enabled the radial-velocity variations to be measured for several narrow line variables. No proper spectral "mask" for the velocity scanner is available if the variable has a spectral type earlier than F0. It is difficult to get a perfect match between the variable and the spectral mask especially with the changing spectral characteristics of the variable during the pulsation cycle. Difficulties will also be encountered if the variable has broad lines with vsini greater than $30kms^{-1}$. In fact, no radial-velocity "dip" can be achieved with the DAO RVS

system on the broad-line variable β Cas (Ninkov [1982]). Furthermore, one cannot study line-profile variations with the scanner-type systems. Although some information on the asymmetry of the mean line profile can be inferred from the shape of the cross-correlation function e.g. by Burki and Mayor [1981], one still cannot examine the individual line profiles. The variations in both the profile and the radial velocity may be different for different lines. Generally, the radial-velocity scanner technique has been applied only to the large-amplitude δ Scuti stars.

1.6.2 RECENT OBSERVATIONS

Recent photographic spectroscopic observations include the simultaneous light and radial-velocity measurements of δ Del, ρ Pup, and δ Sct by Kuhi and Danziger [1967]. Leung and Wehlau [1967] also measured the radial-velocity variations of δ Del. Chevalier et al. [1968] obtained simultaneous light and radial-velocity data on 14 Aur. Bessell [1969] used a photoelectric spectrum scanner in addition to the Coudé plates in his study of the energy distribution and line profile variations of the variables ρ Pup, δ Del, and δ Sct. A curve-of-growth analysis was also applied to the variables. Simultaneous light and radial-velocity data were obtained for the variables 28 And, 20 CVn, and HR7331 by Nishimura [1969], Penfold [1971], and Breger et al. [1976], respectively. Breger [1969] was able to show the radial-velocity variations of ϵ Cep using the data of Abt [1965]. Dravins et al. [1977] measured the

radial-velocity variations of ρ Pup. They also reported Ca II K line emission at a certain phase of the pulsation. This may be caused by shocks propagating through the atmosphere. Shock generated emission has also been observed in VZ Cnc by Garbuzov and Mitskevich [1984]. Radial-velocity variations of the variables HR432, HR515, and HR8006 were measured by Valtier et al. [1979]. Auvergne et al. [1979] observed the evolved δ Scuti star γ Boo. They found line core splitting in the Ca II and H I profiles in conjunction with "bumps" in the radial-velocity curves. Meanwhile, Duncan and Preston [1979] measured the radial-velocity variations in both δ Del A and δ Del B with photographic plates. The suspected variable β Ari was also observed with the photographic plates by Barbiano Di Belgioso et al. [1983].

Recent photoelectric radial-velocity scanner observations include the measurement of the radial-velocity variations of several RRs stars by Van Citters [1976]. Imbert [1980] measured the photoelectric radial velocity variations of HD200925. Simultaneous light and photoelectric radial-velocity data on V474 Mon were obtained by Balona and Stobie [1980b]. Simultaneously observed light and photoelectric radial-velocity data were also obtained for the variables ρ Pav, HD37819, and δ Sct by Kurtz [1981], Burki and Mayor [1980,1981], and Balona et al. [1981], respectively.

Campos and Smith [1980] and Smith [1982] used a Reticon detector to measure both the radial-velocity and the

line-profile variations of the variables ρ Pup, δ Sct, 28 And, 44 Tau, δ Del A, δ Del B, V474 Mon, 28 Aql, 14 Aur A, and 20 CVn. Nishimura et al. [1983] used an intensified Reticon detector to measure the radial-velocity variations of 20 CVn. Simultaneous light variations were also obtained. Reay et al. [1983a] used a servo-controlled Fabry-Perot radial-velocity spectrometer to measure the radial-velocity variations of ρ Pup. The International Ultraviolet Explorer (IUE) was used by Fracassini and Pasinetti [1982] and Fracassini et al. [1983] to observe the Mg II H and K line emissions of several δ Scuti variables.

1.6.3 USE OF PRECISION RADIAL-VELOCITY TECHNIQUES

The small 2K values of many of the δ Scuti variables demand that radial-velocity observations should have a precision of at least ± 0.5 kms^{-1}. Heacox [1980] has pointed out the advantages of applying precision radial-velocity techniques to the study of δ Scuti variables. For many δ Scuti stars, the ratio of velocity to light amplitude is about 92 $kms^{-1}mag^{-1}$ (Breger [1979]). Hence, if one can achieve a radial-velocity precision of better than ± 0.1 kms^{-1} in the radial-velocity curves, it would be equivalent to a precision of about ± 0.001 mag in the light curve. Most modern precision radial-velocity techniques can certainly achieve this; in fact, many of the methods can achieve almost ± 0.01 kms^{-1} in precision which is equivalent to having a precision of ± 0.0001 mag in the photometry. This would mean more than an order of magnitude improvement in

the ability to study the δ Scuti pulsation.

The HF absorption cell technique is very suitable in its application to the study of δ Scuti variables. Individual line profiles can also be obtained. This allows the study of the individual line profile variations as well as the determination of precise radial velocities for individual spectral lines. Broad-line stars would not be a problem for the HF technique. A precision of about ±50 ms^{-1} can be achieved with only a moderate s/n for the spectrum and with only a moderate amount of data reduction. One would be able to detect previously unseen low-amplitude pulsation modes. The effects of pulsation on different spectral lines can also be studied. The different pulsation amplitude of different spectral lines may help one to study the structure of the pulsating stellar atmosphere. The observation of the Van Hoof effect (van Hoof [1957]) which is characterised by phase lags between the radial-velocity curves of different spectral lines e.g. hydrogen and the metallic lines, could also be used to probe the structure of the pulsating stellar atmosphere.

Presently, most of the existing mode-typings of δ Scuti stars are based on photometric studies e.g. using the Q values. Spectroscopic data can give another independent determination of the pulsation mode. One can use the observed 2K value of a δ Scuti star to discriminate between radial and nonradial pulsations. Line-profile analysis offers another independent method for mode discrimination. These will enable one to study, using spectroscopic data,

the systematics of the δ Scuti stars at different parts of the instablility strip. Many δ Scuti stars can be studied with the HF technique if one uses a telescope with an aperture similar to that of the CFH 3.6 m telescope. Several δ Scuti variables have been studied using the HF technique. It is the objective here to report on the study.

Chapter two of this thesis discusses the criteria to choose the detector and the reference absorption gas. The Reticon detector is also discussed with particular emphasis on noise reduction, incomplete readout, and the persistence phenomenon. Chapter two also gives a description of the absorption cell and its operation. Chapter three describes the derivation of new molecular constants for HF and hence improved wavelengths for the (3-0) band. The line strengths for the (3-0) band are also calculated. This enables the derivation of relative gas temperature and pressure directly from the observed spectra. The theory of molecular collision self-broadening is also described in Chapter three. This is followed by a theoretical formulation and eventual calculation of the HF linewidths and shifts. Chapter four describes the procedure to preprocess Reticon data in order to achieve optimum s/n for the spectra. The procedure to reduce HF data is also described. There is also discussion on the Fahlman-Glaspey difference technique, barycentric corrections, and velocity accuracy. Chapter five reports on the application of the HF technique to the variable 20 CVn. Chapter six reports on ρ Pup. Chapter seven reports on o^1 Eri while Chapter eight reports on β Cas.

Chapter 2

THE HF ABSORPTION CELL SYSTEM

2.1 INTRODUCTION

One can eliminate most of the problems associated with the use of telluric lines as wavelength reference lines. This is accomplished if the reference lines are generated by an absorption cell containing a selected gas. The absorption cell would be placed in the telescope beam before the starlight enters the spectrograph. Since the temperature and pressure of the absorbing gas can be controlled, the generated absorption lines will be more stable than the telluric lines. Blending problems in the telluric-line technique can be minimised with a careful choice of the absorbing gas. Moreover, as opposed to the case with the telluric lines, stellar spectra with or without the imposed absorption lines as well as spectra with only the imposed absorption lines can be easily generated. These spectra are very useful in removing the line-blending-induced errors in line-position measurements.

2.2 CHOOSING THE DETECTOR

Measuring very accurate line positions requires very high signal-to-noise ratios for the spectra. Photon noise is the dominant source of noise in high s/n spectra. Therefore, in order to achieve high s/n, large numbers of photons must be detected. This would imply the detector must have a large dynamic range. It is also desirable for the detector to have

a linear response. High positional stability is important in order that instrumental induced spectral shifts (raster shifts), as seen in television type detectors or image tubes, would not occur. The detector should have high detective quantum efficiency (DQE). The sensing area of the detector should also be large and in a configuration suitable for spectroscopy. This is important in the consideration to maximise the number of detected photons.

The detector which satisfies most of the above mentioned criteria is a linear Reticon photodiode array. The DQE of the Reticon can be as high as 75% in the λ8000 spectral region (Walker et al. [1985]). This is higher than most conventional detectors e.g. photographic plates and most CCDs. The Reticon also does not have the inefficient charge transfer problem as found in many CCDs. The rectangular shape (large aspect ratio) of the Reticon sensing area (diode) is more suitable for spectroscopy than the square-shaped pixel of the CCD. The necessity to sum a column of CCD pixels negates the very-low-readout-noise advantage of the CCD over the available low-readout-noise Reticon (Walker et al. [1985]). Johnson [1984a] has pointed out that, in the future, the summation along a column of CCD pixels can be accomplished within the chip such that the readout noise of the summed column is the same as that of a single CCD pixel. At the present, only three pixels in the same column can be added in this manner. In any case, readout noise is not the dominant source of noise in high s/n spectra. The Reticon array also has excellent

geometrical stability, a large charge storage capacity i.e. large dynamic range, as well as having no dead (insensitive) space between diodes.

2.3 THE RETICON DETECTOR

2.3.1 INTRODUCTION

Reticon is the commercial name of a group of self-scanned or integrated diode arrays (IDA). The silicon diode array is a large scale integrated circuit fabricated on a single silicon chip. The chip is mainly a 300μm thick n-doped silicon substrate. It has thin channels of p-doped silicon at regular intervals on the surface and a common gold substrate on the bottom as anode. The number of channels corresponds to the number of photodiodes in the array. A transparent layer of SiO_2 covers the whole surface of the chip to reduce the effective reflectivity of the array. When a reverse bias of 5 volts is applied to the diodes, a space-charge layer (depletion region) is created at the interface between the n-doped and the p-doped silicon. Absorption of photons with sufficient energy (to raise the electrons into the conduction band of the semiconductor) within the silicon will form electron/hole pairs. If these excess free charge carriers are formed in the p-doped silicon, they will drift to the depletion region and partially discharge the bias. And if they are formed in the n-doped silicon, they also will move by diffusion to the depletion region. This results in having effectively no dead

space between diodes. When the diode is rebiased again after a set exposure time, the amount of charge required to restore the original 5 volts potential will give a measure of the number of absorbed photons. In a readout (rebiasing the diodes), a shift register is clocked to connect each diode sequentially to its appropriate video output line. The analog output signal from the video line is first amplified and then digitised for storage in a computer.

Higher energy (blue) photons tend to generate the electron/hole pairs more easily than the lower energy (red) photons. Hence the red photons have a longer penetration depth into the silicon. If the wavelength of the photons is too long for electron/hole pair generation i.e. beyond the red cutoff, the photons may be reflected back from the bottom gold substrate of the chip and interfere with incoming photons to produce fringing effects. Geary [1976] has pointed out that, for the thick arrays, such interference effects are small. This is because the rear surface of the chip would be required to have a very fine finish in order to produce collimated reflections. In any case, proper flat-field calibration procedure can remove any small-amplitude fringe pattern from the spectrum.

The electron/hole pairs created by the absorption of the photons can recombine before reaching the space-charge layer. This leads to a reduced responsive quantum efficiency (RQE). The density of the recombination centres is higher near the surface of the silicon (Geary [1976]). Consequently, the blue photons, which have short penetration

depths, are more seriously affected. Of course, the response is still dominated by the reflectivity of silicon. The response in the far red will also be affected by the increased recombination loss due to the longer distance the charges have to travel to reach the space-charge layer. With the long distance of travel by the free charges, there will also be a higher chance that the free charges would diffuse to adjacent pixels rather than the one directly above. This will result in gradual loss of spatial resolution with increasing wavelength. In fact, at the spectral region chosen for the HF program, the instrumental point-spread function is dominated by this effect. The cross talk between adjacent diodes due to charge spillover from saturated (the space-charge layer completely discharged) diodes has been found to be very small (Talmi and Simpson [1980]).

2.3.2 DARK CURRENT

Dark current (thermal leakage) exists when free charges are thermally generated to discharge the space-charge layer. It reduces the effective dynamic range of the array as well as adding an extra noise component into the system. Thermal dark current is also nonlinear with exposure time. This is because of the dependence of the leakage on the width of the depletion region and hence the number of absorbed photons. Some of the diodes (hot diodes) can also have a much higher amount of thermal leakage than the average diode in the array. The amount of dark current, however, can be reduced by cooling the diode array. At an operating temperature of

-130°C with liquid N_2 cooling, the dark current becomes almost negligible (Vogt et al. [1978], Vogt [1981]). The cooling of the array, however, will increase the bandgap energy as well as the penetration depth of the photons. Vogt et al. [1978] reported a marked drop in the RQE in the longer wavelengths (redward of λ7000) with cooling. The peak RQE for Reticons cooled to 90K is about 80% at about λ7000 (Geary [1976]).

To avoid large systematic readout errors from differential heating (Campbell et al. [1981]) as well as dark signal from "charge pumping" effects (Vogt [1981]), clock pulses to the array are turned off between readouts. Vacuum housing for the array provides temperature insulation and prevents the formation of frost on the cooled array surface. The UBC built array housing (cold box) is first rough pumped with a mechanical pump. The cryogenic pumping material, zeolite, will then generate a good vacuum by absorbing the residue gas when cooled (Campbell et al. [1981]). Temperature stability of the UBC built Reticon detectors is maintained to ±0.2°C by a heater/diode-temperature-sensor loop (Campbell et al. [1981]).

2.3.3 LINEARITY IN RESPONSE

The linearity of the Reticon response has been examined by Geary [1976], Campbell [1977], Vogt et al. [1978], Talmi and Simpson [1980], and Vogt [1981]. Existence of the nonlinear dark current in the signal will certainly produce

a nonlinear response. Nonlinearity can also result from imperfect removal of the additive fixed pattern signal (baseline) from the data. Furthermore, the amplifiers and the analog-to-digital converters of the array output can have nonlinear characteristics. Generally, with the Reticon properly cooled, the signal is linear over four orders of magnitude. Small nonlinearities in the response can be removed with proper instrumental calibration and data reduction procedure. The dynamic range of the Reticon depends on the amount of charge sufficient to saturate a silicon photodiode. The saturation charge of a RL-1872F/30 Reticon photodiode is 3.2 pcoul or 2×10^7 equivalent photons.

2.3.4 FIXED LINE PATTERN

The output signal contains an additive fixed pattern component. It is the result of capacitive coupling of the clock-driver signals onto the video output lines. The amplitude of this fixed pattern is usually large. The fixed pattern has a saw-tooth waveform with spatial periods in multiples of the number of output video lines. It, however, can be very constant over long periods of time if the clock signal waveforms are stable and the temperature of the Reticon is kept constant. Consequently, it can be easily removed by numerically subtracting off a second readout obtained shortly after the initial readout of the data frame (Walker et al. [1976]). Because of array self-heating and other phenomena, a small-amplitude residual fixed pattern can still remain after the subtraction of the second readout

(baseline). This can be removed with proper instrumental calibration and data-reduction procedure.

2.3.5 REDUCTION OF READOUT NOISE

The readout noise of a properly cooled Reticon is dominated by the reset (KTC) noise. In rebiasing a diode, the Johnson noise in the resistance of the shift-register switch causes an uncertainty in the amount of restoring charges applied to the diode. The rms noise ΔQ is given by Walker et al. [1985]:

$$\Delta Q = 2.5 \times 10^9 \sqrt{(kTC)} \qquad (2.1)$$

Where ΔQ is in number of equivalent photons

C is the diode capacitance in pF

k is the Boltzmann's constant

T is the temperature in kelvin

The diode capacitance is about 0.6 pF. Hence, if there is no other stray capacitance, the reset noise would be less than 300 e^- at an operating temperature of 150K. In conventional readout schemes of the diode array, however, the video line voltage is monitored with respect to ground both before and after rebiasing each diode. This would subject the measured charge of the diode to the KTC noise associated with the shunt capacitance of the video line which is typically about 50 pF. This problem has been minimised by Walker et al. [1985] using the signal processing technique of correlated double sampling (CDS) (White et al. [1974], Geary [1979]). The CDS signal for the nth diode is the difference between the measured signal after rebiasing the (n-1)th diode (with

the video line shunt capacitor short-circuited and the (n-1)th diode connected to the video line) and the measured signal after connecting the nth diode to the video line (with the (n-1)th diode disconnected from the video line). Within the short double sample interval, the noise from the video line is correlated and is removed in the difference. Only the uncorrelated noise due to the difference between the (n-1)th and the nth diode remains. This is the reset noise with a characteristic capacitance of the same magnitude as that of a single diode.

The readout noise in analog-to-digital convertor units (adcu) is easily obtained from the variance of a short dark exposure. It is 2 adcu rms per diode per readout for the current UBC-built DAO 1872-Reticon detector operating in the high gain mode of the amplifiers. In order to make comparison with the number of detected photons, one needs to know the conversion factor between adcu and the number of equivalent photons. This can be accomplished in two ways. Knowing both the number of adcu for a saturated diode and the manufacturer specified saturation charge, a conversion factor of 185 e^- per adcu was obtained for the UBC-built DAO Reticon detector (Walker et al. [1985]). By computing the residual between two spectra of heavy modulation i.e. a large range of signal levels, one can plot the signal variance against the signal. The conversion factor will then be the reciprocal of the slope. Walker et al. [1985] used spectra of Betelgeuse exposed to the same signal level for this alternate calibration method. The large number of

TABLE 2.1 UBC-built 1872-Reticons

Telescope	e^-/adcu (hi gain)	e^-/adcu (lo gain)
DAO 1.2m/1.8m	185	185x5
CFHT 3.6m	250	250x3.5
UBC 0.4m	150	150x3.5

strong absorption lines in the spectrum provided the range in the signal levels. A conversion factor of 180 e^- per adcu was obtained. This agrees very well with the previous calibration and implies a noise level of only 370 equivalent photons in a single readout. Recent improvements in the electronics have further reduced the readout noise to be less than 320 equivalent photons. The UBC-built CFHT Reticon has similar noise characteristics.

Table 2.1 lists the three current UBC-built Reticons and their e^-/adcu conversion factors. The values listed for the CFHT Reticon are based on "real" adc units. The CFHT Reticon-control software uses a "pseudo" adc unit (logically shifted by one bit) which is equivalent to two "real" adc unit. Hence the corresponding conversion factors based on this pseudo unit would be half of those listed in Table 2.1.

2.3.6 THE INCOMPLETE READOUT PHENOMENON

It has been reported that a residual charge can still remain after a readout (Livingston et al. [1976], Vogt et al. [1978]). This phenomenon of incomplete readout or readout lag, however, was found to be negligible by Geary

[1976] and Talmi and Simpson [1980]. If the diodes are not rebiased back to the original operating potential (5 volts) after a readout, it would have the same effect as a reduced response. Moreover, the residual charge will contaminate the next exposure. The incomplete readout can be reduced or eliminated by having a sufficiently low scan rate for the readout to allow for more complete rebiasing. Multiple erasure readouts can also be used to insure that all diodes are fully charged before the start of an exposure (Vogt et al. [1978]). The power dissipation in a quick sequence of readouts, however, will cause self-heating of the array. This will raise the level of the dark current as well as it would take time for the array to reach temperature equilibrium again.

The effect of incomplete readout has been examined with the DAO Reticon. This is accomplished by setting a relatively long exposure time for a Hg arc spectrum. But before the end of the exposure duration, the arc is switched off and the optical path to the spectrograph blocked off in front of the image slicer. This is to eliminate any after glow from the arc. The Reticon is set to continue performing exposures (readouts). The first readout would be saturated at the positions of the strong arc lines and can be discarded. The second readout, however, should be a dark exposure. After subtracting off the underlying baseline, any signal detected in this readout would then represent residuals left behind by the incompleteness of the first readout. Figure 2.1 shows this remnant spectrum together

Figure 2.1 Residuals from incomplete readout.

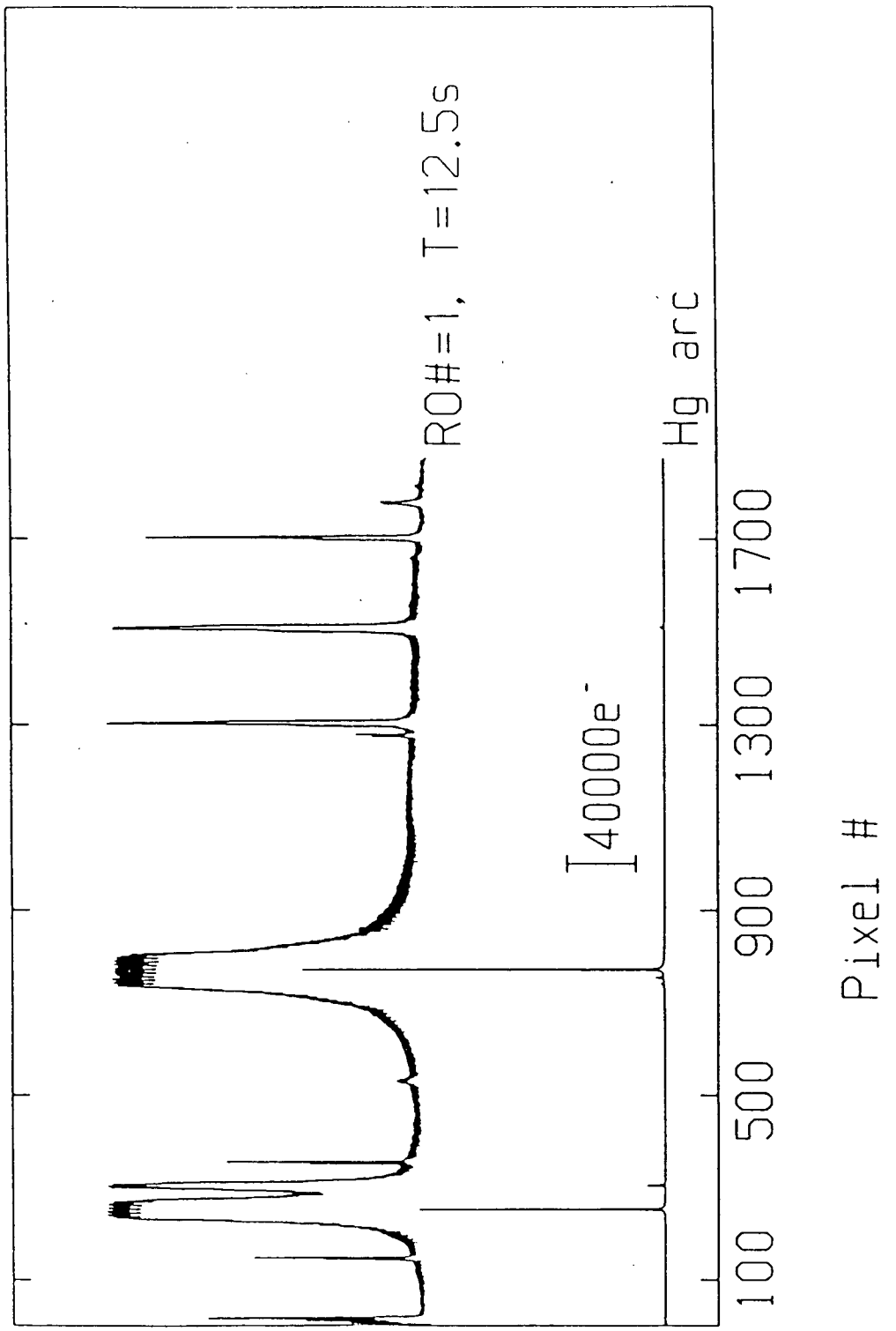

Figure 2.2 The persistence phenomenon.

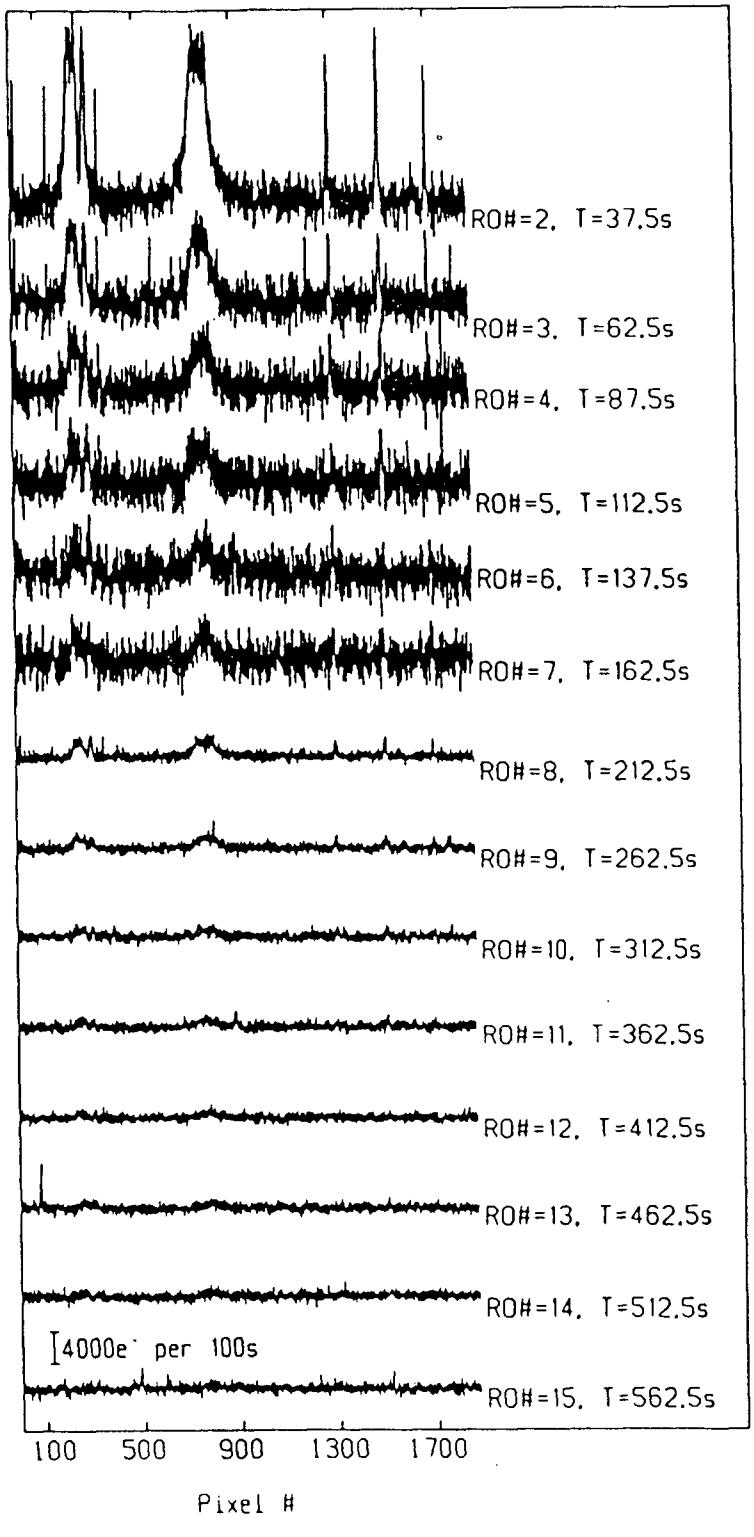

Figure 2.3 Time decay of the persistence phenomenon.

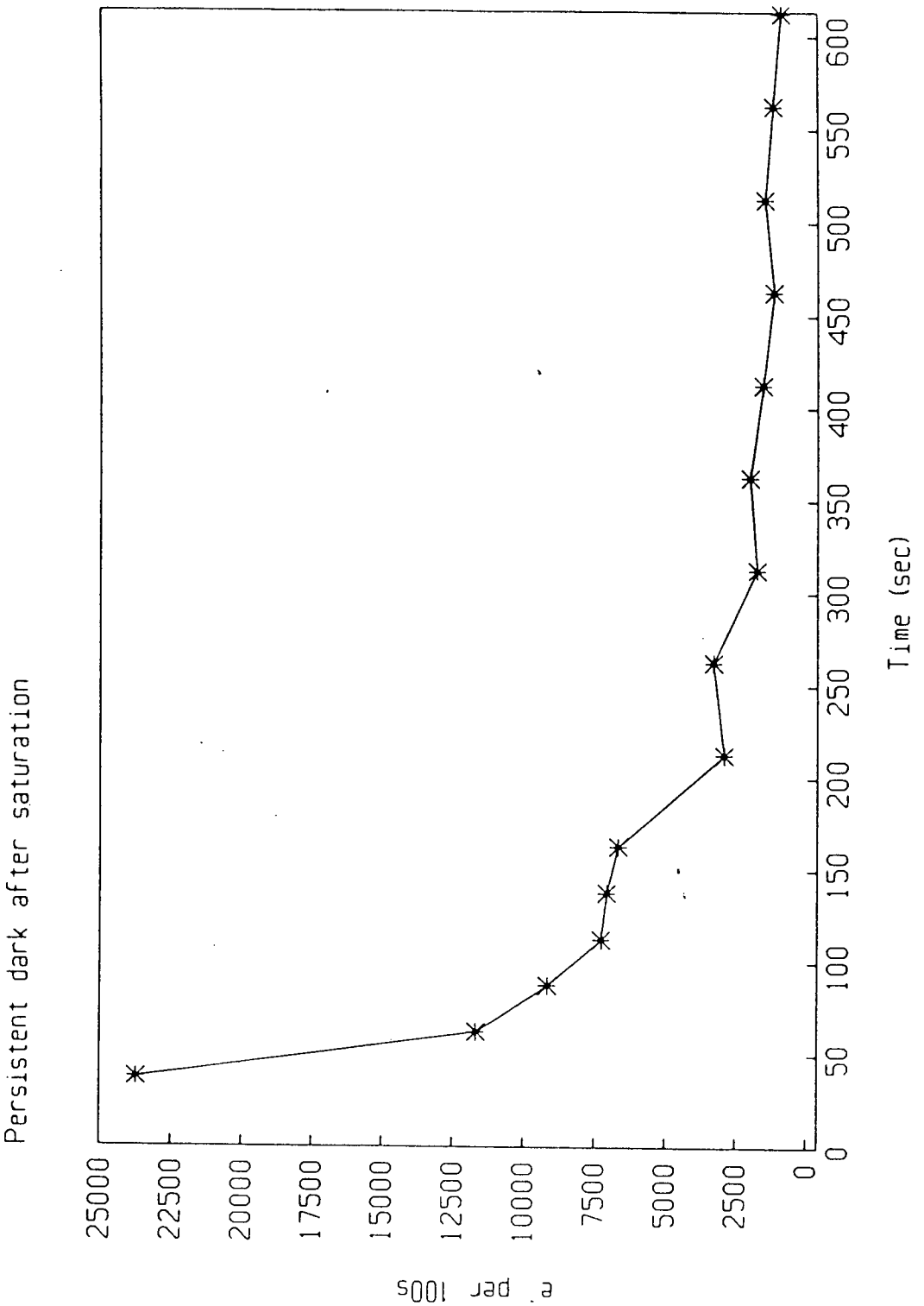

with an unsaturated Hg arc spectrum. The sharp weaker lines in the remnant spectrum would correspond to lines not saturated in the first readout. The equally strong lines (each of about $1.8 \times 10^5 e^-$) would correspond to positions of saturated lines in the first readout. Since the saturation charge is $2 \times 10^7 e^-$, this would imply that almost 1% of the signal could be retained by the incompleteness of a single readout. This is a rather large effect. Consequently, multiple erasure readouts should normally be used.

2.3.7 THE PERSISTENCE PHENOMENON

Figure 2.2 shows the result of subsequent readouts after the incomplete readout test. The readout number and the time elapsed since the initial readout are also shown for each spectrum. The initial saturated readout would have a readout number RO#=0. The spectra are all scaled to the same exposure time of 100 seconds. The apparent higher noise in the first couple of spectra is the artifact of scaling from a shorter exposure time. One can observe from this time series in Figure 2.2 that the residuals at the positions of the arc line persist for a long time and after many readouts. This persistence phenomenon does not have the same characteristics as the effect of incomplete readout discussed earlier. The effect cannot be reduced by performing multiple readouts. It would decay only as time elapses. The reason for this persistence phenomenon is still unknown. There has been suggestion that it results from the creation of surface states in the silicon by the initial

light exposure. The electron/hole pairs from these regions would diffuse towards the depletion region only over a long time scale. Figure 2.3 shows the time decay of the phenomenon. In view of this, one really should delay new exposures for a certain amount of time after a strong exposure. This is especially important if the new exposure is long and weak.

2.3.8 COSMIC-RAY EVENTS

Electron/hole pairs can be generated in the silicon diode from the passage of a cosmic ray event. Such event will produce a narrow emission spike of several pixels in width, superimposed on the spectrum (Vogt [1981]). Because the frequency of such occurrence is about one in two to four hours (Vogt et al. [1978]), long exposures can be affected. Johnson [1984b], however, has pointed out that sharp emission spikes in the spectra can also be the result of high frequency (around the sampling frequency) noise pickups. Cosmic-ray events have been observed with the UBC-built Reticons on long exposures or time series. In fact, one can see a few of these spikes on the time series plot in Figure 2.2. The two most noticeable but typical spikes can be seen in the spectra at T=263s and at T=463s. The cosmic-ray spikes are generally each of about 2000e^- in height. Their occurrence in Reticon spectrum is about ten per hour at DAO and about twice this at CFHT. Naturally, their pixel positions on the spectrum are random. At times, there can also be spikes caused by alpha particles from the

nuclear decay of radioactive elements in the detector. These are very energetic events of several hundreds of thousands of equivalent photons. A more detailed discussion on the cosmic ray phenomenon can be found in Ninkov [1985]. Reviews on Reticon detectors can be found in Livingston et al. [1976], Walker et al. [1976], Geary [1976], Livingston [1976], Campbell [1977], Vogt et al. [1978], Geary [1979], Percival and Nordieck [1980], Talmi and Simpson [1980], Cochran and Barnes III [1981], Campbell et al. [1981], Vogt [1981], Timothy [1983], and Walker et al. [1985].

2.4 THE GAS ABSORPTION SYSTEM

2.4.1 CHOOSING THE ABSORBING GAS

A suitable gas for the absorption cell should have absorption lines in the spectral region where the Reticon has high detective quantum efficiency. The reference spectral lines should at least be as strong as the stellar lines in the region. The line strength, of course, will be limited by a fixed absorption path length. A convenient length for the absorption cell in most telescope Coudé installations is about one metre. It is desirable for the spectrum of the reference absorption lines to be simple with very few weak lines while the stellar spectrum has some fairly strong lines in the same spectral region. The reference absorption lines should preferably be distributed evenly in wavelength across the coverage of about 150 angstroms by the Reticon array at a reciprocal

dispersion commonly between 2 Å/mm and 10 Å/mm. It is also important for the number of reference lines in the spectrum to be sufficient in the calibration of any high or low frequency structure in the dispersion relation. But there should still be sufficient gaps between the reference lines where unblended stellar lines can be found. Conversely, it is also desirable for the reference lines not to be blended too heavily with strong stellar features. The blending between the lines is, however, constrained by the range of the topocentric velocities of the stars. A rotational band structure from a selected gas of diatomic or linear polyatomic molecules would satisfy the above criteria. In this case, the reference absorption band of the molecule should not be contaminated by other stable isotopic bands of the molecule. Moreover the spectral region is to be chosen such that contamination by telluric lines would be minimal. This is important in order to avoid the line-blending problems caused by the variable telluric lines.

Campbell and Walker [1979] selected hydrogen fluoride (HF) to be the absorbing gas as suggested by Gerhard Herzberg. The R-branch of the (3-0) vibration rotation band of HF in the λ8700 region fulfils most of the mentioned criteria. For a given radial-velocity change, the λ8700 region also gives a factor of two larger Doppler shift in wavelength than in the conventional blue spectral region. There are several weakly-blended strong stellar lines in the spectral region around λ8700 for stars of spectral type between F5 and K. Figure 2.4 shows several typical spectra

Figure 2.4 Stellar spectra in the region of λ8700

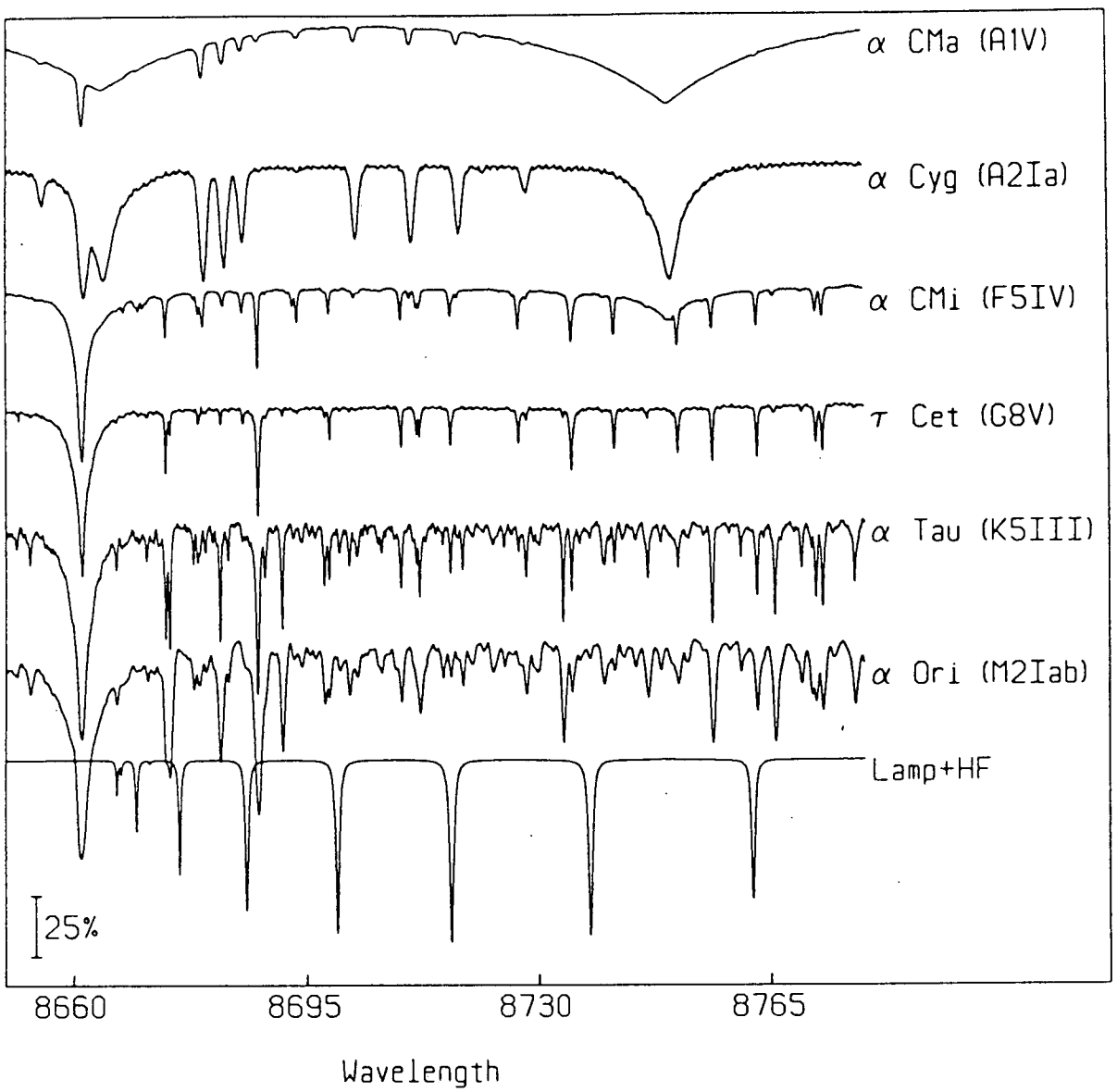

in this spectral region. The prominent stellar lines in the region are various Fe I lines and the Ca II λ8662 line. For stars of earlier spectral type than F5, several Paschen and N I lines are also present. There are almost no telluric lines in this particular spectral region except towards the longer wavelength where the P-branch of the absorption band is located. Fluorine has no other stable isotope while the molecular bands of DF are not in the same spectral region. For similar reasons, the HF spectrum in the infrared has been considered to be the most suitable for the study of diatomic molecular line shapes (Kuipers [1958]). Moreover, there is an increased interest in the use of HF lasers to deliver large specific power densities (Hough [1977]). Consequently, HF has also been one of the most completely studied diatomic molecules in chemistry. Wavelengths and other parameters for the absorption lines in the band are much better known than for other molecules. Cochrane et al. [1982], after an extensive search, have also concluded that HF may be the most suitable gas.

There are some disadvantages in using the (3-0) HF lines. HF is a dangerous gas and is not the easiest to handle. Moreover, the absorption cell must also be heated to 100°C in order to avoid polymerisation of the HF molecules. The λ8700 region of the (3-0) band also coincides with the low reflectivity dip of aluminum. For freshly deposited aluminum, the reflectance at λ8700 is only about 89%. The reflectance of overcoated aluminum is very much lower. Because there are up to ten or more reflections in a

Coudé-Reticon system, the loss in the through-put becomes very high. The use of silver high red reflecting surfaces to improve on the through-put is almost mandatory. The reflectance of silver at λ8700 is over 98%. The silver optics on the DAO 1.22m telescope, however, deteriorate badly within a week after they are freshly re-surfaced. This implies that the high red reflectance Coudé train would not be readily available at all times. This rapid deterioration of the red optics has not been observed on the red Coudé train at either CFHT or UBC. This may be helped by the much drier conditions at CFHT while an air conditioning system is used at the UBC 0.4m telescope. Gold optics have now been used at the DAO 1.22m Coudé train to improve the red through-put. One way to alleviate the problem is to use the (4-0) band at λ6750 instead of the (3-0) band. More (4-0) HF lines can also be observed over the same amount of spectral coverage. This may help to improve the wavelength calibration. At the present time, however, the available absorption cells are too short such that the (4-0) HF lines are only about 10-15% in depth compared to about the 60-70% depth for the (3-0) lines. To increase the HF line strength, one has to increase the absorption path length and this will imply the use of multi-pass absorption cell. There are also a few more telluric lines in the region of λ6750 to complicate matters.

2.4.2 PHYSICAL AND CHEMICAL PROPERTIES OF HF

Hydrogen fluoride (anhydrous hydrofluoric acid) has a chemical formula of simply HF. It is colourless and has a boiling point of 19.51°C. Hence it can be in liquid or gas phase over the normal range of observatory temperatures. It is a very strong dehydrating agent. In fact, because of its strong affinity for water, a leak of HF gas into moist air will produce visible fumes. There will also be a high heat release when HF is dissolved in water. HF is very corrosive and will rapidly attack quartz, silicates, and glass. Steel will be readily corroded by HF at temperatures above 65°C. Being an acid, HF will react with oxides and hydroxides of metals to form water and fluoride salts. It is also a catalyst for organic reactions. The physical and chemical properties of HF have been described in Simons [1950,1964].

2.4.3 SAFETY PRECAUTIONS ON WORKING WITH HF

HF is toxic. Inhalation of HF vapour can cause coughing and a sense of hampered breathing. The sharp and penetrating odour of the vapour, however, will usually limit the amount of inhalation to below a serious toxic level. In the event that one cannot escape from the vapour, breathing through dry clothing or cloth may save one's life. Inhalation of 100% oxygen must be administered to the victim immediately after the exposure to HF vapour. HF in either the vapour or liquid phase is very corrosive and will attack unprotected skin. One who has contact with HF must be subjected immediately to a drenching shower of water. A physician

should be consulted as soon as possible after any exposure, even if the injury appears to be minor. Adequate safety precautions must be taken when and wherever HF is involved. Availability of adequate gas masks, HF resistant gloves, goggles, and head coverings is essential. One should also have a full coverage of clothing at all times when working with HF. Even with caution, accidents can still happen e.g. the HF equipment may explode due to sudden pressure buildup as a result of reaction with contaminants. A more detailed discussion on the safety precautions as well as recommended procedure in the case of accidental exposure is given in the published data sheet on hydrogen fluoride by the Matheson Gas Products company.

2.4.4 THE ABSORPTION CELL

The HF system is essentially a closed system consisting of a gas absorption cell which is connected to a reservoir (sample line) of liquid HF. This reservoir of liquid HF will be maintained at a constant temperature to ensure a constant gas pressure (HF vapour pressure) for the cell. The absorption cell itself will also be maintained at a constant operating temperature. The temperature of the cell may be different than that of the HF sample line. The gas handling system consists of various control valves, manometer, and connecting tubings for use in the introduction and removal of HF from the system. The whole system has to be leak proof.

The absorption cell itself is basically a metal tube with windows at both ends. The length of the cell is limited by the amount of available space in front of the Coudé entrance slit in the particular observatory. This is generally about one metre. The inside diameter of the cell should be large enough to accommodate the particular Coudé light beam. This is to ensure that vignetting would not occur when the cell is moved into the beam. At CFHT, this is accomplished by a cell with a large diameter. The HF system used at the DAO 1.22m telescope, however, has a cell with two different inside diameters to match the size of the converging Coudé beam. The large inside diameter at one end of the cell is about 4.0cm while the smaller diameter at the other end of cell, towards the spectrograph entrance slit, is about 1.0cm. The outside diameter of the cell is also smaller at the small end to avoid getting in the way of the guiding beam.

HF gas molecules have a tendency to form polymers at temperatures less than 70°C (Meredith [1972b]). In addition to the monomers, dimers $(HF)_2$, zig-zag shaped chain tetramers $(HF)_4$, and the ring shaped cyclic hexamers $(HF)_6$ are also present at lower temperatures. Discussions on the polymerisation of gaseous HF molecules can be found in Jarry and Davis [1953], Smith [1958,1959], Herget et al. [1960], Huong and Couzi [1969], Janzen and Bartell [1969], Himes and Wiggins [1971], and Hinchen and Hobbs [1979]. The presence of these polymers would greatly reduce the number of monomeric HF molecules available for the formation of the

reference absorption lines. Consequently, the HF absorption cell has to be heated and maintained at a temperature greater than 100°C in order to minimise polymerisation (Kuipers [1958], Herndon et al. [1962], Meredith and Smith [1974]).

Operation at the high temperature is accomplished by heating coils wrapped around the cell and part of the gas handling system. A thermocouple is used to monitor the temperatures at both ends of the cell. A feed-back temperature control unit was originally used to maintain a stable temperature. It was found that a stable voltage applied to the heating coil would be sufficient. It takes several hours for the temperature of the cell to reach equilibrium after the start of the heating process. The average temperature obtained from the two ends of the cell may not be the same as that of the HF gas inside the cell. It is also quite conceivable for the HF gas to have a rather non-uniform temperature profile along any cross-section of the cell. The heated absorption cell is thermally insulated from the surroundings in order to minimise its effect on the seeing condition of the stellar image. This also helps to maintain a stable cell temperature. Fibreglass is used to provide the insulation. An earlier version of the HF system even has the entire cell placed in a polyethylene covering. Continuous forced air circulation to the outdoor was then applied to the polyethylene cover. This also helps to minimise the danger of a possible HF gas leakage from the system. The system at CFHT uses a plexiglass cover instead

of the polyethylene covering.

At room temperature, steel HF absorption cells had been used in chemistry experiments (Naude and Verleger [1950], Jaffe et al. [1965]). Some metals become HF resistant after a coating of fluorides has been formed on the surface. Nickel is one such metal and it has been used for the construction of HF absorption cells or parts of the associated gas handling system (Kuipers et al. [1956], Kuipers [1958], Smith [1958], Rothschild [1964], Huong and Couzi [1969]). The fluorocarbon polymer Kel-F (copolymers of vinylidene fluoride and chlorotrifluoroethylene) has also been used for the construction of HF cells and gas handling systems (Hinchen [1974], Hinchen and Hobbs [1979], Wickliffe and Rollefson [1979]). Discussions on the properties of Kel-F can be found in Bryce [1964]. The most common material used for the contruction of HF cells and gas handling systems in chemistry experiments is monel (Kuipers et al. [1956], Kuipers [1958], Herndon et al. [1962], Mason and Nielsen [1967], Janzen and Bartell [1969], Huong and Couzi [1969], Wiggins et al. [1970], Himes and Wiggins [1971], Meredith [1972b], Spellicy et al. [1972], Guelachvili [1976]). Monel is one of the most HF resistant metals at high temperatures. Consequently, it has been chosen for the construction of the HF cell and the associated gas handling system for both HF systems at CFHT and DAO. It is advantageous to use the same metal for both the cell and the gas handling system. Differential thermal expansion between different metals could cause gas leakage at the various

joints in the system. Control valves as well as the pressure gauge used in the gas handling system are also HF resistant.

2.4.5 THE CELL WINDOWS

The transparent windows for the cell must also be HF resistant at the high operating temperatures. Many types of window, depending on the spectral region, have been used on HF cells in chemistry experiments. Rothschild [1964] used polyethylene windows for the cell. Silver chloride windows have also been used (Adams and Katz [1956], Smith [1958], Mason and Nielsen [1967]). Kuipers et al. [1956] and Kuipers [1958] used calcium fluoride windows. Huong and Couzi [1969], however, used all three types of window depending on the wavelength region. Plexiglass windows have also been used (Naude and Verleger [1950], Fishburne and Rao [1966]). Plexiglass windows were once used on the DAO system. Their transmission property deteriorated rapidly after reacting with HF at the high operating temperatures. The most common types of window used for HF cells in chemistry experiments are made of sapphire (Herget et al. [1960], Mann et al. [1961], Herndon et al. [1962], Webb and Rao [1966], Wiggins et al. [1970], Himes and Wiggins [1971], Spellicy et al. [1972], Meredith [1972b], Hinchen [1974], Guelachvili [1976], Hinchen and Hobbs [1979]). Sapphire has excellent optical quality and is very HF resistant at the high operating temperatures. Consequently, sapphire windows were chosen for the HF cells at both CFHT and DAO. The sapphire windows are also made with optimum transmission at the λ8700

region. Teflon (tetrafluoroethylene polymers) rings or gaskets are used to seal the windows onto the absorption cell.

Thin windows give higher transmission and are more easily heated to the operating temperature. They are, however, more fragile and have been known to crack under pressure during the tightening-down process. Thick windows have the advantage of minimising the effect of interference fringe pattern generated from poor quality thin windows. Basically, a thin window can act as a Fabry-Perot etalon. Fringe patterns had been observed with defective thin windows. Figure 2.5 shows the spectrum of α Lyrae taken with and without the HF absorption cell containing the defective window. Figure 2.5a is the spectrum taken without the cell in the beam. Figure 2.5b is that taken with an empty (no HF) absorption cell in the beam. Figures 2.5c and 2.5d are, respectively, spectrum of α Lyrae and a flat-field lamp taken with the loaded (containing HF) absorption cell in the beam. The observed fringe pattern is wavelength dependent and is not perfectly reproducible. Flat-fielding techniques are not adequate to reduce the residual fringe pattern to much below one percent of the continuum. Figure 2.6a shows the fringe pattern after dividing a lamp spectrum taken with an empty HF cell by another lamp spectrum taken with the cell out of the beam. Figure 2.6b shows the pattern after dividing the spectrum in Figure 2.5b by that in Figure 2.5a. Figure 2.6c shows the residual of the fringe pattern after dividing the spectrum in Figure 2.5b by those in Figures

Figure 2.5 Fringe pattern from defective cell window

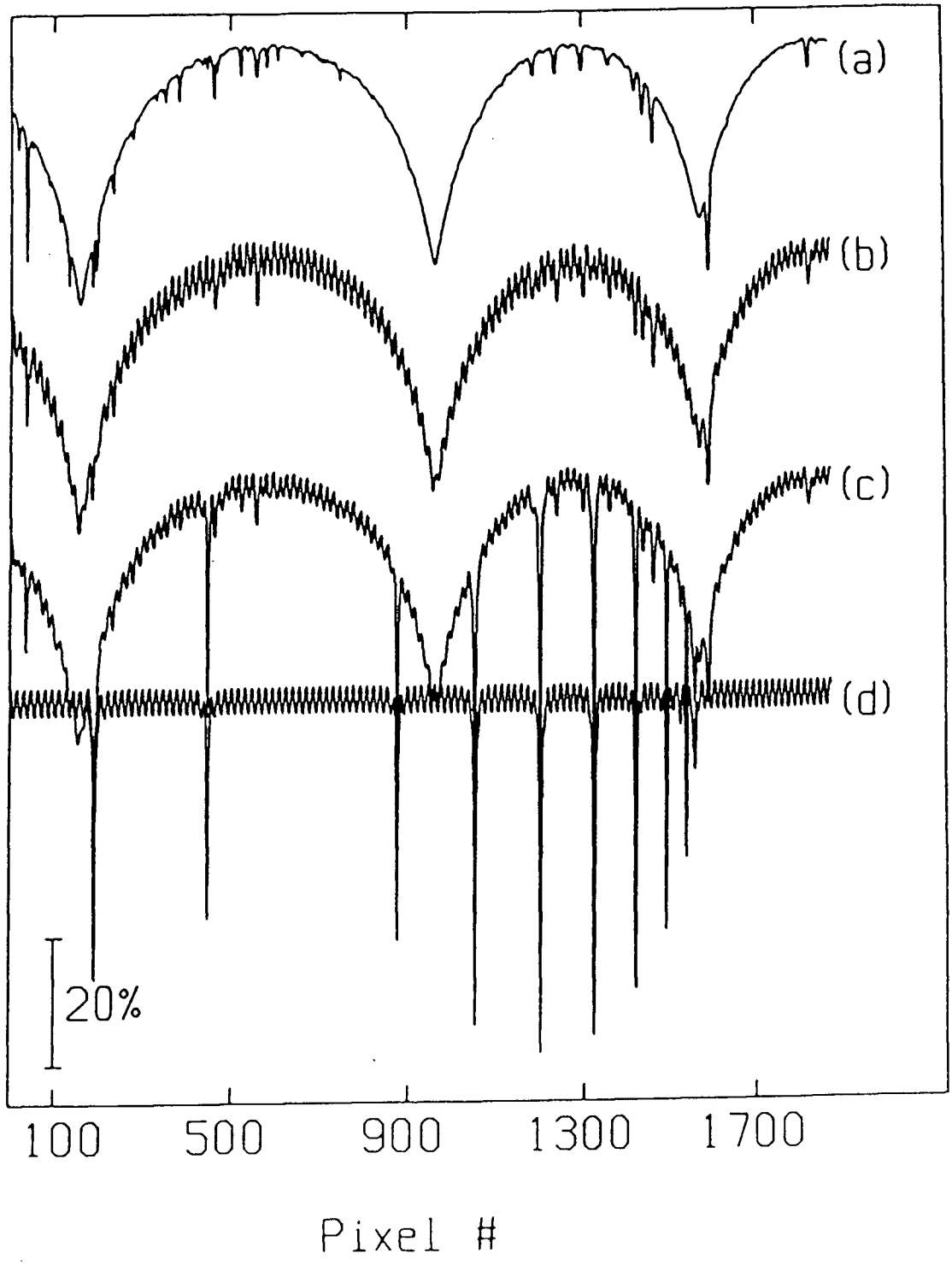

Figure 2.6 Attempts to flat-field the fringes

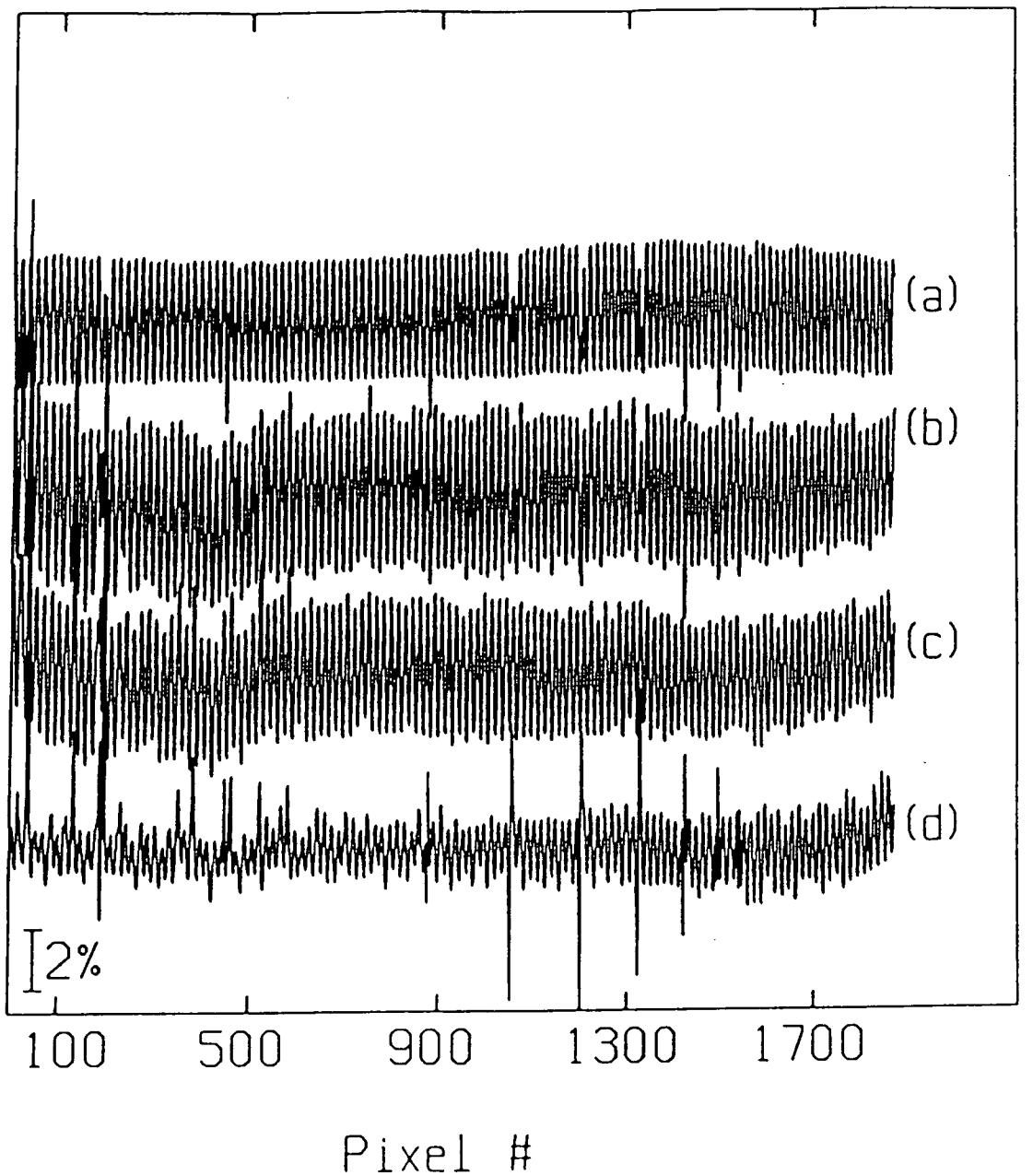

2.5a and 2.6a. Figure 2.6d shows the result of dividing the spectrum in Figure 2.5c by those in Figures 2.5a and 2.5d.

2.4.6 OPERATION OF THE GAS HANDLING SYSTEM

The HF system has to be leak-proof. A leak of HF gas into the surroundings could be disastrous to the optics in most observatories. A leak of air into the HF system can also be very undesirable. Contaminants e.g. water vapour can react with the HF and cause severe damage (corrosion) to the entire HF system. The pressure gauge is especially vulnerable to this type of corrosion. Collision of the HF molecules with foreign gases will both broaden and alter the rest wavelengths of the HF reference lines. This highly variable systematic error is almost impossible to correct at the time of data reduction. A rough search for possible leaks in the system can be accomplished using the pressure gauge and the various control valves to isolate, one at a time, selected sections of the system. A helium leak-tester is required for a more detailed check on the system. It is desirable to mount the whole gas handling system on a single metal plate. This will help to minimise vibration-induced leaks when the system is being transported. Joints have been known to become loose during transportation of the HF system.

There are several operation modes for the HF system. They are :

(a) distillation of sufficient HF from the lecture bottle into the HF reservoir (sample line).

(b) introduction of the HF gas into the heated absorption cell and maintaining a constant HF gas pressure by using a melting ice bath around the sample line.

(c) condense all the HF gas from the absorption cell back into the sample line.

(d) removing all the HF gas from the system.

Normal usage of the HF system involves only the operation modes (b) and (c). Modes (a) and (d) are used only very infrequently. Operations of the HF system should be performed near an exhaust fume-hood. This is especially recommended for the modes (a) and (d).

Figure 2.7 shows the schematic of a generalised HF system. Half-inch monel tubings are used throughout the system. This large diameter helps to speed up any HF distillation process. The valve V6 is the control valve associated with the commercial lecture bottle of HF e.g. from Matheson Gas Products. It is closed for most of the times. For the operation mode (a), all the control valves in the system are initially closed after achieving a good vacuum throughout the entire the system. With the Kel-F tube immersed in a methanol-dry-ice bath, the valves V6 and V5 are opened. The amount of HF distilled over into the Kel-F tube can be measured by examining the level of the liquid HF in this translucent tube. A lamp is usually required to help observe the liquid in the tube. Pure liquid HF should be colourless. Any visible colour seen on the liquid in the Kel-F tube would imply that the HF is probably contaminated

Figure 2.7 Schematic of a generalised HF system

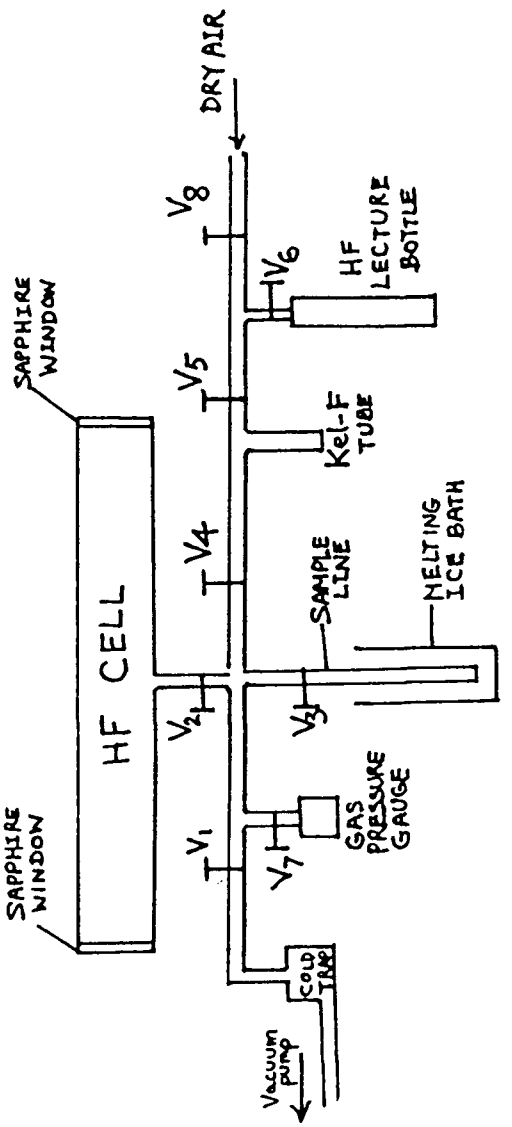

and should be discarded. This can be accomplished by first closing valve V6 and immersing the cold trap in a liquid-nitrogen bath. With the vacuum pump turned on, opening valves V1 and V4 will remove all the HF from the system into the cold trap. The vacuum pump and cold trap (in a methanol-dry-ice bath) can also be used to speed up the distillation of HF from the lecture bottle into the Kel-F tube.

If the HF visible in the Kel-F tube is clear, it can be distilled into the sample line. With valve V6 closed and a methanol-dry-ice or liquid-nitrogen bath around the sample line, opening valves V4 and V3 will transfer all the HF from the Kel-F tube into the sample line. The procedure can be repeated until an appropriate amount of HF has been distilled into the sample line. This is about 6 cm^3 of liquid HF for the HF system at DAO. The amount distilled is monitored by the intermediate transfer into the Kel-F tube of known volume. There should be sufficient HF in the sample line such that some liquid HF would still remain in the sample line after HF gas is released into the absorption cell. This also imposes a lower limit on the volume of the sample line. Initially, additional HF is also required to form the fluoride coatings on the inner surface of the cell and gas handling system. After completing the transfer, valve V3 can be closed and residual HF in the rest of the system is removed using the vacuum pump and cold trap. With valve V3 opened and a methanol-dry-ice bath around the sample line, any foreign gas in the system can also be

removed using the pump and cold trap. This should be a very brief process since the vapour pressure of HF is non-zero at dry-ice temperature. Using liquid nitrogen, however, would also freeze any trapped air. A more involved procedure to distill higher purity HF from the standard commercial HF lecture bottle is described by Wickliffe and Rollefson [1979].

For operation mode (b), most of the non-essential parts of the system can be removed. These are the vacuum pump, cold trap, Kel-F tube, and HF lecture bottle. The valves V1 and V4 are closed for the entire duration of the operation. The HF absorption cell must be heated to the operating temperature of about 100°C prior to the introduction of the HF gas. Condensation of the HF gas can occur if the cell is not heated when the HF gas enters the cell. Brown coloured liquid condensations on the windows may be related to this problem. Heating the windows with a 'heat-gun' may remove the condensation. With a heated cell, opening valves V2 and V3 will introduce HF gas into the cell. A melting-ice bath is placed around the sample line to ensure a constant gas pressure in the system. This will be the vapour pressure of HF at 0°C and is about 360 mm Hg. The fact that the pressure is less than the atmospheric pressure has added an extra margin of safety to the operation. If a leak develops, air will leak into the system rather than having substantial amount of HF leaking out. Valve V7 can be opened to allow the pressure gauge to monitor the HF pressure. The vapour pressure of HF is given by Jarry and Davis [1953] :

$$\log_{10}P = A - B / (C + t) \qquad (2.2)$$

where P = HF vapour pressure in mm Hg

A = 8.38036 ± 0.10896

B = 1952.55 ± 125.85°

C = 335.52 ± 8.15°

t = temperature in °C

In order to maintain a more consistent temperature everytime, one uses distilled water and ice formed from distilled water for the ice bath. A more stable temperature can be maintained if the ice is crushed into smaller pieces before being used in the ice bath.

For operation mode (c), collecting the HF back into the sample line can be accomplished by slowly freezing the sample line to liquid nitrogen temperature. Rapid freezing may cause clotting of the system by frozen HF. Residual HF or foreign gases in the system can again be removed with the vacuum pump and cold trap. Similarly, for operation mode (d) to remove all HF from the system, the vacuum pump and cold trap are used with valves V1, V2, V3, V4, V5, and V7 opened. Dry air or nitrogen can also be introduced to flush the system by opening valve V8. In this case, the vacuum pump and cold trap would be replaced by a tubing to bubble the output gas through a sodium-hydroxide solution and into an exhaust fume-hood.

2.4.7 PLACEMENT OF THE CELL

Instead of the conventional slit, an image slicer is generally used to reduce the loss in through-put caused by

poor seeing conditions. The image slicer would also reduce the amount of guiding error. At both CFHT and DAO, the HF cell is placed between the last Coudé flat mirror and the image slicer. The cell can also be accurately and easily moved in or out of the Coudé beam. The alignment of the cell with respect to the beam has to be accurate in order to avoid vignetting. Generally, the cell is aligned against the iris diaphragm that is in place for use on the lamp exposures. This iris diaphragm is generally well aligned with respect to the beam. At DAO, the alignment of the iris can be checked by viewing the primary mirror through the iris from behind the image slicer. This is accomplished by pointing the telescope at the blue sky or reflecting light off the inside of the dome. The image slicer may also be replaced by a small circular aperture for this purpose. To align the cell with the image slicer in place, one can shine light along the beam path from behind the image slicer by way of the viewing optics. Alignment of the cell can then be accomplished by viewing the light rays coming through both the cell and the iris.

Chapter 3

THE HF SPECTRUM

3.1 INTRODUCTION

The chosen wavelength reference lines arise from the vibration-rotation transitions in the ground electronic state ($X^1\Sigma^+$) of HF between the vibrational level v=0 (ground level) and v=3 i.e. they belong to the second overtone of the vibration-rotation band, where v is the vibrational quantum number. The earliest experimental study of the HF vibration-rotation band (that of the (1-0) fundamental) was carried out by Imes [1919]. The second overtone (3-0) band as well as the (4-0) band were first photographed by Kirkpatrick and Salant [1935]. Since then, the wavenumbers of the various vibration-rotation bands have been measured. The (1-0) and the (2-0) bands were measured by Talley et al. [1950], Kuipers et al. [1956], Herget et al. [1962], Webb and Rao [1968], and Guelachvili [1976]. Naude and Verleger [1950] measured the (2-0), (3-0), and the (4-0) bands while Mann et al. [1961] measured, from flame spectra, 23 different bands ranging from (1-0) through (9-4). Deutsch [1967a] measured the (1-0), (2-1), and (3-2) vibration-rotation bands from HF laser transitions while Kwok et al. [1970] measured only the (1-0) and (2-1) bands. Sengupta et al. [1979] measured the HF laser transitions from the (1-0) through to the (6-5) band. The most recent measurement of the (3-0) band was performed by Fishburne and Rao [1966] who also observed the (4-0) and (5-0) bands. Pure

rotational transitions of HF have also been observed by Kuipers et al. [1956], Rothschild [1964], Deutsch [1967b], Mason and Nielsen [1967], Akitt and Yardley [1970], and Sengupta et al. [1979]. Meanwhile, electronic transitions have been observed by Safary et al. [1951], Johns and Barrow [1959], Di Lonardo and Douglas [1973], and Douglas and Greening [1979]. Most of the above references also provided experimentally derived molecular constants for HF.

The rotational selection rule for the vibration-rotation bands is $\Delta J=\pm 1$ with J being the rotational quantum number. The $\Delta J=+1$ transitions give rise to the lines in the R-branch of the band while $\Delta J=-1$ transitions form the P-branch. There is no Q-branch ($\Delta J=0$ transitions) for HF. The various transitions in the (3-0) vibration-rotation band are illustrated in Figure 3.1. The running index number m is equal to J_i+1 (or J_f or J') for the lines in the R-branch. And it takes on the values of $-J_i$ (or -J") for the lines in the P-branch. J_i (or J") and J_f (or J') are, respectively, the J values in the lower ($v=0$) and the upper ($v=3$) vibrational level.

3.2 MOLECULAR CONSTANTS FOR HF

3.2.1 BASIC EQUATIONS AND CONSTANTS

The wavenumber of a line can be obtained directly from the difference between the particular upper and lower energy levels. The term value $T(v,J)$ for the v-vibration and J-rotation level is the sum of a vibration term $G(v)$ and a

Figure 3.1 The (3-0) vibration-rotation band of HF

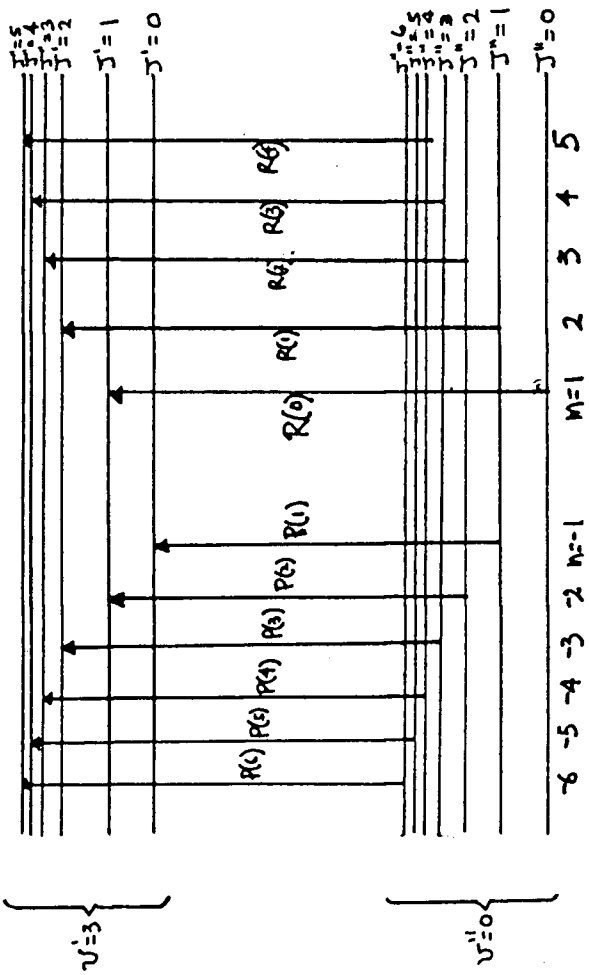

rotation term $F_v(J)$:

$$T(v,J) = G(v) + F_v(J) \tag{3.1}$$

$$G(v) = \omega_e(v+1/2) - \omega_e x_e(v+1/2)^2 + \omega_e y_e(v+1/2)^3 - \omega_e z_e(v+1/2)^4 \tag{3.2}$$

$$F_v(J) = B_v J(J+1) - D_v J^2(J+1)^2 + H_v J^3(J+1)^3 - L_v J^4(J+1)^4 \tag{3.3}$$

The terms ω_e, $\omega_e x_e$, $\omega_e y_e$, and $\omega_e z_e$ are some of the anharmonic constants. The values of these constants are listed in Table 3.1. Other anharmonic constants can be found referenced in Huber and Herzberg [1979].

The rotation constants B_v, D_v, and H_v can be expressed in power series of $(v+1/2)$ with the anharmonic constants as coefficients (Herzberg [1950], Rao and Mantz [1972], Johns and Barrow [1959]). The anharmonic constants themselves can be expressed in terms of the Dunham coefficients. The correspondence between the anharmonic constants and Dunham coefficients, Dunham corrections, can be found in Dunham [1932]. The term value $T(v,J)$ as well as $G(v)$, B_v, D_v, and H_v can be expressed more explicitly using the Dunham coefficients:

$$T(v,J) = \Sigma_{im} Y_{im}(v+1/2)^i J^m(J+1)^m \tag{3.4}$$

$$G(v) = \Sigma_i Y_{i0}(v+1/2)^i \tag{3.5}$$

$$B_v = \Sigma_i Y_{i1}(v+1/2)^i \tag{3.6}$$

$$D_v = -\Sigma_i Y_{i2}(v+1/2)^i \tag{3.7}$$

$$H_v = \Sigma_i Y_{i3}(v+1/2)^i \tag{3.8}$$

$$L_v = -\Sigma_i Y_{i4}(v+1/2)^i \qquad (3.9)$$

The values for most of the Dunham coefficients can be found in Webb and Rao [1968]. Values for Y_{04} and Y_{13} can be found in Deutsch [1967b] and Mann et al. [1961], respectively. The Dunham anharmonic coefficients are usually expressed in terms of B_e, ω_e, and the Dunham potential constants $a_1,\ldots,$ a_6. Formulae for the Dunham coefficients have been published by Dunham [1932], Sandeman [1940], Woolley [1962], Niay et al. [1977], Bouanich [1978a], and Ogilvie and Tipping [1983]. The conversion formulae between the potential constants a_i and c_i are given in Sandeman [1940]. Theoretical Dunham coefficients have been calculated with contributions up to the order of $(a_1)^6$. The values for the potential constants a_i used in the calculation are taken from Ogilvie and Koo [1976]. The formulae used for Y_{06}, Y_{15}, and Y_{24} are taken from Woolley [1962] while those for Y_{07}, Y_{08}, and Y_{16} are from Ogilvie and Tipping [1983]. Formulae for the other coefficients are taken from Bouanich [1978a]. These calculated Dunham coefficients provide a easy way to compute the various energy levels which will be required in any line-strength and linewidth calculations.

3.2.2 DERIVATIONS OF NEW CONSTANTS AND WAVELENGTHS

Using Equation 3.3, one can derive the wavenumbers of lines in a $(v-0)$ vibration-rotation band. The wavenumbers are functions of the v and J values, the band centre ν_0 (the wavenumber corresponding to which would be the pure

Table 3.1 Published molecular constants for HF

	reference
ω_e = 4138.7666 cm^{-1}	Webb and Rao [1968]
$\omega_e x_e$ = 89.88 cm^{-1}	Webb and Rao [1968]
$\omega_e y_e$ = 0.90 cm^{-1}	Webb and Rao [1968]
$\omega_e z_e$ = -0.0110 cm^{-1}	Webb and Rao [1968]
B_e = 20.9561 cm^{-1}	Ogilvie and Koo [1976]
a_e = 0.798 cm^{-1}	Webb and Rao [1968]
γ_e = 1.27×10^{-2} cm^{-1}	Webb and Rao [1968]
D_e = 0.0021497 cm^{-1}	Ogilvie and Koo [1976]
β_e = 6.133×10^{-5} cm^{-1}	Ogilvie and Koo [1976]
H_e = 1.6445×10^{-7} cm^{-1}	Ogilvie and Koo [1976]
r_e = 0.9168Å	Ogilvie and Koo [1976]
ν_0 (1-0) = 3961.4229±0.00025 cm^{-1}	Guelachvili [1976]
ν_0 (2-0) = 7750.7949±0.0015 cm^{-1}	Guelachvili [1976]
ν_0 (3-0) = 11372.807±0.007 cm^{-1}	Fishburne and Rao [1966]
ν_0 (4-0) = 14831.627±0.007 cm^{-1}	Fishburne and Rao [1966]
B_0 = 20.559743±0.000014 cm^{-1}	Guelachvili [1976]
D_0 = $(2.120480 \pm 0.000046) \times 10^{-3}$ cm^{-1}	Sengupta et al. [1979]
H_0 = $(1.6653 \pm 0.0064) \times 10^{-7}$ cm^{-1}	Sengupta et al. [1979]
L_0 = $(1.81 \pm 0.12) \times 10^{-11}$ cm^{-1}	Sengupta et al. [1979]
B_1 = 19.787478±0.000014 cm^{-1}	Guelachvili [1976]
D_1 = $(2.063996 \pm 0.000056) \times 10^{-3}$ cm^{-1}	Sengupta et al. [1979]
H_1 = $(1.5942 \pm 0.0068) \times 10^{-7}$ cm^{-1}	Sengupta et al. [1979]

$L_1 = (1.46\pm0.11)\times10^{-11}$ cm^{-1}	Sengupta et al. [1979]
$B_2 = 19.034931\pm0.000032$ cm^{-1}	Guelachvili [1976]
$D_2 = (2.00958\pm0.00011)\times10^{-3}$ cm^{-1}	Sengupta et al. [1979]
$H_2 = (1.523\pm0.013)\times10^{-7}$ cm^{-1}	Sengupta et al. [1979]
$L_2 = (1.32\pm0.12)\times10^{-11}$ cm^{-1}	Sengupta et al. [1979]
$B_3 = 18.2995\pm0.0005$ cm^{-1}	Fishburne and Rao [1966]
$D_3 = (1.948\pm0.006)\times10^{-3}$ cm^{-1}	Fishburne and Rao [1966]
$H_3 = (1.43\pm0.10)\times10^{-7}$ cm^{-1}	Mann et al. [1961]
$B_4 = 17.5829\pm0.0007$ cm^{-1}	Fishburne and Rao [1966]
$D_4 = (1.911\pm0.006)\times10^{-3}$ cm^{-1}	Fishburne and Rao [1966]
$H_4 = (1.23\pm0.15)\times10^{-7}$ cm^{-1}	Mann et al. [1961]

****

vibrational transition), and the rotation constants B_0, D_0, H_0, L_0, B_v, D_v, H_v, and L_v. For example, Mann et al. [1961] have given a power-series representation for the wavenumbers. The recently published values of various ν_0, B_v, D_v, and H_v for the (1-0), (2-0), (3-0), and (4-0) bands are listed in Table 3.1. The most recent values for the other rotation constants can be found in Mann et al. [1961], Fishburne and Rao [1966], and Di Lonardo and Douglas [1973].

A set of consistent molecular constants is required for the calculation of the wavenumbers. The fact that the values for B_0, D_0, H_0, and L_0 have been accurately determined by Sengupta et al. [1979], implies that only the five molecular constants ν_0, B_3, D_3, H_3, and L_3 remain to be determined from published experimental wavenumbers. The problem is basically a least-squares problem to find the five constants

which would minimise the sum of the squares of residuals between the experimental wavenumbers of the lines and the calculated values. This can be accomplished by optimisation methods. The experimental wavenumbers used for the (3-0) band are those from Fishburne and Rao [1966]. A "state of the art" optimisation program has been used to determine optimal values for the constants. The theory of the optimisation method as well as the program is described in Moore [1984]. A review on using the least-squares method to estimate molecular constants is given by Albritton et al. [1976]. As expected from the accuracy of the experimental data, the procedure gives reasonable values for ν_0, B_3, and D_3 but not for H_3 and L_3. A better approach is to derive the values for H_3 and L_3 independently of the data and solve for only ν_0, B_3, and D_3 in the optimisation process.

With the improved values of H_0, H_1, and H_2 from Sengupta et al. [1979], one can solve for Y_{03}, Y_{13}, and Y_{23} in Equation 3.8 with terms up to i=2. The terms H_v for $v \geq 3$ can then be evaluated using Equation 3.8. This is essentially solving for H_v as a function of v, H_0, H_1, and H_2. A similar approximation formula for H_3 in terms of only H_0 and H_1 has been given by Rank et al. [1965]. A value of $1.4523 \times 10^{-7} cm^{-1}$ is subsequently derived for H_3. Similarly, a value of $1.39 \times 10^{-11} cm^{-1}$ is calculated for L_3 using the improved molecular constants from Sengupta et al. [1979]. Most of the derived rotation constants are within the uncertainties of their experimental values. This is also the first time that L_3 is determined. The method is limited by

having accurate rotation constants only for v=0, 1, and 2. Hence, truncation errors are introduced by using only up to the i=2 term in the equations.

After adopting the derived values for H_3 and L_3, the optimisation procedure is used to derive the other three constants from the data. This proves very successful. The final results for the three constants are all compatible with their experimental values given in Table 3.1. The mean residual between the experimental wavenumbers and the calculated values, however, is reduced from ± 0.02 cm^{-1} in using the old molecular constants to ± 0.005 cm^{-1} with the new molecular constants. In fact, this is even slightly smaller than the residual obtained in a forced fourth order polynomial fit of the data. A small improvement may be obtained if one includes the experimental data from Sengupta et al. [1979] on the (3-2) band in the optimisation process. This, however, will add more unknowns into the problem e.g. the (3-2) band centre. The final adopted values for the molecular constants are listed in Table 3.2. Table 3.3 lists both the experimental vacuum wavenumbers and the wavenumbers calculated with the adopted constants. The corresponding J_i, J_f, and m values for each line are also listed.

The vacuum wavenumbers can be converted into air wavelengths by knowing the refractive index of the air. The air refractive index, however, is a function of the wavelength, temperature, air pressure, and water-vapour pressure. The relevant formulae are given in Edlen [1966]. Table 3.4 lists the standard-air wavelengths for both the

Table 3.2 Adopted molecular constants for the (3-0) band

****

ν_0 = 11372.8108 cm^{-1}

B_0 = 20.559743 cm^{-1}

D_0 = 2.12048x10^{-3} cm^{-1}

H_0 = 1.6653x10^{-7} cm^{-1}

L_0 = 1.81x10^{-11} cm^{-1}

B_3 = 18.30016 cm^{-1}

D_3 = 1.9551x10^{-3} cm^{-1}

H_3 = 1.4523x10^{-7} cm^{-1}

L_3 = 1.39x10^{-11} cm^{-1}

****

Table 3.3 Vacuum wavenumbers for the (3-0) band of HF

****

J_i	J_f	m	experimental	calculated
3	2	-3	11236.129 cm^{-1}	11236.1296 cm^{-1}
2	1	-2	11286.120 cm^{-1}	11286.1211 cm^{-1}
1	0	-1	11331.707 cm^{-1}	11331.6998 cm^{-1}
0	1	1	11409.413 cm^{-1}	11409.4033 cm^{-1}
1	2	2	11441.428 cm^{-1}	11441.4304 cm^{-1}
2	3	3	11468.841 cm^{-1}	11468.8493 cm^{-1}
3	4	4	11491.616 cm^{-1}	11491.6213 cm^{-1}
4	5	5	11509.714 cm^{-1}	11509.7119 cm^{-1}
5	6	6	11523.092 cm^{-1}	11523.0911 cm^{-1}
6	7	7	11531.735 cm^{-1}	11531.7330 cm^{-1}
7	8	8	11535.614 cm^{-1}	11535.6160 cm^{-1}

****

experimental and calculated values as well as the corresponding air refractive indices. The "standard air" or the spectroscopic standard temperature and pressure (SSTP) is at 760 torrs, 15°C, and zero water-vapour pressure (Edlen [1966]).

Before the radial velocity of a particular stellar line can be obtained, one has to convert the measured position of the stellar line on the spectrum into a wavelength measurement. The relationship between positions on the spectrum and wavelengths is the dispersion relation. The HF lines are the wavelength-calibration marks on the spectrum. Each HF line provides a correspondence between one position measurement and an absolute wavelength. One of the simplest ways of expressing the dispersion relation is in terms of a polynomial fit between the positions and wavelengths of the HF lines. The accuracy of a radial-velocity determination depends critically on how well this polynomial represents the dispersion relation. There are many causes that can affect the accuracy of the polynomial representation. Two of the most simple causes are the accuracy of the HF line-position measurements and the accuracy of their corresponding absolute wavelengths. The latter, of course, depends somewhat on the criteria of how the line positions are determined. This would be a systematic effect. Systematic zero-point errors may also exist in the experimental values from Fishburne and Rao [1966]. Meanwhile, random experimental errors in these wavelength measurements would also be introduced into the polynomial

Table 3.4 SSTP wavelengths for the (3-0) band of HF

m	experimental	calculated	refractive index
8	8666.4256Å	8666.4241Å	1.00027467
7	8669.3408Å	8669.3423Å	1.00027467
6	8675.8433Å	8675.8440Å	1.00027467
5	8685.9275Å	8685.9291Å	1.00027466
4	8699.6069Å	8699.6029Å	1.00027466
3	8716.8828Å	8716.8765Å	1.00027465
2	8737.7680Å	8737.7662Å	1.00027464
1	8762.2864Å	8762.2939Å	1.00027463
-1	8822.3731Å	8822.3788Å	1.00027460
-2	8858.0087Å	8858.0078Å	1.00027458
-3	8897.4193Å	8897.4189Å	1.00027457

dispersion fit. This would be a random effect. The experimental values from Fishburne and Rao [1966] might also contain line-to-line wavelength variations caused by pressure-induced differential shifts. The amount of these shifts is not appropriate for the particular operation condition of the HF cell. It is probably more satisfactory to adopt the wavelengths calculated from molecular constants to be the absolute reference wavelengths. Appropriate shift corrections can then be applied to them. A very small zero-point error may still exist in the adopted reference wavelengths. This would be caused by zero-point error in the experimental data of Fishburne and Rao [1966]. For most applications and especially in relative radial-velocity

works, however, the adopted values should be adequate. Further improvement on the reference wavelengths can be achieved when line-to-line pressure-induced line shifts are taken into account. This is especially the case for application at the 360 torrs pressure of the HF cell. Small line shifts caused by slight temperature and pressure deviations from the mean operation condition of the cell can also be corrected. This point will be discussed in detail later in the chapter.

A third order polynomial dispersion fit was applied to a typical HF spectrum taken at the CFHT Coudé. The reciprocal dispersion was 4.8Å/mm or 0.0713Å/pixel. A rms residual of ±0.00224Å was obtained for the fit when the experimental values from Table 3.4 were used as the reference wavelengths. An improved rms residual of ±0.00155Å was obtained when the calculated values from Table 3.4 were used as the reference wavelengths. The improved fit may imply an improved representation of the dispersion relation.

3.3 THE TEMPERATURE AND PRESSURE OF THE HF GAS

3.3.1 INTRODUCTION

One of the technical difficulties with the HF technique is the inability to measure the temperature and pressure of the HF gas accurately inside the cell. The temperature measured with the thermocouple is only the mean outside surface temperature of the cell. The temperature of the HF gas inside the cell can be quite different. Moreover, there

may not be a uniform temperature profile on the cross-section of the cell. This cross-sectional temperature profile may also be variable along the length of the cell. This is especially the case near the windows as well as the location where colder HF molecules are introduced into the heated cell. Hence, depending on the particular path of the stellar beam through the cell, the effective temperature of the HF gas forming the HF reference lines can be different. This difference may depend on many factors such as alignment of the cell with respect to the stellar beam, the atmosphere and Coudé seeing, temperature stability of the cell, as well as the focus of the beam. The measured pressure is subjected to zero-point error of the manometer as well as temperature variations of the ice bath around the sample line.

It is important to maintain a constant temperature for the HF gas throughout any long-term HF project. Assuming the usual temperature-dependent Boltzmann distribution for the population at the various energy levels of HF, a change in temperature would affect the line strength of the HF lines. Many numerical techniques to reduce the observational data e.g. to determine relative HF line positions, would be affected by having to compare HF lines which are different in strength and shape. The pressure-induced line shifts of the HF lines are also sensitive to temperature variations. This can be explicitly due to the variations in the Maxwellian velocity distribution as well as implicitly from the variations in the energy level population. The temperature, of course, would also affect the relative

number of monomers $(HF)_1$ and hexamers $(HF)_6$. This affects both the line strength as well as the pressure shifts. All these problems can be minimised if one can determine the temperature and pressure of the HF gas directly from the observed spectrum. With known temperature and pressure, line-shift corrections can be made at the time of the data reduction.

3.3.2 HF LINE STRENGTH

3.3.2.1 Basic equations

The line strength of a vibration-rotation line per unit-atmosphere gas pressure and in units of $(atm.cm^2)^{-1}$ has been given by Meredith [1972b] and Pugh and Rao [1976] as:

$$S(m) = \{ (1.01325 \times 10^6)\, 8\pi^3 |m| \nu N / (3hcpZ) \} \{ \exp(-E(v_i,J_i)/kT) |\langle v_i J_i | \mu(r) | v_f J_f \rangle|^2 \} \qquad (3.10)$$

where
- c = speed of light
- h = Planck constant
- k = Boltzmann's constant
- T = temperature in kelvin
- ν = wavenumber of line
- m = the running index of the line
- N = number of absorbing molecules per cm^3
- p = gas pressure in atmospheres
- Z = total partition function
- $E(v_i,J_i)$ = energy level of the lower state

$\mu(r)$ = electric dipole moment function

Equation 3.10 uses the convention of subscript i (or double primes) and subscript f (or single prime) to indicate the lower and upper energy level, respectively. The Dirac bra < | and ket | > representations are also used to express the matrix element of the electric dipole moment. Equation 3.10 does not take into account the effects of induced emission by not including the factor $\{1-\exp(-hc\nu/kT)\}$. This factor, however, is very close to 1 for vibration-rotation transitions in the infrared and at moderate temperatures (Pugh and Rao [1976]).

3.3.2.2 The Herman-Wallis factors

Herman and Wallis [1955] have pointed out that the electric dipole matrix elements $|\langle v_i J_i|\mu(r)|v_f J_f\rangle|^2$ can be written as the product of a vibrational factor and a vibration-rotation interaction function $F(v_i, v_f, m)$:

$$|\langle v_i J_i|\mu(r)|v_f J_f\rangle|^2 = |\langle v_i|\mu(r)|v_f\rangle|^2 \, F(v_i, v_f, m) \qquad (3.11)$$

The term $F(v_i, v_f, m)$ is the Herman-Wallis factor or F factor. It can be calculated directly from the ratio between the theoretical vibration-rotation and rotation electric dipole matrix elements. This method has been discussed by Bouanich [1977,1978b] who has also given theoretical expressions for the matrix elements. Direct formulae for the factors were first given by Herman et al. [1958] for the (1-0), (2-0), (3-0), and (2-1)

Table 3.5 The a_i's and the M_i's for HF

****

$a_1 = -2.2538$

$a_2 = 3.4882$

$a_3 = -4.4986$

$a_4 = 4.704$

$a_5 = -2.91$

$a_6 = -1.76$

$M_0 = 1.80306$

$M_1 = 1.39366$

$M_2 = -0.0583$

$M_3 = -0.8861$

$M_4 = -0.599$

$M_5 = -0.931$

****

transitions. Improvements on these formulae have been given by Toth et al. [1969,1970], Tipping and Herman [1970a], Tipping and Forbes [1971], Meredith [1972b], Tipping [1976], Ogilvie et al. [1980], Tipping and Ogilvie [1982], and Ogilvie and Tipping [1983]. Several of these recent publications also give formulae for the higher-overtone transitions. The factor can be expressed in terms of a power series expansion in m :

$$F(v_i,v_f,m) = 1 + C(v_i,v_f)m + D(v_i,v_f)m^2 \qquad (3.12)$$

The functions $C(v_i,v_f)$ and $D(v_i,v_f)$ are expressed in terms of the equilibrium internuclear separation r_e, the Dunham potential constants a_i's, $\langle v_f|\mu(r)|v_i\rangle$, B_e, ω_e, and the

M_i's. The M_i's are the coefficients in the power series expansion of the electric dipole moment:

$$\mu(r) = \Sigma_i \, M_i[(r-r_e)/r_e]^i \qquad (3.13)$$

The values for these M_i's have been evaluated by Spellicy et al. [1972], Meredith and Smith [1973], Lie [1974], Sileo and Cool [1976], and Ogilvie et al. [1980]. Meanwhile, the a_i's have been evaluated by Mann et al. [1961], Webb and Rao [1968], and Ogilvie and Koo [1976]. Table 3.5 lists the values of the M_i's from Ogilvie et al. [1980] as well as the values of the a_i's from Ogilvie and Koo [1976]. The vibrational factor $\langle v_i|\mu(r)|v_f\rangle$ can also be expressed in terms of these constants:

$$\langle v_i|\mu(r)|v_f\rangle = \Sigma_i \, M_i\langle v_i|(r/r_e)^i|v_f\rangle \qquad (3.14)$$

Formulae for the expectation values $\langle v_i|(r/r_e)^i|v_f\rangle$ in terms of B_e, ω_e, the a_i's, and M_i's are given in Tipping [1973]. More general expressions can be found in Niay et al. [1979].

The Herman-Wallis factors have not been explicitly published for the (3-0) band of HF. One, however, can derive their values from the ratios between the experimental $\langle v_i|\mu(r)|v_f\rangle$ and $\langle v_iJ_i|\mu(r)|v_fJ_f\rangle$ values measured by Spellicy et al. [1972]. These are listed in Table 3.5. Applying a least-squares optimisation procedure on the experimental data, optimal values of -1.0788×10^{-2} and 6.3528×10^{-4} are determined for $C(v_i,v_f)$ and $D(v_i,v_f)$, respectively. The least-squares fitted factors are also listed in Table 3.5. Theoretical values

Table 3.6 Herman-Wallis factors for the (3-0) band of HF

m	experimental	least-squares fitted
-4	1.0676	1.0533
-3	1.0301	1.0381
-2	1.0086	1.0241
-1	1.0068	1.0114
1	0.9969	0.9899
2	0.9908	0.9810
3	0.9601	0.9734
4	0.9920	0.9670
5	0.9386	0.9619
6	0.9668	0.9581
7	0.9546	0.9556

for the Herman-Wallis factors have been calculated using the formulae given independently in Tipping and Ogilvie [1982], Tipping and Forbes [1971], and Toth et al. [1969]. The agreement between the theoretical and experimental values is not very satisfactory. This may be caused by the inadequacies of the theories. The experimental values may also carry sizeable errors. In view of these, choosing the least-squares fitted factors for the calculation of gas temperature may be more appropriate.

3.3.2.3 Derivation of gas temperature

For two lines, m_1 and m_2, in the same vibration-rotation band, the ratio between their line strength as given by Equation 3.10 will simply be:

$$S(m_1) / S(m_2) = A\ B \exp([E_2-E_1]/kT) \qquad (3.15)$$

$$A = \{|m_1|\nu_1\} / \{|m_2|\nu_2\} \qquad (3.16)$$

$$B = F(\upsilon_i,\upsilon_f,m_1) / F(\upsilon_i,\upsilon_f,m_2) \qquad (3.17)$$

The m values, Herman-Wallis factors, and the wavenumbers ν are known for the (3-0) band of HF. The difference in energy, E_2-E_1, between the level of the two J states in the ground vibrational level is simply the difference between the corresponding values of $F_\upsilon(J)$ in Equation 3.3 multiplied by hc. Values for B_0, D_0, H_0, and L_0 are accurately known. Hence, if the two lines have different values of J_i, the temperature T can be calculated from Equation 3.15.

The Beer-Lambert law gives the relation which describes the transmission of radiation through a homogeneous gas as:

$$I(\nu) = I_0 \exp(-\kappa(\nu)pL) \qquad (3.18)$$

The terms I_0 and $I(\nu)$ are the continuum and line intensity, respectively. The function $\kappa(\nu)$ is the absorption coefficient. The term L is the length of the absorption path, and p is the pressure of the absorbing gas. The line shape depends on the form of $\kappa(\nu)$. Expressions for $\kappa(\nu)$ in the cases of Gaussian, Lorentzian, and Voigt profiles have been given by Mandin et al. [1980]. The line strength S is simply the

integrated absorption coefficient (Pugh and Rao [1976], Lowry and Fisher [1982], Overend [1982]):

$$S = \int_{line} \kappa(\nu)\, d\nu \qquad (3.19)$$

The relationship between line strength and equivalent width is given in Overend [1982] and Korb et al. [1968]. By considering the dispersion of the spectrum, the integral in Equation 3.19 can be performed over the line limits in pixel number. The dispersion is simply the derivative of the polynomial fit between the wavenumbers of the lines and the corresponding line positions. This together with Equations 3.18 and 3.19 gives:

$$S = (-1/pL) \int_{line} \mathrm{Ln}(I(x)/I_0)\, |d\nu/dx|\, dx \qquad (3.20)$$

The function $I(x)/I_0$ is simply the rectified spectrum. Equation 3.20 can be used with Equation 3.15 to determine the temperature of the gas. The constants p and L are cancelled from the equation when, in the temperature determination, one considers only the ratios between the line strengths. Average temperatures of 360.9±1.4K and 368.2±4.3K have been calculated for the two sets of line strengths published in Spellicy et al. [1972]. These agree with the assumed temperature of about 100°C.

The procedure has also been applied to a typical HF spectrum obtained from the CFH Coudé. The line limits for all the HF lines have been set at positions of only 0.6% absorption with respect to the continuum. A temperature of 373.7±0.7K is obtained. This agrees very well with the expected temperature of 100°C. The

accuracy of the procedure depends critically on the accuracy of the measured line strengths which are essentially the equivalent widths of the logarithm of the lines. The main source of error is in the placement of the continuum. This is hampered mainly by the collisionally broadened line profiles. Blendings at the far wings of the lines may become significant and would restrict the choice of line limits. Correction curves for the effects on measured line strengths and widths from instrumental broadening have been generated by Meredith [1972]. An iterative method to correct for the loss of the far wings of the line in the measurement of line strength and equivalent width has been described in Korb et al. [1968] and Giver et al. [1982]. Pugh and Rao [1976] and Overend [1982] have suggested the use of curve-of-growth procedure to measure the line strengths. Nevertheless, since only the ratios between line strengths are used by the present procedure, any multiplicative systematic error in the equivalent-width measurements would have no effect on the result. Meanwhile, the use of other Herman-Wallis factors e.g. those theoretical values from Ogilvie and Tipping [1982], could increase the mean temperature by as much as 10K. In spite of this, to monitor the relative changes in the temperature, the present procedure is probably adequate.

The difference between the equivalent width of lines can be more easily measured from a difference

spectrum (Campbell [1984a]). Consequently, strengths of HF lines in a particular spectrum can be measured by examining the difference spectrum produced by subtracting a "standard" HF spectrum. The HF lines in the "standard" spectrum would have known equivalent widths and line strengths. Relative line strengths can then be calculated with respect to these "standard" lines. These can then be used to determine a temperature relative to that calculated for the "standard" HF spectrum.

3.3.2.4 Derivation of the gas pressure

The HF gas pressure p in Equation 3.20 can be evaluated if one can calculate the theoretical line strength per unit-atmosphere using Equations 3.10 and 3.11. By assuming ideal gas law for the HF gas, the term N/p in Equation 3.10 would become 1/kT. The total partition function Z in Equation 3.10 can be expressed as:

$$Z(T) = \Sigma_{\upsilon}\Sigma_{J}\ (2J+1)\ \exp(\ -E(\upsilon,J)/kT\ ) \qquad (3.21)$$

The energy level $E(\upsilon,J)$ can be calculated from the term value obtained through Equation 3.4 using the calculated Dunham coefficients. In Equation 3.11, the term $\langle \upsilon_i | \mu(r) | \upsilon_f \rangle$ can be calculated from Equation 3.14 together with formulae for $\langle \upsilon_i | (r/r_e)^i | \upsilon_f \rangle$ which are given in Tipping [1973]. A value of 1.6095×10^{-21} esu.cm (1 debye is 10^{-18} esu.cm) is obtained when the various constants listed in Table 3.5 are used in the

Table 3.7 Line strengths of the (3-0) band of HF

m	experimental.	calculated
-3	0.0235 $cm^{-2}atm^{-1}$	0.02285 $cm^{-2}atm^{-1}$
-2	0.0245 $cm^{-2}atm^{-1}$	0.02467 $cm^{-2}atm^{-1}$
-1	0.0164 $cm^{-2}atm^{-1}$	0.01697 $cm^{-2}atm^{-1}$
1	0.0193 $cm^{-2}atm^{-1}$	0.01970 $cm^{-2}atm^{-1}$
2	0.0327 $cm^{-2}atm^{-1}$	0.03324 $cm^{-2}atm^{-1}$
3	0.0353 $cm^{-2}atm^{-1}$	0.03574 $cm^{-2}atm^{-1}$
4	0.0287 $cm^{-2}atm^{-1}$	0.02903 $cm^{-2}atm^{-1}$
5	0.0188 $cm^{-2}atm^{-1}$	0.01881 $cm^{-2}atm^{-1}$
6	0.0099 $cm^{-2}atm^{-1}$	0.00996 $cm^{-2}atm^{-1}$
7	0.0039 $cm^{-2}atm^{-1}$	0.00437 $cm^{-2}atm^{-1}$

calculation. This agrees with the experimental value of 1.628×10^{-21} esu.cm measured by Spellicy et al. [1972]. Other experimental and theoretical values for this matrix element can be found referenced in Werner and Rosmus [1980]. The minute effect of induced emission on the line strength can also be taken into account by including the factor $\{1-\exp(-hc\nu/kT)\}$ into Equation 3.10. With all these terms known, theoretical line strengths can then be calculated as a function of temperature. Table 3.7 lists both the experimental and calculated line strengths per unit atmosphere for the (3-0) band of HF. The experimental values are those given in Spellicy et al. [1972] corresponding to the 0.467atm data. The calculated values used the

temperature of 360.9K obtained from the temperature-determination method described earlier. The agreement between the two sets of values in Table 3.7 is very good.

Pressure of the HF gas can be determined by comparing the measured line strength against the corresponding theoretical unit-atmosphere line strength. The procedure has been applied to the "standard" CFHT HF spectrum used earlier in the temperature determination. In fact, that particular determined temperature is used in this calculation. A value of 300.4±0.7 torrs is obtained for the gas pressure. This is about 17% lower than the expected value of 360 torrs. The small statistical standard error associated with the determined value as well as the excellent result obtained earlier with the ratios of the line strengths in the temperature determination, would strongly suggest that the problem here is the existence of a multiplicative systematic error factor. The fact that there is a good agreement between the theoretical calculations and the result of Spellicy et al. [1972], implies the source of error is probably in the measured line strengths. The relative error in the equivalent-width measurements caused by scattered light is of the order of only 3% for the CFH Coudé spectrograph. Systematic errors in the placement of continuum for the spectrum could not be the sole cause for the large discrepancy. The error caused by the fact

that the chosen line limits are not at the true continuum should be small. Furthermore, since the logarithm of the spectrum is used in the computation of the line strengths, the small multiplicative error factor in the continuum placement would become an additive factor. One of the multiplicative factors used in the calculation of the line strengths is the dispersion of the spectrum. However, it is difficult to understand the existence of any large error in this parameter. Another multiplicative factor used in the calculation is the optical absorption path length of the cell. The chosen value of 100 cm is the measured length of the absorption cell. This assumption that the effective absorption path length is the same as the length of the cell, however, may not be quite correct. The colder HF molecules near the windows as well as the ones freshly introduced into the heated cell from the sample line would be $(HF)_6$ hexamers rather than monomers. They would then not contribute towards the observed absorption lines. It is conceivable that they may be in significant numbers in the cell near the windows and the location where the sample line is connected. This has the effect of reducing the effective absorption path length, and hence reducing the observed line strengths.

Although absolute pressure determination using this line strength method is not possible, relative pressure determinations should be possible. One can use the

Figure 3.2 The temperature dependence of HF line strengths

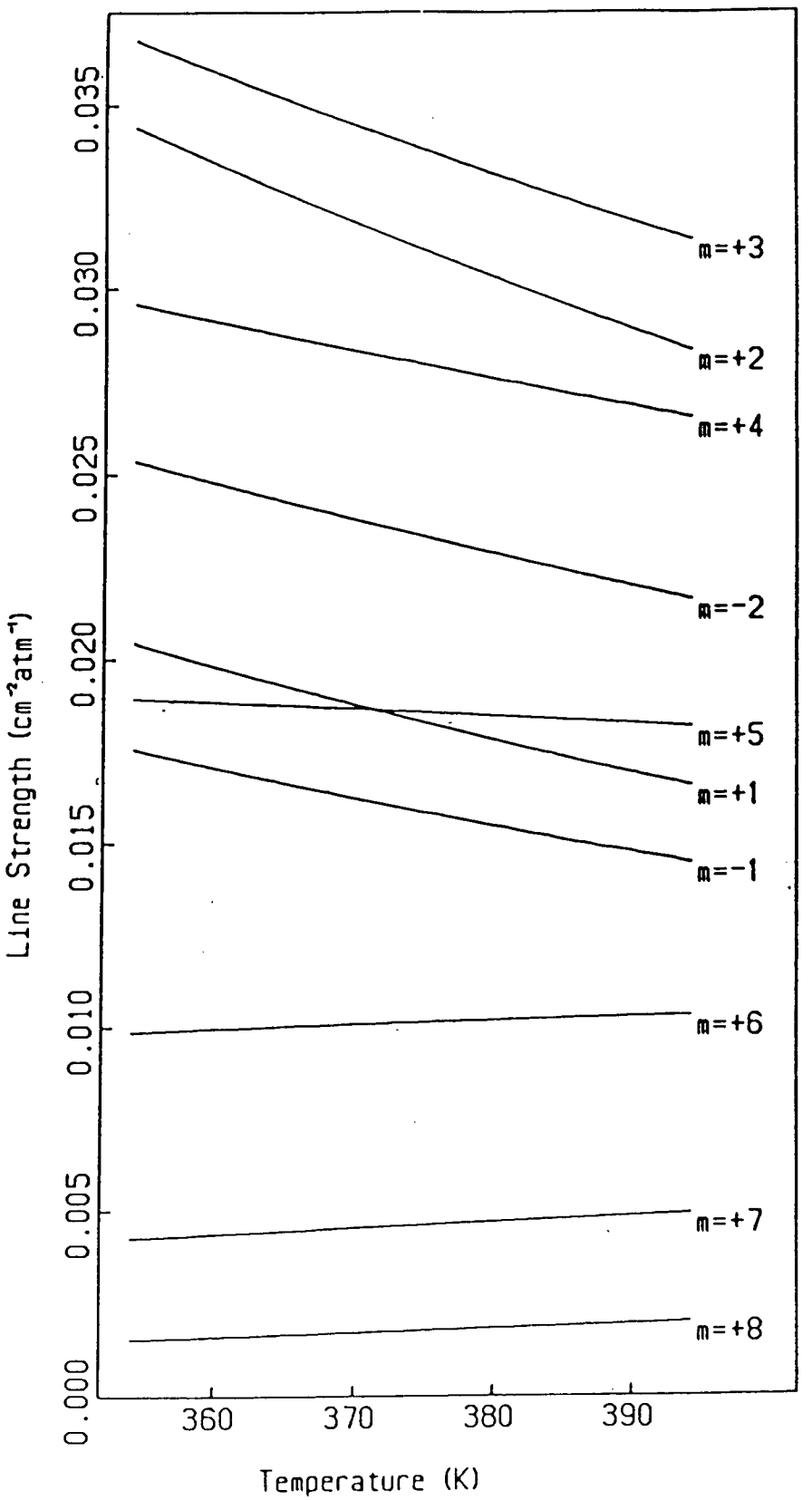

method to monitor the variations in the gas pressure with respect to that of a "standand" HF spectrum. The relative temperature dependence of the line strengths for the various HF lines can be studied with the theoretical line-strength calculations. Figure 3.2 shows the line-strength variations with temperatures for the (3-0) band of HF. At the cell operation temperature of about 100°C, the HF lines of $|m| \leq 5$ would decrease in strength with temperature while lines of $m \geq 6$ would increase in strength with temperature. Meanwhile, the pressure of the gas is directly proportional to the measured line strengths. For each individual line, the ratio between the measured line strength and pressure would be equal to the corresponding theoretical unit-atmosphere line strength. This value is constant for a given temperature.

3.4 THE COLLISIONALLY BROADENED LINEWIDTHS

3.4.1 INTRODUCTION

The pressure of the HF gas can also be determined from the linewidths of the HF lines. This involves calculating the theoretical collisionally broadened linewidths. The broadening is a function of both the temperature and pressure of the gas. The amount of broadening is different for each HF line. A very much related phenomenon is the collisionally induced line shifts. One needs to know these shifts as functions of both temperature and pressure in

order to make corrections to the reference wavelengths. The shifts, to a certain extent, determine the ultimate accuracy of the reference wavelengths. They are different in both direction and magnitude for each reference HF line.

In chemistry, the study of linewidths and shifts can be used to determine the intermolecular forces between the constituents of the gas e.g. the electric quadrupole and octopole moments of many molecules have been determined in this manner. The application of theoretical broadened linewidths of molecules is numerous. The CO concentration and temperature in combustion exhaust can be determined from the broadened linewidths (Lowry and Fisher [1982]). It is also important to the design and operation of molecular lasers, the study of pollutants in the atmosphere, as well as the study of radiative transfer in terrestrial and planetary atmospheres. Line-broadening theory has been applied to determine the ozone density distribution in the atmosphere (Monnanteuil and Colmont [1983]). Abundances of helium in Jupiter can be determined from the helium collisionally broadened linewidths of CH_3 lines (Varanasi [1971]). The pressure and temperature in the Jovian atmosphere can also be determined from the broadening of the methane lines (Margolis [1971]). Meanwhile, collisionally broadened HCl and HF linewidths in CO_2 atmospheres have been studied for application on Venus (Shaw and Lovell [1969], Varanasi et al. [1971]).

3.4.2 THEORIES ON COLLISIONAL LINE BROADENING

The shape of spectral lines can be altered by the interaction of each individual radiating molecule with other surrounding molecules. Line-broadening effects have generally been divided into two limiting cases: the low-pressure impact (interruption) broadening and the high-pressure statistical broadening. Statistical broadening theory was first given by Margenau [1935]. Impact broadening, however, was first considered by Michelson [1895] and Lorentz [1906]. Early impact theories are summarised and expanded in Foley [1946] and Mizushima [1951]. These early impact theories assume the radiating molecule to be a classical oscillator and that the collisions are strong enough that the oscillation process is interrupted. Formulations in formal quantum-mechanical framework have been given by Baranger [1958ab], Kolb and Griem [1958], and Fano [1963]. Recent formulations using the binary-collision approximation have been given by Ross [1966], Gordon [1966], Bezzerides [1967ab], Murphy and Boggs [1967ab,1968], Zaidi [1968], Di Giacomo and Tarrini [1970], Smith et al. [1971ab], Nielsen and Gordon [1973], Smith et al. [1976], Lam [1977], Boulet and Robert [1978], and Clough et al. [1983]. More elaborate formulations involving the use of statistical mechanics and quantum many-body techniques have been given by Zaidi [1972], Davies [1975], Roney [1975ab], and Davies and Oli [1978]. Recent reviews on line broadening theories include Boggs [1972], Rabitz [1974], Leavitt [1980], Breene [1981], Leavitt and Korff [1981], and

Buffa and Tarrini [1983].

Anderson [1949] applied perturbation methods to a semiclassical impact theory and produced computational expressions for general pressure broadening. This was later extended by Tsao and Curnutte [1962], Robert et al. [1969], Leavitt [1980], and Leavitt and Korff [1981]. Hewitt [1976], Frost [1976], and Boulet et al. [1977] extended the Anderson theory to permit calculation of line shifts. Early extensions of the impact theory to calculate noble-gas pressure-induced linewidths and shifts include Ben-Reuven et al. [1963], Herman [1963], Tipping and Herman [1970b], Herman and Tipping [1970], Levy et al. [1973], Boulet et al. [1973], and Jarecki and Herman [1975].

The Anderson-Tsao-Curnutte (ATC) theory is the most widely used for the computation of collisionally broadened linewidths. The MB method proposed by Murphy and Boggs [1967a] produces linewidths which are in better agreement with experimental results than the early ATC formalism. The later modified ATC theories (Frost and MacGillivray [1977], Leavitt and Korff [1981]), however, can produce as good if not better agreement. The ATC theory is also generally considered to be founded on more acceptable physical premises than the MB theory. The Quantum Fourier Transform (QFT) method proposed by Davies [1975] has not been as widely used as the other two methods. Mandin et al. [1980] have applied all three methods to the calculation of self-broadened H_2O lines. They found that there is not much difference between the ATC and QFT methods, while the

results from the MB method are systematically too low. Frost and MacGillivray [1977] have also found that the MB method gives poorer calculated line shifts. The modified MB method (Cattani [1972], Frost and MacGillivray [1977]), however, is comparable to the modified ATC method in accuracy. Leavitt and Korff [1981] have shown that early phase-shift theories (Van Vleck and Weisskopf [1945]), the semiclassical theory of Gordon [1966], and the MB theories are all limiting cases of the modified ATC theory.

3.4.3 THE ANDERSON-TSAO-CURNUTTE (ATC) THEORY

3.4.3.1 Basic approach

The ATC theory uses a semiclassical perturbation approach with the binary-impact approximation. In the impact approximation, the duration of the collisions which affect the states of the absorbing (or radiating) molecules by shifting their phases or causing transitions is assumed to be short in comparision with the time interval between successive collisions. This enables one to treat the individual molecular collisions as uncorrelated with the radiative process, since they occur on different time scales. The molecular translation would then be decoupled from the internal degrees of freedom of the molecules. Quantum mechanics can then be used to treat the internal degrees of freedom while the translational motion is treated classically. A straight-line classical trajectory is generally used for the collision. This procedure is

quite common for most semiclassical theories. Smith et al. [1976], however, have proposed the use of a curved classical trajectory. The time-evolution operator (collision matrix) which describes the collision dynamics is expanded by perturbation theory in the ATC approach to obtain a simple and practical computational procedure. The phenomenon of resonance broadening is considered in the ATC theory. Normally, the perturber molecules are distinguishable from the radiator molecules as in the case of foreign-gas broadening. In the case of self-broadening, however, excitation can be transferred from one molecule to another and one of the molecules can still be considered as among the radiators. In this case, excitation can be transferred with a zero net change in the internal energy of the two-molecule system. The distinction between the perturber and radiator would become meaningless. This has the effect of shortening the lifetime of the excited state or broadening the upper state. This would increase the amount of line broadening relative to the case of distinct perturber-radiator interaction. Both elastic and inelastic collision effects are considered by the ATC theory. The collision effect of reorientation (Gordon [1966], Sharma [1971]), however, is not considered by most early ATC theories. This is the effect in which the direction of angular momentum of the radiator is changed in the collision while the internal energy is unaltered.

3.4.3.2 Collision cross section

In the ATC theory, the linewidth γ and line shift δ per unit-atmosphere gas pressure of the perturber and in units of cm^{-1} are related to the complex collision cross section $\sigma(v)$:

$$\gamma = (1.01325 \times 10^6) N/(2\pi c p) \int_0^\infty vF(v)\sigma_R(v)\, dv \quad (3.22)$$

$$\delta = (1.01325 \times 10^6) N/(2\pi c p) \int_0^\infty vF(v)\sigma_I(v)\, dv \quad (3.23)$$

$$\sigma(v) = \sigma_R(v) + i\ \sigma_I(v) \quad (3.24)$$

The function F(v) is the Maxwellian probability distribution for the relative velocity v. The function $\sigma_R(v)$ is the real part of $\sigma(v)$ while $\sigma_I(v)$ is the imaginary part. The function $\sigma(v)$ is a complex quantity because of the noncommutative characteristic of the collision matrix (Herman [1963]). The integration over the velocity distribution can be removed if one uses the approximation:

$$\int_0^\infty vF(v)\sigma(v)\, dv \simeq \langle v \rangle\ \sigma(\langle v \rangle) \quad (3.25)$$

$$\langle v \rangle = \sqrt{(8kT / (\pi M))} \quad (3.26)$$

The term $\langle v \rangle$ is the mean collision velocity and M is the reduced mass of the molecule. This is a very commonly used approximation and may affect the calculated linewidth by only a few percent. This point has been investigated by many researchers. Rabitz [1974] has pointed out that the small error is the result of the fact that, at room temperature, the cross section tends to peak near the peak of the velocity distribution function. This condition may not be valid in all

applications. Buffa and Tarrini [1983] have also pointed out that even if the approximation is good for the calculation of linewidths, a large error can be introduced into the line-shift calculations. Meanwhile, Hewitt [1976] found no significant difference between the use of <v> and explicit numerical integration over the velocity distribution.

3.4.3.3 The collision efficiency function

The collision cross section $\sigma(v)$ is related to the collision efficiency function S(b,v), where b is the impact parameter. In the ATC theory, S(b,v) is perturbation expanded in powers of the interaction potential between the perturber and radiator:

$$S(b,v) = S_0 + S_1(b,v) + S_2(b,v) + \ldots \qquad (3.27)$$

The sum is usually truncated after the second order term. The zeroth order term S_0 is zero. The first order term $S_1(b,v)$ is imaginary and would be a contributor to only the line shifts. Frost [1976] has shown that $S_1(b,v)$ can vanish in some applications. Boulet et al. [1977] have remarked that $S_1(b,v)$ would vanish unless one considers the contributions from the internal vibrational degrees of freedom. Contribution to the linewidth comes from the real part of the second order term $S_2(b,v)$ while those for the line shift are from $S_1(b,v)$ and the imaginary part of $S_2(b,v)$. The function $S_2(b,v)$ has also been referred to as the interruption function. The functions σ_R and σ_I can then be written as:

$$\sigma_R(v) = \Sigma_{v_2 J_2} \rho_{v_2 J_2} \sigma_R(v, v_2, J_2) \quad (3.28)$$

$$\sigma_I(v) = \Sigma_{v_2 J_2} \rho_{v_2 J_2} \sigma_I(v, v_2, J_2) \quad (3.29)$$

$$\sigma_R(v, v_2, J_2) = \int_0^\infty 2\pi b \, \mathrm{Re}\{S_2(b, v, v_2, J_2)\} \, db \quad (3.30)$$

$$\sigma_I(v, v_2, J_2) = \int_0^\infty 2\pi b \, [S_1(b, v, v_2, J_2) + \mathrm{Im}\{S_2(b, v, v_2, J_2)\}] \, db \quad (3.31)$$

$$\rho_{v_2 J_2} = (2J_2+1) \exp(-E(v_2, J_2)/kT) / Z(T) \quad (3.32)$$

The variables v_2 and J_2 refer to the vibrational and rotational quantum number of the perturber, respectively. The function Z(T) is simply the total partition function from Equation 3.21.

3.4.3.4 Cutoff procedure for small impact parameter

The function $S_2(b,v)$ produced by the ATC theory, however, will diverge for small values of b. In early ATC theories, $S_2(b,v)$ is real and a cutoff procedure of assuming $S_2(b,v)=1$ for $b \leq b_0$ is used. Equation 3.30 would then become:

$$\sigma_R(v, v_2, J_2) = \pi b_0^2 + \int_{b_0}^\infty 2\pi b \, \mathrm{Re}\{S_2(b, v, v_2, J_2)\} \, db \quad (3.33)$$

The term b_0 is the cutoff impact parameter and is defined by the condition that $S_2(b_0,v)=1$. If one considers the contribution of the imaginary part of $S_2(b,v)$ as well, the condition defining b_0 would be one of the followings:

$$\mathrm{Re}\{S_2(b_0, v)\} = 1 \quad (3.34)$$

$$(\mathrm{Re}\{S_2(b_0, v)\})^2 + (\mathrm{Im}\{S_2(b_0, v)\})^2 = 1 \quad (3.35)$$

$$\mathrm{Re}\{S_2(b_0,v)\} + |\mathrm{Im}\{S_2(b_0,v)\}| = 1 \qquad (3.36)$$

Equation 3.34 was used by Sharma and Caledonia [1971] while Equation 3.36 was recommended by Tipping and Herman [1970b]. Equation 3.35, however, is more natural and has been more widely used. Other cutoff criteria are summarised in Rabitz [1974]. Frost and MacGillivray [1977] have suggested that a cutoff procedure would not be necessary if $S_2(b,v)$ is replaced by a new convergent collision efficiency function $X(b,v)$:

$$X(b,v) = 1 - \exp(-S_2(b,v)) \qquad (3.37)$$

$$\mathrm{Re}\{X(b,v)\} = 1 - \cos(\mathrm{Im}\{S_2(b,v)\})\exp(-\mathrm{Re}\{S_2(b,v)\}) \qquad (3.38)$$

$$\mathrm{Im}\{X(b,v)\} = \sin(\mathrm{Im}\{S_2(b,v)\})\exp(-\mathrm{Re}\{S_2(b,v)\}) \qquad (3.39)$$

The function $X(b,v)$ would approach 1 for small b and $S_2(b,v)$ for large b.

3.4.3.5 The cutoff-free theory

The most sophisticated formulation in the ATC framework is given by Leavitt [1980] and Leavitt and Korff [1981]. A $S(b,v)$ which is bound and integrable over all values of b has been derived for the cutoff-free theory. The effect of anharmonicity in the internal vibrational motion of the molecule (Giraud et al. [1973]) has also been included in the formulation. The collision efficiency function is given as:

$$S(b,v) = 1 - \exp(-i\Delta_i + i\Delta_f - S_{2,i}^{outer} - S_{2,f}^{outer} - S_2^{middle}) \qquad (3.40)$$

The subscripts i and f refer to the initial and final optical state of the particular spectral line transition, respectively. The most detailed expressions for the contributors Δ, S_2^{outer}, and S_2^{middle} are given in Leavitt [1980]. They are functions of the b-dependent intermolecular potential between the colliding molecules e.g. electric dipole-dipole, dipole-quadrupole, and quadrupole-quadrupole interactions. These are functions of the various molecular constants e.g. polarizability, electric dipole, quadrupole, and octopole moments. Higher-order interactions are summarised in Townes and Schawlow [1975] and Buckingham [1967]. The contributors to S(b,v) also depend on the Clebsch-Gordan coefficients corresponding to each possible collision-induced transition. Some higher order terms also depend on the Racah coefficients. There is also a dependence on the various "resonance functions" $f_n(k)$, $g_n(k)$, $If_n(k)$, and $Ig_n(k)$. The variable k is the resonance parameter and is a measure how close the various states are to exact resonance:

$$k = 2\pi b/(hv) \left(E_i^A - E_i^B + E_2^A - E_2^B \right) \qquad (3.41a)$$

or

$$k = 2\pi b/(hv) \left(E_f^A - E_f^B + E_2^A - E_2^B \right) \qquad (3.41b)$$

The superscripts A and B indicate the states before and after the collision, respectively. The subscripts i and f refer to the upper and lower states of the active molecule, respectively. The subscript 2 indicates the state of the perturber. The resonance functions

$f_n(k)$ and $g_n(k)$ are even functions while $If_n(k)$ and $Ig_n(k)$ are odd. Explicit expressions for all the resonance functions in terms of the modified Bessel functions are given in Leavitt [1980]. Power- series approximations for some of the resonance functions are given in Frost [1976] and Messer et al. [1982].

3.4.3.6 Basic formulations of simplied theory

Less elaborate expressions for S(b,v) have been used in the calculations of broadened (3-0) HF linewidths. Spellicy et al. [1972] considered only the real part of S(b,v) together with the cutoff procedure in Equation 3.33. A more sophisticated but still rather simple expression for S(b,v) in the case of self-broadening can be formulated as:

$$\mathrm{Re}\{S(b,v)\} = \Sigma_{if} [\Sigma_j b^{-4} c_{1j} A_1(v) f_1(k) + \Sigma_j b^{-6} c_{2j} A_2(v) f_2(k) + \Sigma_j b^{-8} c_{3j} A_3(v) f_3(k)] \quad (3.42)$$

$$\mathrm{Im}\{S(b,v)\} = -\Sigma_{if} [\Sigma_j b^{-4} c_{1j} A_1(v) If_1(k) + \Sigma_j b^{-6} c_{2j} A_2(v) If_2(k) + \Sigma_j b^{-8} c_{3j} A_3(v) If_3(k)] \quad (3.43)$$

$$A_1(v) = (4/9)\ \mu^4\ [2\pi/(hv)]^2 \quad (3.44)$$

$$A_2(v) = (4/45)\ \mu^2\theta^2\ [2\pi/(hv)]^2 \quad (3.45)$$

$$A_3(v) = (1/25)\ \theta^4\ [2\pi/(hv)]^2 \quad (3.46)$$

This simplified S(b,v) includes contributions from only

the intermolecular electric dipole-dipole, dipole-quadrupole, and quadrupole-quadrupole interactions. The contributions are summed over the upper and lower states of the active molecule to take into account collision-induced transitions from those states. The functions $A_1(v)$, $A_2(v)$, and $A_3(v)$ are taken from Tsao and Curnutte [1962]. The parameters μ and θ in the above formulae are the electric dipole and quadrupole moments, respectively. The c_{nj}'s are Clebsch-Gordan coefficients and are given in Benedict and Herman [1963]. Equations 3.42 through 3.46 can be used with Equations 3.37 through 3.39 in a cutoff-free application of the ATC theory.

3.4.4 SURVEY OF EXPERIMENTS AND CALCULATIONS

Collisionally broadened linewidths and shifts of HF lines have been measured by many researchers. Kuipers [1958] and Herget et al. [1962] measured both the self-broadened linewidths and shifts of HF lines belonging to the (1-0) band. Lovell and Herget [1962] and Hinchen and Hobbs [1979] also measured the linewidths of self-broadened (1-0) band HF lines. Meredith [1972] and Spellicy et al. [1972] have measured the self-broadened linewidths of lines in the (2-0) and (3-0) bands, respectively. Self-induced line shifts in the (2-0) band have been measured by Guelachvili and Smith [1978]. Meanwhile, Campbell and Walker [1979] and Campbell [1983] have measured the line shifts for the lines in the (3-0) band. Jaffe et al. [1956], Wiggins et al. [1970], and

Pine [1980] measured the rare-gas-induced linewidths and shifts of the HF lines in the (1-0) and (2-0) bands. Shaw and Lovell [1969] and Varanasi et al. [1972] measured the CO_2 induced linewidths and shifts of the lines in the (1-0) band. Meredith and Smith [1973] measured the N_2-, H_2-, and D_2-induced linewidths of the (1-0) HF lines. Guelachvili and Smith [1978] have measured the rare-gas-, CO_2-, N_2-, and HCl-induced shifts for lines in the (1-0) and (2-0) bands.

Calculations of self-broadened linewidths for the (1-0) HF lines include those by Benedict and Herman [1963] and Hough [1977]. Meredith [1972] and Spellicy et al. [1972] calculated the self-broadened linewidths for the lines in the (2-0) and (3-0) bands, respectively. Meanwhile, Boulet et al. [1977] calculated the linewidths and shifts for the lines in the (0-0), (1-0), (2-0), and (3-0) bands. Calculations of rare-gas-induced linewidths and shifts for lines in the (0-0), (1-0), and (2-0) bands were made by Jarecki and Herman [1975], Jarecki [1977], and Pine [1980]. Smith and Meredith [1974], meanwhile, also calculated DF-induced linewidths for lines in the (1-0) band.

3.4.5 THE CALCULATION OF LINEWIDTHS AND LINE SHIFTS

The cutoff-free collision efficiency function described in Equations 3.38 and 3.39 has been used to calculate self-induced linewidths and shifts for the (3-0) HF lines. Contributions from intermolecular interactions to the collision efficiency function were taken to be those given in Equations 3.42 through 3.46. The dipole moment for HF was

taken to be 1.80306×10^{-18} esu.cm (Ogilvie et al. [1980]). This is the same as the coefficient M_0 listed in Table 3.5. The quadrupole moment for HF was taken to be the observed value of 2.21×10^{-26} esu.cm^2 (De Leeuw and Dymanus [1973]). Other values for the constants are given in Werner and Ramus [1980], Sileo and Cool [1976], Lie [1974], Meredith and Smith [1973], and Muenter and Klemperer [1970]. They are also referenced in the calculations by Boulet et al. [1976] and Benedict and Herman [1963]. A 32-point Gauss-Laguerre-quadrature numerical integration was used for the semi-infinite range integration of Equations 3.43 and 3.44. The same method can also be applied to the integration over the velocity distribution in Equations 3.42 and 3.36. In fact, a 7-point Gauss-Laguerre quadrature was used by Boulet et al. [1976]. In the actual calculation, however, because of limited computing resources, the approximation in Equations 3.25 and 3.26 was used instead of the explicit numerical integration over velocities. The calculation considers all contributions which have Boltzmann factors greater than that of v=0 and J=23. This should be sufficient to account for most of the energy-level population at the low temperature of 100°C for HF. In fact, Benedict and Herman [1963] have pointed out that even at 1200K, less than 0.3% of the molecules are in rotational states J>20. The method requires many evaluations of the various energy levels. The amount of computation can be greatly reduced if one establishes a common database on the energy levels. This can then be referenced by the various parts of the computer

program and hence would eliminate any repeated energy-level calculation.

The calculated γ and δ are the unit-atmosphere linewidth and shift, respectively. The linewidth is defined as the halfwidth of the line at 50% of the maximum line absorbance. From the definition of the line absorbance function $\kappa(\nu)$ in Equation 3.18, the linewidth would be the halfwidth at half maximum of the function $-\mathrm{Ln}(I(\nu)/I_0)$. The functions $I(\nu)$ and I_0 are the line and continuum intensity, respectively. Reviews on the definitions of various line-shape parameters are given in Meredith [1972] and Mandin et al. [1980].

3.4.6 CALCULATED LINEWIDTHS FOR THE HF LINES

To test the theory and the computational procedure, linewidths for the lines in the (1-0) and (2-0) bands are calculated. They are then compared against the experimental values. A gas temperature of 373.15K has been used in the calculations. In general, the calculated values are consistently lower than the experimental values by several percent for lines in the P-branch. The agreement for lines in the R-branch is better. Table 3.8 lists the linewidths for the lines in the (1-0) band. The experimental values are taken from Lovell and Herget [1962]. The agreement between the calculated and experimental linewidths is quite good especially for the R-branch lines with m<6. For the lines in the (2-0) band, the agreement is excellent. Table 3.9 lists the calculated and experimental values for the lines in the

Table 3.8 Linewidths of the (1-0) band of HF

m	calc.	expt.
-1	0.4336 $cm^{-1}atm^{-1}$	0.462 $cm^{-1}atm^{-1}$
1	0.4310 $cm^{-1}atm^{-1}$	0.458 $cm^{-1}atm^{-1}$
2	0.5016 $cm^{-1}atm^{-1}$	0.501 $cm^{-1}atm^{-1}$
3	0.5133 $cm^{-1}atm^{-1}$	0.563 $cm^{-1}atm^{-1}$
4	0.4555 $cm^{-1}atm^{-1}$	0.454 $cm^{-1}atm^{-1}$
5	0.3636 $cm^{-1}atm^{-1}$	0.345 $cm^{-1}atm^{-1}$
6	0.2821 $cm^{-1}atm^{-1}$	0.259 $cm^{-1}atm^{-1}$
7	0.2058 $cm^{-1}atm^{-1}$	0.173 $cm^{-1}atm^{-1}$

Table 3.9 Linewidths of the (2-0) band of HF

m	calc.	expt.
-1	0.4263 $cm^{-1}atm^{-1}$	0.459 $cm^{-1}atm^{-1}$
1	0.4090 $cm^{-1}atm^{-1}$	0.406 $cm^{-1}atm^{-1}$
2	0.4586 $cm^{-1}atm^{-1}$	0.464 $cm^{-1}atm^{-1}$
3	0.4696 $cm^{-1}atm^{-1}$	0.471 $cm^{-1}atm^{-1}$
4	0.4268 $cm^{-1}atm^{-1}$	0.419 $cm^{-1}atm^{-1}$
5	0.3493 $cm^{-1}atm^{-1}$	0.347 $cm^{-1}atm^{-1}$
6	0.2738 $cm^{-1}atm^{-1}$	
7	0.2064 $cm^{-1}atm^{-1}$	0.184 $cm^{-1}atm^{-1}$
8	0.1536 $cm^{-1}atm^{-1}$	0.140 $cm^{-1}atm^{-1}$

Table 3.10 Linewidths of the (3-0) band of HF

m	calc.	expt.
-2	0.4492 $cm^{-1}atm^{-1}$	0.506 $cm^{-1}atm^{-1}$
-1	0.4136 $cm^{-1}atm^{-1}$	0.447 $cm^{-1}atm^{-1}$
1	0.3975 $cm^{-1}atm^{-1}$	0.397 $cm^{-1}atm^{-1}$
2	0.4268 $cm^{-1}atm^{-1}$	0.443 $cm^{-1}atm^{-1}$
3	0.4473 $cm^{-1}atm^{-1}$	0.453 $cm^{-1}atm^{-1}$
4	0.4201 $cm^{-1}atm^{-1}$	0.412 $cm^{-1}atm^{-1}$
5	0.3514 $cm^{-1}atm^{-1}$	0.331 $cm^{-1}atm^{-1}$
6	0.2820 $cm^{-1}atm^{-1}$	0.254 $cm^{-1}atm^{-1}$
7	0.2187 $cm^{-1}atm^{-1}$	0.164 $cm^{-1}atm^{-1}$

(2-0) band. The experimental linewidths, in this case, are taken from Meredith [1972]. The result for the (3-0) band is given in Table 3.10. The experimental values are taken from Spellicy et al. [1972]. Again, the agreement is quite good for the R-branch lines with $m<6$. Of course, the agreement is much better than the result from the less sophisticated calculation by Spellicy et al. [1972].

Figure 3.3 shows the linewidth variations with temperature for the (3-0) band. The result is not unexpected. It can be seen from Equation 3.22 that γ is proportional to the number density of the perturber n, and the gas velocity v. For constant gas pressure, n is inversely proportional to temperature T while v is proportional to $\sqrt{T}$. Hence γ would be inversely proportional to $\sqrt{T}$. The temperature dependence of the collision cross

section is small for the very small change in temperature considered here. Meanwhile, the observed linewidths should be directly proportional to the pressure. Linewidths are known to have a nonlinear pressure dependence (Meredith and Smith [1974], Smith and Meredith [1974]). But the nonlinearity is very small over the pressure range of interest here.

3.4.7 CALCULATED LINE SHIFTS FOR THE HF LINES

In comparing the calculated line shifts for the (1-0) band against the experimental values from Herget et al. [1962], the agreement is poor. Generally, there is agreement only to the same order of magnitude. The calculated shifts tend to be progressively too positive for lines with $m>4$. The situation is the same when comparing the calculated line shifts for the (2-0) band against the experimental values from Guelachvili and Smith [1978] or the calculated values from Boulet et al. [1976]. Table 3.11 lists the calculated line shifts for the (3-0) band. The experimental values in the table are taken from Campbell and Walker [1979]. There is slight agreement between the calculated and experimental values for lines with $m<5$.

Although the calculations for the linewidths and shifts are based on the same theory, the calculated linewidths appear to be significantly more accurate that those of the line shifts. This phenomenon has been commented on by Buffa and Tarrini [1983] to be a consequence of using the approximation in Equation 3.25 instead of performing an

Figure 3.3 The temperature dependence of the linewidths

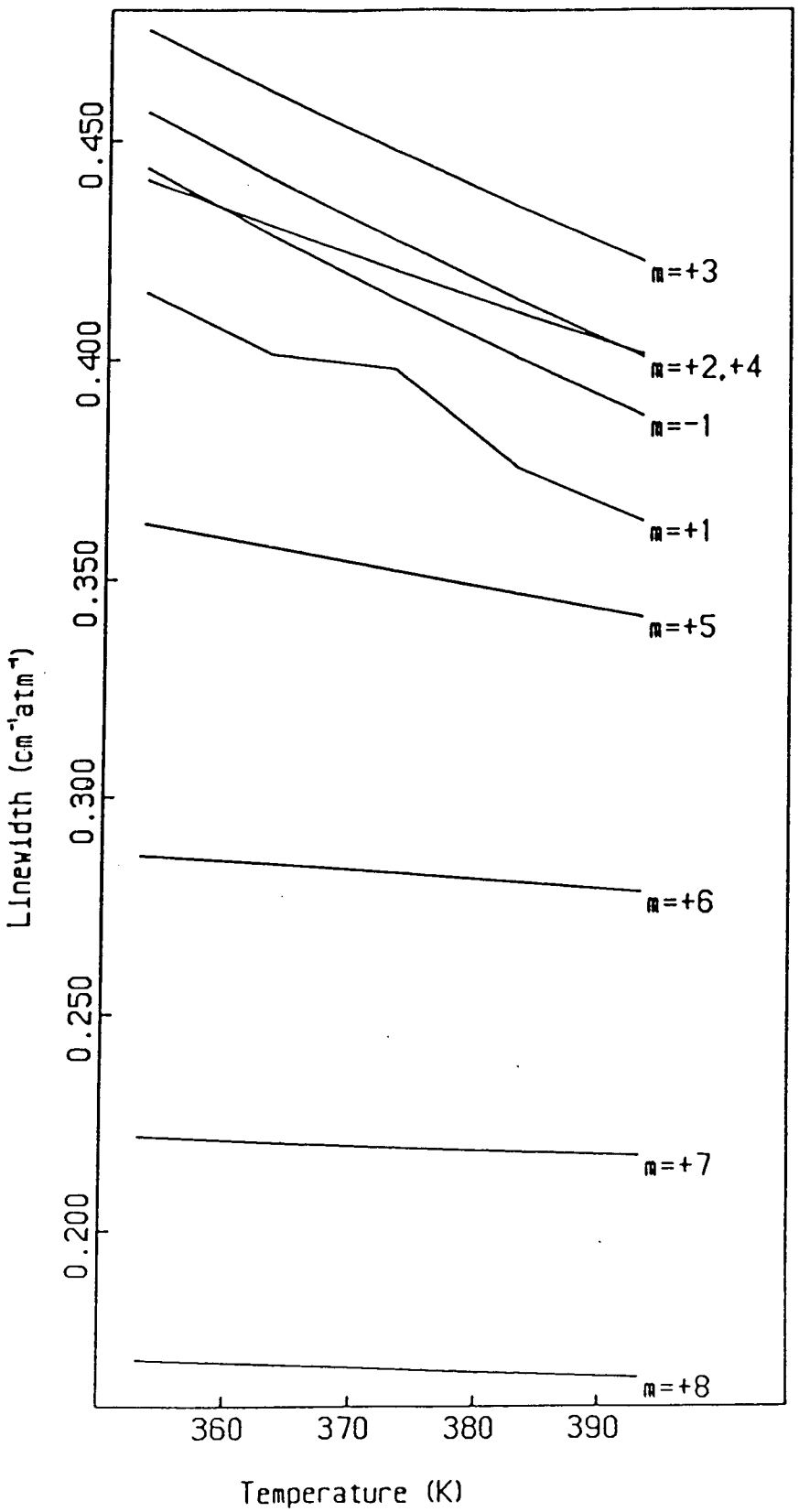

Table 3.11 Line shifts of the (3-0) band of HF

m	calc.	expt.
-2	+0.0288 $cm^{-1}atm^{-1}$	
-1	+0.0763 $cm^{-1}atm^{-1}$	
1	+0.0763 $cm^{-1}atm^{-1}$	+0.0445 $cm^{-1}atm^{-1}$
2	+0.0061 $cm^{-1}atm^{-1}$	+0.0070 $cm^{-1}atm^{-1}$
3	-0.0237 $cm^{-1}atm^{-1}$	-0.0140 $cm^{-1}atm^{-1}$
4	-0.0046 $cm^{-1}atm^{-1}$	-0.0171 $cm^{-1}atm^{-1}$
5	+0.0281 $cm^{-1}atm^{-1}$	-0.0201 $cm^{-1}atm^{-1}$
6	+0.0541 $cm^{-1}atm^{-1}$	-0.0101 $cm^{-1}atm^{-1}$
7	+0.0758 $cm^{-1}atm^{-1}$	-0.0121 $cm^{-1}atm^{-1}$

explicit velocity integration. The simplified theory also ignores the terms $i\Delta_i$ and $i\Delta_f$ from Equation 3.40. These terms are pure imaginary quantities and hence will contribute towards the line shifts and not the linewidths. Boulet et al. [1976], using a more sophisticated theory together with explicit velocity integration, have produced calculated line shifts for the (1-0) and (2-0) bands which are in better agreement with the experimental values. In fact, for lines with m>4, Boulet et al. [1976] have produced calculated line shifts in the (2-0) band which agree in the shift direction with those of the (3-0) band measured by Campbell and Walker [1979]. The use of a more sophisticated theory like that by Leavitt [1980] to improve the calculated result is beyond the scope of this initial study. In fact, it will significantly deplete the available computing

resources which would, at the present time, be more fruitfully utilised on spectral data reduction.

3.4.8 SHIFT-CORRECTED REFERENCE WAVELENGTHS

Table 3.12 lists the vacuum wavenumbers and standard-air wavelengths of the (3-0) band lines. These have been corrected for shifts at a gas temperature of 100°C and pressure of 360 torrs. This is accomplished by applying the experimental shifts of Campbell and Walker [1979] to the adopted wavenumbers listed in Table 3.6. Listed in Table 3.13 are the unit-atmosphere shifts as given by Campbell and Walker [1979]. The temperature dependence of the unit-atmosphere shifts, $\partial\delta/\partial T$, are also listed in Table 3.13. These are the experimental values taken from Campbell [1983]. Again, the shifts are linear in pressure over the small range considered here. This has been demonstrated by Campbell and Walker [1979]. The use of the shift-corrected wavelengths from Table 3.12 has further reduced the residual in the earlier dispersion fit of the standard HF spectrum. The rms residual is reduced from ±0.00155Å down to ±0.00128Å. This corresponds to an improvement from $\pm 53 ms^{-1}$ to $\pm 44 ms^{-1}$ in velocity.

3.4.9 DOPPLER AND CELL-WALL BROADENING

There are other line-broadening mechanisms besides molecular collision broadening. These are summarised in Townes and Schawlow [1975]. The two more significant ones are the Doppler broadening and the collision broadening with

Table 3.12 Shift-corrected wavenumbers and wavelengths

m	ν	λ
1	11409.4244 cm^{-1}	8762.2777Å
2	11441.4337 cm^{-1}	8737.7637Å
3	11468.8426 cm^{-1}	8716.8815Å
4	11491.6132 cm^{-1}	8699.6090Å
5	11509.7024 cm^{-1}	8685.9363Å
6	11523.0863 cm^{-1}	8675.8476Å
7	11531.7272 cm^{-1}	8669.3466Å

Table 3.13 Line shifts for the R-branch of the (3-0) band

m	δ	$\partial\delta/\partial T$
1	-0.0342 Å.atm^{-1}	-0.115 mÅ.$K^{-1}atm^{-1}$
2	-0.0053 Å.atm^{-1}	+0.013 mÅ.$K^{-1}atm^{-1}$
3	+0.0106 Å.atm^{-1}	+0.036 mÅ.$K^{-1}atm^{-1}$
4	+0.0129 Å.atm^{-1}	-0.006 mÅ.$K^{-1}atm^{-1}$
5	+0.0152 Å.atm^{-1}	-0.044 mÅ.$K^{-1}atm^{-1}$
6	+0.0076 Å.atm^{-1}	-0.084 mÅ.$K^{-1}atm^{-1}$
7	+0.0091 Å.atm^{-1}	-0.082 mÅ.$K^{-1}atm^{-1}$

the absorption cell wall. Doppler broadening is caused by the motion of the molecule in the direction parallel to that of the radiation being absorbed. The Doppler halfwidth γ_D has been given in Townes and Schawlow [1975] as:

$$\gamma_D = (\nu/c) \sqrt{((2kT/M) \ln 2)} \qquad (3.47)$$

The term M in the above equation is the molecular mass. At the operation temperature of 100°C of the HF cell, γ_D is of the order of $0.02cm^{-1}$ for the (3-0) lines. The lines are also broadened by the molecules colliding against the absorption cell wall. The collision would interrupt the absorption process and hence cause line broadening. A rigorous treatment to calculate the wall-collision halfwidth γ_w has been given by Danos and Geschwind [1953]. A simpler but adequate expression has been given in Townes and Schawlow [1977] as:

$$\gamma_w = (A/V) \sqrt{((RT) / (8\pi^3 M))} \qquad (3.48)$$

In the above equation, A is the total inside surface area of the cell, V is the volume of the cell, R is the gas constant, and M is the molecular mass. The value of γ_w is generally much less than the pressure-broadened width.

Chapter 4

HF DATA REDUCTION

4.1 INTRODUCTION

The most time-consuming part of the HF program is the reduction of the observed spectra to obtain relative radial velocities. The very high precision required for the radial velocities causes the data-reduction procedure to be more complex and detailed than in conventional techniques. Considerations have to be made for effects too minute to be important in conventional data reduction but which would affect the result in the high-precision case. The data-reduction procedure can be roughly divided into two parts. The first part involves preprocessing the Reticon data into continuum-rectified spectra while the second part involves deducing radial-velocity information from these spectra. The two parts are not mutually exclusive since radial-velocity information is needed in the continuum-rectification procedure. The data reduction of the spectra is accomplished through the use of the data-reduction program Reticent (Yang [1980], Pritchet et al. [1982]).

4.2 PREPROCESSING OF RETICON SPECTRA

4.2.1 BASELINE SUBTRACTION

As mentioned previously, an additive fixed line pattern has to be removed from each raw Reticon spectrum. This can

be accomplished by subtracting a dark (baseline) exposure taken shortly after the data exposure. In many applications, this dark exposure can simply be a short exposure with starlight still incident on the Reticon. The linear response of the Reticon means that any photon signal detected in this short exposure would not affect the spectral characteristics of the longer data exposure after the subtraction. This is especially the case for fainter objects. A dark exposure, however, would be more desirable. A shutter is now available on the CFH Reticon system. It will close and block off all light from the detector during the baseline exposure.

There could be zero-point differences between spectra taken with different exposure times. The amounts of the zero-point drifts are also different between the output video lines. The differences are generally of the order of several adc units depending on the exposure time. It would be the best if the dark baseline exposure has the same exposure time as the data spectrum. This is usually difficult to achieve for the longer exposures. Besides lowering the efficiency in the use of telescope time, the physical state of the Reticon may not remain the same long enough for both the dark baseline and data exposures. Moreover, one would want to use the mean of many dark baseline exposures for the subtraction in order to reduce the noise contribution as well as the effect of cosmic-ray events. Generally, depending on Reticons, a shorter dark exposure would be sufficient. The characteristics of the amplifier electronics become quite constant for exposures

longer than several hundred seconds. Dark baseline exposures of similar exposure times, however, are still desirable for the shorter exposures such as those for the incandescent calibration lamps.

4.2.2 USE OF "EXTRA-READOUT" POINTS

The effect of the zero-point drifts can also be minimised or corrected by the use of "extra-readout" points (Walker et al. [1983]). Basically, these readout points are the result of performing readout sequences on the Reticon but without addressing or rebiasing the individual photodiodes. It is essentially sampling the voltages from the various output video lines. These "extra-readout" points are obtained both before and after the readouts of the 1872 photodiodes. There are about 28 useful "extra-readout" points for each output video line. By comparing the residuals in these "extra-readout" points after subtracting the corresponding ones from the dark baseline exposure, minor zero-point drifts can be numerically corrected for each output video line. The "extra-readout" points are not perfect. It has been found that in incandescent calibration lamp exposures, photon signal is also detected in these "extra-readout" points. This is possibly caused by the fact that the shift registers on the Reticon are also light sensitive and would detect photons if the light intensity is high. Generally, this effect is small in comparison with the amount of zero-point drifts. Some Reticons are also known to contain light signals in the second set of the

"extra-readout" points. These are the points obtained after the readouts of the 1872 photodiodes. The amount of signal in these points is found to be a function of the signal accumulated in the 1872 photodiodes. This behaves as if residual charges are left in the output video lines after the readouts of the photodiodes. Consequently, the second set of the "extra-readout" points may be unsuitable for use in zero-point-drift corrections.

4.2.3 RELATIVE GAIN CORRECTION

4.2.3.1 Line-normalisation procedure

The relative gains of the output amplifiers are usually adjusted only to within 5%. This implies that the gain is slightly different for each output video line. The relative gains effect is a multiplicative effect and a different multiplicative normalisation constant has to be applied numerically to the output from each video line. This is essentially the simple multiplicative line-normalisation process where each normalisation constant is taken to be the ratio between the mean signal of the particular output line and the mean signal over all output lines. The multiplicative effect, however, would be complicated by any residual zero-point drift which is an additive effect. One cannot use a simple numerical additive or multiplicative line-normalisation process to perfectly decouple and correct the two effects. To complicate matters, the gain of each output line also has a small dependence on the

accumulated signal level. This effect is a small nonlinearity. The change in gain is typically about $5x10^{-8}$ per adc unit over the signal range in the high gain mode of the Reticon. It becomes greater at higher signal levels where the accumulated signal is a significant fraction of saturation.

In conventional techniques, the relative gains effect is corrected by dividing the data spectrum by a lamp spectrum exposed to the same continuum signal level. A four- or eight-line multiplicative or additive normalisation process is then applied. Several problems may exist in this procedure. The fact that the data spectrum contains spectral lines which will have signal levels quite different from the continuum signal level, division by a continuous lamp spectrum would cause incorrect gain corrections to be applied to the spectral lines. Residual additive pattern from the baseline subtraction would also affect the accuracy of a simple line-normalisation process.

4.2.3.2 Use of step lamps

One method to calibrate the relative gains effect and the small nonlinearity is through the use of step incandescent lamp spectra. Basically, one obtains a series of continuous lamp spectra with each of them exposed to a different signal level. The series of lamp spectra should cover the entire range of signal levels. One can calculate the multiplicative line-normalisation factors for each spectrum and hence for each different

signal level. A polynomial can then be used to fit the normalisation factors as a function of signal levels in each separate video line. These polynomials can then be used to correct the relative gains and nonlinearity effects for each individual point in the data spectrum. First-order polynomials are generally adequate to provide a good fit over the entire signal level range in the high-gain mode of the Reticon. Higher-order polynomials are needed in order to cover the entire range of signal level up to saturation. Usually, ten or more spectra are required for the fit. The goodness of the polynomial fits depends on the quality of the lamp spectra. Appropriate dark baselines should be used for these lamp spectra. And any zero-point drift as indicated by the extra readout points should also be corrected. The region in the continuous lamp spectra where the normalisation factors are calculated should be relatively flat i.e. have a small range in signal levels. This is usually the case when one is working in the near infrared and at high dispersions. Otherwise, filters have to be used to produce a flat region in the lamp spectra.

4.2.4 FLAT-FIELDING

After dark baseline subtraction and application of the various line-normalisation procedures, the data still have to be flat-fielded. This is to remove diode-to-diode sensitivity variations as well as non-uniformities in the

Reticon and spectrograph spectral responses. Dust particles on the Reticon surface would also alter the uniformity of the response. This is especially relevant to the Reticon detector at CFHT. Removal of non-uniformities in the response across the Reticon spectrum would also ease the application of continuum rectification. Flat-fielding can be accomplished by numerically dividing the data spectrum by an incandescent lamp spectrum. Dark baseline subtraction as well as all the necessary line-normalisation preprocessing should have been applied to this lamp spectrum before the division. Care should be taken to ensure the light beams from both the lamp and the star illuminate all the optics identically. It is especially important for the lamp beam to illuminate exactly the same part of the Reticon array as the stellar beam. This has been achieved to a certain extent by the use of an image slicer which creates a one dimensional equivalent of a Fabry-image (Campbell et al. [1981]). However, small effects may still exist if the lamp and stellar beams are not identically matched.

One method previously used at DAO to match the lamp and stellar beams was to use the lamp light reflected off the inside of the dome. The lamps were mounted on the top end of the telescope. Each lamp spectrum was also taken at the same telescope orientation as the particular star. Excellent flat-field lamp spectra were obtained. This claim is based on how well the lamp spectrum would flat-field the response caused by a dust particle on the Reticon array. One of the major disadvantages of this method to obtain matched

flat-field lamp spectra is that very long exposures are generally needed. This is especially bad when one wants to use the mean of many of these spectra to reduce noise contribution. The bright lamps would also degrade the seeing by warming up the dome as well as attracting moths to the telescope.

Another method is adopted at the present time at both CFHT and DAO. An iris diaphragm is used to isolate the telescope exit pupil formed by the converging lens which is the last element in the Coudé train. A lamp illuminating this pupil would produce a beam which will match the stellar beam. The position of the diaphragm needs to be adjusted for each stellar object because of slight mis-collimation of the Coudé train. The lamp exposures are generally short. If the lamp spectrum has a significant slope, as is the case in the blue spectral region, a low order polynomial fit of the lamp spectrum can be divided out from the lamp spectrum. Otherwise, dividing each point in the lamp spectrum by the mean value would be sufficient to produce a normalised flat-field.

After dividing the stellar spectrum by the flat-field lamp, a four-channels additive line-normalisation procedure can be applied to remove any small residual line pattern. This generally is a very small correction and is of the order of an adc unit or less. If the lamp spectrum was, however, not taken at the same physical state of the Reticon as the stellar spectrum, the four-channels line-normalisation would not reduce the residual line

pattern. This can occur when the lamp or stellar spectrum was taken when the Reticon was in the process of reaching temperature equilibrium after a liquid-N_2 refill. An eight-channels line normalisation may be useful in this case. If the lamp spectrum is of poor quality, it should be smoothed to about 5% of the Nyquist frequency to avoid degrading the stellar spectrum. The additive line-normalisation process should not be applied to arc spectra.

4.3 REDUCTION OF HF DATA

4.3.1 CONTINUUM RECTIFICATION

There are four types of spectra one has to obtain in an observing run in order to produce a relative radial-velocity measurement. These are the stellar spectra with imposed HF lines, the stellar spectra with no imposed HF lines, the continuous lamp spectra with HF lines, and the continuous lamp spectra without the imposed HF lines. All these spectra are used in the data-reduction procedure to measure radial velocities for the stellar lines in the spectrum with the imposed HF lines.

For greater consistency, the identical spectral region is used at all times in the HF programs. In fact, the same coverage is used at both DAO and CFHT where the reciprocal dispersion is the same 4.8Å/mm. The identical spectral coverage is achieved by aligning the Reticon and spectrograph such that the arc line Ar I λ8667 would always

locate at the same pixel position of 351 on the Reticon array. Furthermore, to avoid any inconsistency in the focus of the spectra due to the curved focal plane, the same criteria are used to focus the Reticon. The Hartmann mask is always used to obtain optimum focus on the same arc line of Fe I λ8689. This is essentially to monitor the pixel position of the arc line when different parts of the beam are masked off.

In most HF programs, a stellar spectrum is generally used as a radial-velocity standard (or reference) spectrum for that same star. Similarly, an HF spectrum is used as a reference spectrum for HF lines in all spectra. These standard spectra can also be used as the spectral standards for pseudo-continuum rectification of the data stellar spectra. The standard stellar spectra are generally taken without the imposed HF lines. Pseudo-continuum rectification of the standard spectra is the same as in conventional techniques. This is achieved by dividing the spectrum by a polynomial fit to the continuum points in the spectrum. Each continuum point in the fit is generally taken to have the mean signal of several neighbouring points. Due to the paucity of good available continuum points, a low-order polynomial fit is generally used. This is especially the case for the spectra with strong and broad lines e.g. those of α Lyr. A similar procedure can be applied to the standard HF spectrum which is a continuous lamp spectrum imposed with HF lines. More continuum points are available in this particular application and a higher-order polynomial fit can

be used. Again, the continuum points are chosen to avoid the broad wings of the HF lines.

A general way to continuum rectify a data spectrum is first to divide the data spectrum by the rectified standard stellar spectrum. Division by the rectified HF standard spectrum is also performed if the data spectrum contains the imposed HF lines. The residual ratio spectrum is then fitted by an appropriate function (polynomial or others). A rectified data spectrum is then obtained by dividing the original data spectrum by this function fit. The residual ratio spectrum generally contains besides the general shape of the spectral response, many features such as low-spatial-frequency variations and even fringe patterns. Generally, these patterns appear when one divides the data spectrum by a standard spectrum taken on another observing date or run. The patterns are much less visible when the data spectrum is compared to a standard spectrum taken on the same night. In most applications, one can actually ignore all these small features. It is only when one is going for very high precision i.e. better than $\pm 20 ms^{-1}$ that they may become important. A single polynomial fit to all the features in the complicated spectrum is usually impossible. One can, however, subdivide the spectrum into smaller sections and apply polynomial or sinusoidal function fits to each individual section. The discontinuous joints between the polynomial fits from different sections can be numerically smoothed. A simpler method is to use a cubic-spline fit rather than the pseudo-piecewise-polynomial

fit. The goodness of fit to the residual spectrum is very dependent on how well the standard spectrum matches the particular data spectrum. This is one of the main reasons why the standard spectrum is usually that of the same star. Other factors that would affect the match include differences between the instrumental profile, focus, radial velocity, and dispersion. The former are generally kept to a minimum by careful alignment of the equipments while the latter can be corrected by numerical methods. However, one will have difficulties if there are intrinsic line-profile variations.

Radial-velocity and dispersion corrections can be applied to the standard spectrum to produce a better matching spectrum. This, however, requires the knowledge of at least rough radial-velocity and dispersion information. A better method would be the use of a polynomial fit between the positions of corresponding spectral lines in the data and standard spectra. Based on the polynomial fit, an interpolation procedure can then be applied to the standard spectrum to produce a better matching spectrum. However, this method would become rather complicated for variable-star spectra where different lines may have different velocities. It is also difficult for a single polynomial to represent all the higher-frequency dispersion variations. A more suitable method is again the use of a cubic-spline fit between the two sets of line positions. A sinc-interpolation method is generally used with the fit to produce the matching spectrum. The same procedure is also

applied to the continuum rectification of the HF spectra. The final residual spectrum will probably still contain effects of poor line cancellations. These can be "overlooked" in the continuum fit by careful choice of the continuum points. Imperfect cancellation between lines will be discussed in more detail later when its effect on line-position determinations is examined.

4.3.2 LINE-POSITION DETERMINATION

4.3.2.1 Line cancellations

The data stellar spectra have both HF and stellar lines. Blendings between the two sets of lines would seriously affect any direct line-position measurement from the spectra. Dividing the data spectrum by the matched standard HF system will give a stellar spectrum essentially free of the contaminations by the HF lines. Any small residual due to imperfect line cancellations would not be a serious problem. One can simply ignore the few affected stellar lines and there would still be plenty of unaffected stellar lines left. The stellar line positions can be derived from the relative line positions obtained by comparing this HF-free stellar spectrum with the standard stellar spectrum. This is accomplished for each individual line by means of the difference technique described by Fahlman and Glaspey [1973]. Since one is comparing the corresponding individual line profiles, it is not necessary to use the matched spectrum as the reference spectrum. The original

standard spectrum is sufficient for the purpose. Any difference in the dispersion between the spectra over the narrow width of the individual stellar line profile is negligible. In fact, one should use the same standard spectrum as the comparison spectrum for all other data spectra of the same star. This will ensure that the same criteria are used to determine each relative line position. Relative radial velocities determined for each individual line will be internally consistent for all the spectra of the same star. One can then make direct comparison between these velocities without the need of any additional correction.

The HF line positions can also be measured with the difference technique by comparing the HF lines in the data spectrum against those in the standard HF spectrum. Dividing the data spectrum by the matched stellar spectrum will give an HF spectrum almost free of the contaminations by the stellar lines. The contaminations by the stellar lines can also be minimised by dividing the data spectrum by a stellar spectrum which has been numerically shifted in pixel position. The amount of shift used is such that it would produce minimal residual in the neighbourhood of the HF lines after the spectrum division. A rough line cancellation can be achieved if a single mean shift is used. For more refined work, different optimal values of shift can be used for different HF lines. However, this would imply a significant increase in the amount of required

computation when individual spectrum cancellation is used for each HF line-position determination. Moreover, different difference-technique calculation has to be applied to each line. The same technique can also be used to numerically minimise the contaminations on the stellar lines by the HF lines.

No matter which line-cancellation technique is used, there will always be small residuals due to imperfect line cancellations. These residuals are caused by a variety of small effects. These include intrinsic line-profile variations, imperfect preprocessing of the Reticon spectra, and imperfect dispersion match. One of the most serious limitations is an effect caused by the nonzero-width of the instrumental profile and line blendings.

Campbell and Walker [1985] have pointed out that the observed spectrum is actually the convolution between the intrinsic spectrum with the instrumental profile $I(\lambda)$. For the intrinsic stellar spectrum $S(\lambda)$ and the HF spectrum $H(\lambda)$, the observed spectra are $S(\lambda)*I(\lambda)$ and $H(\lambda)*I(\lambda)$, respectively. The operation symbol * denotes convolution. Similarly, the observed stellar spectrum with imposed HF lines would then be $[S(\lambda)H(\lambda)]*I(\lambda)$. Consequently, line cancellation by flat-fielding-type division technique is not quite correct i.e.

$$\{[S(\lambda)H(\lambda)]*I(\lambda)\}/[H(\lambda)*I(\lambda)] \neq S(\lambda)*I(\lambda) \qquad (4.1)$$

$$\{[S(\lambda)H(\lambda)]*I(\lambda)\}/[S(\lambda)*I(\lambda)] \neq H(\lambda)*I(\lambda) \qquad (4.2)$$

Equality in Equations 4.1 and 4.2 would hold only if there is no blending between the stellar and HF lines or the instrumental profile is very narrow. However, either of these conditions is almost impossible to attain. There will always be stellar lines blended with the HF lines especially for the later-spectral-type stars. The instrumental profile is fixed by the projected slit width of the image slicer and by the red resolution loss of the Reticon. It is the line blendings that nullify the equality in Equations 4.1 and 4.2 and hence contribute to the residual in the line cancellations. The residual is a function of the relative line strengths between the stellar and HF lines, the linewidths, the relative line positions, and the criteria used to determine line positions. The line blendings also change with the apparent radial-velocity variations of the star. Different stellar lines will be blended with the HF lines as the apparent radial velocity of the star changes with the barycentric Earth's orbital motion, Earth's rotation, and any intrinsic radial-velocity variations of the star. These cause the residual from imperfect line cancellation to be radial velocity and spectral type dependent.

The effect of contamination by HF line residuals on stellar lines is not critical since one can simply ignore the more seriously affected stellar lines. In the case of the contamination by stellar line residuals on HF lines, the problem cannot be ignored. There are only

a few HF lines in the spectrum. Campbell and Walker [1985] have studied the problem in detail. They adopted a more passive and numerically stable method to correct the effect than the obvious method of direct instrumental profile deconvolution. Appropriate artificial $S(\lambda)$, $H(\lambda)$, and $I(\lambda)$ are first generated in order to compute the artificial spectra $S(\lambda)*I(\lambda)$, $H(\lambda)*I(\lambda)$, and $[S(\lambda)H(\lambda)]*I(\lambda)$. The ratio spectrum $\{[S(\lambda)H(\lambda)]*I(\lambda)\}/[S(\lambda)*I(\lambda)]$ can then be constructed for different relative stellar-HF line positions. If the blending is not severe, correction to any measured HF line position can be made by comparing the observed and artificially generated residuals. Generally, these corrections are necessary only if one wants to achieve a velocity precision of better than $\pm 20 ms^{-1}$. Young [1978] has also studied the effect of line shifts due to line blending.

When one is comparing spectra taken from different observing runs, imperfect cancellations of the stellar lines can also be caused by changes in $I(\lambda)$ between the runs. It has been noticed in spectra of the same star that the stellar lines may appear more asymmetric in some observing runs. Correction for this effect is generally difficult and may have to rely on the comparison between the standard spectra (both HF and stellar) taken in the different observing runs.

4.3.2.2 Line position in standard spectra

The line positions in the standard spectra are generally determined by the criterion of intensity-weighted centre-of-gravity:

$$x = (\Sigma_i I_i^n x_i) / (\Sigma_i I_i^n) \qquad (4.3)$$

The measured line position is x, and I_i is the line intensity corresponding to the point or pixel x_i. The power n would be equal to one for the usual centre-of-gravity criterion. The condition n=2 could result in a better dispersion fit to arc lines. The summation is carried over the whole line profile between a short-wavelength line limit and a long-wavelength line limit. It would be optimal if these limits coincide with the positions of zero-percent line absorption. To use the line-position definition as specified in Equation 4.3, the spectrum has to be continuum rectified and inverted such that absorption lines would appear as emission lines. The advantage of the intensity-weighted centre-of-gravity criterion is that it is a nonparametric estimation of the line position. It can be considered simply as the arithmetic mean position of the line profile with each point weighted by its intensity. No theory of the line shape is utilised as compared to most line-profile-fitting techniques. This is especially important for variable stars where line-profile variations may occur. If one is, however, only interested in the relative radial velocities of the star, the criterion of how one would determine the line

positions in the standard spectrum is not important.

4.3.2.3 Use of the derivative of the line profile

The main weakness of the intensity-weighted centre-of-gravity criterion is the requirement of line limits. This is not a serious problem for isolated lines as in the HF spectrum where positions of nearly zero-percent absorption can be found. Line blendings, however, would limit the ability to place limits for the stellar lines. One should use a consistent criterion to locate line limits. Criteria such as using the positions of 50% line absorption etc. are good except that they cannot be easily and unambiguously measured from the digital data. A more easy and practical approach is to choose the positions coinciding with the maximum and minimum of the first derivative of the line profile. Figures 4.1, 4.2, and 4.3 show the first derivative of the HF spectrum, the ρ Pup spectrum, and the 38 Eri spectrum, respectively. It can be seen from the figures that the positions corresponding to the maximum and minimum in the derivative of the line profiles are sharply defined. The zero-crossings in the derivative spectrum correspond to the positions of maximum line absorption i.e. "peak" line positions. The pixel positions for the two limits are obtained by simply examining the derivative spectrum. For a symmetric line profile, the two limits will also have the same percentage of line absorption. In fact for a Gaussian line profile, the two limits correspond to the positions

Figure 4.1 The first derivative of the HF spectrum

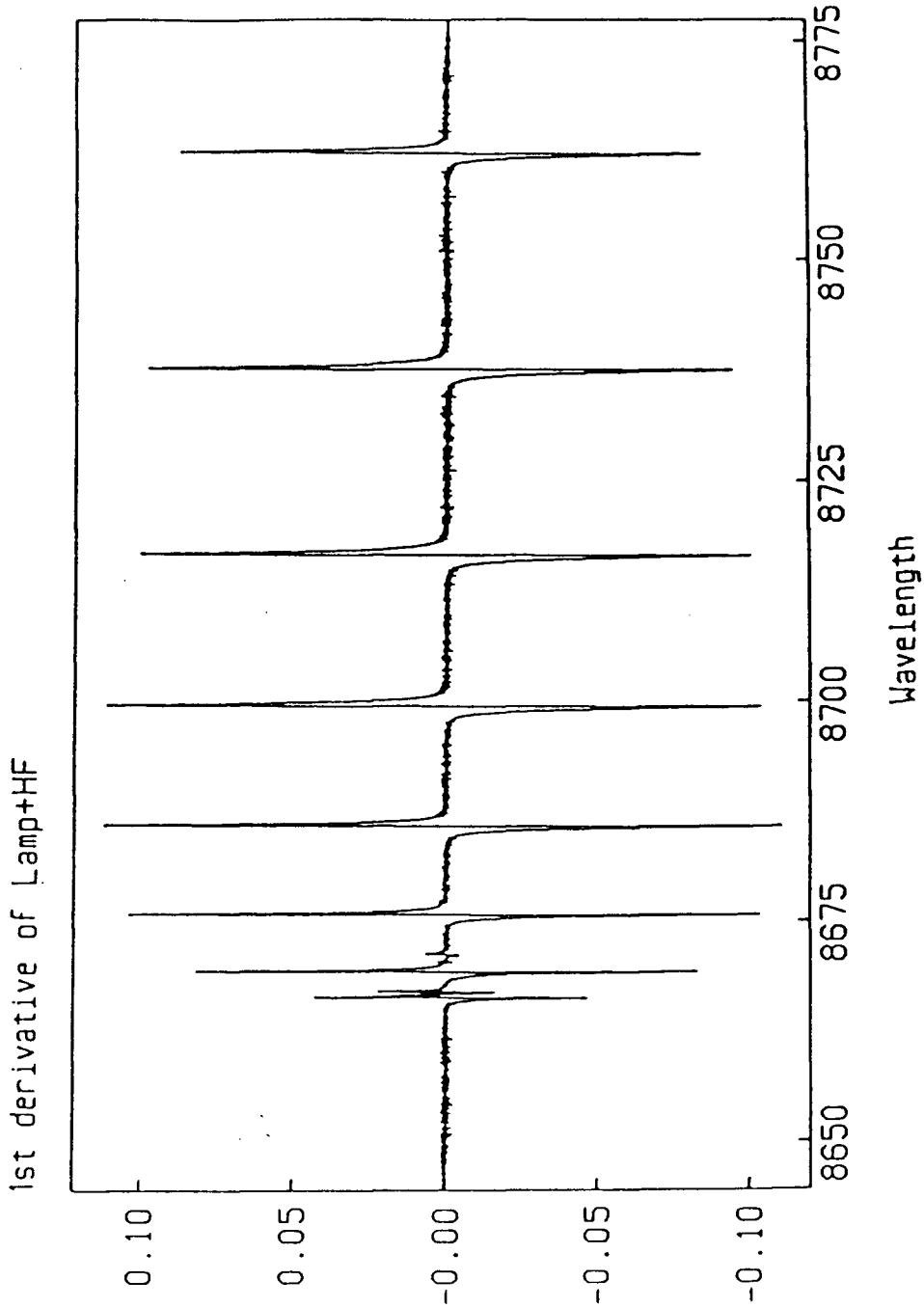

Figure 4.2 The first derivative of the ρ Pup spectrum

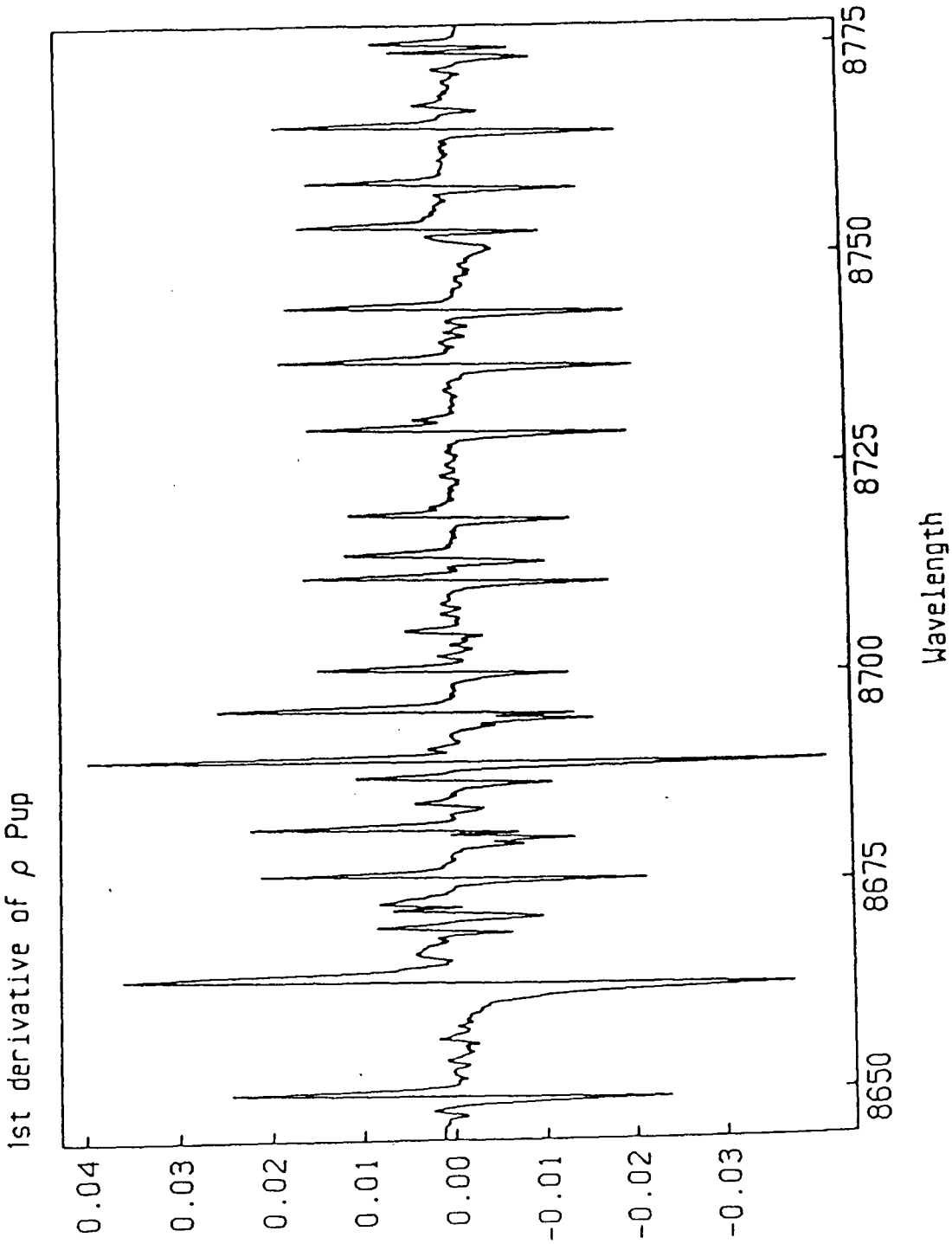

Figure 4.3 The first derivative of the 38 Eri spectrum

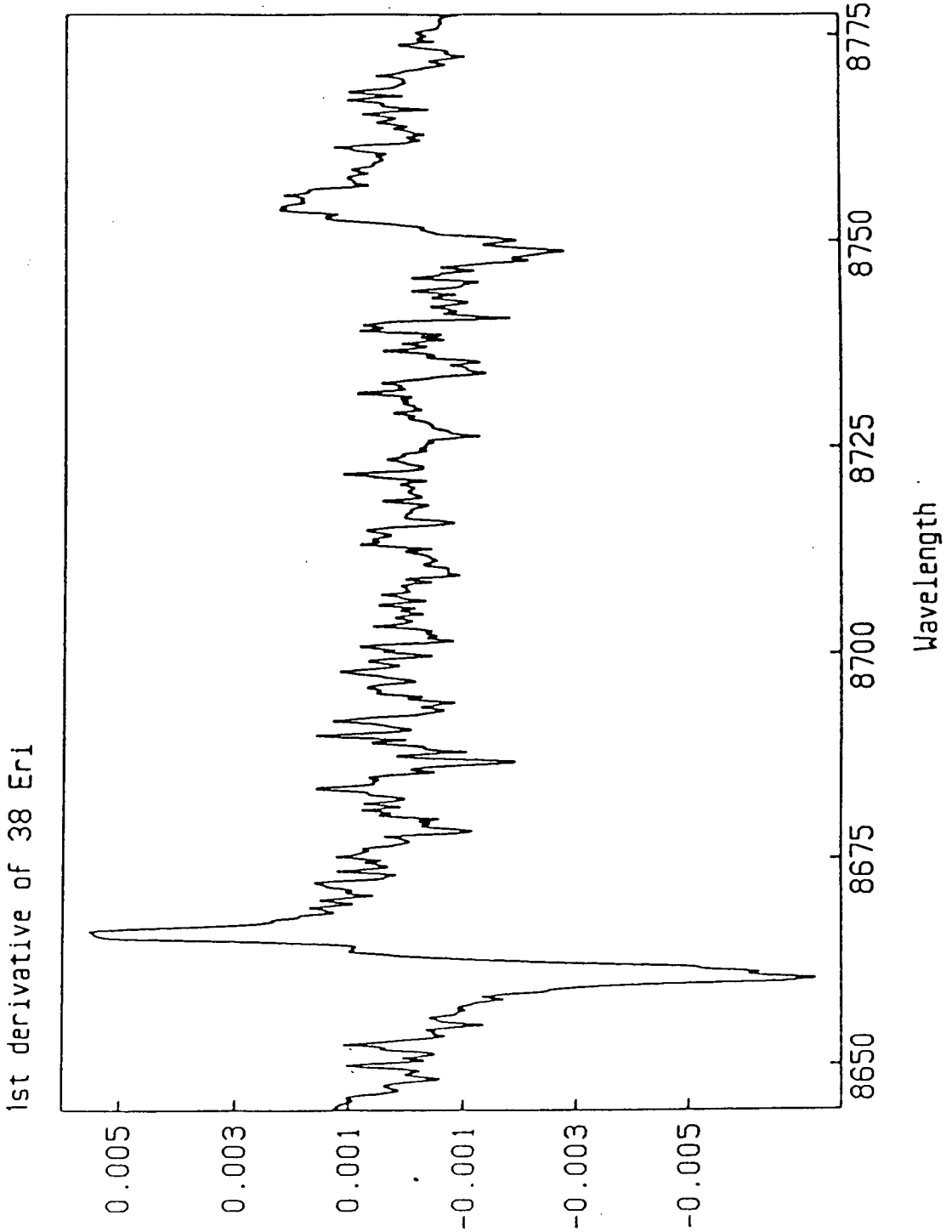

defining the σ halfwidth of the line profile, where σ is the standard-deviation parameter for the Gaussian line profile. Of course, in order to include more of the line profile, one can choose limits corresponding to $m\sigma$, where m is greater than one e.g. $m=\sqrt{(2\ln 2)}$ would be equivalent to the halfwidth at half the line depth. The effect of line blendings will, however, become proportionally greater. If one wants to locate the positions of the two limits more precisely than to the nearest pixel, one can numerically find the corresponding zero-crossings in the second derivative spectrum. The derivative of a spectrum can be easily computed numerically using the Fourier Transform method. For a spectrum $S(\lambda)$ and its Fourier Transform $T(\omega)$, the first derivative is simply the inverse Fourier Transform of $i\omega T(\omega)$. Similarly, the second derivative is simply the inverse Fourier Transform of $-\omega^2 T(\omega)$. For low s/n data, the derivative spectrum may have to be smoothed before it can be used.

The method of intensity-weighted centre-of-gravity is not the most ideal for very high precision determination of relative line positions. It is quite sensitive to the choice of line limits. Fahlman [1982] has shown that error terms will be introduced into the result if the limits are not chosen to be at the positions of zero-percent line absorption. The error terms will also be cancelled if both limits are chosen at the positions which have the same percentage of line

absorption. None of these conditions can be easily achieved. The necessity to sum between non-integer-valued line limits is not an easy computational procedure, even if the limits can be defined with sufficient accuracy. The presence of nonsymmetrical line profiles will further complicate the problem. It is more desirable to use a method for the determination of relative line positions which is less sensitive to the accuracy in the placement of line limits but would still preserve the nonparametric estimation property of the centre-of-gravity criterion.

4.3.2.4 The Fahlman-Glaspey difference technique

The most general and nonparametric technique to determine the relative position between two spectral lines is probably the technique of cross-correlation. The maximum of the cross-correlation function between two line profiles will occur at the position corresponding to the relative shift between them. A similar method is the difference-function technique described by Fahlman and Glaspey [1973]. In fact, finding the minimum of the difference function is mathematically equivalent to finding the maximum of the cross-correlation function (Fahlman [1984]). The difference-function technique is, however, more intuitively attractive as it can be expressed in terms of least-squares minimisation. It can also provide an error estimate for the calculated relative line shift. Similar to the centre-of-gravity method, the accuracy of

a line-shift measurement with the difference-function technique depends on the equivalent width of the line i.e. the amount of information in the line. This conclusion, however, does not include any consideration of the noise. This point will be discussed later in the chapter.

Basically, the data spectrum $B(\lambda)$ is numerically shifted (displaced in pixel position) by various amounts and subtracted from the standard spectrum $A(\lambda)$. The sum of squares of the residuals in the difference spectrum over the particular line profile is computed for each different shift of the data spectrum. One can then formulate a difference function $D(s)$ which is a function of the shift s, and takes on the value of the corresponding sum of squares of the residuals:

$$D(s) = \Sigma_i \; [\; A(\lambda_i) - B(\lambda_i+s) \;]^2 \qquad (4.4)$$

The term $A(\lambda_i)$ is the intensity at pixel i in the spectrum $A(\lambda)$. The minimum of the difference function would give the optimal shift which would produce the minimum sum of the squares of the residuals. As in the case of the cross-correlation technique, non-integer values for s are generally required for high precision results. Interpolation has to be used to produce a spectrum shifted by a non-integer amount. This can be easily accomplished by the Fourier Shift theorem. The shifted spectrum $B(\lambda+s)$ is simply the inverse Fourier Transform of $\exp(i\omega s)T(\omega)$, where $T(\omega)$ is the Fourier Transform of $B(\lambda)$. This procedure is equivalent to the

sinc interpolation. An assumption of identical line shape for both $A(\lambda)$ and $B(\lambda)$ would mean $B(\lambda) = A(\lambda - s_0)$, where s_0 is the intrinsic relative line shift. Fahlman and Glaspey [1973] have shown that under this assumption, $D(s)$ in Equation 4.4 is a parabola when $A(\lambda + s - s_0)$ is Taylor expanded to the first order of $s - s_0$. This means a second-order polynomial fit to the difference function is optimal and the minimum of the parabola corresponds to the optimal shift. The Taylor expansion carries the additional assumption that $s - s_0$ is small. This assumption is almost always true since any integer portion of the shifts can be explicitly corrected before application of the method. Generally, for the high s/n HF data, sixth-order polynomials are found to provide better fits to the difference functions. This is using about 14 different values of s in steps of 0.05 pixel about the difference function minimum. The parabola fits, however, are still very good approximations near the minimum of the difference functions. The position of the minimum difference is found by numerically solving for the roots to the derivative of the polynomial fit. Discrimimating the roots is not a problem. Conceivably, with increased computation, one can dispense with the polynomial fit and apply optimisation techniques to find the minimum of the difference function directly.

Generally, the difference function technique is applied to individual lines. The summation in Equation

4.4 is best to be performed over the whole line profile. If the line limits for the summation are defined over only a partial line profile, it will result in the calculation of a difference function different than that summed over the whole profile. But if the residuals are the result of pure relative line-position shift, this difference function should also be minimal at the same shift position as that summed over the whole profile or any other part of the profile. Therefore, the calculated relative line shift is not very sensitive to the accuracy in the placement of the line limits. In cases of small intrinsic shifts, residuals in the difference spectrum at the far wings of the line are usually small compared to that from the line core. The squaring of the residuals in Equation 4.4 further decreases the relative contribution from the wings to the difference function. Consequently, for relative radial-velocity work, a consistent criterion to define line limits covering the whole line core would be adequate. Of course, the more of the profile is utilised, the more velocity information is used, and hence a more accurate determination will result. However, the wider the line limits, the more acute will be the imperfect line-cancellation effects caused by increased stellar-HF line blendings. In fact, this is one of the major limitations on the accuracy of the measured HF line positions and hence the accuracy of the measured velocities. Consequently, the line limits for the HF

lines are usually more restricted than the corresponding ones used for the centre-of-gravity line-position measurements in the standard spectrum. A set of line limits corresponding to twice that indicated by the positions of maximum and minimum in the derivative is generally used. Less restrictive limits may be used for the imposed HF lines from broad-stellar-line spectra. In this case, the imperfect line-cancellation effect is less severe. For the stellar lines, the same line limits used for the centre-of-gravity line-position measurements in the standard spectrum are also used for the difference-function technique.

4.3.2.5 Line-profile variations

In the case of line-profile variations, a consistent criterion to define the line limits becomes important. Line-profile variations can be quantified in terms of relative radial-velocity variations. The difference function technique can also be applied to measure these pseudo radial-velocity variations. In this case, the residuals in Equation 4.4 are produced by profile variations rather than by pure displacement of the line profile. The residuals will be different at different parts of the profile and will also be a function of the type of profile variations. Hence the criterion to choose the line limits for the difference-function technique is essentially the criterion to sample a particular part of the profile variations. The line limits also determine the relative

contributions toward the measured pseudo radial velocity from different parts of the profile. As for example, in most types of profile variations, the variations near the line core are greater than those at the line wings. The measured radial-velocity amplitude for the variations would then be proportional to the line limits' relative coverage between the core and the wings. Similarly, the effects on the shape and phase of the radial-velocity curve in cases where the line-profile variations are characterised by "features" moving across the line, would be even more complicated. To make a comparison between results from different stars or with model calculations, it is important to have a consistent criterion to choose the line limits. In general, for narrow-line spectra with or without profile variations, the adopted criterion is to choose the line limits as the positions coinciding with the maximum and minimum in the first derivative of the line profile. For broad-line spectra, broader line limits may be possible depending on the severity of the line blendings. The line limits are always chosen to be those on the standard spectrum. This is a computational detail to ensure that the same line limits and criteria are used for the same stellar line in all of the spectra. And hence is the main reason why in Equation 4.4 that the shifts are applied to the data spectra $B(\lambda)$ and not to the standard spectrum $A(\lambda)$.

4.3.2.6 Optimising difference function

Besides line-profile variations and radial-velocity shifts, there are other systematic effects which could contribute to the residuals and the difference function. They are the very small effects caused by imperfect data preprocessing, presence of dark current or persistence phenomenon induced non-zero offsets in the detector's response, imperfect continuum rectification, and differences between the instrumental profiles. These effects should be removed or corrected from the difference function such that the accuracy of the function to measure spectral shifts is limited by only the finite s/n of the spectra. This can be accomplished to a first approximation by normalising the two spectra $A(\lambda)$ and $B(\lambda)$ to have the same line depth or equivalent width etc. One of the most effective yet still very simple procedures is to formulate a modified difference function $E(s)$:

$$E(s) = \Sigma_i \; [\; (A(\lambda_i)-a) - \beta(B(\lambda_i+s)-b) \;]^2 \qquad (4.5)$$

The term a is the mean of the spectrum $A(\lambda)$ over the line limits, and b is the mean of the spectrum $B(\lambda+s')$ over the line limits. The term s' is the initial estimate for the intrinsic relative line shift s_0. It is calculated as the position of $D(s)$'s minimum. The term β is a scale factor that would minimise $E(s')$. An analytic expression for β can be derived from the condition $\partial E(s,\beta)/\partial\beta = 0$ at $s = s'$. One obtains:

$$\beta = [\; \Sigma_i A(\lambda_i)B(\lambda_i+s') - nab \;] \; /$$

$$[\ \Sigma_i B(\lambda_i+s')^2 - nb^2\ ] \qquad (4.6)$$

$$E(s) = \Sigma_i A(\lambda_i)^2 - 2(a-\beta b)\Sigma_i A(\lambda_i) - 2\beta\Sigma_i A(\lambda_i)B(\lambda_i+s) + \beta^2\Sigma_i B(\lambda_i+s)^2 - 2\beta(a-\beta b)\Sigma_i B(\lambda_i+s) + n(a-\beta b)^2 \qquad (4.7)$$

$$D(s) = \Sigma_i A(\lambda_i)^2 - 2\Sigma_i A(\lambda_i)B(\lambda_i+s) + \Sigma_i B(\lambda_i+s)^2 \qquad (4.8)$$

The term n is the number of points over the line limits. Equations 4.7 and 4.8 are mathematically equivalent to Equations 4.6 and 4.5, respectively. The function $E(s)$ is rewritten in a more easy computational form such that it can be constructed from the same basic information computed in obtaining s' from $D(s)$. This avoids the need to apply additional shifts to $B(\lambda)$ and calculating more residuals. The modified difference function $E(s)$ is basically the result of adjusting $A(\lambda)$ and $B(\lambda+s)$ to the same mean value or offset and then applying a scale factor to modify the line depth of $B(\lambda+s)$. This procedure results in minimising the difference function. The position of minimal $E(s)$, s'', would be an improved estimate for the optimal shift over s'. In fact, $E(s'')$ is always less than $D(s')$. The differences between the two values are usually small except in cases where the required corrections are large i.e. a being quite different than b, or β not close to one. Of course, one should be aware of the consequences in applying $E(s)$ rather than $D(s)$ for lines with intrinsic profile

variations.

4.3.2.7 Error estimation

The minimum of the difference function represents the minimal mean square residual possible under the effect of noise present in the spectra. In the case of noise-free data, the minimum of the function would be zero. This will also happen if the noise is correlated between A(λ) and B(λ) such that the residual goes to zero at $s = s"$. The minimum value of the difference function can provide a measure of the accuracy in the measured relative shift. Fahlman [1984] has pointed out that the minimum of the difference function follows a χ^2_ν distribution with $\nu = 2(n-1)$ degrees of freedom. In the case of $E(s)$ or other modified difference functions, the number of degrees of freedom would be decreased by the number of additional estimated parameters in the formula e.g. a, b, and β. Since $s"$ is only an estimate for the true shift s_0, $E(s")$ is also an estimate for the true minimal difference. With a confidence interval, e.g. 68.3% for equivalence to that one standard deviation, χ^2_ν can be evaluated and one can then get an estimate for the standard deviation σ of $E(s")$:

$$\sigma = \nu \, E(s") \; / \; \chi^2_\nu \qquad (4.9)$$

This implies that there is a 68.3% chance that the true minimal difference would lie within σ of $E(s")$. This standard deviation can then be translated directly from the shape of the difference function into a standard

deviation for the measured optimal shift s", and hence, a standard deviation for the measured relative radial velocity. The reciprocal of the difference function minimum should also provide an estimate for the effective s/n of the spectra. If the noise in A(λ) is very small, then the s/n of B(λ) is essentially $b/\sqrt{E(s")}$.

4.3.2.8 Dispersion relation

The absolute position of any line can be derived from its relative line shift with respect to the absolute line position on the standard spectrum. The position is then corrected for the effect of imperfect line cancellations caused by line blendings and convolution with the instrumental profile. To translate the line position into a wavelength measurement, the dispersion relation has to be calculated. A polynomial fit to the HF line positions against their wavelengths would provide the dispersion calibration. The HF wavelengths used in the dispersion fit would be the adopted absolute wavelengths corrected for any absolute or differential line shifts induced by the temperatureand pressure-dependent molecular collisions. Generally, thirdor lower-order polynomials are used to fit the HF lines. This is imposed by the fact that a higher- order polynomial fit is not feasible for the small number of HF lines in the spectrum. Each line is weighted by the square of its line depth in the dispersion fit. For consistency, the same weight is used

for the same line in all of the spectra. The particular choice of the weighting function has been shown by Fahlman [1984] to be a direct consequence of minimising the difference function for the multi-line case. Without the detailed line-position or reference-wavelength shift corrections, a standard deviation of the order of 0.0015Å can be achieved in a dispersion fit of the HF spectrum from the CFHT Coudé. This corresponds to a standard deviation of $50ms^{-1}$ for the velocities.

The dispersion fit is basically the mean dispersion relation for the spectrum and it can be evaluated at any stellar line position to give the observed wavelength of that line. The HF lines in the spectrum are separated from each other by about 10 to 25 angstroms. Hence only the low-frequency components of the dispersion relation are calibrated by the HF lines. High-frequency structure may still be present in the dispersion relation. This structure could be the result of optical effects within the spectrograph as well as irregular spacing between the Reticon photodiodes. Differences in the shape of the photometric response across each individual photodiode would be manifested as differences in the spacings between each photodiode's optical centres. For a velocity precision of $\pm 10ms^{-1}$, the wavelengths have to be measured to an accuracy of $\pm 3 \times 10^{-4}$Å. Hence if the high-frequency structure can cause a difference from the mean dispersion relation of more than $\pm 3 \times 10^{-4}$Å, very-high-precision results can be affected.

To decrease the effects of the high-frequency structure in relative radial-velocity work, the Reticon is always aligned such that the HF lines are at the same positions on the Reticon array i.e. having the same identical spectral region at all times. The mean dispersion relation can be improved by including the stellar lines into the dispersion fit. In this case, the stellar wavelengths are the apparent wavelengths with the same velocity shift for all lines. Hence an iterative procedure has to be used between the dispersion relation and the derived velocity in order to achieve internal consistency. Of course, this cannot be applied to variable stars where different lines can have different velocities. One simple ad hoc way to take into account the intermediate-frequency structure in the wavelength calculation of a stellar line is to weight each HF line inversely with its separation from the particular stellar line. A different dispersion relation can be generated for each HF line such that the wavelength residual at the position of the HF line is zero. This is accomplished by retaining all the high-order terms from the mean dispersion fits but correcting the zeroth-order term to give zero residual at the particular HF line position. Hence for N HF lines in the spectrum, there would be N different dispersion relations. And N different wavelength measurements can then be evaluated for a particular stellar line. The observed stellar line wavelength would then be the

weighted average of these N wavelengths. Each weight is inversely proportional to the separation between the particular HF line and the stellar line as well as directly proportional to the square of the HF line depth. Generally, the result of this weighted wavelength is different by about several metres per second in velocity from those obtained directly through the mean dispersion relation.

Campbell et al. [1981] have studied in detail the high-frequency structure of the dispersion relation. A Fabry-Perot étalon was used to impose a fringe pattern on incandescent lamp spectra. The fringes are about one angstrom apart and their relative wavelengths can be derived from their order numbers. These can then be compared to those calculated from the mean dispersion relation which was derived from the HF lines. By tilting the Fabry-Perot étalon, the fringes can be made to move along the Reticon array. This enables the relative wavelengths at different pixel positions to be calculated. The high-frequency structure in the dispersion relation can be examined by calculating the residuals $\Delta\lambda$ between the mean dispersion relation wavelengths and the Fabry-Perot wavelengths. Campbell et al. [1981] found high-frequency structure with $\Delta\lambda$ ranging between ± 0.001Å and ± 0.002Å. This is larger than the point-to-point scatter for $\Delta\lambda$ of about ± 0.00012Å which could be caused by the errors in the fringe wavelengths. A single structure is generally greater

than 100 pixels in width. Its shape also appears to be constant within the same observing night but varies between nights. Consequently, one can use the Fabry-Perot fringe patterns to calibrate nightly the high-frequency components of the dispersion relation. This would provide correction terms $\Delta\lambda$ to the wavelengths derived from the mean dispersion relation. These corrections are generally not necessary unless one is aiming at an accuracy of better than $\pm 20 ms^{-1}$. In fact, Campbell [1984] has found that for low-amplitude relative radial-velocity work, the nightly corrections can only improve the velocity precision by about $1 ms^{-1}$.

4.3.3 EFFECTIVE REST WAVELENGTHS

To convert the measured wavelengths of the stellar lines into velocities, one has to know the effective rest wavelengths of these lines. For solar-type stellar spectra, the most recently measured rest wavelengths are those on the solar line list by Pierce and Breckinridge [1973]. Identifications for these lines can be found in earlier solar line lists by Moore et al. [1966] and St. John et al. [1928]. Most wavelengths for other lines are referenced in the second M.I.T. wavelength catalogue by Phelps [1982]. It is adequate to use exclusively wavelengths for HF lines and stellar lines which are defined with the refractive index of standard air i.e. at a temperature of 15°C and an air pressure of 760 torrs. The smooth change in the air refractive index over temperature and air pressure are

implicitly corrected in the dispersion fit when standard-air wavelengths are used consistently. Basically, an almost constant refractive index factor is included in all the coefficients of the fitted dispersion relation. Hence one can use standard-air wavelengths in almost all applications even when the conditions at the observatories are far from standard e.g. air pressure at CFHT is always about 60% less than one standard atmosphere.

For a given line, the effective wavelength that one should adopt depends on several factors. These include the particular criteria used to measure line positions and blendings with weaker lines. Hence, the effective wavelength is also spectral type, resolution, and dispersion dependent. One can perform a dispersion fit to the line positions on the standard spectrum using the catalogue rest wavelengths and then adopt the least-squares-fitted wavelengths as the effective rest wavelengths for that star. As pointed out in Chapter one, the derived absolute velocities cannot be accurate down to the precision possible in the HF technique. Moreover, it may not be possible to place these velocities onto a stellar radial-velocity system which is calibrated by radial-velocity standard stars. With the high precision, even IAU radial-velocity standard stars may show velocity variations. In almost all applications, however, one is only interested in the relative radial velocities. The accuracy of the derived relative velocities is not dependent on the effective wavelengths as long as the same consistent values are used for the same star. In some stellar spectra,

different stellar lines may have different velocities. In this case, one is interested in the relative radial-velocity variations in the individual stellar lines.

4.3.4 BARYCENTRIC CORRECTIONS

Before one can make use of the observed velocities in any application, one has to convert them into observed barycentric velocities. This involves correcting for the observer's motion with respect to the barycentre of the solar system. Similarly, one should convert the topocentric times of the observed velocities into barycentric date i.e. the time that the starlight would have reached the barycentre of the the solar system. This involves correcting the observer's position with respect to the barycentre of the solar system. Conventional techniques only apply the corrections with respect to the Sun as the velocity frame of reference i.e. to obtain heliocentric velocities and heliocentric dates. A computer program to calculate heliocentric velocity corrections has been given by Gordon [1976]. It has an absolute accuracy of about $20ms^{-1}$. With the high precision of the HF technique, the perturbations by the planets become important especially for long-term projects. The planetary perturbations can cause a velocity variation of about $13ms^{-1}$ (Gordon [1976]).

It is convenient to perform most of the velocity and position calculations in the equatorial rectangular coordinate system (or direction cosines). In this coordinate system, a star with right ascension α and declination δ will

have the direction cosines (u,v,w):

$$u = \cos\alpha \cos\delta \tag{4.10}$$

$$v = \sin\alpha \cos\delta \tag{4.11}$$

$$w = \sin\delta \tag{4.12}$$

If the observer's barycentric coordinate and velocity are (x,y,z) and (V_x,V_y,V_z), respectively, the star will have a radial-velocity contribution V_r and a tangential-velocity component V_t:

$$V_r = -\left(uV_x + vV_y + wV_z \right) \tag{4.13}$$

$$V_\alpha = -V_x \sin\alpha + V_y \cos\delta \tag{4.14}$$

$$V_\delta = -V_x \cos\alpha \sin\delta - V_y \sin\alpha \sin\delta + V_z \cos\delta \tag{4.15}$$

$$V_t = \sqrt{\left(V_\alpha^2 + V_\delta^2 \right)} \tag{4.16}$$

A spectral line of wavelength λ will be Doppler shifted by the velocities to λ':

$$(\lambda/\lambda') = \sqrt{\left(1 - V^2/c^2 \right)} \,/\, \left(1 + V_r'/c \right) \tag{4.17}$$

$$V^2 = V_x^2 + V_y^2 + V_z^2 \tag{4.18}$$

$$V_r' = -\left(u'V_x + v'V_y + w'V_z \right) \tag{4.19}$$

$$u' = u + (1/c)(V_x+uV_r) + (1/2c^2)(\kappa u+V_xV_r) \tag{4.20}$$

$$v' = v + (1/c)(V_y+vV_r) + (1/2c^2)(\kappa v+V_yV_r) \tag{4.21}$$

$$w' = w + (1/c)(V_z+wV_r) + (1/2c^2)(\kappa w+V_zV_r) \tag{4.22}$$

$$\kappa = 2V_r^2 - V^2 \tag{4.23}$$

Equations 4.17 through 4.23 are taken from Stumpff [1979]. The term V_r' in Equations 4.17 and 4.19 is the apparent radial velocity and includes the effect of aberration. The use of V_r rather than V_r' in Equation 4.17 would introduce an

error in $\Delta\lambda/\lambda$ of up to 10^{-8}. The second-order Doppler contribution from V_t is also included in Equation 4.17. Stumpff [1979] has pointed out that this contribution is significant in high-precision measurements. The observer's barycentric velocity is composed of both the barycentric velocity of the Earth and the observer's velocity due to Earth's rotation:

$$(V_x,V_y,V_z) = (E_x+T_x,E_y+T_y,E_z+T_z) \qquad (4.24)$$

The vector (E_x,E_y,E_z) is the Earth's barycentric velocity and (T_x,T_y,T_z) is the diurnal rotation velocity of the telescope. The daily values of (E_x,E_y,E_z) are given in the Astronomical Almanac. They are the results generated by the relativistic ephemeris program JPL DE200. It performs simultaneous integration of the equations of motion of the Sun and Moon as well as of the principal and minor planets. An algorithm to calculate (V_x,V_y,V_z) and (x,y,z) has been given by Stumpff [1977,1979,1980]. This method has been compared against an earlier ephemeris program JPL DE96. The maximum errors are of the order of $42cms^{-1}$ for the velocities and $4.6x10^{-5}$Au for the barycentric coordinates. Heliocentric velocities and coordinates are also calculated by the program given in Stumpff [1980].

In order to reduce the time of reception of the starlight to a common origin at the barycentre, a time correction has to be added to the observed time. This correction Δt is simply:

$$\Delta t = (1/c) (ux + vy + wz) \qquad (4.25)$$

The diurnal rotational velocity of the telescope can be

calculated from the figure of the Earth:

$$C = 1 / \sqrt{(\cos^2\phi + (1-f)^2 \sin^2\phi)} \qquad (4.26)$$

$$T = (2\pi/p) (aC + h) \cos\phi \qquad (4.27)$$

$$T_x = -T \sin\psi \qquad (4.28)$$

$$T_y = T \cos\psi \qquad (4.29)$$

$$T_z = 0 \qquad (4.30)$$

where a = equatorial radius of the Earth

f = flattening factor for the Earth

p = sidereal rotation period of the Earth

ϕ = geodetic latitude of the observatory

h = elevation of the observatory

ψ = local mean sidereal time

Equation 4.26 is taken from Gurnette and Woolley [1974]. It enables the use of geodetic latitude rather than geocentric latitude in Equation 4.27. The latest formulae to calculate p and ψ can be found in the Astronomical Almanac by Vohden and Boksenberg [1984]. It also contains the I.A.U. newly adopted values for all the relevant astronomical constants e.g. a and f. Equations 4.10 through 4.30 can also be used to obtain heliocentic radial velocities and time corrections if the corresponding heliocentric velocities and positions are used in the equations.

Although the precision in the calculated (E_x, E_y, E_z) from Stumpff [1980] is high, the final precision in the derived velocity corrections depends very much on the use of appropriate stellar coordinates (α, δ). Stumpff [1980] has pointed out that the E-terms of aberration must first be

removed from the position. The E-terms correct the effect on the aberration caused by the ellipticity of the Earth's orbit (Vohden and Boksenberg [1984]). These elliptical aberration terms are always present in the fundamental stellar positions which are in the FK4 catalogue. However, they will be absent from the new equinox 2000 FK5 catalogue. The formula to remove the E-terms is given in Vohden and Boksenberg [1984]. The effect of proper motion should also be included in (α,δ). If the applied proper motions are based on the old precession constants, any subsequent precession applied to the positions must also be based on the old precession constants. Corrections to the proper motions must be made if the new equinox 2000 precession constants are used. Formulae to convert the old 1950 positions and proper motions to the new system can be found in Vohden and Boksenberg [1984]. Of course, corrections will not be necessary if the positions and proper motions are taken from the new FK5 catalogue. Stumpff [1979] has pointed out another possible source of error in the choice of (α,δ). The positions should be referenced to the same equator and equinox as the calculated (E_x,E_y,E_z). If (α,δ) is corrected for precession, the velocity components should also be precessed accordingly. Similarly, if nutation corrections have been applied to produce true equator and equinox positions, the same corrections must also be applied to the velocity components.

4.4 SIMULATION STUDIES

4.4.1 BASIC APPROACH

The precision of stellar line-position measurement depends on many factors. These include the s/n of the spectrum, the depth of the line, the width of the line (when noise is included), line-blending effects, and the effect of cosmic-ray events. One of the simplest ways to study the various effects is through the use of numerical simulation. Artificial absorption line spectra can be numerically generated with the various effects included or excluded. One can then apply the various data-reduction procedures to measure the line position on these spectra. Since the intrinsic position of the artificial line is known, the accuracy of the measurent can be assessed.

4.4.2 NOISE GENERATION

The two types of noise to be included in the artificial spectra are the readout noise of the Reticon and the photon shot noise. The readout noise would affect equally all the pixels in the spectrum. The amount of readout noise for each pixel can be obtained through a random-number generator with a Standard Normal probability distribution. The mean value of the distribution is taken to be the mean readout noise of $350e^-$. The photon noise should follow a Poisson distribution. However, as a computational convenience, a Standard Normal distribution random-number generator is also used. The mean value of this distribution is the square root

of the amount of detected photons at the particular pixel. This is actually a very good assumption considering the large number of detected photons. The Central Limit theorem states that the Poisson (or any) probability distribution should approach the Normal distribution for large numbers. A Gaussian line shape has been used for the simulation. For simplicity, only an isolated absorption line is considered in this initial study. Artificial flat-field lamp spectra are also generated in the same manner for division into the absorption line spectrum. The lamp spectra have the same signal level as the continuum of the stellar spectra. Each generated line spectrum contains the effect of noise reduction by using the mean of eight baselines. The mean of four generated flat-field spectra is used in all cases. For simplicity, each individual pixel has been assumed to have zero width and hence a delta-function-type response. For a more realistic simulation of Reticon spectra, the non-zero width of each pixel can be taken into account by integrating over the line profile with the overlapping trapezoidal response function of the individual pixel.

4.4.3 REDUCTION OF THE ARTIFICIAL SPECTRA

The method which is applied to the real spectra is used to measure the line positions on these artificial spectra. This involves the use of the Fahlman-Glaspey difference technique. A different artificial standard spectrum of the same signal level and other attributes is generated for each artificial data spectrum. The standard spectrum, however,

has the line centred at pixel 150 while the line position in the data spectrum is pixel 151.3535. The two spectra are continuum rectified before the unoptimised difference function in Equation 4.4 is applied to measure the relative shift between them. The line limits used are the ones corresponding to the maximum and minimum in the first derivative of the standard line profile. In this case, the line limits also correspond to $\pm\delta$, where δ is the standard-deviation parameter of the Gaussian line profile. At least five pairs of these spectra are used to produce five independent measurements of the shift in each estimation of the accuracy. The standard deviation of these values from the intrinsic value of -1.3535 would give a measure of the accuracy.

The simulation trials can also be used to study the error estimate derived by the Fahlman-Glaspey technique. Out of 636 independent applications of the Fahlman-Glaspey method on the artificial spectra, only in 27 of these cases did the intrinsic shifts lie outside the error bounds predicted by Equation 4.9. In another 24 cases, the intrinsic shifts lie almost exactly at the boundary of the predicted error bounds. Therefore, the error estimate given by Equation 4.9 is good on over 92% of all applications. This implies that the error estimate gives a 2σ confidence level, rather than the usual one-σ level.

4.4.4 THE EFFECT OF S/N

The effect of s/n on the accuracy can be examined by varying the signal level of the spectra while keeping all other parameters constant. The s/n of the generated spectra can be measured directly from the standard deviation in their continua. Figure 4.4 shows σ^{-1} plotted against s/n. The error σ is in unit of pixels and is the standard deviation calculated from six independent line-shift measurements. The line used in the simulation has a depth of 0.4 with respect to a continuum of 1. The standard-deviation-halfwidth δ of the line is 4 pixels. The straight-line fit of the plot gives:

$$\sigma^{-1} = 0.1306\ (s/n) - 1.71 \qquad (4.31)$$

The linear relation is not unexpected. Campbell and Walker [1979] have given a relation which states that the velocity error is inversely proportional to the s/n. The velocity error here is simply (σ x c x dispersion) / λ. . The zeroth-order term in Equation 4.31 is nearly zero as one would expect.

4.4.5 THE EFFECT OF LINE DEPTH

The effect of line depth on the accuracy is examined in Figure 4.5 where σ^{-1} is plotted against line depth. The line depths are in fractions of the continuum. The line has a standard-deviation-halfwidth of 4 pixels and a s/n of about 1350. Each point on the graph is the result of five independent measurements of the relative line shift. A linear fit of the plot gives:

Figure 4.4 The effect of s/n on accuracy

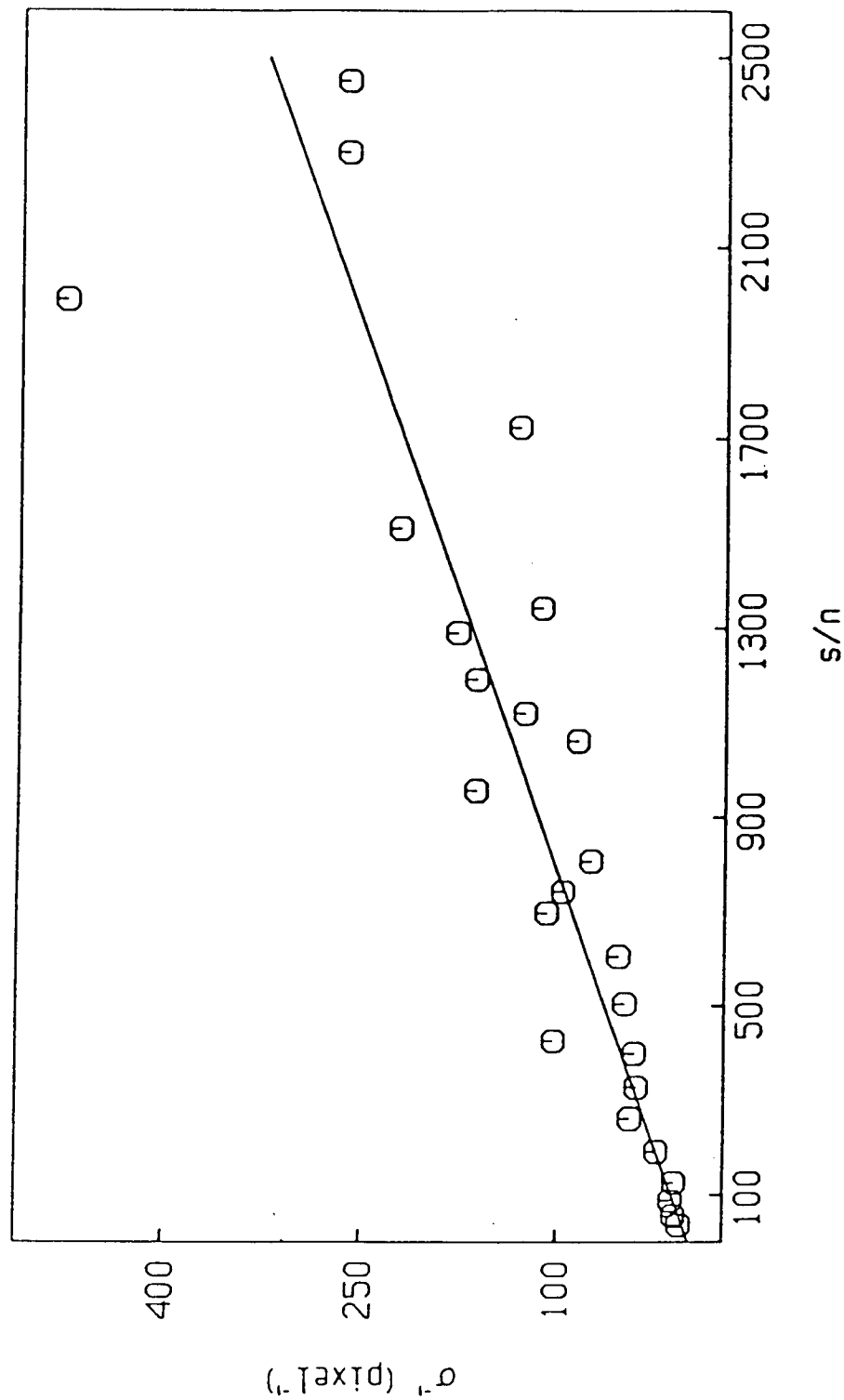

Figure 4.5 The effect of line depth on accuracy

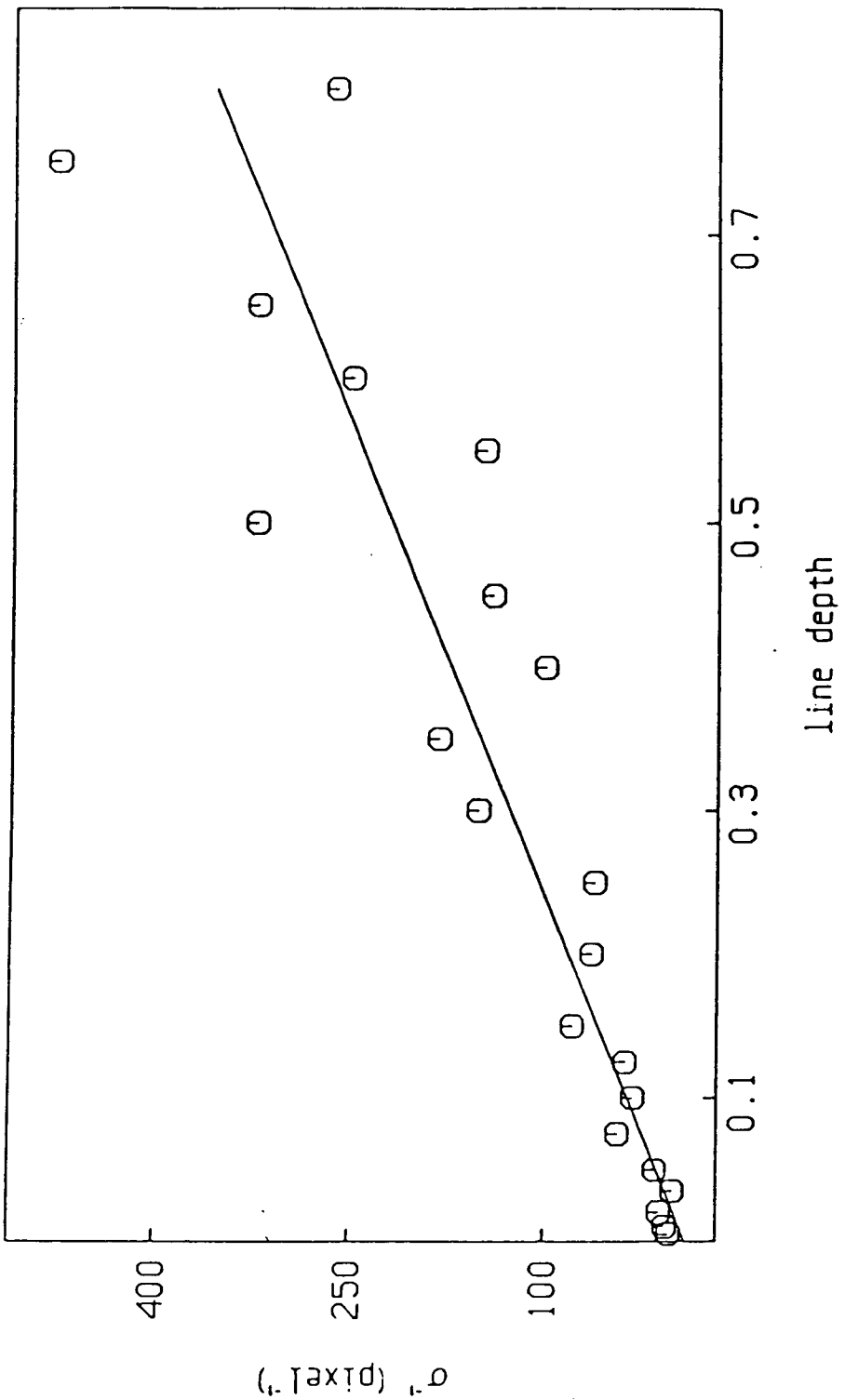

$$\sigma^{-1} = 457.7 \text{ (line depth)} - 10.1 \qquad (4.32)$$

This relation is again not unexpected. Campbell and Walker [1979] have given an inverse relationship between the velocity error and line depth.

4.4.6 THE EFFECT OF LINEWIDTH

The effect of linewidth on the accuracy is examined in Figure 4.6 where σ is plotted against the standard-deviation-halfwidth δ of the line. Figure 4.6 shows the effect of changing the linewidth but keeping the equivalent width constant. The line depth in each spectrum of different linewidth is adjusted such that the equivalent width of the line is the same as the case with δ being 4 pixels and line depth being 0.4. The s/n in the spectra is about 1350. The line limits ($\pm\delta$) in each case are varied to preserve the same criterion of choosing the positions at extremal first derivative. Each point in Figure 4.6 is the result of five independent line-shift measurements. The fit of the points gives:

$$\sigma = 0.00038\delta^2 - 0.0018\delta + 0.0091 \qquad (4.33)$$

The trend between σ and δ is not unexpected. One would expect the velocity error to increase when more pixels are included within the line limits. This is because of the fact that each additional pixel would add more noise (readout and photon) to the line measurement while the equivalent width (information content) of the line has been kept constant. The amount of readout noise would increase linearly with the number of pixels. The photon noise, however, would increase

Figure 4.6 The effect of linewidth on accuracy

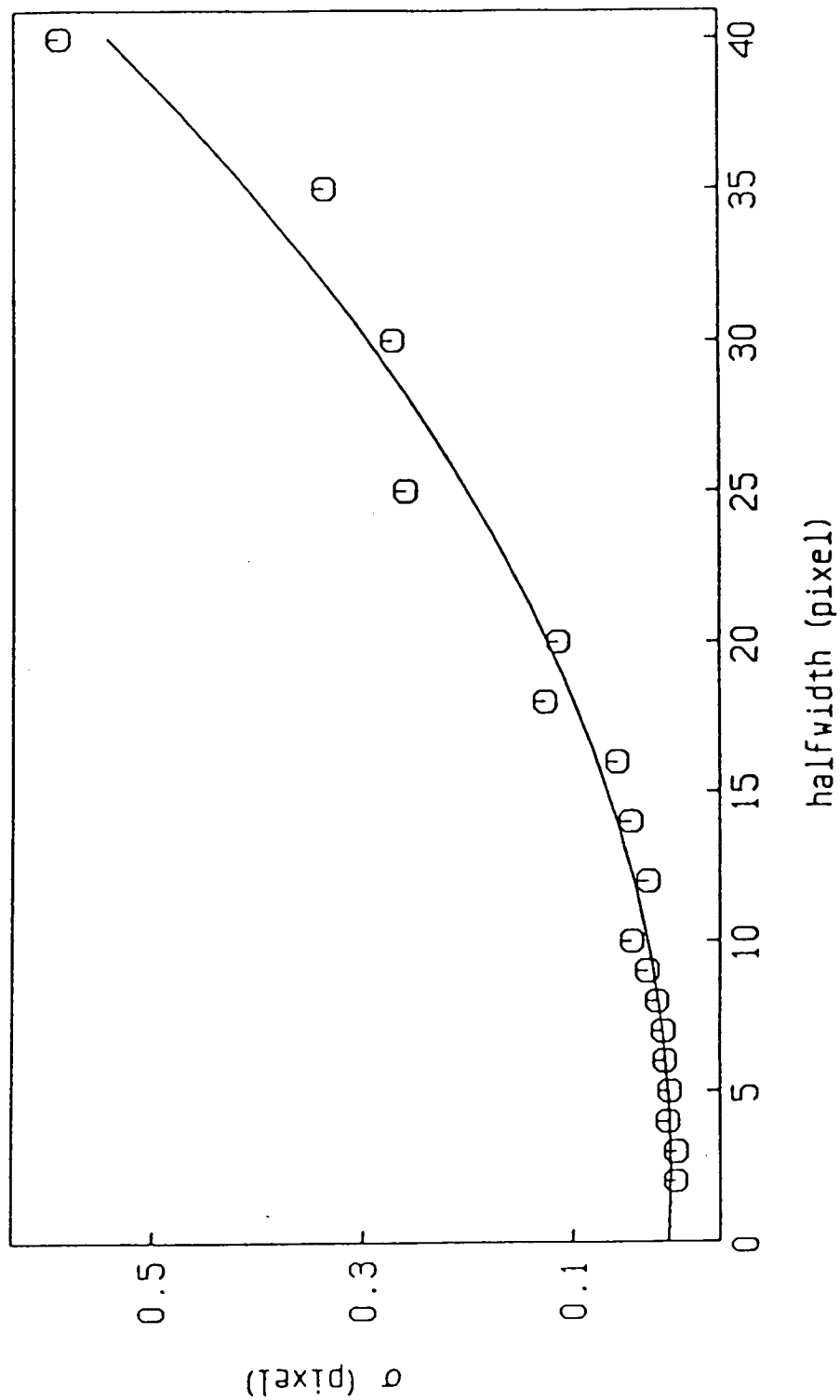

faster than linearly with the number of pixels. This is mainly because of the fact that the line becomes shallower as the linewidth increases hence the photon noise at each pixel also increases.

Figure 4.7 shows the conversion between signal (in adcu) and s/n. A readout noise of 350e^- is used in the calculation. Moreover, Figure 4.7 also assumes that eight baselines and four flat-field lamps are used in the preprocessing of the data. A conversion factor of 250 equivalent photons per adcu has been used. This factor is appropriate to the high-gain mode of the CFHT 1872-Reticon.

4.4.7 THEORETICAL LINE-POSITION ACCURACY

Walker [1982] has derived a simplified expression for the accuracy of a line-position measurement. One possible definition of a line position is the position of the line bisector which divides the line profile into two halves of equal number of detected photons. How well this bisection can be performed is affected by the amount of noise in each half of the line profile. The bisection is essentially to determine a value for the halfwidth of the line profile at the continuum. Let this halfwidth in pixels be h. For simplicity, one can consider a triangular absorption line shape with a line depth d. If N is the number of detected photons per pixel at the continuum, and S is the number of detected photons in each half of the line, then one obtains:

$$S = N\ h\ (\ 1\ -\ d/2\ ) \qquad (4.34)$$

$$\delta S = N\ (\ 1\ -\ d/2\ )\ \delta h \qquad (4.35)$$

Figure 4.7 s/n as a function of signal (in adcu)

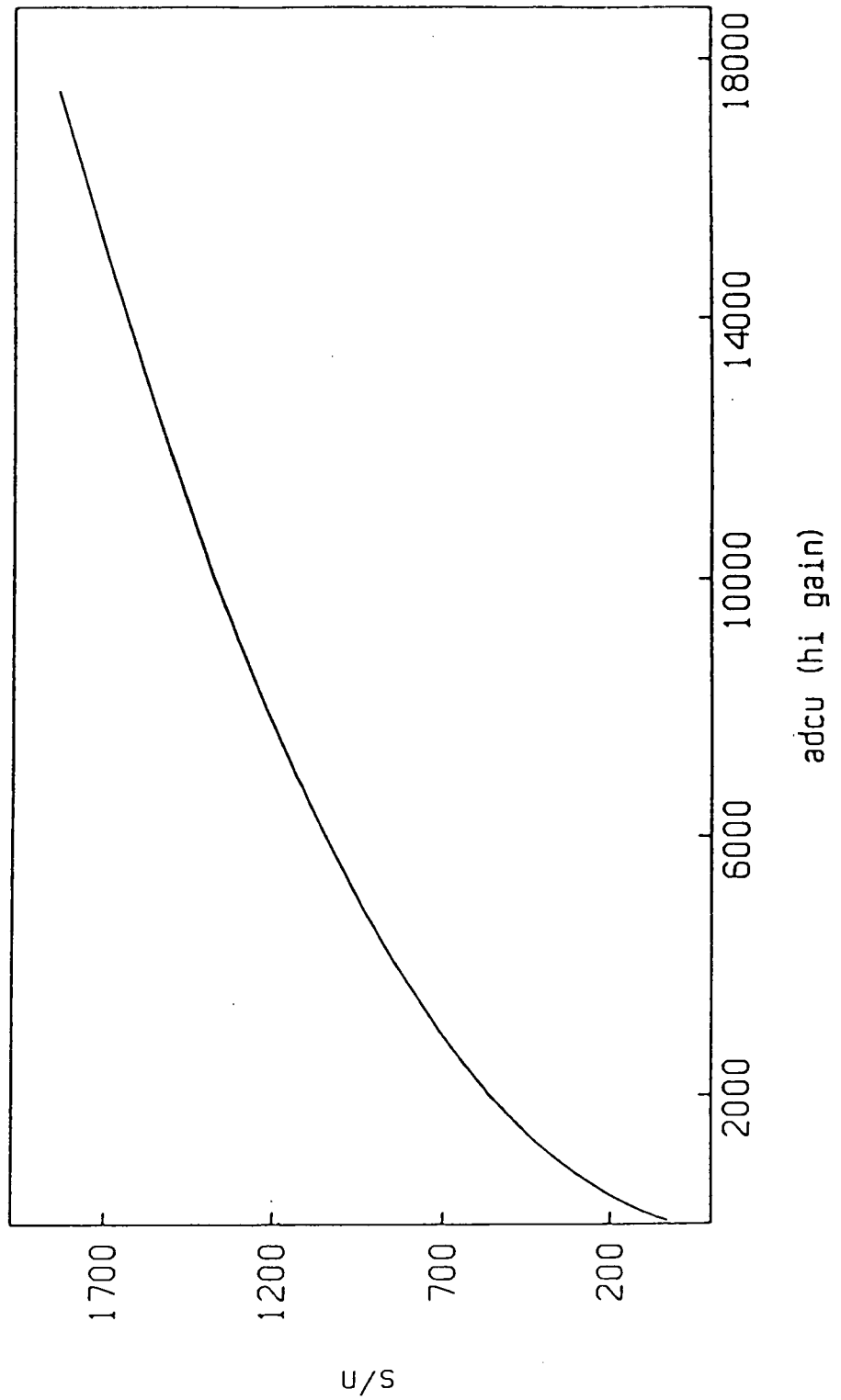

$$(\delta S)^2 = S \qquad (4.36)$$

$$(\delta h)^2 = h \; / \; (\; N \; (\; 1 - d/2 \;) \;) \qquad (4.37)$$

$$\sigma = \delta h = \sqrt{(\omega/(2N(1-d/2)))} \qquad (4.38)$$

Equation 4.36 considers only photon noise. This is a good assumption for high s/n data. The term ω in Equation 4.38 is the full width of the line profile at the continuum and would be equal to $2h$ in this simple symmetric line profile. Equation 4.38 states the fact that for a triangular line profile, σ, which is the uncertainty in the line position measurement is the same as δh which is the uncertainty in the halfwidth of the line at the continuum level. A similar method can be used to study the effect of a cosmic-ray event. In this case, δS in Equation 4.36 would become the amount of equivalent photons in a cosmic-ray spike.

Equation 4.38 gives the accuracy estimate of an absolute line-position measurement under a specific line-position criterion while the simulation studies give only the accuracies of relative line-position measurements. In spite of this and approximating the line shape by a triangular function, Equation 4.38 should still give at least an order-of-magnitude accuracy estimation for comparison against the simulation results. Consider a high s/n case in which N is 16000x250 detected photons. Figure 4.7 would then imply a s/n of about 1700. With d=0.4 and ω=16, Equation 4.38 would then imply a line-position accuracy of about 1.5×10^{-3} pixel. The simulation study in Figure 4.4, however, gives an accuracy of 4×10^{-3} pixel for a s/n of about 1700. It is not unexpected that the simulation

study should give a lower value for the precision, since realistic noise contributions have been included in the simulation study e.g. readout noise and noise contribution from the flat-field spectrum. The simulation study is based upon the use of a standard spectrum with the same s/n. Hence, if a much higher s/n standard spectrum is available, the precision should increase.

Chapter 5

THE DELTA SCUTI VARIABLE 20 CVN

5.1 INTRODUCTION

The star 20 Canum Venaticorum (AO CVn, HR5017) is a δ Scuti variable with δ Delphini-type anomalous abundances. Parameters for 20 CVn are summarised in Table 5.1. Other parameters can be found in Tsvetkov [1982b], Breger [1979], Baglin et al. [1972], Gupta [1978], Breger and Bregman [1975], Leung [1970], and Hoffleit and Jaschek [1982]. Morgan and Abt [1972] have pointed out that the Ca II lines in 20 CVn are weaker than those in other stars of similar spectral type and luminosity class. Meanwhile, the Mg II λ4481 line has been commented on by Hoffleit and Jaschek [1982] to be anomalously strong in 20 CVn. Abundance analyses of 20 CVn have been performed by Dickens et al. [1971], Ishikawa [1975], Kurtz [1976], and Hauk et al. [1985]. The value of 0.80 for [Fe/H] determined by Kurtz [1976] is higher than the more typical value of 0.44 for the Hyades of which 20 CVn may be a member. Leung [1970] has pointed out that there is a discrepancy between the various reported values for the absolute visual magnitude M_V of 20 CVn. Membership in the Hyades would imply a value of about 0.45 for M_V while Stromgrens photometry gives a value of about 1.27.

5.2 VARIABILITIES OF 20 CVN

The star 20 CVn was first reported to be a variable by Wehlau et al. [1966] and Danziger and Dickens [1966]. Other light curves for 20 CVn have been given by Danziger and Dickens [1967], Breger [1969], Shaw [1976], Pena and Gonzalez [1981], Chun et al. [1983], and Bossi et al. [1983]. Radial-velocity variations have been measured by Smith [1982b]. Simultaneous radial-velocity and photometric time-series observations have been performed by Penfold [1971] and Nishimura et al. [1983].

Early photometric data of 20 CVn suggested a pulsation period between 0.13 and 0.14 day together with an amplitude Δm_v of about 0.03^m. Valtier [1972] gave a recalculated period of 0.135 day and an amplitude of 0.035^m. Shaw [1976] determined a period of 0.12168 day or a frequency of 8.2183 day^{-1} for the photometric variations. An amplitude of 0.0292^m was also measured for the brightness variations in the blue while the amplitude in yellow light was measured to be 0.0196^m. Smith [1982b] adopted a value of 0.031^m for Δm_v. This light amplitude has been standardised to a colour of (b-v) = 0.20 for the star. An amplitude of 0.022^m has been measured off the V data of Pena and Gonzalez [1981] by Bossi et al. [1983]. Chun et al. [1983] have observed amplitudes between 0.02^m and 0.04^m. Bossi et al. [1983] have determined a frequency of 8.21 day^{-1} and a V amplitude of 0.0174^m. Hence both the period and the photometric amplitude appear to be stable over the 14 years span of observations. Penfold [1971] obtained a radial-velocity amplitude 2K of $1.5km^{-1}$.

Table 5.1 Parameters for 20 CVn

****

	Reference
HD number : 115604	
SAO number : 44549	
DM number : +41 2380	
R.A. (1950) : $13^h\ 15^m\ 18.151^s$	
Dec. (1950) : 40° 50' 7.483"	
Annual parallax : +0.19"	
Proper motion in R.A. : -0.127"/yr	
Proper motion in Dec. : +0.017"/yr	
l_{II} : 102.73°	
b_{II} : 75.52°	
Spectral type : F3 III-IV	Pena et al. [1981]
Radial velocity = 7.4 kms^{-1}	Smith [1982b]
Vsini = <5 kms^{-1}	Smith [1982b]
M_v = +0.5	Eggen [1979]
T_{eff} = 7500K	Kurtz [1976]
log g = 3.7 (cgs)	Kurtz [1976]
Broad band photometry :	Iriate et al. [1965]
V = 4.73^m	
B - V = $+0.30^m$	
U - V = $+0.50^m$	
V - R = $+0.25^m$	
V - I = $+0.40^m$	
Infared photometry :	Verma et al. [1983]
J = 4.14^m	

$H = 4.17^m$

$K = 3.95^m$

Intermediate band photometry : Kurtz [1976]

$\beta = 2.780^m$

$b - y = 0.180^m$

$m_1 = 0.231^m$

$c_1 = 0.913^m$

$\delta m_1 = -0.035^m$

****

Smith [1982b] measured a radial velocity amplitude of 1.3kms^{-1} and a period which is the same as that given by Shaw [1976]. Nishimura et al. [1983] measured a period of 0.127 day from their spectroscopic data. One can also determine a 2K value of 1.7kms^{-1} from the data. From one night of simultaneous radial-velocity and photometric observations by Penfold [1971], there appears to be a phase shift of 0.37 period between the radial-velocity and light curves. This phase shift is defined as the fraction of the period that the radial-velocity minimum lags behind the light maximum. The simultaneously observed spectroscopic and photometric data by Nishimura et al. [1983] indicate that the light maximum occurs at about 0.1 period before the minimum radial velocity. This is a typical phase-shift value for δ Scuti stars (Breger et al. [1976]).

Table 5.2 Mid-exposure times for the 20 CVn spectra

#	24 Jan 83 UT+	Barycentric JD	hour angle
0	(13:11:30.20)	2445359.0520520	2h 14m 00s East
1	(13:33:22.89)	2445359.0672461	1h 52m 04s East
2	(13:50:38.61)	2445359.0792343	1h 34m 45s East
3	(14:07:49.78)	2445359.0911698	1h 17m 31s East
4	(14:25:07.75)	2445359.1031841	1h 00m 10s East
5	(14:42:16.58)	2445359.1150925	0h 42m 59s East
6	(14:59:25.59)	2445359.1270030	0h 25m 47s East
7	(15:16:31.50)	2445359.1388777	0h 08m 38s East
8	(15:33:42.47)	2445359.1508109	0h 08m 36s West
9	(15:50:56.96)	2445359.1627849	0h 25m 53s West
10	(16:08:07.57)	2445359.1747139	0h 43m 06s West

5.3 THE OBSERVATIONS

The star 20 CVn was observed spectroscopically with the HF absorption cell at the Canada-France-Hawaii 3.6m telescope on the 24th of January 1983 UT. The time series of spectra was obtained with the red Coudé train and image slicer. The spectrograph used was the f/7.4 Coudé four-grating-mosaic spectrograph (Brealey et al. [1980]). The CFHT RL1872F/30 Reticon detector was used unintensified at the focus of the spectrograph. The grating is blazed at λ8000 and gives a reciprocal dispersion in the first order of 4.8Å/mm at λ8700. This corresponds to a dispersion of about 0.071Å/pixel on the Reticon array. The image slicer gives a projected slit width of about 33μ (Campbell et al.

[1985]). The 15μ width of a Reticon pixel would then imply a resolution of about 0.16Å. The spectral coverage in each spectrum is about 130Å. The exposure time for each spectrum was 1000 seconds. This corresponds to about one-tenth the "cycle-count" period of 0.12168 day (2.92 hours). The time series of ten spectra covered one period. Stellar and lamp spectra without the imposed HF lines were also obtained. These are shown in Figure 5.1. The mean stellar+HF spectrum with either the stellar or HF lines numerically removed are also shown. Each stellar+HF spectrum has a mean s/n of about 266 at each point on the continuum. The mid-exposure times of the spectra are summarised in Table 5.2. Spectrum #0 in Table 5.2 is the 20 CVn spectrum without the imposed HF lines. Approximate radial velocities can still be measured from spectrum #0 by using the dispersion relation determined for spectrum #1. For this set of observations, the barycentric times lag the heliocentric times by about 2.0 seconds.

5.4 THE DATA REDUCTION

The data were processed and reduced using the procedure described in the previous chapter. A mean stellar spectrum is calculated for the time series of spectra. This spectrum with the HF lines numerically removed has been chosen to be the radial-velocity standard spectrum. It provides both the line shape and position references in the application of the Fahlman-Glaspey difference technique in determining the relative shifts of individual spectral lines. The choice of

Figure 5.1 The 20 CVn spectrum

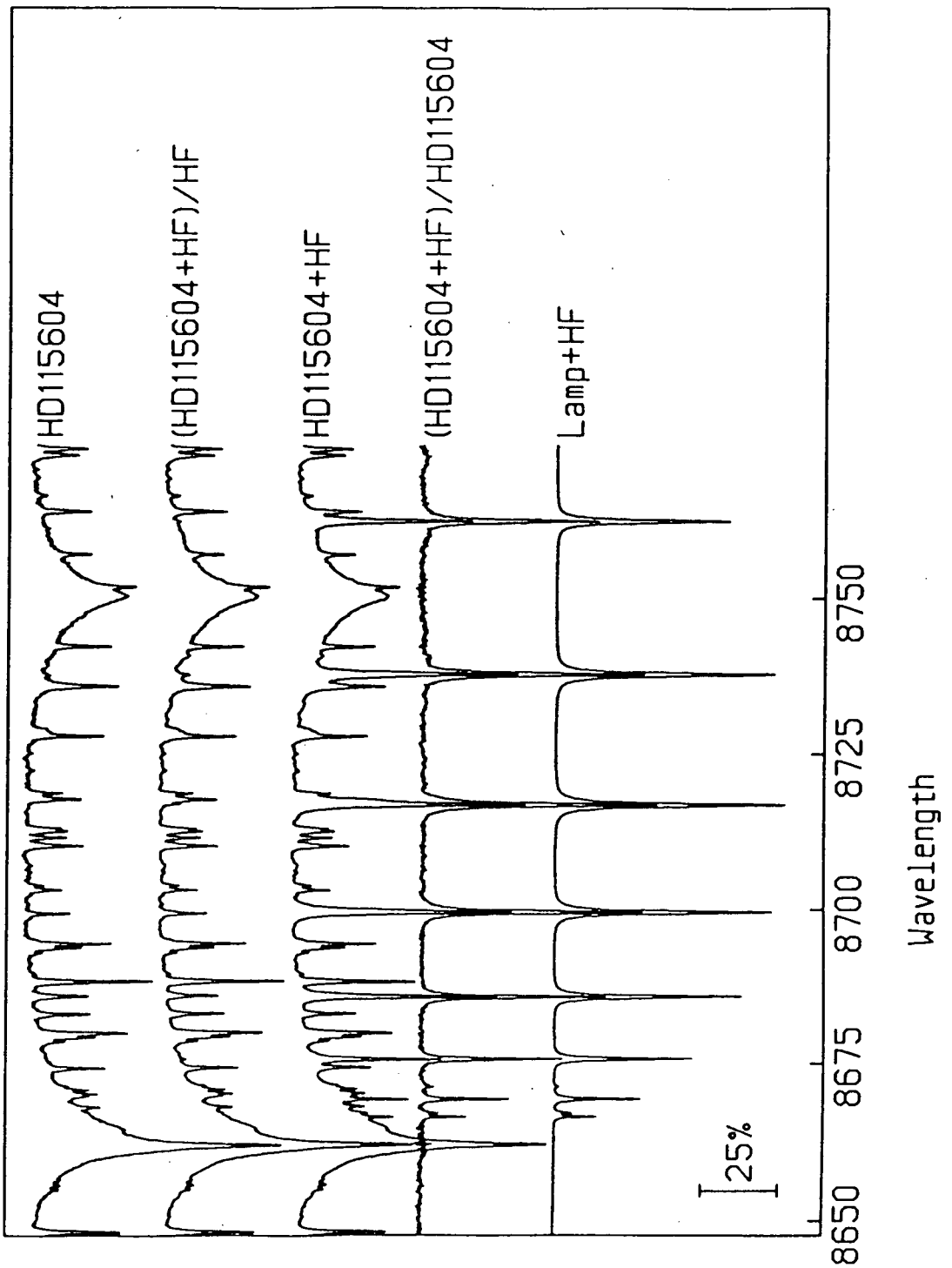

using a mean spectrum would imply an increased s/n spectrum is used as the standard spectrum. The phase-smearing effect would broaden the spectral lines in the mean spectrum relative to those in the individual spectrum. This effect is very small in this case because of the very small velocity amplitude. Moreover, in a second "pass" or iteration of the the data-reduction procedure, the relative velocity shifts between individual spectra can be corrected before forming the mean spectrum. The chosen line limits for the stellar lines are those corresponding to the maximum and minimum values in the first derivative of the line profiles.

In the determination of the HF line positions, the numerical cancellations of the stellar lines are achieved by dividing the data spectrum by an appropriately shifted spectrum #0. The amount of shift applied to spectrum #0 before each spectrum division is chosen such that it would minimise the total residual over the positions of all the stellar lines in the spectrum. This is essentially a mean value of the shift over all the stellar lines for the particular data spectrum. A similar procedure of dividing the data spectrum by an appropriately shifted HF standard spectrum is used to achieve numerical HF line cancellations. The application of an optimal shift for each individual line should result in better line cancellations. However, this would increase the amount of numerical computation i.e. computation cost by more than one order of magnitude.

The unadjusted difference function from Equation 4.4 has been used for the stellar lines in the application of

the Fahlman-Glaspey difference technique. This is to ensure that the measurement of any velocity shift caused by line-profile variations would not be affected by artifacts of minimising the difference function. In any case, the differences between the velocities derived using the unmodified and the modified difference function were found to be very small. This may be an indication of very little profile variations happening in the lines. The line limits for the stellar lines are chosen to be those corresponding to the maximum and minimum in the first derivative of the line profile. A typical set of limits is about 7 pixels in width. The line limits for the HF lines are chosen to be twice as broad as those corresponding to the maximum and minimum values in the first derivative of the line profile. A typical set of limits is about 16 pixels in width. The relative HF line shifts are measured using the modified difference function from Equation 4.5. The same order of polynomial has been used to fit the dispersion relations of all the spectra. This should minimise the possibility that any small variation in the measured velocities could be caused by inconsistencies between the dispersion fits.

Individual radial-velocity curves have been obtained for the stellar lines Ca II λ8662, Fe I λ8675, λ8689, λ8710, λ8763, Si I λ8728, λ8742, λ8752, S I λ8680, λ8695, Mg I λ8718, λ8776, Al I λ8773, λ8774, and N I λ8683. The s/n of the spectra are too low for a determination of the H I λ8750 velocity curve. A mean systemic velocity of 9.532kms^{-1} is measured over the observed cycle. This was obtained by

averaging the velocities of all the lines from all the spectra. It is different from the value of 7.4kms^{-1} measured by Smith [1982b]. Generally, one is only interested in the velocity variations of the star. Hence relative velocities rather than absolute velocities are sufficient for the purpose. A relative radial-velocity curve is obtained by subtracting a mean velocity for the particular line.

5.5 THE RADIAL VELOCITIES

The relative radial-velocity curve based only on the Ca II λ8662 line is shown in Figure 5.2. The mean one-standard-deviation uncertainty in each Ca II line position measurement is about ±0.093kms^{-1}. This error estimate is derived from the formal error estimate obtained with the Fahlman-Glaspey method. The theoretical formulations to calculate this effective error estimate have been described in the previous chapter. The radial-velocity curve based on the weaker line Fe I λ8689, is shown in Figure 5.3. The mean one-standard-deviation uncertainty in each of these line-position measurements is about ±0.104kms^{-1}. The one-standard-deviation uncertainties for the other even weaker lines are mostly between ±0.1 and ±0.3kms^{-1}. In order to increase the precision, a weighted average velocity curve is calculated for the weak lines i.e. all lines except the Ca II line. The chosen weight for each individual velocity curve is proportional to the square of the line depth and inversely proportional to the square of the velocity precision. The mean one-standard-deviation

Figure 5.2 The Ca II λ8662 velocity curve of 20 CVn

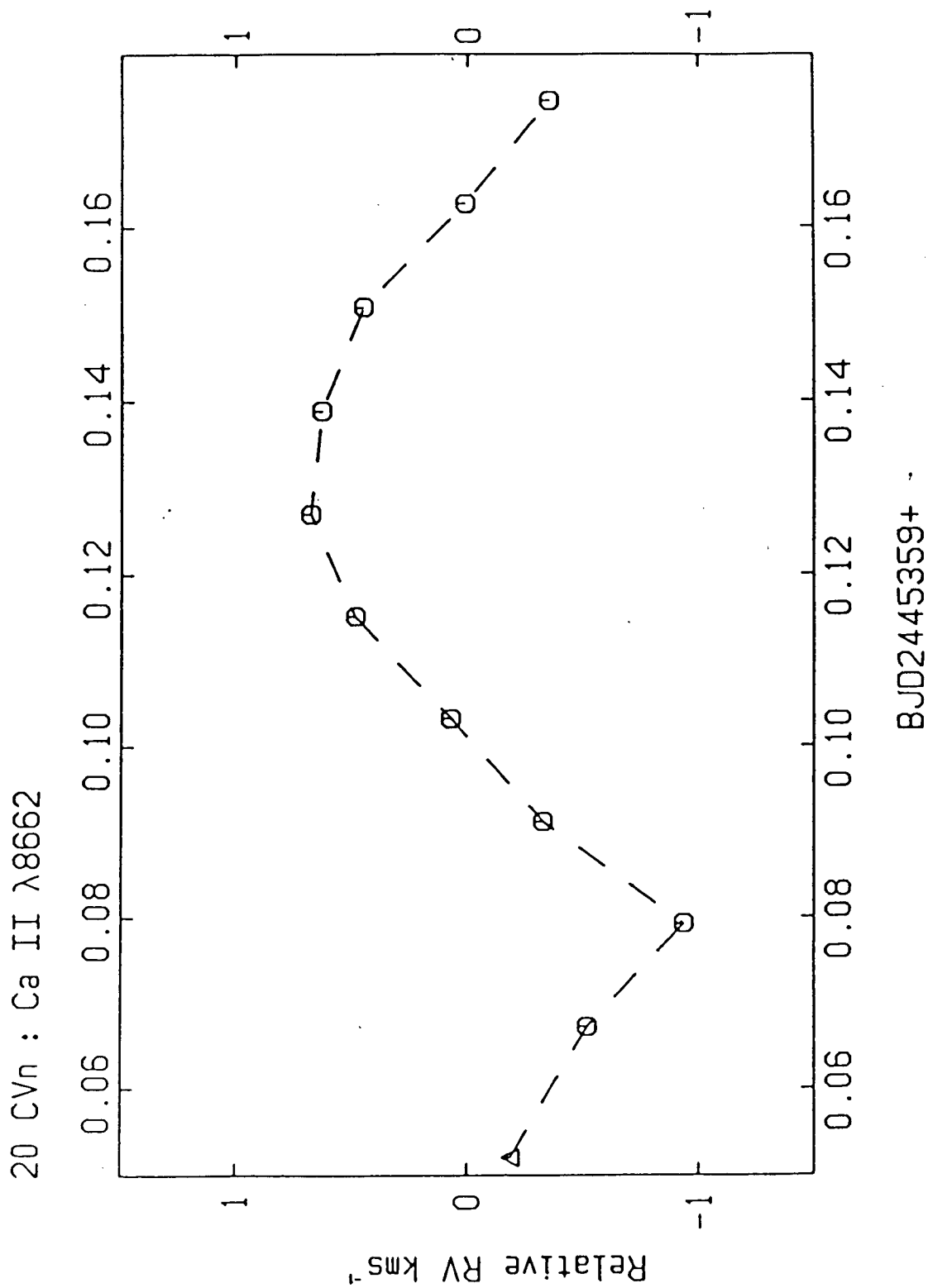

Figure 5.3 The Fe I λ8689 velocity curve of 20 CVn

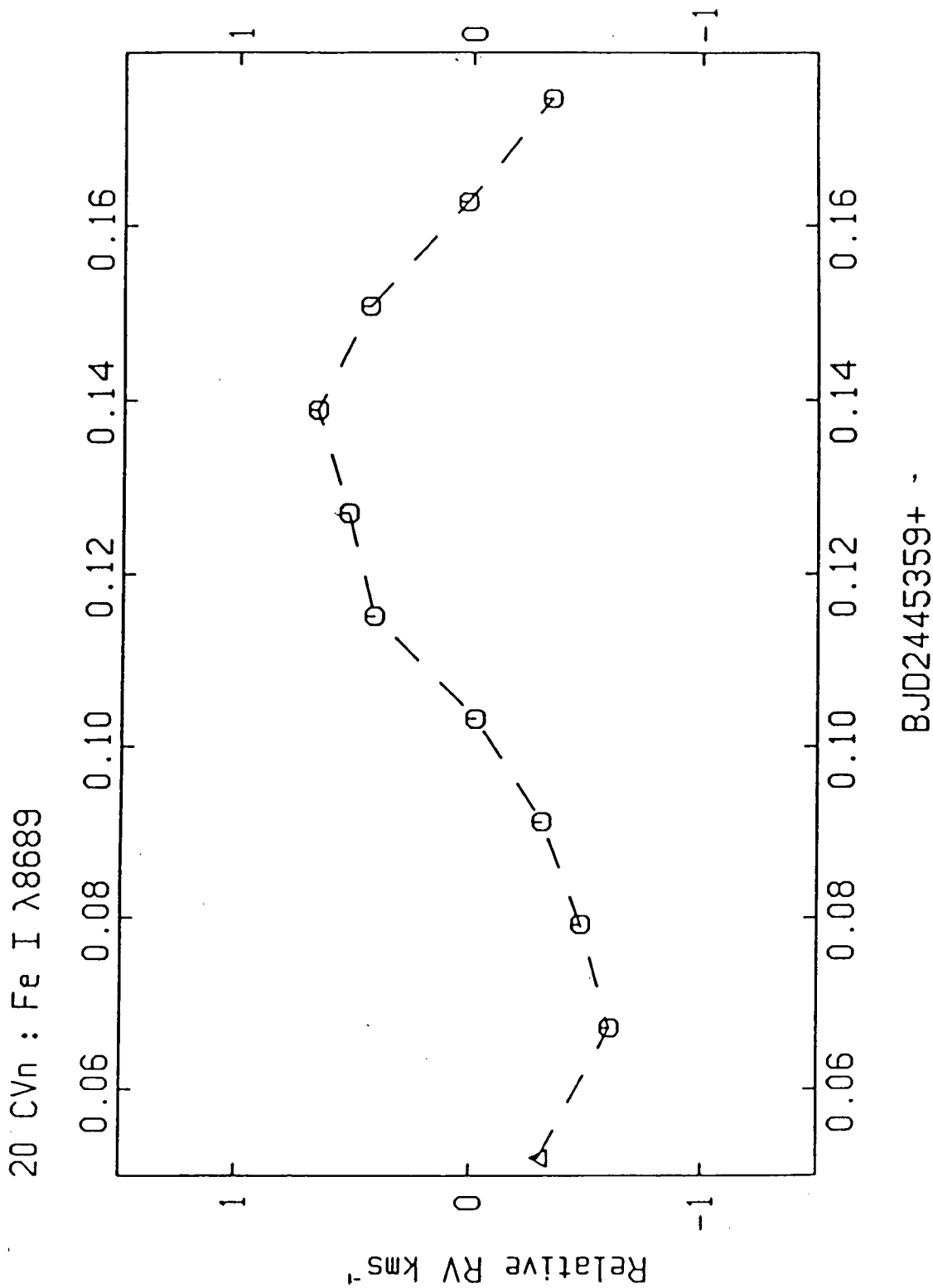

Figure 5.4 The mean velocity curve of 20 CVn from weak lines

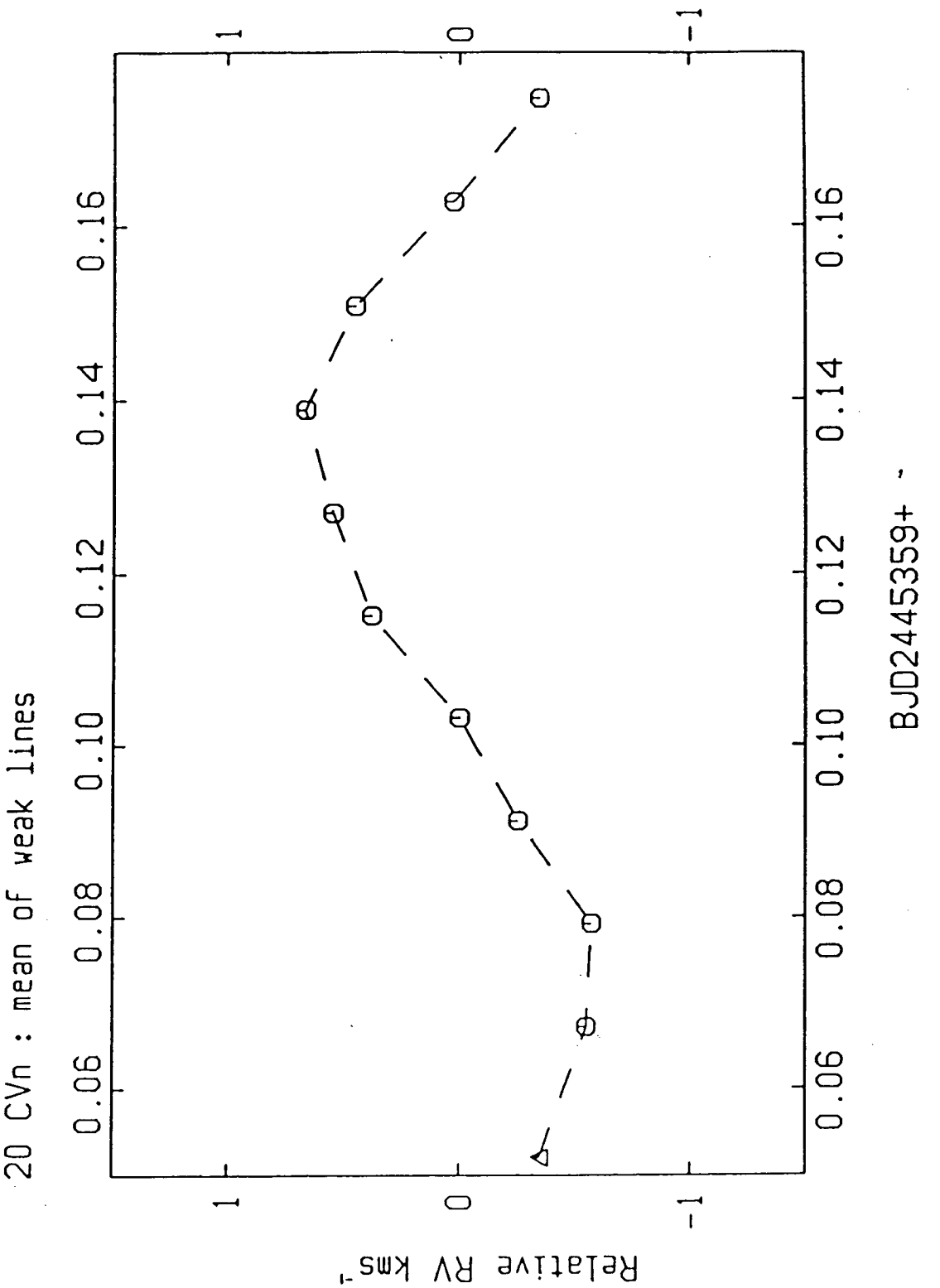

uncertainty for this mean curve has a contribution of $0.083 kms^{-1}$ per velocity point from the stellar line-position measurements. This mean curve is shown in Figure 5.4.

Dispersion fits to the HF lines in the spectra would contribute about $\pm 60 kms^{-1}$ to the uncertainties of all velocity points. This is the mean standard error in the dispersion fits and is caused mainly by the uncertainties in the HF line-position measurements. A similar value is obtained if the standard error is calculated from the uncertainty estimates of the HF line-position measurements. Taking this uncertainty of the dispersion relation into account, the mean curve would have an uncertainty of about $\pm 0.102 kms^{-1}$ per velocity point while the corresponding value for the Ca II curve would be $\pm 0.111 kms^{-1}$. Table 5.3 lists the velocities shown in Figures 5.2 through 5.4. The errors in the mid-exposure times due to guiding inconsistencies are very small. Large guiding errors would have caused large shifts in the HF line positions between the spectra. This was not observed. In fact, the rms scatter of the HF line positions (that of the $\lambda 8717$ line) is only about ± 0.042 pixel over the entire time series. This small guiding error is realised through the use of the image slicer. The moderate exposure time of 1000 seconds would also help to smooth out any short-term effects. In any case, the exposure-meter output was rather uniform for each exposure. Of course, it would be better to use a weighted mean time for each exposure. In this case, the weight could be the intensity output from the exposure meter.

Table 5.3 Relative radial velocities of 20 CVn

#	Ca II λ8662	Fe I λ8689	mean weak lines
0	-0.188 kms^{-1}	-0.302 kms^{-1}	-0.344 kms^{-1}
1	-0.519 kms^{-1}	-0.605 kms^{-1}	-0.547 kms^{-1}
2	-0.934 kms^{-1}	-0.478 kms^{-1}	-0.568 kms^{-1}
3	-0.327 kms^{-1}	-0.309 kms^{-1}	-0.249 kms^{-1}
4	+0.071 kms^{-1}	-0.078 kms^{-1}	+0.001 kms^{-1}
5	+0.484 kms^{-1}	+0.414 kms^{-1}	+0.376 kms^{-1}
6	+0.677 kms^{-1}	+0.525 kms^{-1}	+0.541 kms^{-1}
7	+0.630 kms^{-1}	+0.660 kms^{-1}	+0.661 kms^{-1}
8	+0.450 kms^{-1}	+0.437 kms^{-1}	+0.446 kms^{-1}
9	+0.011 kms^{-1}	+0.022 kms^{-1}	+0.027 kms^{-1}
10	-0.354 kms^{-1}	-0.347 kms^{-1}	-0.345 kms^{-1}

5.6 DISCUSSION

The Ca II velocity curve in Figure 5.2 has a 2K amplitude of 1.4kms^{-1} while the mean velocity curve in Figure 5.4 has an amplitude of 1.2kms^{-1}. These agree well with the value of 1.3kms^{-1} derived by Smith [1982b] from the Fe I λ4476 and Fe II λ4508 lines. As in Smith [1982b], no correction is applied to remove the phase-smearing effect caused by the length of each exposure. In any case, the required correction is probably very small. The use of 10% of the dominant period as the exposure time should cause less severe phase smear than in the case in Smith [1982b] which used between 15% and 20% of the period as the length of exposure. Smith [1982b] has estimated that, even in that

case, the amount of reduction in the 2K values caused by phase smear would be less than 10%.

Figure 5.5 gives the velocity difference between the Ca II λ8662 velocity curve and that from the mean of weak lines. There appears to be a marked deviation at BJD2445359.08. The Ca II line appears to be shifted shortward from the other lines by about $0.37 kms^{-1}$. In fact, a small gradual trend towards shorter wavelengths can be seen from the neighbouring velocity points. The result at BJD2445359.08 does not appear to be the effect of a single aberrant velocity point. In order to ensure that one is sampling the identical pulsation phenomenon from each line, the same criteria have been used to determine all the stellar line limits. This could not be achieved perfectly because of the round-off error imposed by the integer-valued line limits. However, the use of the Fahlman-Glaspey technique to determine relative line positions is not very sensitive to the choice of line limits. Moreover, this discretisation error is less severe for the broad Ca II line and it is minimal for a mean velocity curve. The observed deviations may still be caused by the fact that a different part of the pulsation was sampled by the Ca II velocities. The Ca II line has a slightly different line shape than the other lines; therefore, the line limits determined by the extrema of the profile derivative may have a different meaning than in the case of the other lines. Furthermore, the Ca II line has an excitation potential quite different from those of the other lines and may have been formed at a

Figure 5.5 Velocity difference (Ca II curve - mean curve)

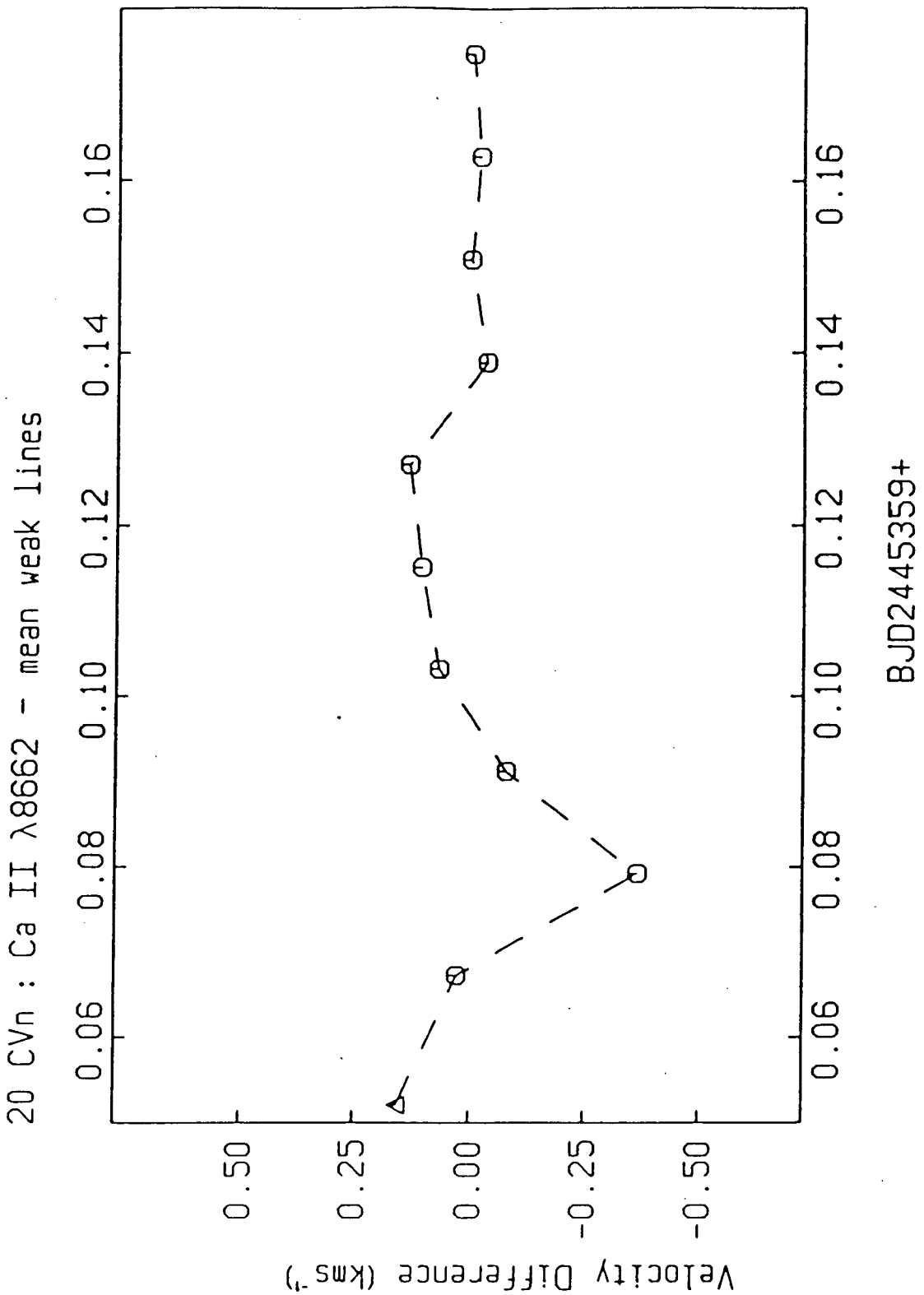

Figure 5.6 Velocity difference (mean curve - Fe I curve)

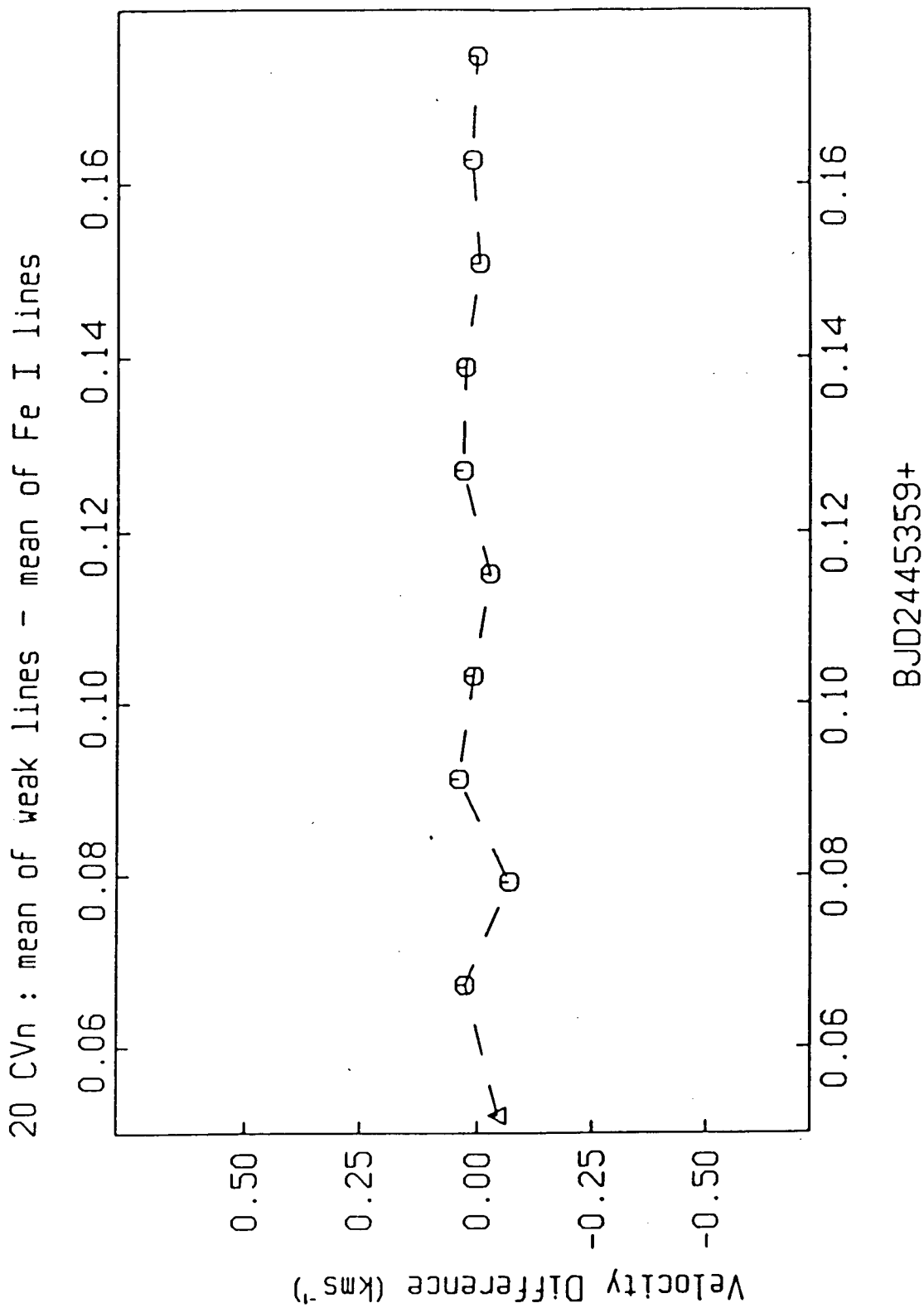

Figure 5.7 Velocity difference (Fe I curve - Si I curve)

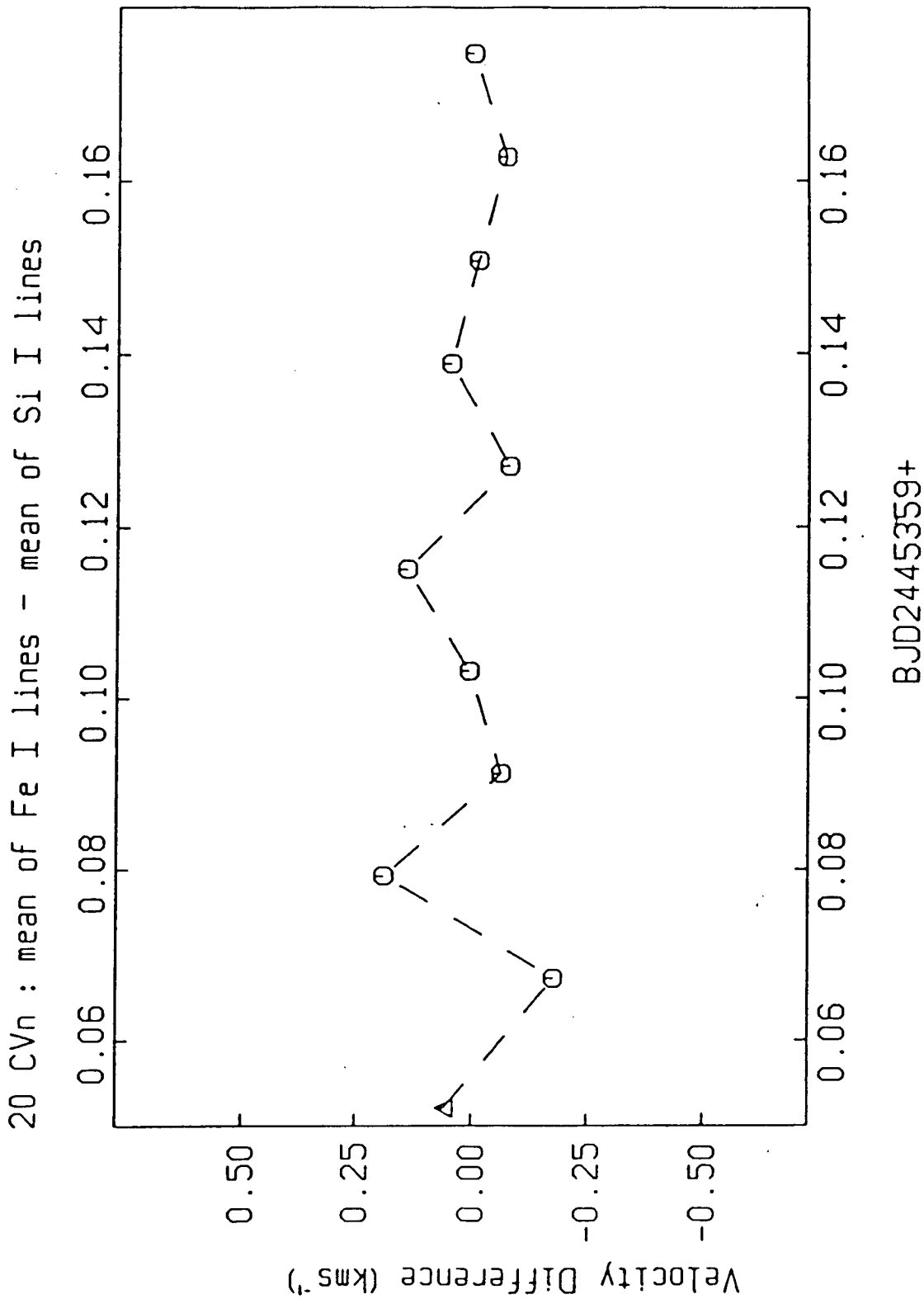

Figure 5.8 Velocity difference (Fe I curve - S I curve)

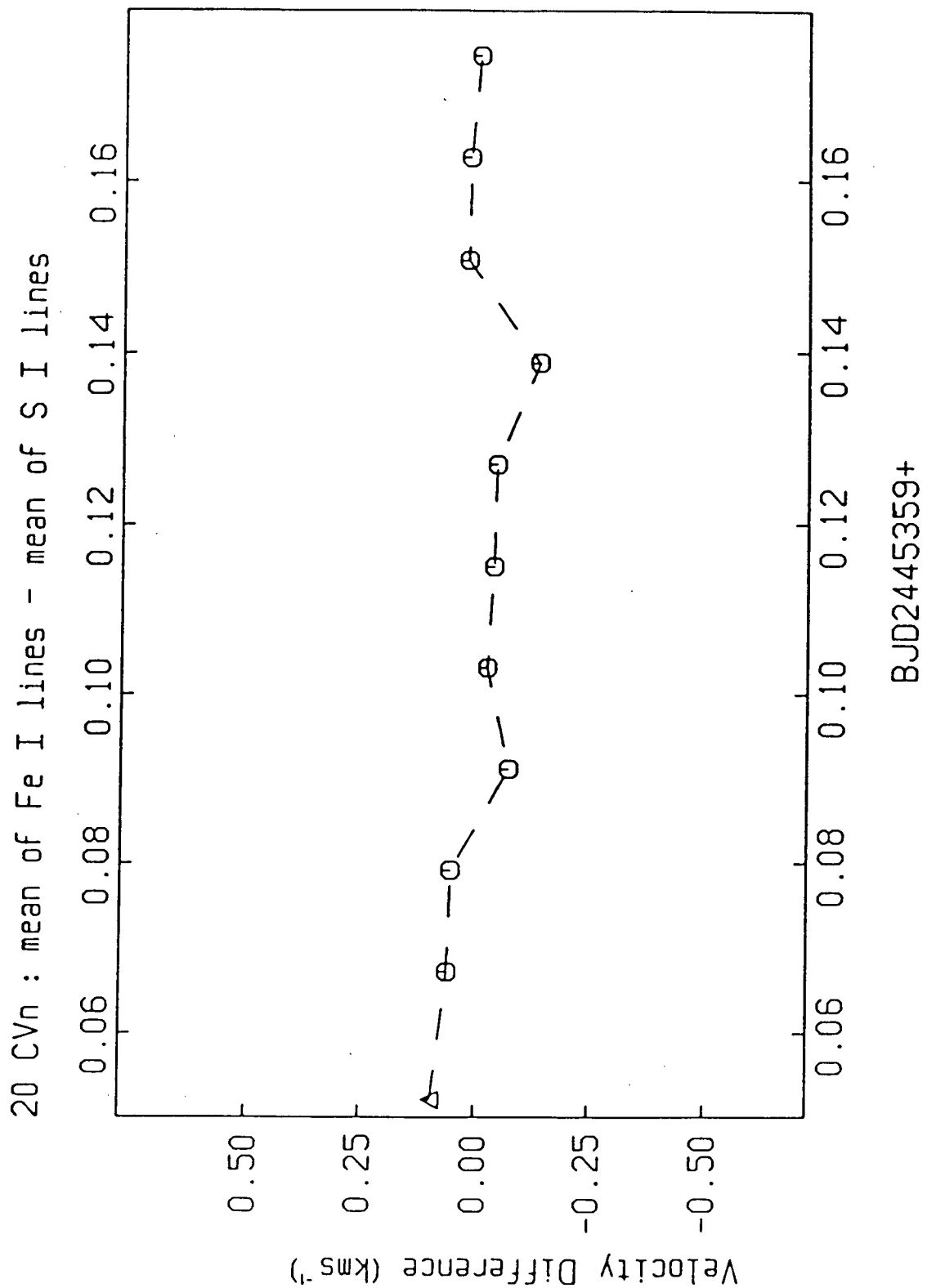

different region of the pulsating stellar atmosphere. On the other hand, the propagation of shocks in the pulsating atmosphere could alter the Ca II line profile and hence the deduced velocity displacement. In fact, shock-generated shortward-shifted emission in the Ca II K line has been reported in another δ Del type δ Scuti variable, ρ Pup, by Dravins et al. [1977]. Shock-generated emission has also been observed in the large-amplitude δ Sct variable, VZ Cnc (Garbuzov and Mitskevich [1984]). The Ca II lines in 20 CVn have been found to be anomalous in strength by Morgan and Abt [1972]. At the present, no concrete explanation can be offered for the observed effect. In fact, one cannot even begin to speculate on whether it is related to the metallicism or solely to the δ Scuti pulsation of the star.

Figure 5.6 gives the velocity difference between the mean curve and that derived from the mean of the Fe I lines. Figure 5.7 shows the velocity difference between the mean Fe I curve and the the mean Si I curve while the difference between the mean Fe I curve and the mean S I curve is shown in Figure 5.8. There appears to be no systematic deviation in any of these three curves. In fact, the scatter in each curve is probably a reasonable indication of the individual velocity precision. Figure 5.6 has a standard deviation of $\pm 36 ms^{-1}$. Figure 5.7 has a standard deviation of $\pm 109 ms^{-1}$ while Figure 5.8 has a standard deviation of $\pm 70 ms^{-1}$. The smaller scatter in Figure 5.6 is probably caused partially by the fact that the Fe I lines do contribute significantly towards the mean curve because of their large number.

The short duration of the observed time series will cause large uncertainty in any pulsation period derived from the data. Nevertheless, a pseudo "cycle-count" period can be inferred from the observed change of almost one cyclic variation in the velocities. The periodogram and Maximum Likelihood power-spectrum analysis of the Ca II velocity curve in Figure 5.2 gives a period of 0.1266^{d}. Similarly, an analysis of the mean velocity curve in Figure 5.4 gives a period of 0.1336^{d}. Averaging the two gives a mean period of 0.130^{d} or a mean frequency of 7.69 day^{-1}. These results agree very well with the spectroscopic result of Nishimura et al. [1983] and are not too different from the values given by Shaw [1976], Smith [1982b], and Bossi et al. [1983]. However, any agreement achieved here may be purely accidental. The derived pulsation period carries a large uncertainty because of the limited time coverage. Moreover, Smith [1982b] has reported that the radial-velocity variations of 20 CVn can be quite different on different nights. The velocities were found to be sinusoidal on one night while on the night before, they were monotonically decreasing. Smith [1982b] attributed this to the beating effect caused by a second period modulating the primary period of 0.122^{d}. Bossi et al. [1983] have reported modulation in the photometric amplitude which may be caused by a beat between the main period and a second period at 0.143^{d}. The amplitudes of the two periods are 0.0200^{m} and 0.0054^{m}, respectively. The period ratio, however, would disagree with the identification of the second overtone

radial pulsation as the main oscillation by Pena and Gonzalez [1981]. This mode typing was based on their derived value of 0.02 day for Q, the pulsation constant. Tsvetkov [1982b,1984], on the other hand, has adopted a Q value of 0.041 day for 20 CVn. Applying the parameters in Table 5.1 to Equation 1.11, one obtains a Q value of 0.025 day for 20 CVn. This value implies first overtone radial pulsation or even nonradial pulsation for 20 CVn.

Tsvetkov [1984] has placed 20 CVn in a list of nine peculiar δ Scuti variables. These peculiar stars all have large discrepancies between their calculated evolutionary masses and pulsation masses. Smith [1982b] has suggested a beat period of 2 days and hence excluded the common radial and nonradial period ratios. Furthermore, Smith [1982b] has found a sharp separation between the $2K/\Delta m_v$ values for the radially and nonradially pulsating δ Scuti stars. Based on a low value of $42 kms^{-1}mag^{-1}$ adopted for 20 CVn, Smith [1982b] has suggested that the dominant mode in 20 CVn is probably nonradial. This is in spite of the fact that the sharpness of the lines in 20 CVn has prevented Smith [1982b] from mode typing using line-profile analysis.

The nature of 20 CVn's pulsation is still unclear and the star deserves more extensive observations. The sky condition was poor when this set of data was taken. In fact, there was a strong 60-knot wind which was also the main reason for the short time coverage. The noise characteristics of the Reticon at CFH have since been improved. This together with the improved through-put of the

CFH red Coudé train implies that higher s/n data are now possible with the same instrumental setup at CFH.

Chapter 6

THE DELTA SCUTI VARIABLE ρ PUP

6.1 INTRODUCTION

The star ρ Puppis (HR3185) has also been called ι Argus by Reese [1903]. It is a δ Scuti variable with δ Delphini-type anomalous abundances. Parameters for ρ Pup are summarised in Table 6.1. Additional parameters are summarised in Tsvetkov [1982b], Halprin and Moon [1983], Gupta [1978], Breger and Bregman [1975], Leung [1970], Antonello et al. [1981], Breger [1979], Baglin et al. [1972], and Hoffleit and Jaschek [1982]. Abundance analysis of ρ Pup has been performed by Greenstein [1948], Bessell [1969], Breger [1970], and Kurtz [1976]. A slightly enhanced value of 0.54 has been determined for [Fe/H]. Kurtz [1976] also found among the lighter elements that the Ca I, Sc II, Ti II, and V II abundances appear to be slightly deficient. Bidelman [1951] has given ρ Pup a MK classification of F6II. However, Bidelman [1951], McNamara and Augason [1962], and Morgan and Abt [1972] have pointed out that Ca II is weak in ρ Pup when compared to stars of similar spectral type.

6.2 VARIABILITIES OF ρ PUP

The star ρ Pup was first reported to exibit variable radial velocities by Reese [1903] and Campbell and Moore [1928]. In fact, Spencer Jones [1928] has derived a velocity range of 11.6 kms^{-1} for ρ Pup. Photometric variations were first reported by Cousins [1951] and Eggen [1956,1957].

Table 6.1 Parameters for ρ Pup

****

	Reference
HD number : 67523	
SAO number : 175217	
DM number : -23 6828	
R.A. (1950) : $8^h\ 5^m\ 24.798^s$	
Dec. (1950) : -24° 9' 32.312"	
Annual parallax : +0.031"	
Proper motion in R.A. : -0.088"/yr	
Proper motion in Dec. : +0.048"/yr	
l_{II} : 243.15°	
b_{II} : 4.40°	
Spectral type : F5 IIp	Morgan and Abt [1972]
Radial velocity = 46 kms^{-1}	Eggen [1979]
Vsini = 14 kms^{-1}	Kurtz [1976]
M_V = +1.7	Eggen [1979]
T_{eff} = 7100K	Kurtz [1976]
log g = 3.25 (cgs)	Kurtz [1976]
Broad band photometry :	Iriate et al. [1965]
V = 2.82^m	
B - V = $+0.44^m$	
U - V = $+0.63^m$	
V - R = $+0.37^m$	
V - I = $+0.58^m$	
Infrared photometry :	Verma et al. [1983]
J = 2.13^m	

$H = 2.02^m$

$K = 1.99^m$

Intermediate band photometry : Eggen [1979]

$\beta = 2.715^m$

$b - y = 0.260^m$

$m_1 = 0.215^m$

$c_1 = 0.730^m$

$\delta m_1 = -0.040^m$

****

Light curves for ρ Pup have also been given by Ponsen [1963], Thulsassi Doss [1969], and Trodahl et al. [1973]. Radial-velocity curves have been given by Struve et al. [1956], Buscombe [1957], Campos and Smith [1980], and Fracassini et al. [1983]. The velocity oscillation has been measured with a servo-controlled Fabry-Perot radial-velocity spectrometer by Reay et al. [1983a]. Simultaneous radial-velocity and photometric time-series observations have been performed by Danziger and Kuhi [1966], Dravins et al. [1977], and Balona and Stobie [1983]. Bessell [1969] performed simultaneous radial-velocity and photoelectic spectrum-scanner observation of the continuum. Emission lines have been observed at the Mg II H and K lines by Weiler and Oegerle [1979] with the Copernicus satellite. IUE observations of the emission lines have been given by Fracassini and Pasinetti [1981] and Fracassini et al. [1983].

The early radial-velocity data from the Lick Observatory (Reese [1903], Campbell and Moore [1928]) suggested a radial-velocity amplitude 2K of 8.4kms^{-1}. The data from Struve et al. [1956] has an amplitude of 9.7kms^{-1}. Struve et al. [1956] measured a period of 0.1409^{d} and also suggested a value of 0.14 as the amount in phase by which the radial-velocity minimum lags behind the light maximum. The photometric observations by Cousins [1951] show an amplitude of 0.146^{m}. Eggen [1956,1957] measured an amplitude of 0.107^{m} and a period of 0.14089^{d}. Ponsen [1963] has reanalysed all the early data together with his photometric data and derived a period of 0.14088141^{d} (3.3712 hours) and a blue-light amplitude of 0.127^{m}. The light curve is found to be nearly sinusoidal with the maximum slightly sharper than the minimum. Both the rising and the descending branches of the curve are almost equally steep. Bappu [1959] has measured a light amplitude of 0.16^{m} at λ4050 together with a 300K variation in the colour temperature. The simultaneous photometric and spectroscopic observations by Danziger and Kuhi [1966] give a 2K value of 11kms^{-1}, a light amplitude of 0.15^{m} at λ4566, and an effective-temperature variation of 280K. Minimum light was found to occur at about 0.08 of a period before maximum radial velocity. Bessell [1969] measured a light amplitude of 0.130^{m} at λ4255, and a 2K value of 9.5kms^{-1}. One can see from his data that the radial-velocity minimum lags the maximum of the light curve by 0.075 in phase. Bessell [1969] has reported a temperature variation of 130K and a radius variation of 1.6x10^{4}km.

Thulasi Doss [1969] has observed the photometric variations in the narrow pass bands at λ3858, λ4310, λ4720, and λ5875. The corresponding amplitudes were given as 0.17^m, 0.14^m, 0.12^m, and 0.09^m, respectively. The effective-temperature curve was given with a full amplitude of 320K. A period of 0.14088067^d was also derived for the pulsation. Trodahl and Sullivan [1977] measured a light amplitude of 0.105^m at λ4850 and an effective-temperature variation of 175K. A corresponding amplitude of about 0.033 was given for the relative radius variations ΔR/R. Dravins et al. [1977] measured a phase lag of 0.06 between the radial-velocity minimum and the v light maximum. A temperature variation of 160K was measured from the loop travelled by ρ Pup in the $(c_1,b-y)$-diagram during the pulsation cycle. Dravins et al. [1977] reported emission in the blue wing of the Ca II K line profile at about 0.28 in phase before maximum light. It has been suggested that the emission is caused by a shock wave propagating through the stellar atmosphere (Dravins et al. [1977], Hill [1977], Smith [1982]). With a Reticon detector, Campos and Smith [1980] measured both the radial-velocity and line-profile variations of the lines Fe I λ4476 and Fe II λ4508. A 2K value of $11.5 kms^{-1}$ was determined. Campos and Smith [1980] did not detect any linewidth or line-profile variation greater than 5% of the continuum. Smith [1982b] has adopted a light amplitude Δm_v of 0.102^m and a phase difference of 0.08 between the light maximum and radial-velocity minimum. This light amplitude has been standardised to a colour of (b-v) = 0.20. Reay et

al. [1983a] used a servo-controlled Fabry-Perot radial-velocity spectrometer to measure the radial-velocity variations of ρ Pup. From 226 minutes (3.76 hours) of observations, there was no evidence of periodicities other than the principal period of 0.141^{d}. This is to a limit of $20ms^{-1}$. Fracassini et al. [1983] have reported a time series of high-dispersion observations of the Mg II H and K lines. The time series covers one complete pulsation cycle; the exposure for each spectrogram was about 10 minutes. The Mg II emission was found to be present during the entire pulsation cycle and it increased with increasing luminosity.

6.3 THE OBSERVATIONS

The star ρ Pup was observed spectroscopically with the HF absorption cell at the Canada-France-Hawaii 3.6m telescope on the 22nd, 24th, and 25th of January 1983 UT. The time series of spectra were obtained under the same conditions and with the same instrumental setups as for the time series on 20 CVn described earlier. Similar observing procedures were used. Stellar and lamp spectra with and without the imposed HF lines were obtained. These are shown in Figure 6.1. The mean stellar+HF spectrum with either the stellar or HF lines numerically removed are also shown. The length of each exposure is either 600, 750, or 900 seconds. These correspond, respectively, to 0.05, 0.062, and 0.074 of the "cycle-count" period of 0.141 day (3.37 hours). The time coverage in the three nights is, respectively, 83%, 112%, and 69% of this period. Each spectrum has for each point at

Figure 6.1 The ρ Pup spectrum

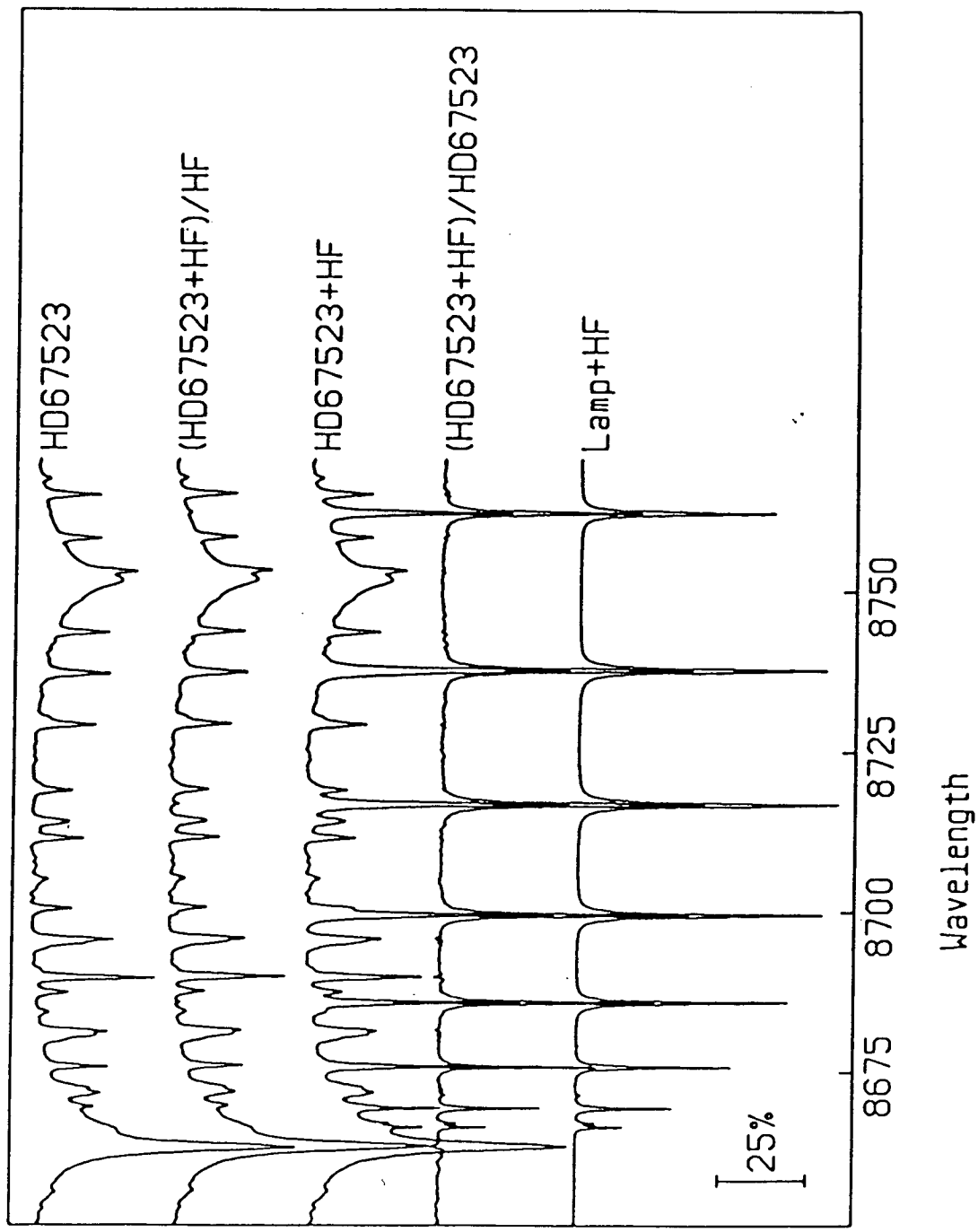

Table 6.2 Mid-exposure times and exposures for ρ Pup

#		Barycentric JD	exposure	hour angle
	22 Jan 83 UT+			
1	(09:31:43.26)	2445356.9011222	600s	0h 52m 20s E
2	(09:42:11.42)	2445356.9083927	600s	0h 41m 50s E
3	(09:52:37.84)	2445356.9156430	600s	0h 31m 22s E
4	(10:03:04.25)	2445356.9228932	600s	0h 20m 53s E
5	(10:13:36.83)	2445356.9302148	600s	0h 10m 19s E
6	(10:24:04.30)	2445356.9374773	600s	0h 00m 10s W
7	(10:34:31.05)	2445356.9447314	600s	0h 10m 39s W
8	(10:44:56.65)	2445356.9519722	600s	0h 21m 06s W
9	(10:55:22.31)	2445356.9592138	600s	0h 31m 33s W
10	(11:05:48.43)	2445356.9664606	600s	0h 42m 01s W
11	(11:16:15.70)	2445356.9737208	600s	0h 52m 30s W
12	(11:26:41.86)	2445356.9809681	600s	1h 02m 58s W
13	(11:37:07.68)	2445356.9882115	600s	1h 13m 26s W
14	(11:47:33.18)	2445356.9954511	600s	1h 23m 52s W
15	(11:57:33.18)	2445357.0027053	600s	1h 34m 21s W
16	(12:08:26.45)	2445357.0099568	600s	1h 44m 49s W
17	(12:20:39.13)	2445357.0184369	600s	1h 57m 04s W
	24 Jan 83 UT+			
18	(08:05:52.14)	2445358.8415243	900s	2h 10m 32s E
19	(08:21:37.01)	2445358.8524604	900s	1h 54m 44s E
20	(08:43:45.99)	2445358.8678423	900s	1h 32m 32s E
21	(08:59:22.30)	2445358.8786793	900s	1h 16m 53s E
22	(09:14:58.28)	2445358.8895125	900s	1h 01m 14s E
23	(09:30:35.19)	2445358.9003565	900s	0h 45m 35s E

24	(09:44:54.45)	2445358.9103017	750s	0h 31m 13s E
25	(09:57:52.83)	2445358.9193108	750s	0h 18m 13s E
26	(10:12:11.03)	2445358.9292438	900s	0h 03m 52s E
27	(10:27:52.65)	2445358.9401423	900s	0h 11m 52s W
28	(10:43:28.79)	2445358.9509774	900s	0h 27m 31s W
29	(10:58:55.78)	2445358.9617065	900s	0h 43m 00s W
30	(11:14:23.19)	2445358.9724405	900s	0h 58m 30s W
31	(11:29:58.27)	2445358.9832633	900s	1h 14m 08s W
32	(11:45:26.52)	2445358.9940071	900s	1h 29m 39s W
33	(12:00:53.85)	2445359.0047401	900s	1h 45m 09s W
34	(12:16:21.09)	2445359.0154722	900s	2h 00m 39s W
35	(12:31:48.55)	2445359.0262068	900s	2h 16m 09s W
	25 Jan 83 UT+			
36	(08:24:20.19)	2445359.8543583	900s	1h 48m 04s E
37	(08:39:45.69)	2445359.8650702	900s	1h 32m 36s E
38	(08:55:12.65)	2445359.8757990	900s	1h 17m 06s E
39	(09:10:39.09)	2445359.8865218	900s	1h 01m 37s E
40	(09:26:18.42)	2445359.8973938	900s	0h 45m 56s E
41	(09:41:48.19)	2445359.9081551	900s	0h 30m 23s E
42	(09:57:19.29)	2445359.9189318	900s	0h 14m 50s E
43	(10:12:48.85)	2445359.9296907	900s	0h 00m 43s W
44	(10:28:19.31)	2445359.9404600	900s	0h 16m 16s W
45	(10:43:45.62)	2445359.9511813	900s	0h 31m 44s W

****

the continuum, a mean s/n of 690, 800, and 400 for the three nights, respectively. The mid-exposure time as well as the length of exposure for each spectrum are summarised in Table 6.2. Spectrum #17, #18, and #19 are the spectra without the imposed HF lines. Again as in the case of 20 CVn, approximate radial velocities can be measured from these spectra using the dispersion relations determined for the other spectra. For the entire ρ Pup data set, the heliocentric times lag the barycentric times by about 0.9 second.

6.4 THE DATA REDUCTION

The data were processed and reduced using the same procedures which were applied to the 20 CVn data. Spectrum #17 has been chosen to be the radial-velocity standard spectrum for all the ρ Pup data. It provides both the line-shape and line-position references used in determining the relative shifts of individual spectral lines. A lamp+HF spectrum taken on the same night, the 24th, was used as the HF standard spectrum. These two standard spectra were used to reduce all three time series. The use of identical standard spectra ensures internal consistency for the measured velocities between the three time series. One can compare the measured velocities of a particular line directly between the three time series without any additional correction.

The same criteria which were used for the 20 CVn reduction were used to choose the line limits for both the

stellar and HF lines. A typical set of stellar line limits is about 10 pixels in width. The unmodified difference function from Equation 4.4 was initially used for the stellar lines in the application of the Fahlman-Glaspey technique. In the case of ρ Pup, the stellar lines are broader than those in 20 CVn. Because of the effect of Doppler imaging, it may be easier to detect line-profile variations if they are present. Hence initially, the use of an optimising difference function is less desirable than in the case of 20 CVn. However, the modified difference function from Equation 4.5 was used for the the HF lines. Individual relative radial-velocity curves were subsequently obtained for the stellar lines Ca II λ8662, H I λ8750, Mg I λ8719, Fe I λ8689, λ8710, λ8713, λ8757, λ8764, S I λ8671, λ8680, λ8695, Si I λ8686, λ8728, λ8742, and λ8752. The relative radial velocity for any particular line was obtained by subtracting a mean velocity calculated over an observed period. In order to preserve the internal consistency between data from different nights, the same value of mean velocity was used for all three time series.

6.5 THE LINE-PROFILE VARIATIONS

Figures 6.2 and 6.3 show the velocity curve measured on the night of the 24th for the Ca II λ8662 and the Fe I λ8689 lines, respectively. The Ca II curve has an average one-standard-deviation uncertainty of about $\pm 0.17 kms^{-1}$ in each stellar line-position measurement. The uncertainty value is the formal error estimate derived from the

Figure 6.2 The unoptimised Ca II λ8662 velocity curve

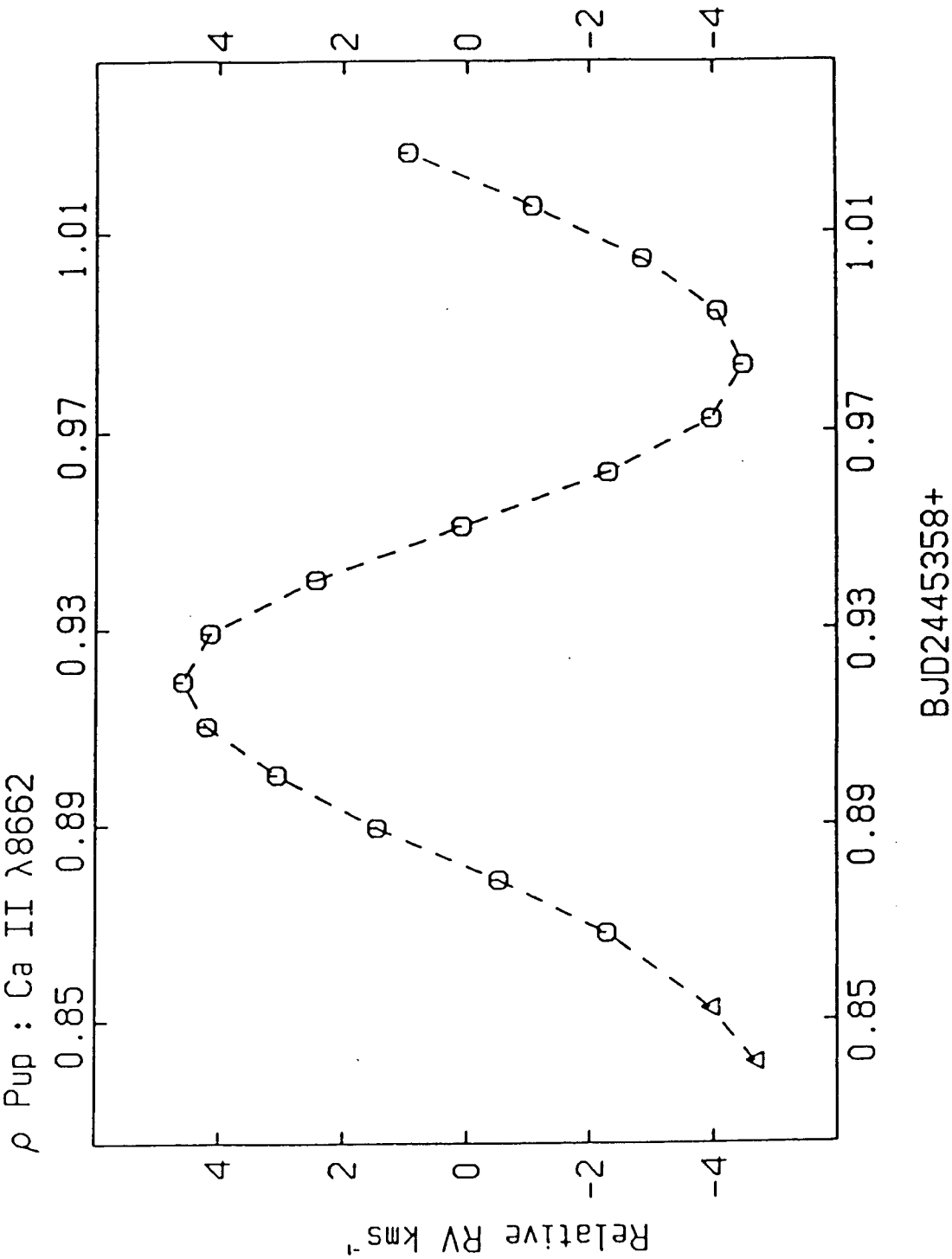

Figure 6.3 The unoptimised Fe I λ8689 velocity curve

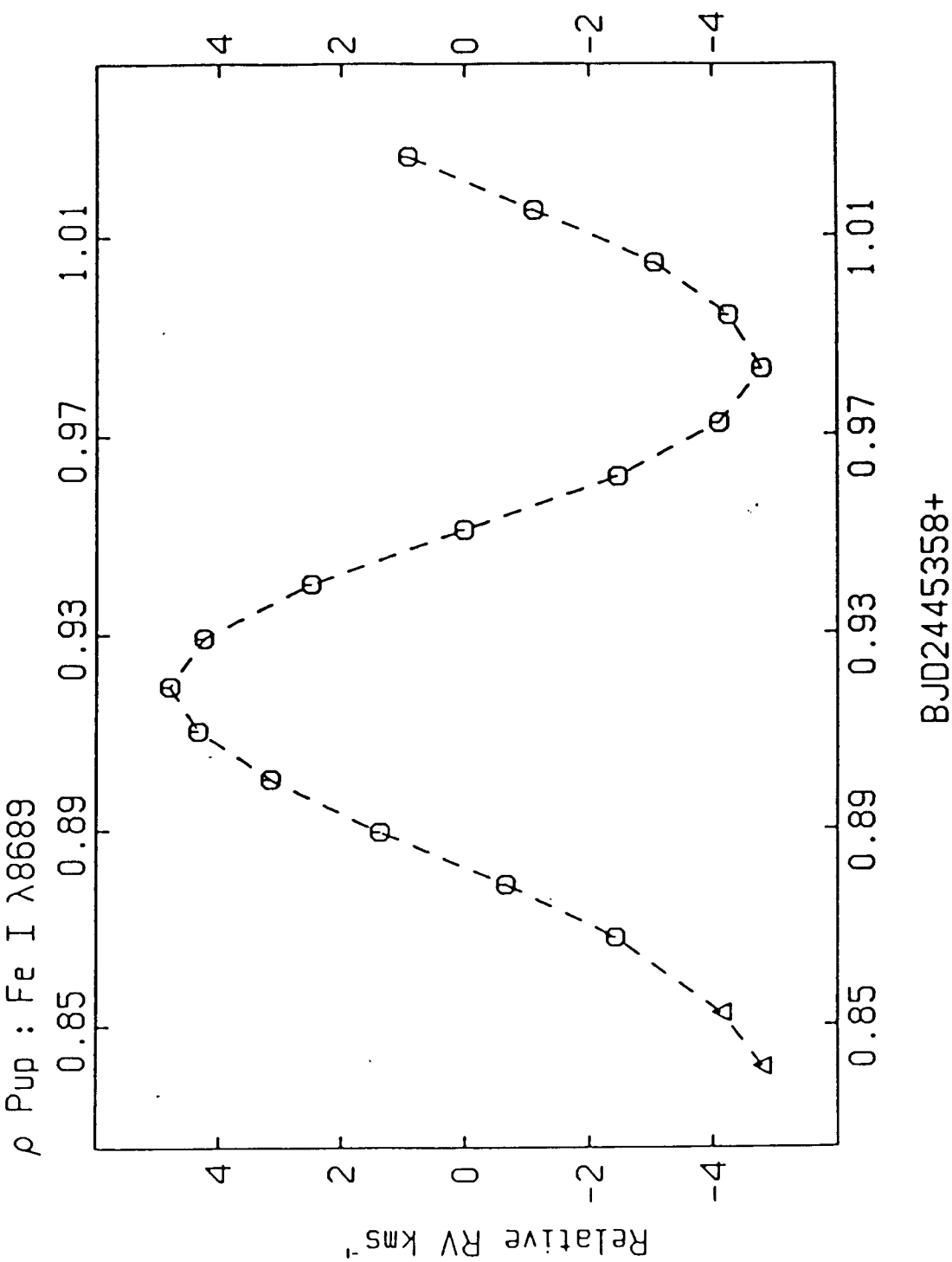

Fahlman-Glaspey technique. It is a very large value in comparison to the corresponding value of about $\pm 0.09 kms^{-1}$ obtained for the much lower s/n 20 CVn data. The fact that the ρ Pup lines are broader than the 20 CVn lines can not be the major reason for the discrepancy. Similarly, the Fe I curve in Figure 6.3 has an one-standard-deviation uncertainty of about $\pm 0.31 kms^{-1}$ in each stellar line-position measurement. This is much larger than the corrresponding value of about $\pm 0.1 kms^{-1}$ obtained for the 20 CVn data.

Figures 6.4 and 6.5 show the individual line-position measurement uncertainties for the Ca II and Fe I curves, respectively. Each of these curves has been corrected for the effect caused by differences in the s/n between the spectra. This is accomplished by multiplying each uncertainty value by the ratio between the spectrum's s/n and a mean s/n. The assumption that the velocity uncertainty is inversely proportional to the spectrum's s/n (Campbell and Walker [1979]) has been used. Comparing Figures 6.3 and 6.5, one sees that the uncertainties peak near the middle of the rising and decreasing branches of the velocity curve. The minima of the velocity uncertainty appear to occur near the minima or maxima of the velocity curve. This effect can be explained if there is a correlation between the velocity uncertainties and the light curve which leads the velocity curve by about 0.08 in phase. Figure 6.6 shows the Fe I λ8757 velocity curve. Superimposed on the plot are the corresponding line-position uncertainties. It is evident

Figure 6.4 Uncertainties in the Ca II λ8662 line positions

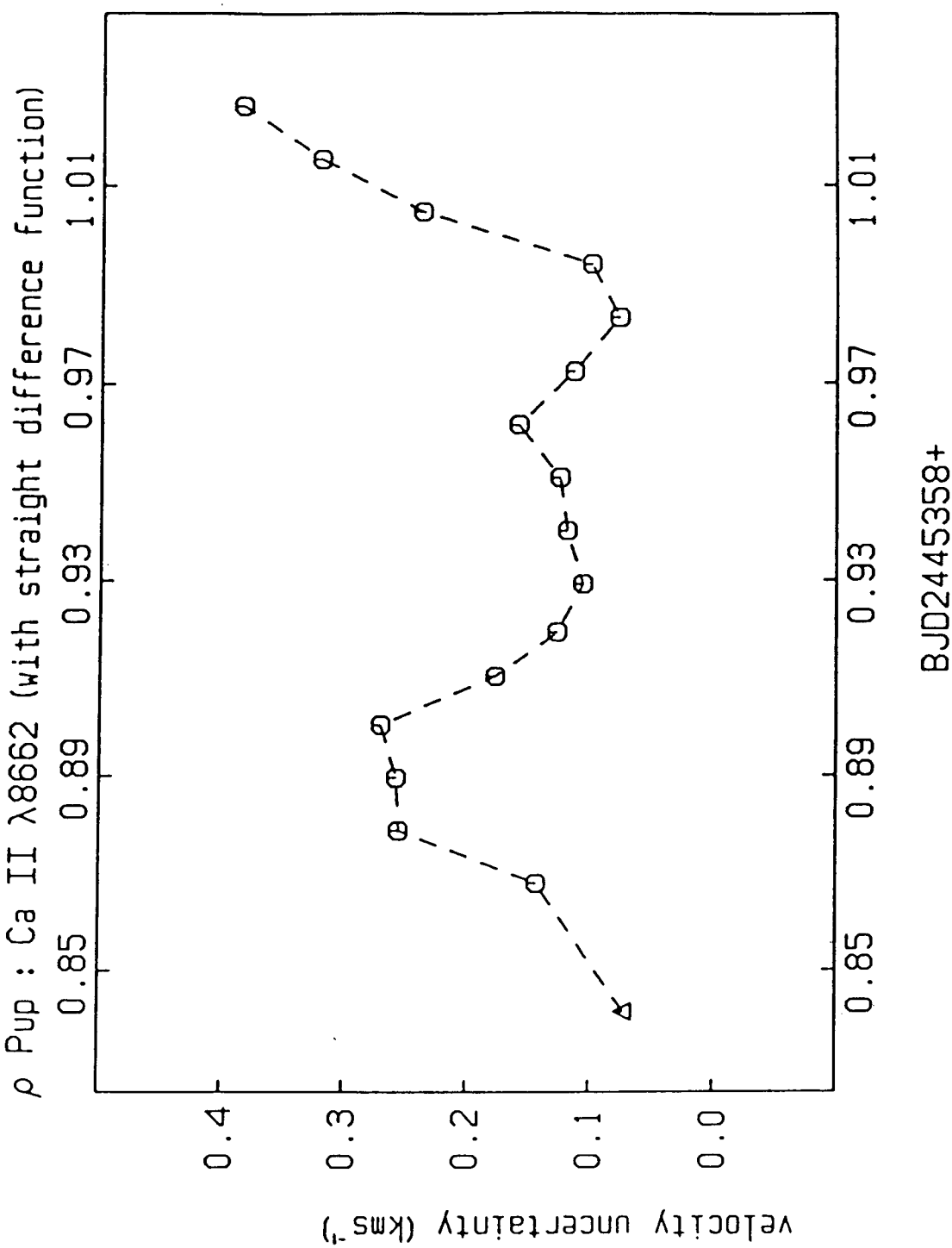

Figure 6.5 Uncertainties in the Fe I λ8689 line positions

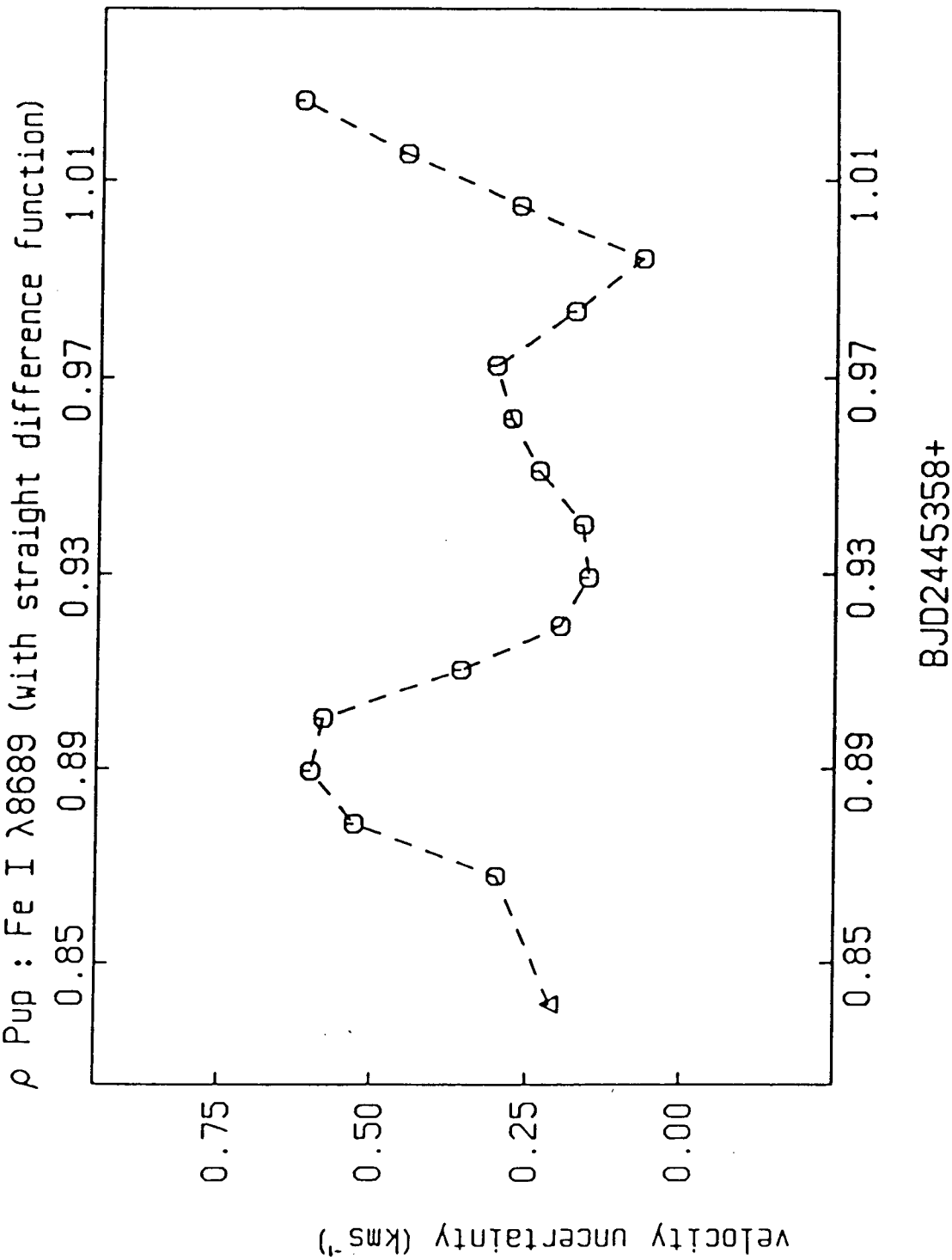

Figure 6.6 The unoptimised Fe I λ8757 velocities

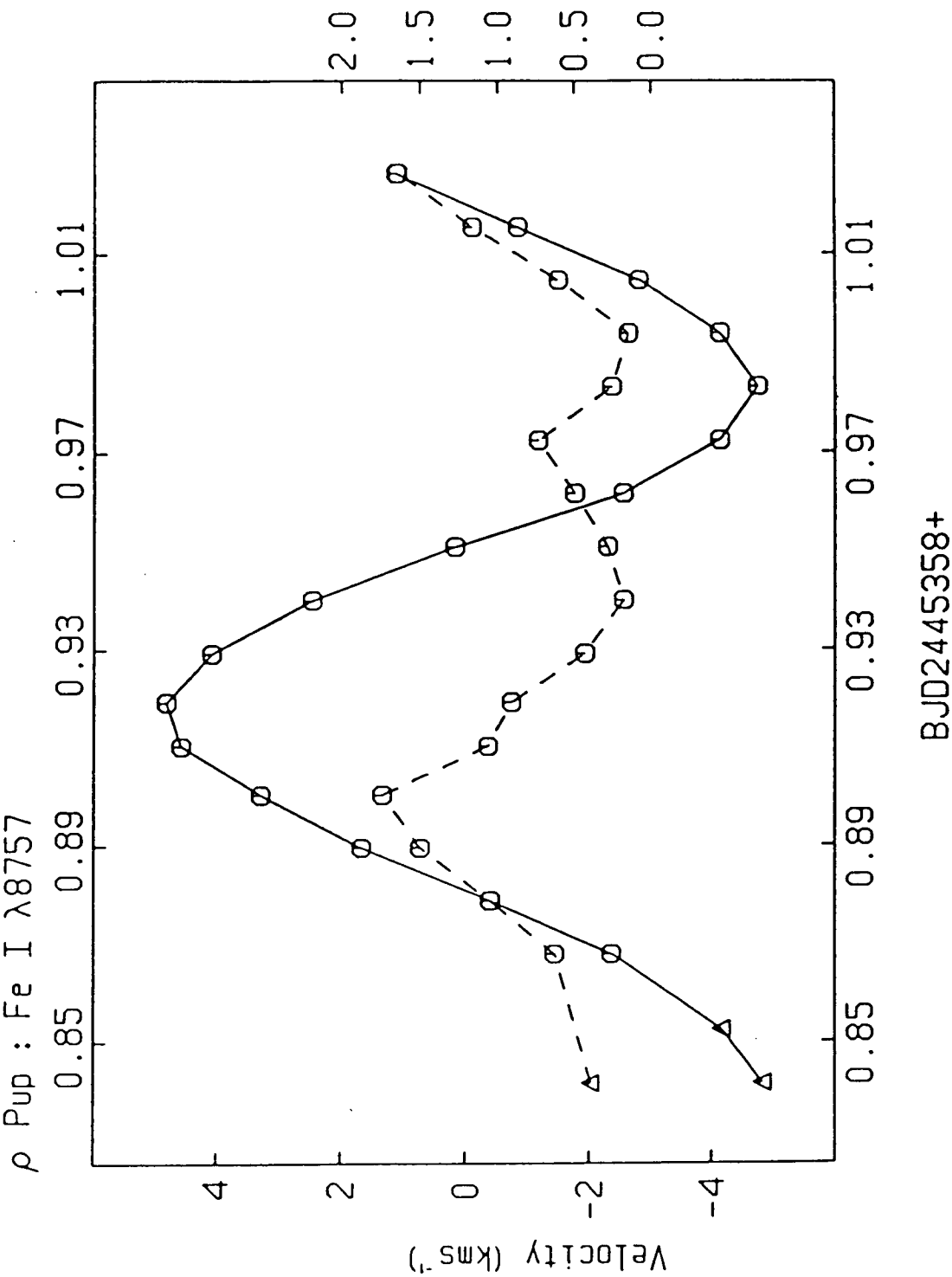

from the plot that the uncertainties and the velocities are correlated. The uncertainty curve is measured to be leading the velocity curve by about 0.07 in phase. Hence the uncertainty curve would be in phase or 180° out of phase with the light curve. The uncertainty peak near BJD2445358.9 coincides with the light minimum.

The derived uncertainties are measures of the residuals after differencing between the standard and the individual line profiles. In addition to the intrinsic s/n limited line-position error, line-profile variations will contribute towards this formal error estimate derived by the Fahlman-Glaspey technique. The systematic variations of the uncertainties strongly suggest that most of them are caused by systematic line-profile variations. A velocity curve with simple line-profile variations will appear more precise or 'smoother' than a corresponding curve with the same estimated formal error but with random noise as the sole source of the uncertainty. This is partly because of the fact that, in the case of simple profile variations, the residuals in the differenced spectra would have a systematic or smooth trend. In the technique's process of minimising the residuals, this systematic trend will be reflected in the measured line positions. In the case of the limited s/n, however, the residuals are random. The formal error estimate from the technique is derived from the sum of the squares of these residuals and hence would not distinguish between the two cases. This is probably the explanation for Figure 6.6 in which the velocity curve appears more precise than its

formal error estimates imply. The sensitivity of the technique to line-profile variations depends very much on the type of variations. Simple variations like line-depth and linewidth variations would not seriously affect the derived velocity curve. Other more complicated line shape variations would affect the derived velocity curve more seriously. Of course, in those cases, it may be the objective to use the velocity curve to parametrise the line-profile variations. Systematic line-profile variations may produce systematic pseudo velocity variations.

The standard profile was taken at BJD2445358.85 which is near a velocity minimum. It is expected that this profile will be similar in line shape to those spectra taken near the other velocity minimum and at a similar photometric phase. This would explain why the uncertainty peak at BJD2445358.9 (near velocity maximum) is stronger than that at BJD2445358.97 (near velocity minimum). The fact that the velocity uncertainties correlate with the light curve rather than with the velocity curve would suggest that the line-profile variations may not be the result of pulsation-generated surface-velocity-field variations. The profile variations may be related to the temperature and spectral-type variations over the pulsation cycle.

Line-profile variations can best be examined from a time series difference-spectrum plot i.e. a stacked plot of the residuals after subtracting a mean line profile from each spectrum. Figure 6.7a shows the region of the Ca II λ8662 line for each spectrum after correcting for the

Figure 6.7 The Ca II λ8662 line profiles and their residuals

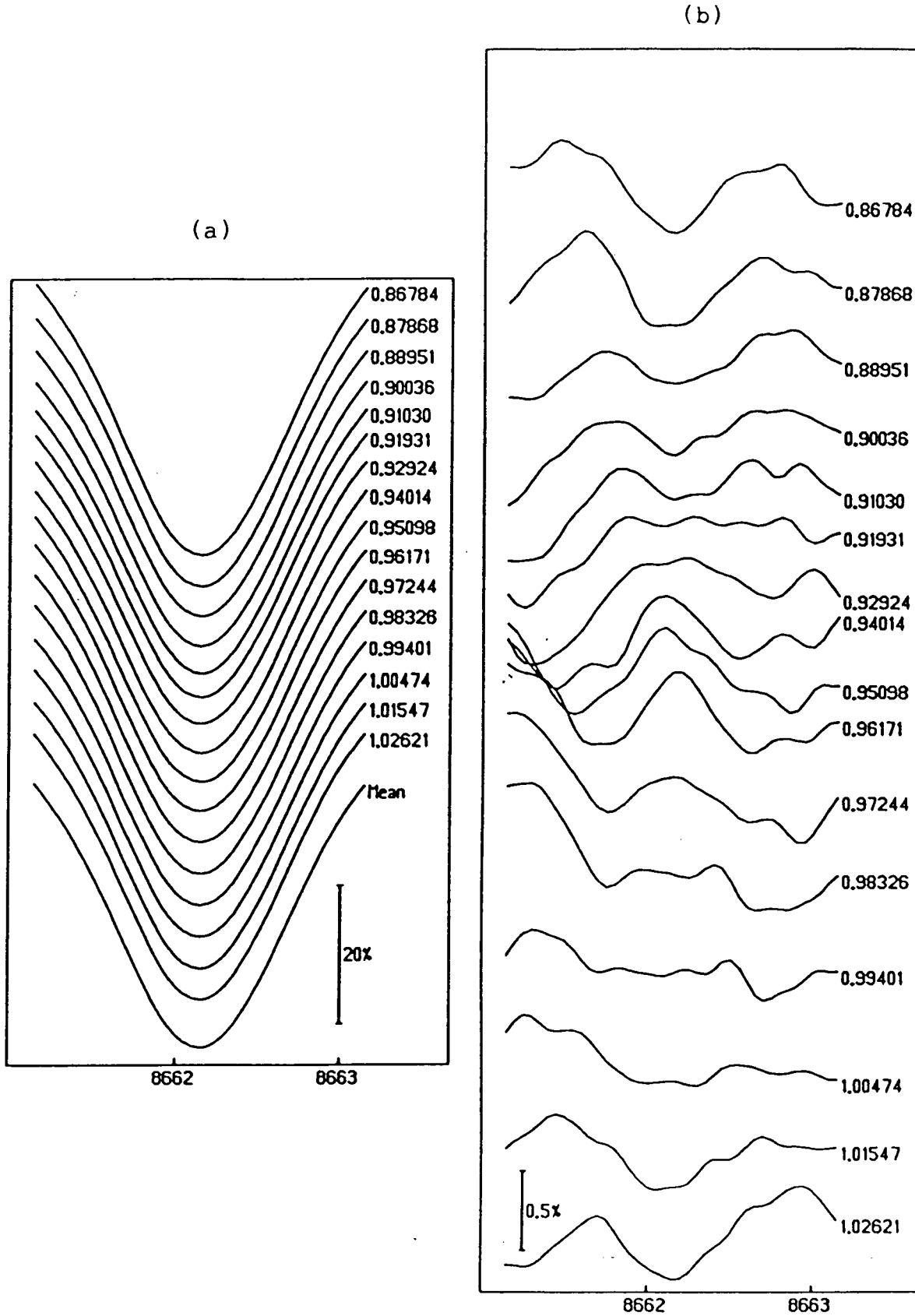

Figure 6.8 The Fe I λ8689 line profiles and their residuals

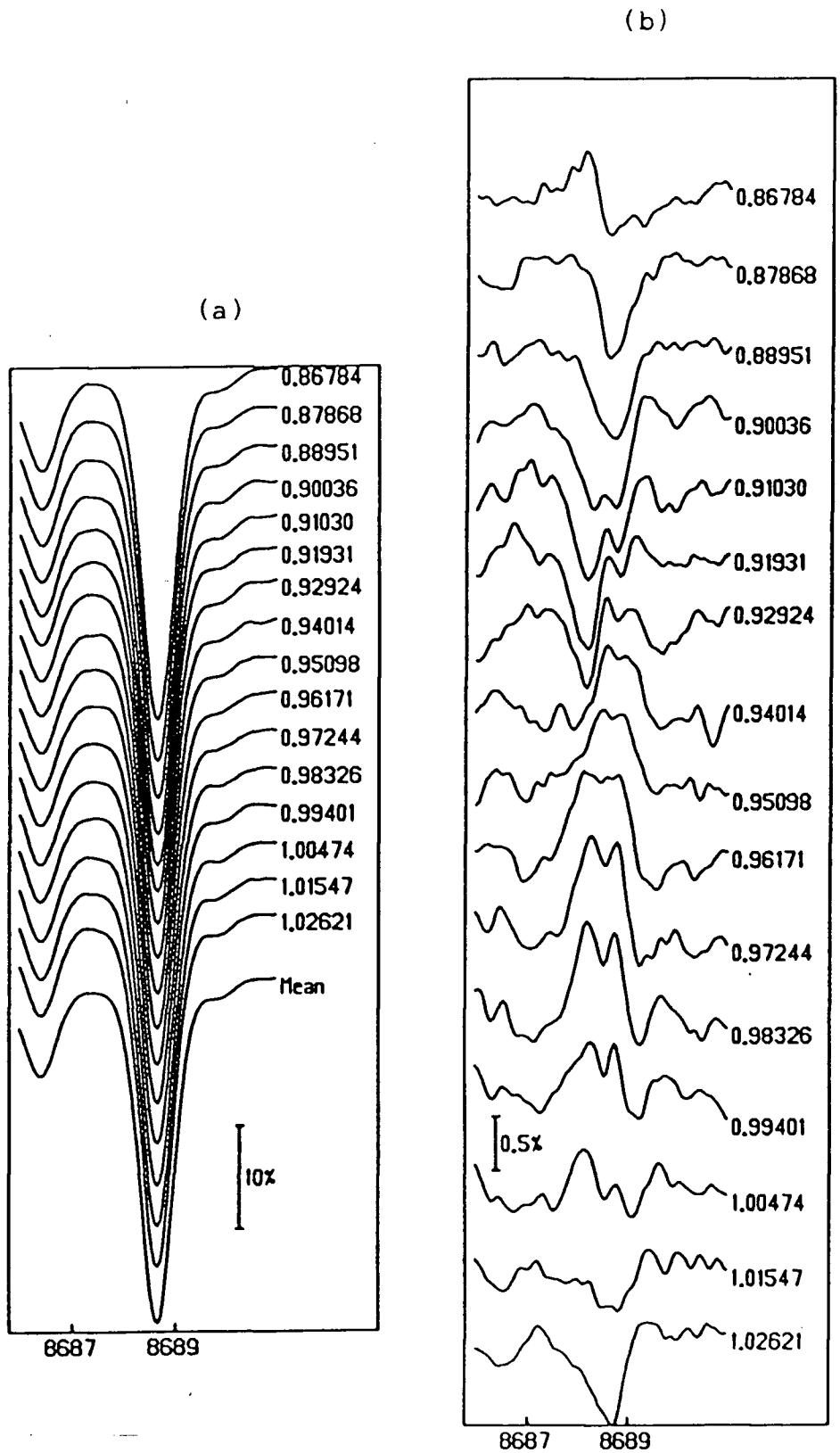

Figure 6.9 The Si I λ8752 and Fe I λ8757 line profiles

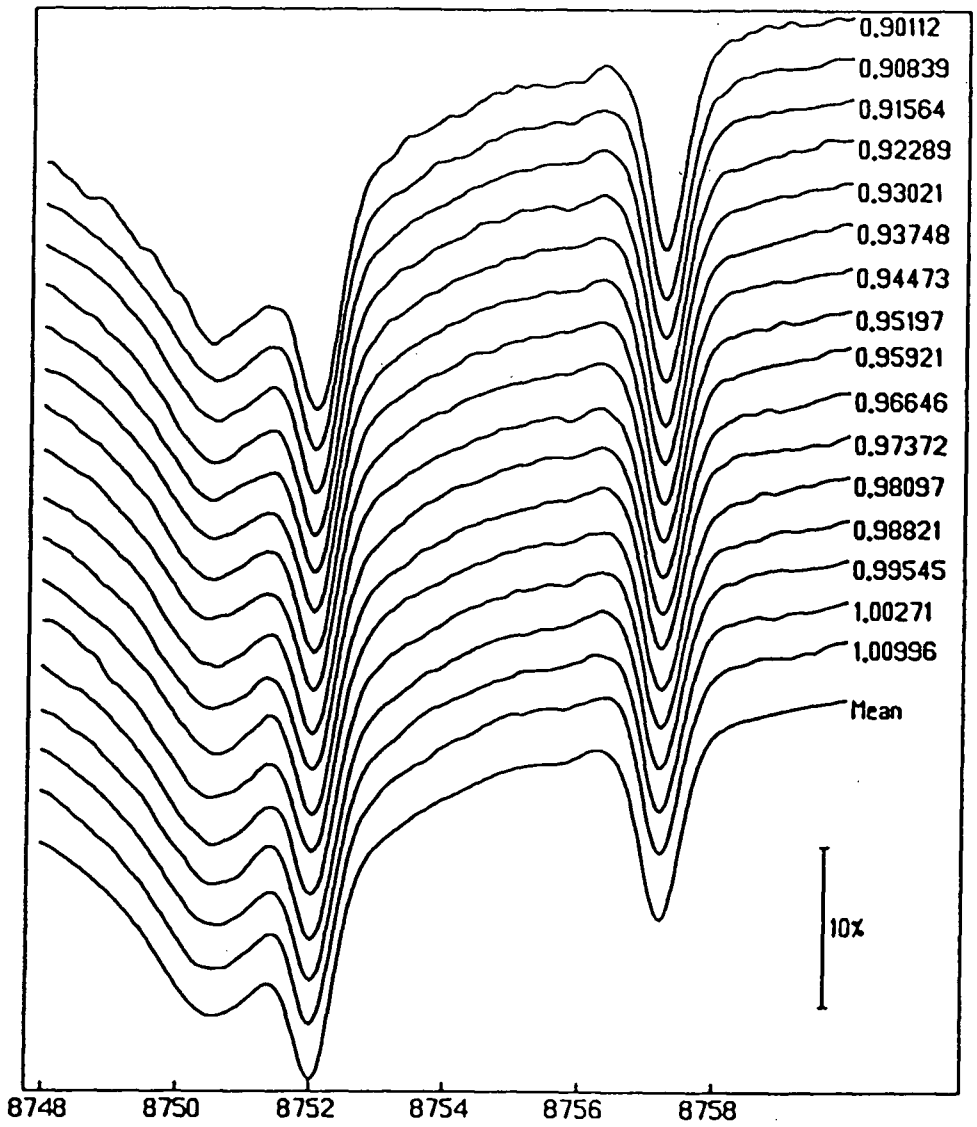

Figure 6.10 The Si I λ8752 and Fe I λ8757 residuals

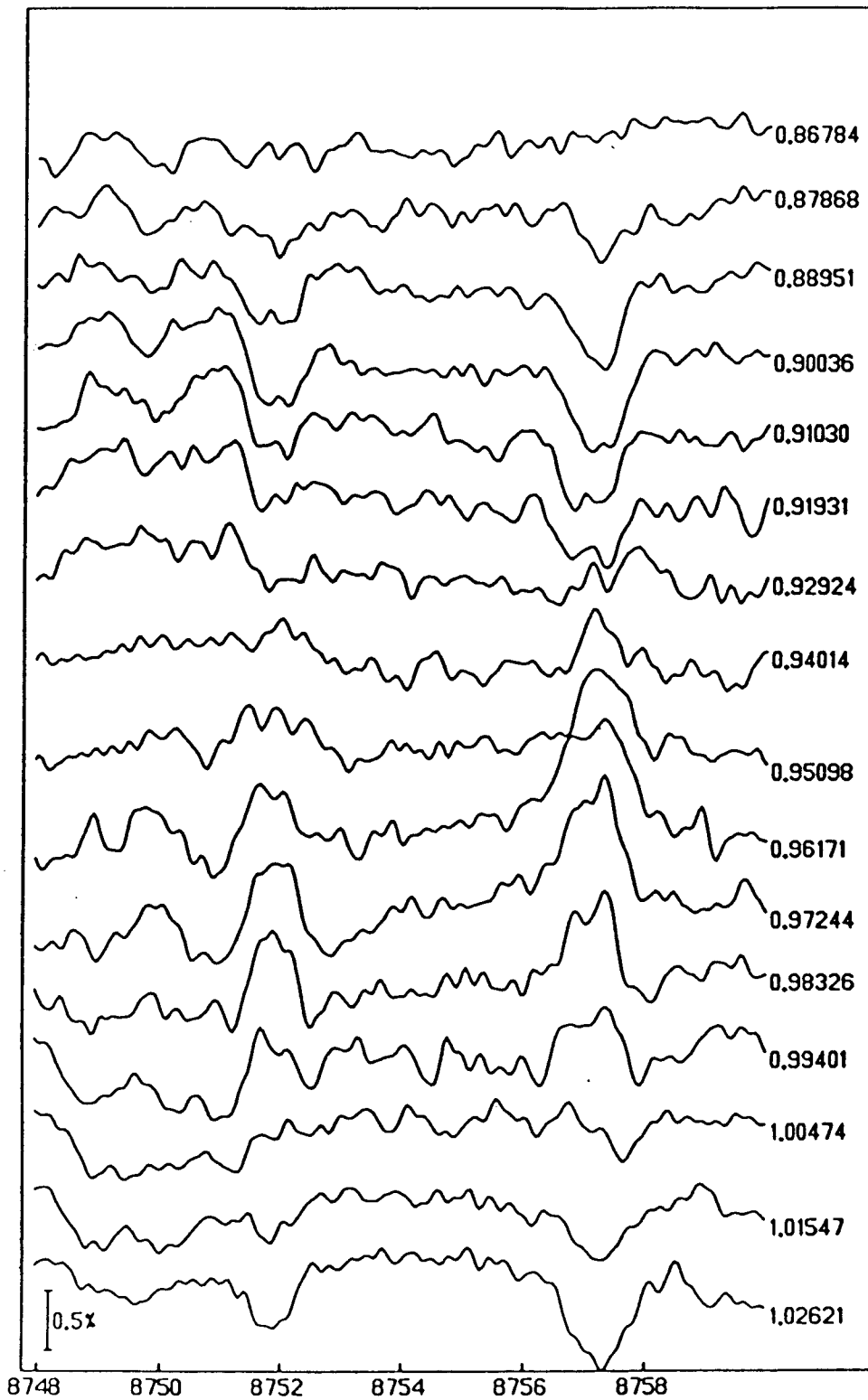

Figure 6.11 The Si I and Fe I residuals from BJD2445356

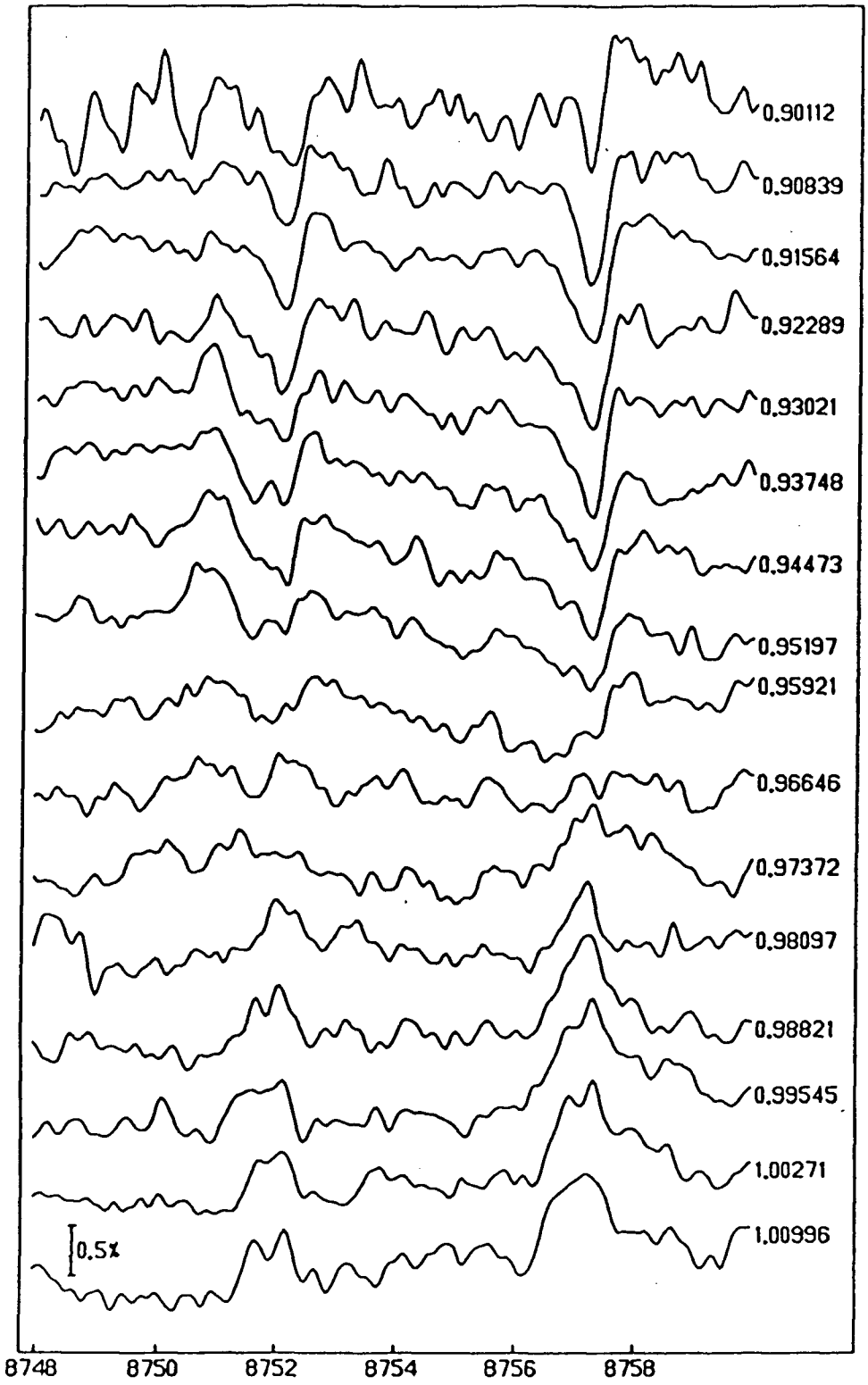

measured velocity shifts. The spectra have been smoothed by a Gaussian transfer function which has a σ of ±0.075Å. The mid-exposure time in fraction of days from BJD2445358 is indicated for each spectrum. Figure 6.7b shows the residuals after subtracting a mean line profile from each spectrum. The mean profile is chosen to be the average of the fifteen line profiles from spectrum #21 through #35. It represents approximately the mean line profile averaged over one pulsation cycle. Figures 6.8a and 6.8b show the time series of Fe I λ8689 line profiles and their residuals, respectively. Figure 6.9 shows the region of the Si I λ8752 and Fe I λ8757 lines in each spectrum. The corresponding residual plot is shown in Figure 6.10. Figure 6.11 shows the residual plot for the same spectral lines but the data are taken from the time series observed on the night of the 22nd of January. The same mean line profiles were used to produce the residuals in both Figures 6.10 and 6.11. The mid-exposure times in fraction of days from BJD2445356 are indicated in Figure 6.11.

It can be seen from Figures 6.8b, 6.10, and 6.11 that the line-profile variations can be characterised as systematic variations in the line depth or equivalent width of the lines. Near the light maxima at both BJD2445358.90 and BJD2445359.03, all the stellar absorption lines are stronger than their mean line profile. But near the light minimum at BJD2445358.97, the stellar lines are weaker than their mean line profiles. Near the nodes of the light curve, the variabilities of the line profiles from their mean

profile are minimal. The amplitudes of the variations are different between the various stellar lines. The variations in the line depth of the Ca II λ8662 line are only at a level of 0.5% of the continuum. The strong Fe I λ8689 line shows variations at the 1% continuum level. The stacked residual plot of the line in Figure 6.8b shows that the variations are more complicated than simple line-depth or line-intensity variations. The inner core of the spectral line appears to vary in the reverse manner with respect to the rest of the line. It is shallower than the rest of the line near light maxima but deeper near the light minimum. The amplitude of this small reversal is less than 0.3% of the continuum. The Si I λ8752 and Fe I λ8757 lines show similar line-intensity variations as the Fe I λ8689 line. However the amplitudes are only about 0.8% of the continuum. The small reverse variations at the inner line core can also be seen in these two weaker lines but at a smaller amplitude.

Similar but larger amplitude variations have been reported in the peculiar large-amplitude δ Sct variable SX Phe (Stock and Tapia [1971], Haefner et al. [1976]). The absorption-line intensities were also found to be minimal at minimum light while the maxima of the line intensities occured near light maxima. This same sequence of line-intensity variations over a pulsation cycle is also well known as the spectral-type variation in Cepheid variables. The spectral type of long-period Cepheids can vary between F5 and K1 over a pulsation cycle. Naturally,

the corresponding line-intensity variations are very much larger than in this case of ρ Pup. The larger effect in Cepheids is essentially caused by their much larger change in the effective temperature over the pulsation cycle. In ρ Pup, the full effective-temperature amplitude is only about 280K.

The observed lines of Ca II, Fe I, Si I, and S I are known to have stronger intensities in stars of spectral type slightly later (or cooler) than ρ Pup. These lines are also weaker in stars of earlier (or hotter) spectral type. Therefore, if the observed line-intensity variations were caused mainly by the temperature variations over the pulsation cycle, the lines should then be stronger at temperature minima (almost coinciding with light maxima) and weaker at temperature maxima (almost coinciding with light minima). This is exactly the sequence of line-intensity variations that is observed in ρ Pup.

Temperature variations affect an observed line depth through the temperature dependence of both the stellar continuum level and the energy-level population of the particular stellar line transition. Considering only weak stellar lines and small temperature variations, one can derive a very simple linear theory to account for the main effect of the observed spectral-type variations. Assuming the continuum opacity κ_c is much larger than the line opacity κ_l, one obtains :

$$d = \kappa_l \; / \; (\; \kappa_l + \kappa_c \;) \qquad (6.1)$$

$$\Delta d/d = (1-d) \; (\; \Delta\kappa_l/\kappa_l - \Delta\kappa_c/\kappa_c \;) \qquad (6.2)$$

$$\kappa_l = A \exp(-E_L/kT) \quad (6.3)$$

$$\Delta\kappa_l/\kappa_l = (E_L/kT)\ (\Delta T/T) \quad (6.4)$$

$$\Delta\kappa_c/\kappa_c = \Delta n_{H^-}/n_{H^-} \quad (6.5)$$

$$K_H = n_{H^+}\ n_e\ /\ n_H \quad (6.6)$$

$$K_{H^-} = n_H\ n_e\ /\ n_{H^-} \quad (6.7)$$

$$n_{H^-} = (\sqrt{(n^3 K_{H^-})})\ /\ K_{H^-} \quad (6.8)$$

$$\Delta n_{H^-}/n_{H^-} = (1/2)\ (\Delta K_H/K_H) - (\Delta K_{H^-}/K_{H^-}) \quad (6.9)$$

$$\log(K_{H^-}) = -(\chi_{H^-})\theta - (3/2)\ \log\theta + \ldots \quad (6.10)$$

$$\log(K_H) = -(\chi_H)\theta - (3/2)\ \log\theta + \ldots \quad (6.11)$$

$$\Delta K_{H^-}/K_H = 2.3\ (\Delta T/T)\ [\ (\chi_{H^-})\theta + 0.65\ ] \quad (6.12)$$

$$\Delta K_H/K_H = 2.3\ (\Delta T/T)\ [\ (\chi_H)\theta + 0.65\ ] \quad (6.13)$$

where $\theta = 5040\ /\ T$

$n = n_H + n_e$

n_e = electron number density

n_H = number density of H

n_{H^-} = number density of H^-

n_{H^+} = number density of H^+

d = line depth

T = temperature in kelvin

k = Boltzmann's constant

E_L = low energy level of the line

χ_{H^-} = 0.75 ev

χ_H = 13.6 ev

Equation 6.2 is obtained by considering the derivative of Equation 6.1. Basically, Equation 6.3 is simply stating that the line opacity is proportional to the number of atoms at the particular energy level. The term A in Equation 6.3 is independent of temperature (Johnson et al. [1972]). The effect of induced emission has been neglected in the formulation. Equation 6.4 is obtained by considering the derivative of Equation 6.3. Equation 6.5 is essentially stating the assumption that the continuum opacity is proportional to the number density of the H^- ions. This is a reasonable assumption for an F6 star where the stellar continuum is the result of mainly free-free and bound-free transitions of the H^- ions. Equations 6.6 and 6.7 are, respectively, the definitions of the dissociation constants, K_H and K_{H^-}. Equation 6.8 is derived by manipulating Equations 6.7 and 6.8 together with the assumption that $n >> n_e$. Equation 6.9 is obtained by considering the derivative of Equation 6.8. Equations 6.10 and 6.11 are Saha equations in the form given by Allen [1973]. Equations 6.12 and 6.13 are the derivatives of Equations 6.10 and 6.11, respectively. The relative change in the line depth $\Delta d/d$ as a function of the relative temperature change $\Delta T/T$ can then be evaluated using Equations 6.2, 6.4, 6.5, 6.9, 6.12, and 6.13 for any of the observed weak lines. For ρ Pup, ΔT is about ± 140K. This is the observed value given by Danziger and Kuhi [1966] and it agrees with most other determinations. The most recent and probably the best determination of T is 7100K by Kurtz [1976]. Therefore,

knowing E_L and d for a line, the corresponding $\Delta d/d$ can be calculated.

The maximum line-depth change observed in the Fe I λ8757 line is about 0.8% of the continuum. Since the line depth is about 10% of the continuum, the observed $\Delta d/d$ values are then +0.08 at temperature minimum and -0.08 at temperature maximum. The E_L value for this line is 2.83ev. The simple theory would then give $\Delta d/d$ a value of -0.081 for ΔT=+140K and a value of +0.081 for ΔT=-140K. These agree very well with the observed values.

The agreement is not as good when one considers the strong Fe I λ8689 line. The calculated $\Delta d/d$ for this line is ±0.08 while the observed value is ±0.03. The discrepancy between the calculated and the observed values becomes even larger when one considers the Ca II λ8662 line. This is not unexpected since the simple theory is only valid for the weak lines. The theory also cannot be applied to the Si I λ8752 line. This line is superimposed on the broad Paschen 12 line; therefore, the H I λ8750 line opacity at the wavelength of the Si I line also has to be taken into account in Equation 6.1. Nevertheless, the theory is still able to predict the direction of the line-depth variations for these lines.

Examining Equations 6.2 and 6.4, one can observe that for a line with a sufficiently large E_L value, the effect of $\Delta\kappa_l/\kappa_l$ would be larger than that of $\Delta\kappa_c/\kappa_c$. This will cause a direction change for $\Delta d/d$. The line would then vary in the opposite direction with respect to the other lines. It would

become strongest at temperature maxima and weakest at temperature minima. The condition is true for the Paschen λ8750 line which has a E_L value of 12.04ev. This is not unexpected since it is well known that the hydrogen lines become progressively weaker in stars of spectral types later (or cooler) than ρ Pup. Moreover, they are progressively stronger in stars of slightly earlier (or hotter) spectral types. Examining the stacked residual plots in Figure 6.10 and 6.11, one can observe that at the position of the Paschen line, the variations do go in the opposite direction with respect to the other lines. In fact, the H I λ8750 residuals make quite a contrast with the residuals of the Si I λ8752 line which varied in the other direction. In spite of the fact that the simple theory predicted the observed variations, it is unable to account for the observed amplitude of the variations. The effects of ionisation and hence depletion of the hydrogen atoms would have to be taken into account.

6.6 THE RADIAL VELOCITIES

The radial-velocity curves shown in Figures 6.2 and 6.3 are measured using the unmodified difference function from Equation 4.4. The line-depth variations would affect the precision of this method to measure relative line shifts. The line-depth variations would cause differences between the individual line profile and the standard line profile. In fact, the residuals have manifested into the large formal error estimates. Since simple line-depth variations should

not alter the line position, the difference function should still be minimal at the same shift position as in the case where there is a perfect match between the profiles. The difference function, however, would be shallower than in the case with the perfect line-profile match. This would then make it more difficult and less precise in measuring the minimum position of the difference function.

One way to minimise, to the first order, the effect of line-intensity variations is to use the modified difference function from Equation 4.5 to measure the relative line shifts. This difference function will scale the individual line profile linearly such that the residual from the standard line profile would be minimal. Consequently, the modified difference function has been applied to re-measure all the stellar line positions in the ρ Pup spectra. Figures 6.12 and 6.13 show the subsequently derived formal error estimates for the Ca II λ8662 and Fe I λ8757 line positions, respectively. Comparing these two figures against the corresponding unoptimised ones in Figures 6.4 and 6.6, one can observe that the periodic trends caused by the line-intensity variations have largely disappeared in Figures 6.12 and 6.13. Moreover, the formal error estimates have also become much smaller and are in agreement with those from the 20 CVn data set. Therefore, it appears that the application of the modified difference function to the stellar lines has been a success.

Figures 6.14, 6.15, and 6.16 show the measured relative velocity curves for the Ca II λ8662, H I λ8750, and Fe I

Figure 6.12 The optimised Ca II λ8662 uncertainties

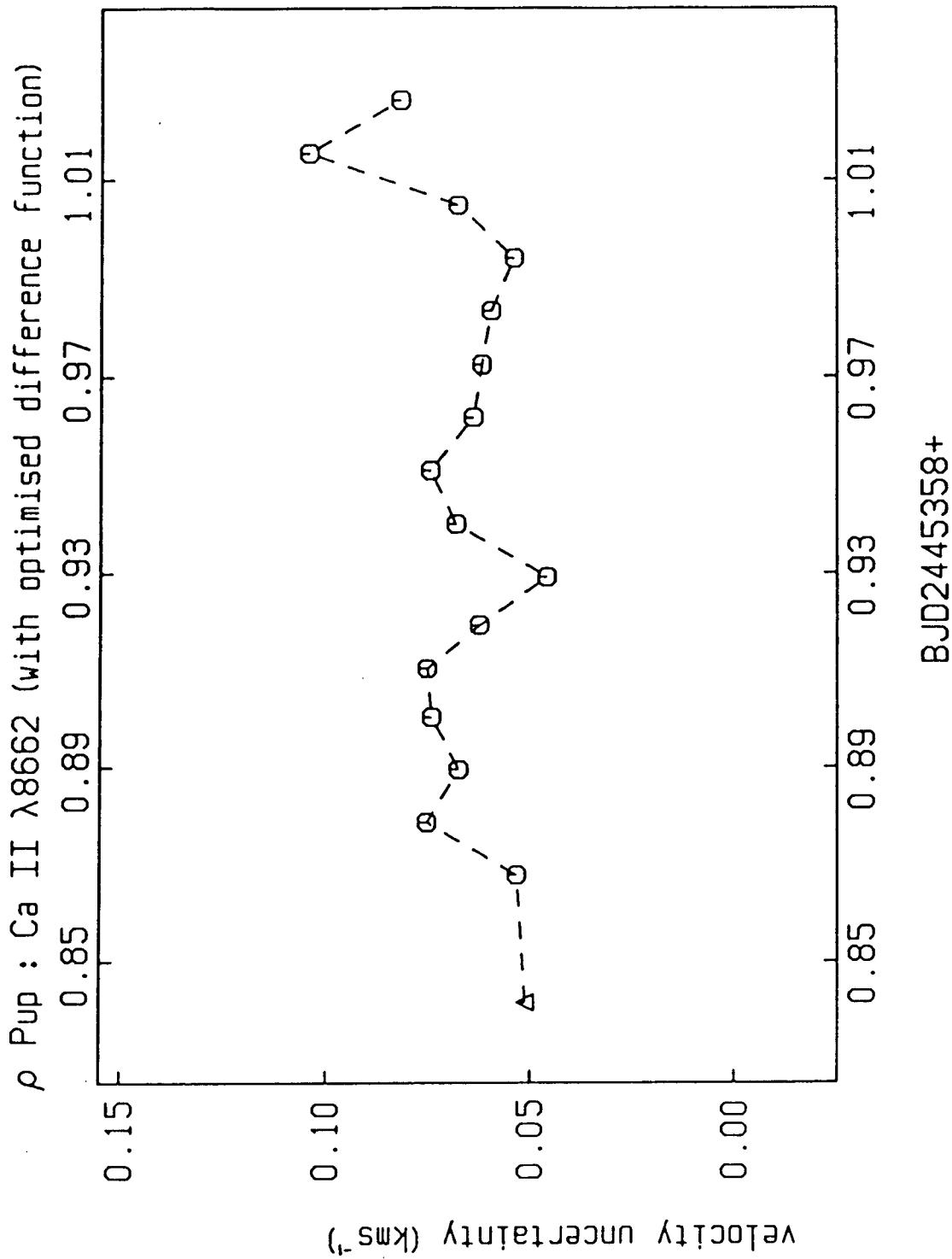

Figure 6.13 The optimised Fe I λ8757 uncertainties

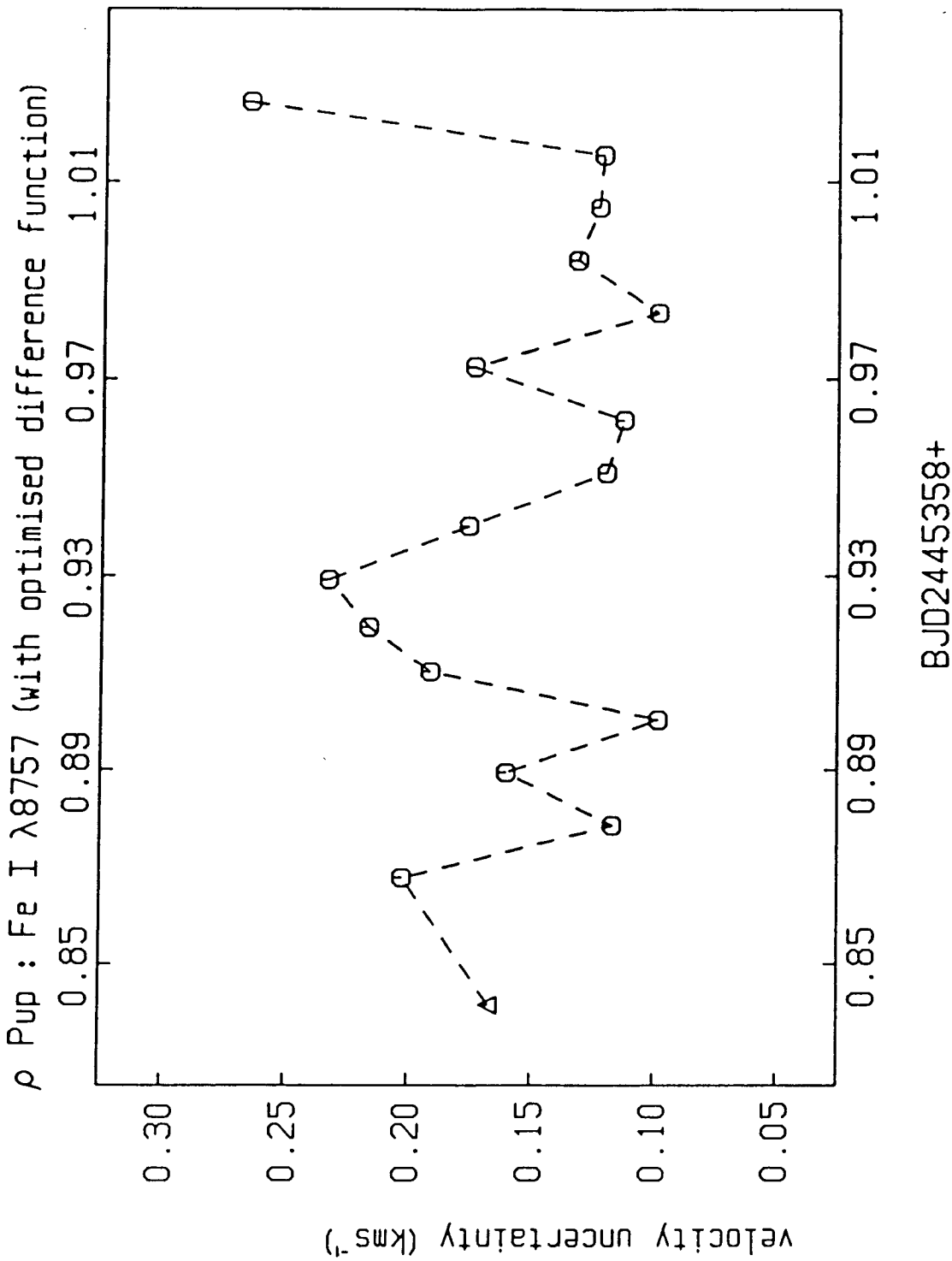

Figure 6.14 The optimised Ca II λ8662 velocity curve

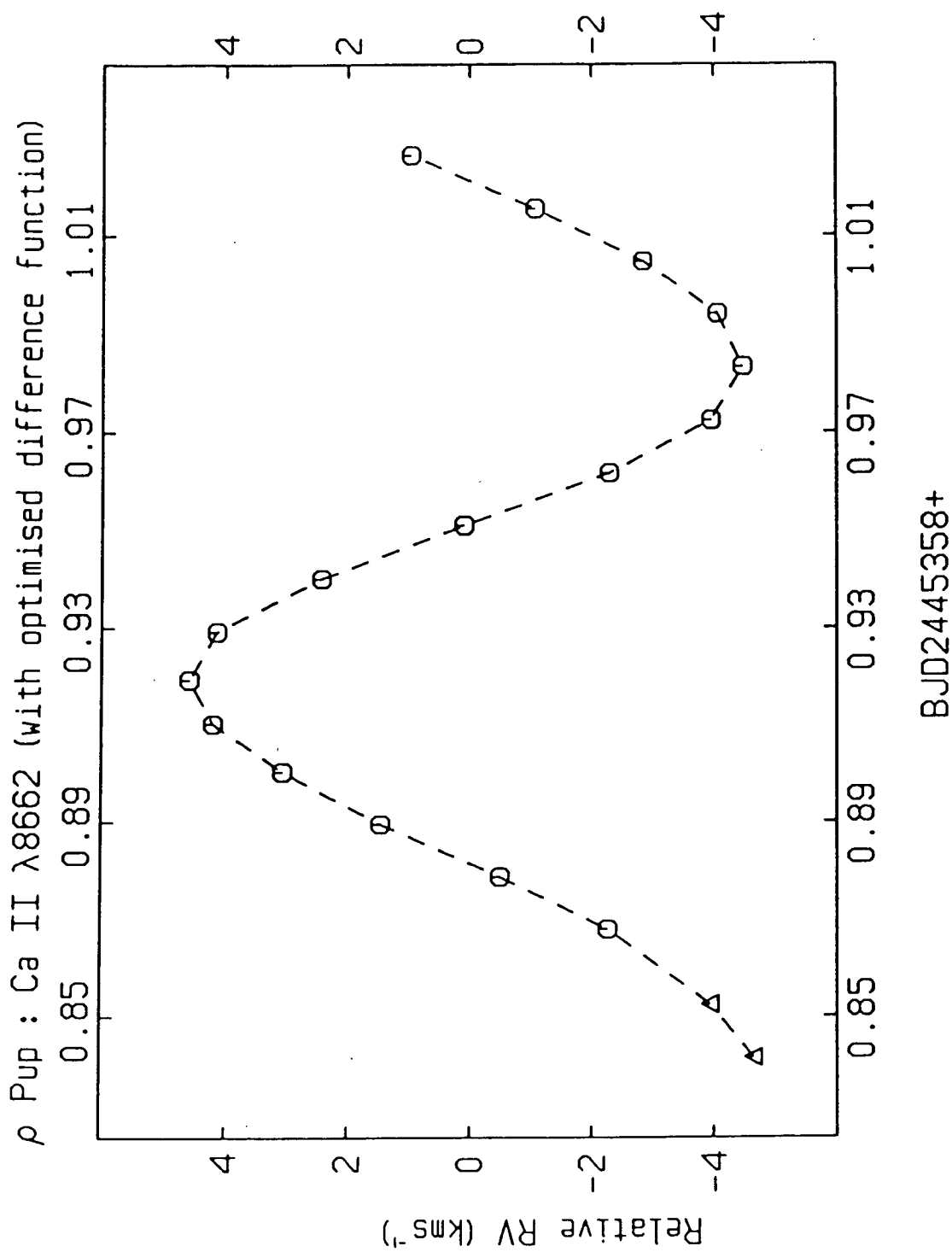

Figure 6.15 The optimised H I λ8750 velocity curve

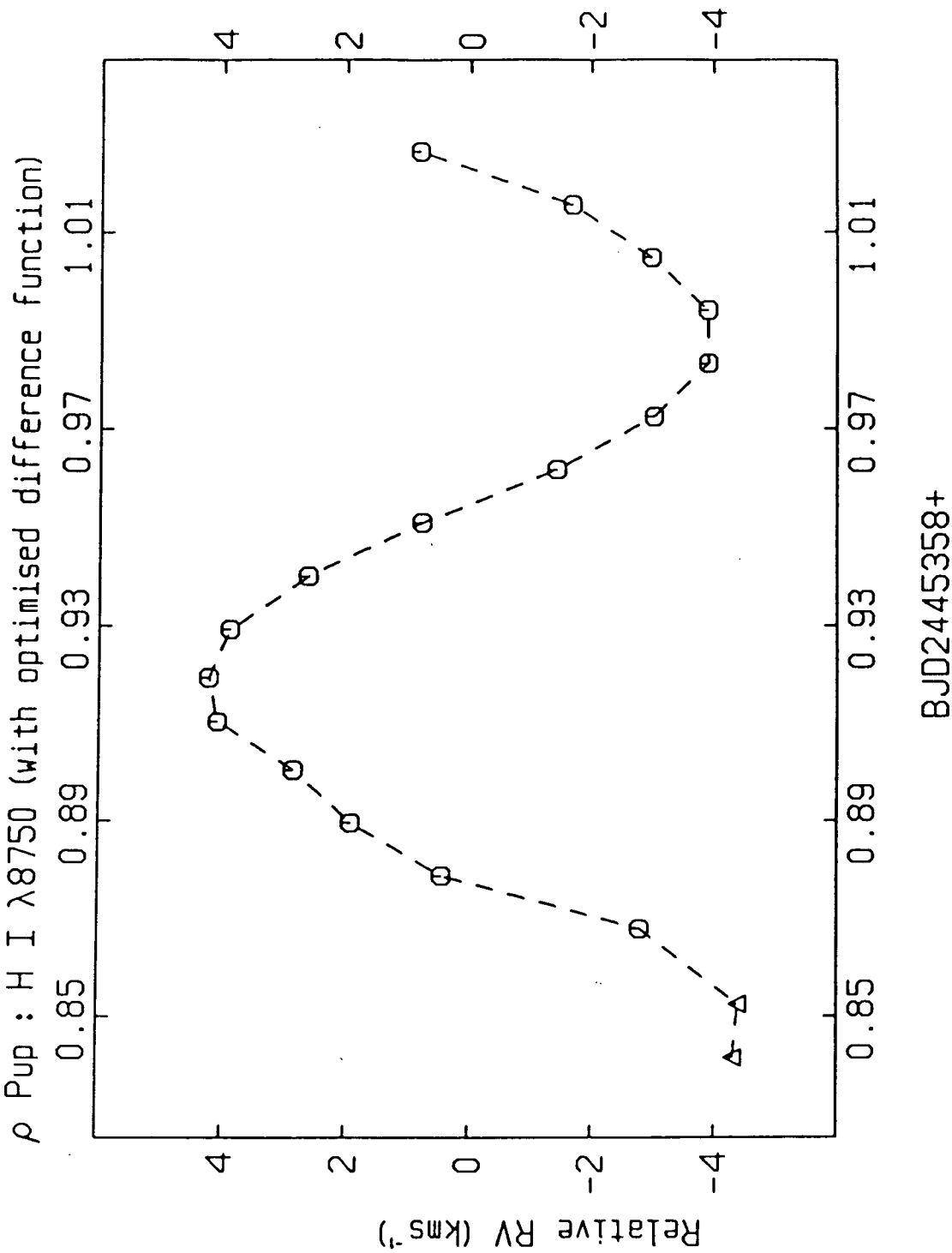

Figure 6.16 The optimised Fe I λ8689 velocity curve

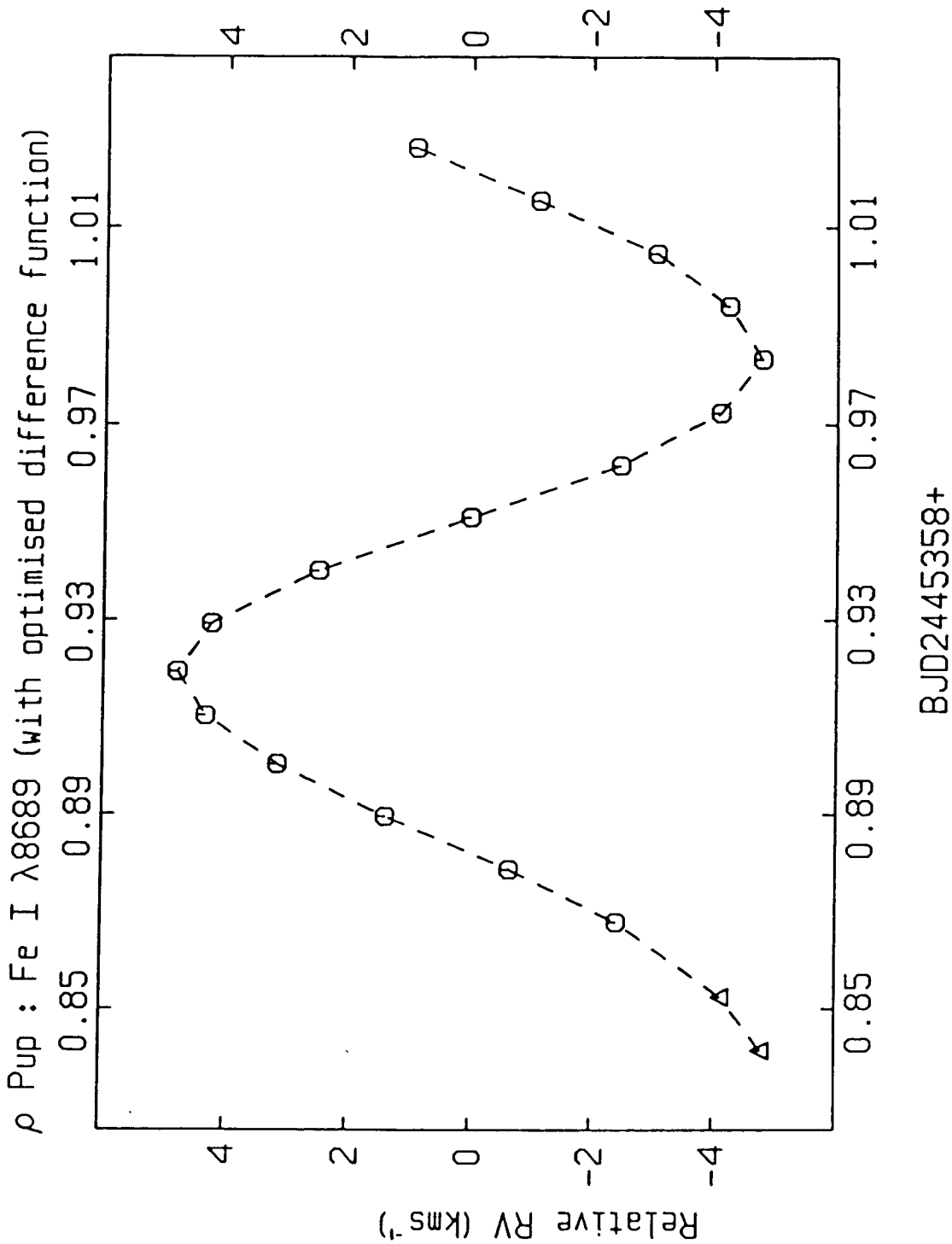

Figure 6.17 The mean optimised Fe I velocity curve

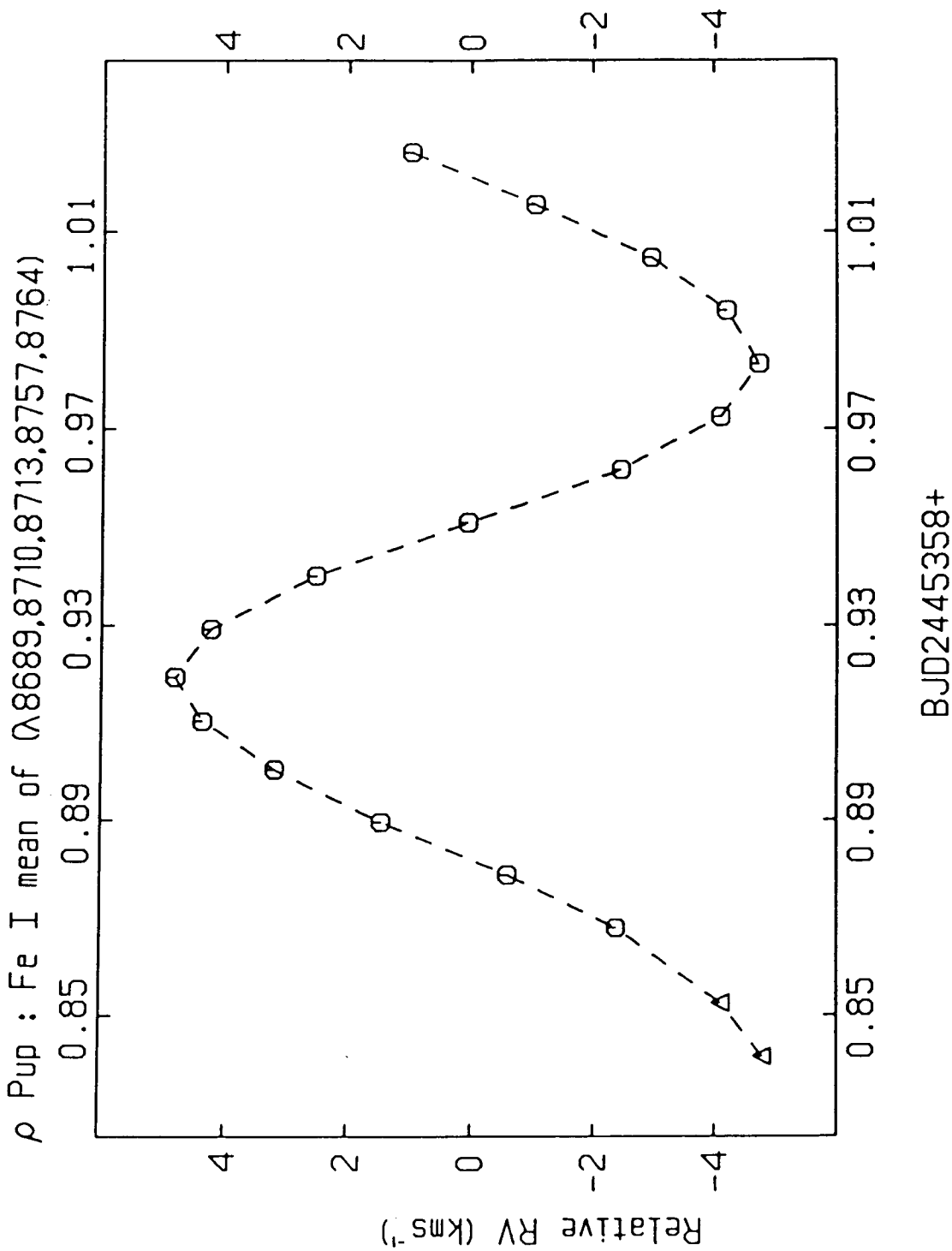

Figure 6.18 The mean optimised Si I velocity curve

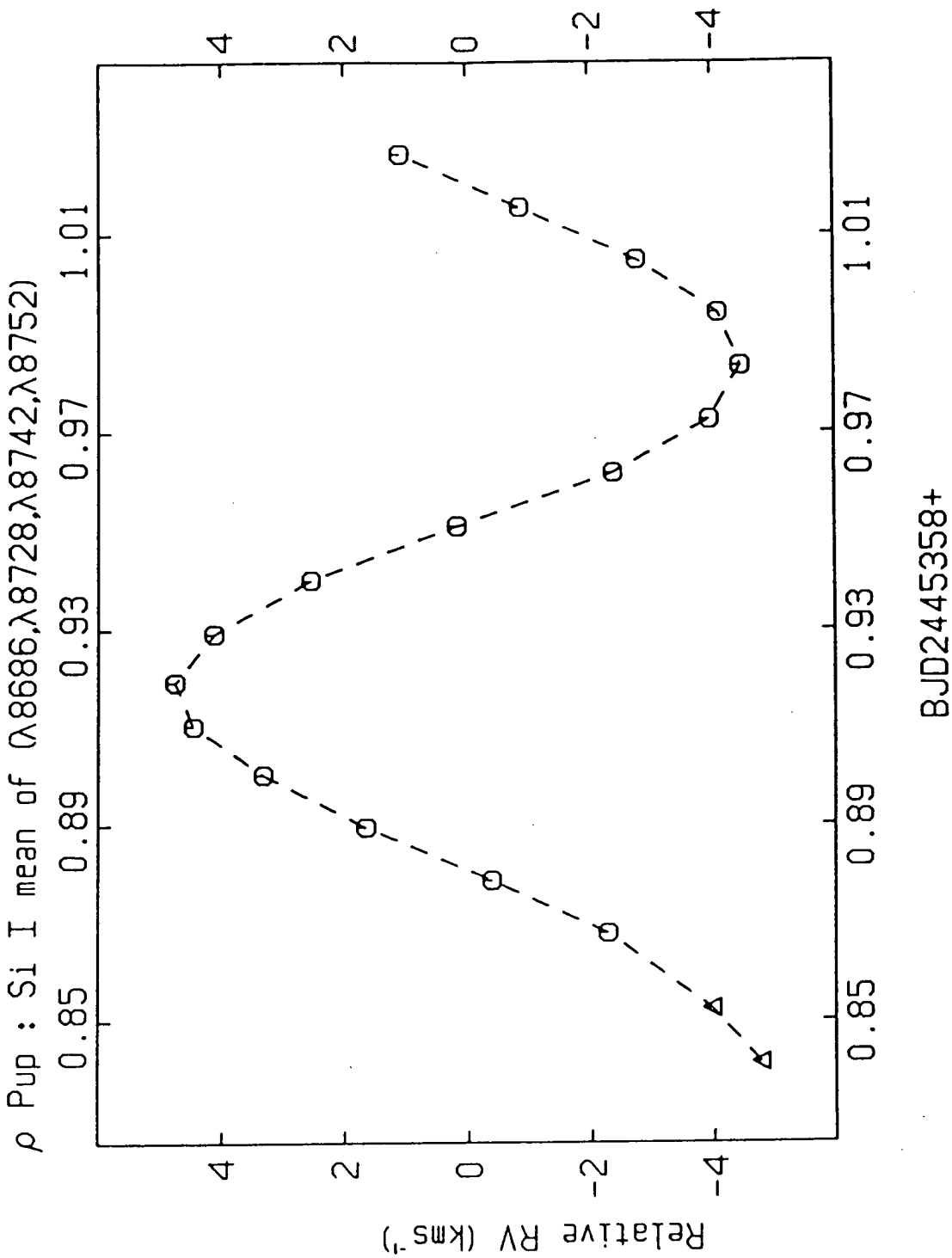

Figure 6.19 The mean optimised S I velocity curve

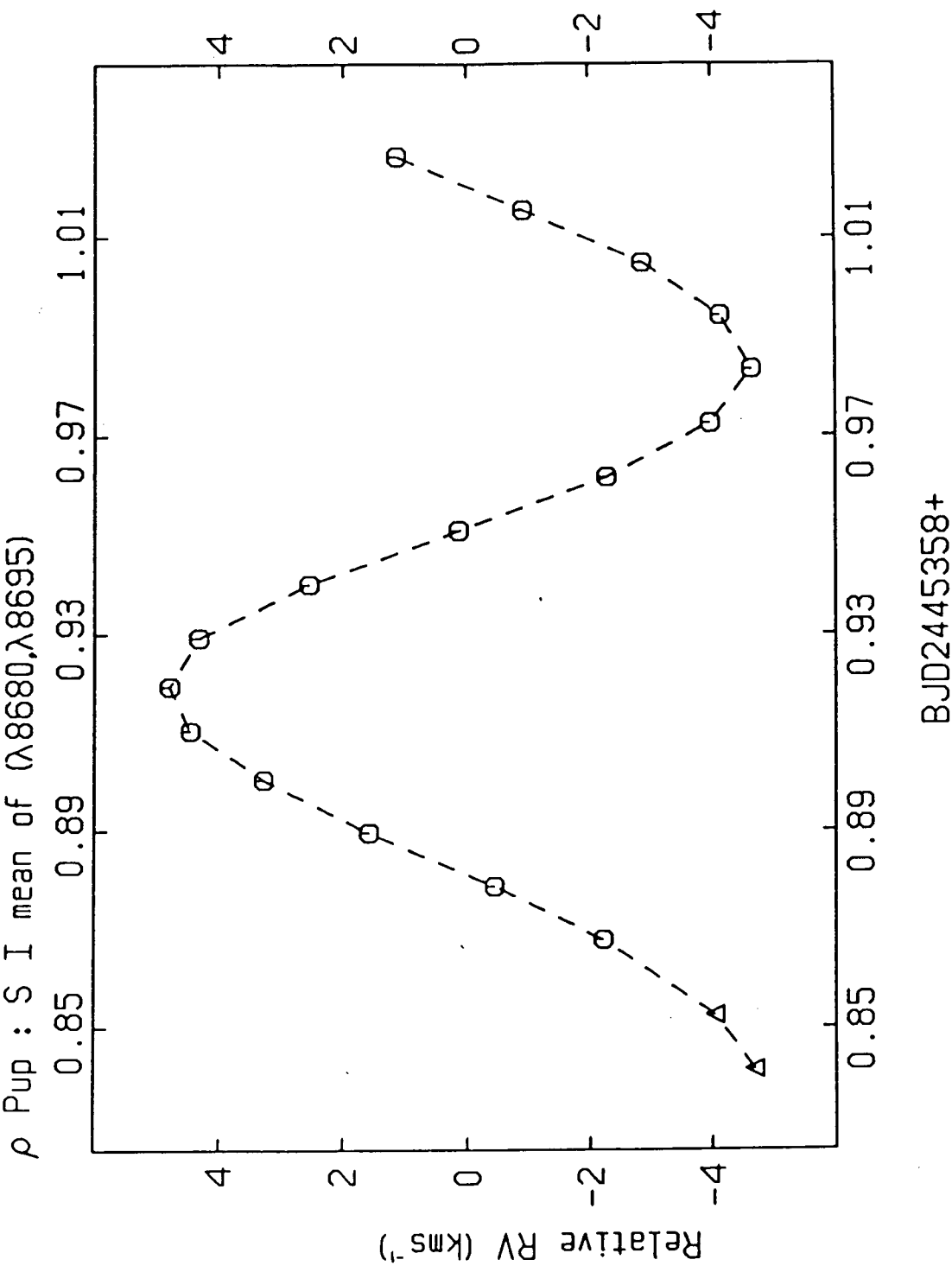

Figure 6.20 The optimised Ca II velocities from the 22nd

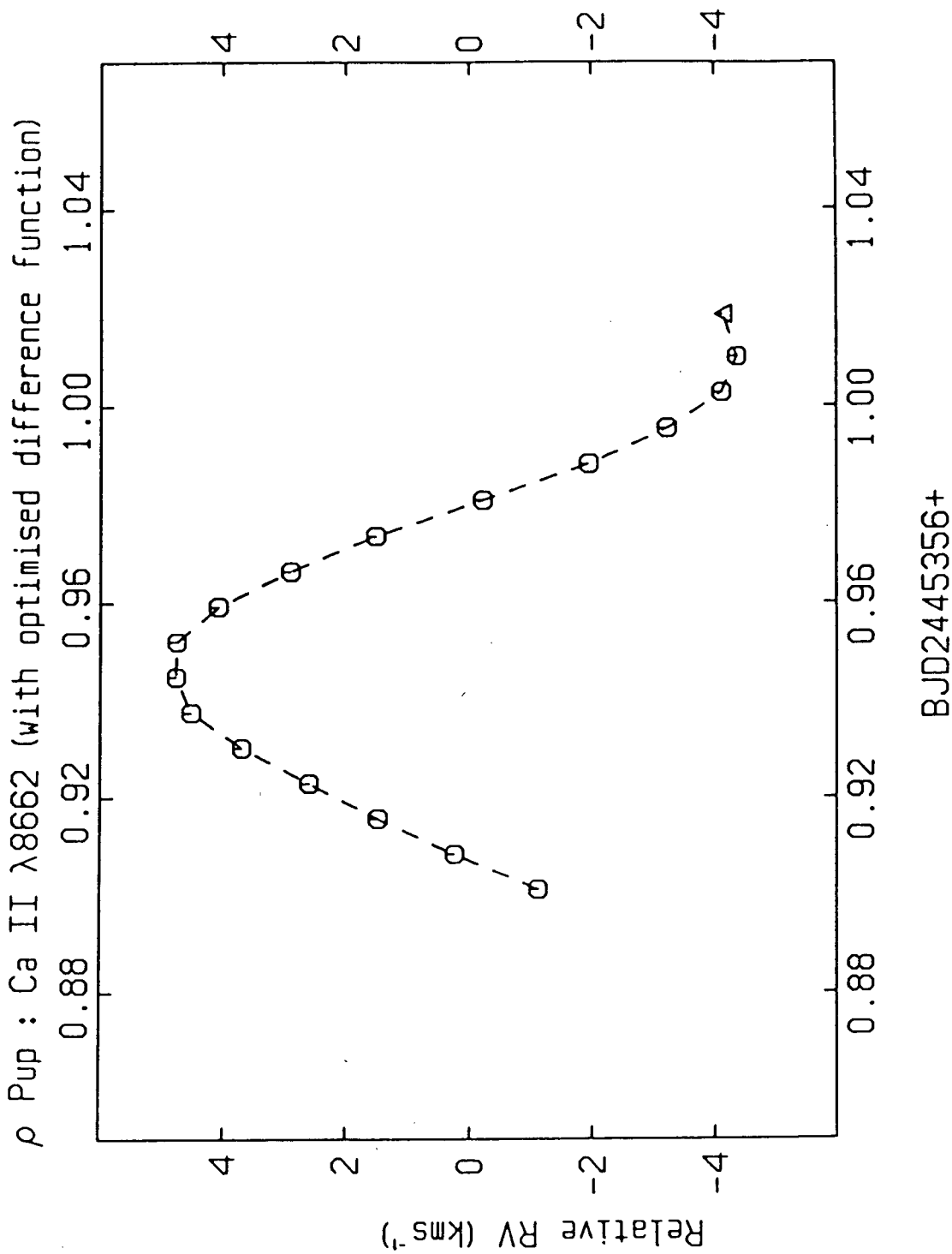

Figure 6.21 The optimised Ca II velocities from the 25th

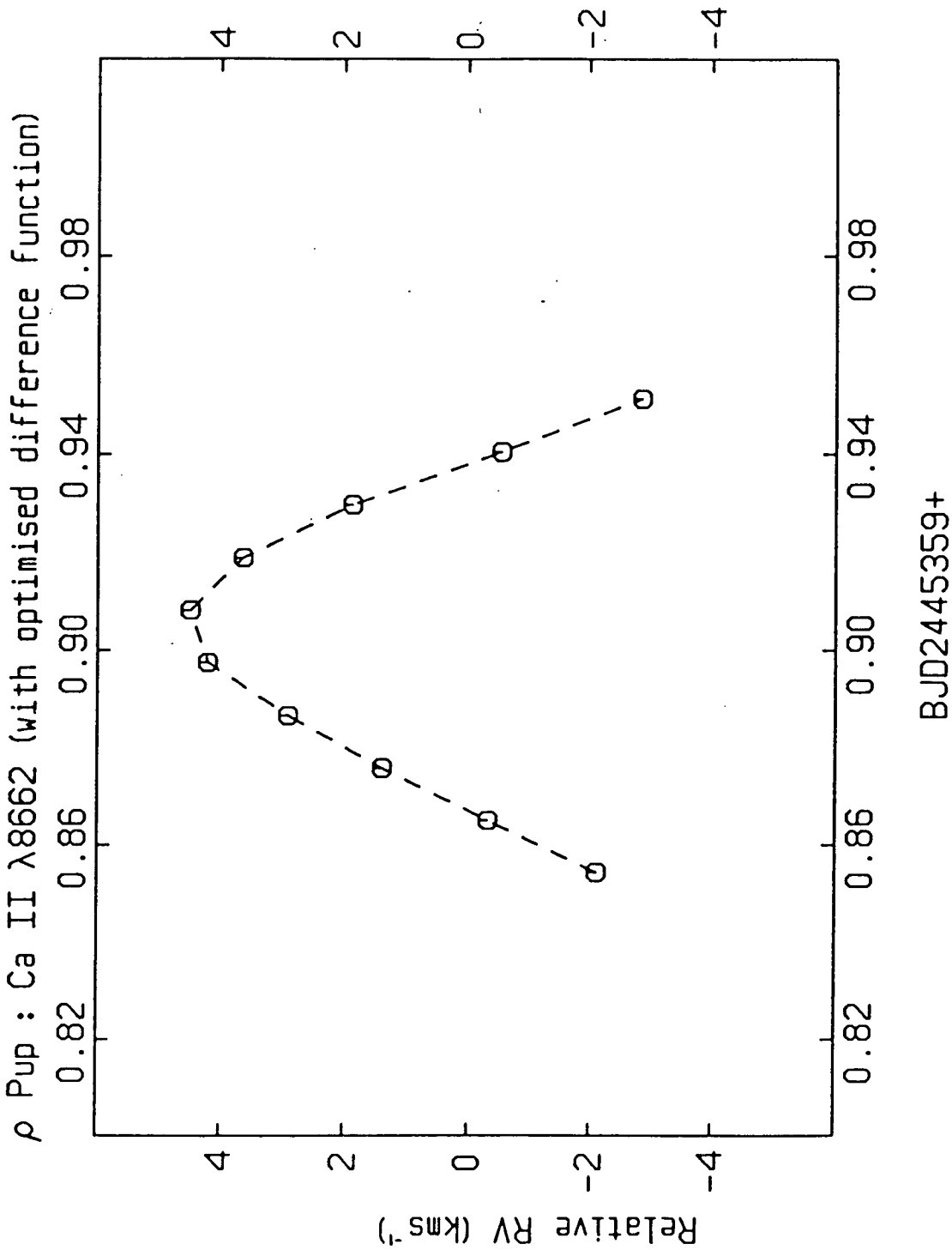

λ8689 lines, respectively. Figures 6.17, 6.18, and 6.19 show the mean velocity curves from the lines of Fe I, Si I, and S I, respectively. Figures 6.20 and 6.21 show the Ca II λ8662 velocity curves from the nights of the 22nd and 25th, respectively. All the velocities from the Ca II λ8662, H I λ8750, Fe I λ8689, and Mg I λ8719 lines are listed in Table 6.3 while all the mean velocities of the Fe I, Si I, and S I lines are listed in Table 6.4. Each mean Fe I velocity was derived from the weighted mean of the λ8689, λ8710, λ8713, λ8757, and λ8764 velocities. The weights have been chosen to be proportional to the square of the mean line depth and inversely proportional to the square of the mean formal error in the line-position measurements. The same weight has also been used for each line over all three nights of data. Similarly, each mean Si I velocity was derived from the weighted mean of the λ8686, λ8728, λ8742, and λ8752 velocities. Meanwhile, each mean S I velocity was derived from the weighted mean of the λ8680 and λ8695 velocities.

The mean error introduced by the uncertainties of the HF line positions was about $30ms^{-1}$ for the data taken on the night of the 24th. Figure 6.22 shows the individual error estimate in the HF dispersion fit. The relative dependence on the s/n has been removed from the plot. The low values shown in Figure 6.22 are the result of the high s/n of the spectra. In spite of this, one can observe that the errors are not random. The errors appear to be periodic with the maximum coinciding with the light minimum of ρ Pup. This effect is most probably caused by the line-intensity

Table 6.3 Relative radial velocities of ρ Pup (I)

#	Ca II λ8662	H I λ8750	Fe I λ8689	Mg I λ8719
1	-1.118 kms^{-1}	+0.106 kms^{-1}	-1.268 kms^{-1}	-0.885 kms^{-1}
2	+0.245 kms^{-1}	+0.014 kms^{-1}	+0.168 kms^{-1}	+0.186 kms^{-1}
3	+1.484 kms^{-1}	+1.710 kms^{-1}	+1.483 kms^{-1}	+1.516 kms^{-1}
4	+2.590 kms^{-1}	+1.973 kms^{-1}	+2.651 kms^{-1}	+2.582 kms^{-1}
5	+3.702 kms^{-1}	+3.425 kms^{-1}	+3.798 kms^{-1}	+3.598 kms^{-1}
6	+4.525 kms^{-1}	+4.806 kms^{-1}	+4.560 kms^{-1}	+4.349 kms^{-1}
7	+4.771 kms^{-1}	+4.100 kms^{-1}	+4.856 kms^{-1}	+4.630 kms^{-1}
8	+4.758 kms^{-1}	+4.151 kms^{-1}	+4.629 kms^{-1}	+4.529 kms^{-1}
9	+4.079 kms^{-1}	+3.323 kms^{-1}	+3.846 kms^{-1}	+3.947 kms^{-1}
10	+2.898 kms^{-1}	+2.256 kms^{-1}	+2.756 kms^{-1}	+2.705 kms^{-1}
11	+1.521 kms^{-1}	+0.136 kms^{-1}	+1.138 kms^{-1}	+0.928 kms^{-1}
12	-0.213 kms^{-1}	-1.060 kms^{-1}	-0.602 kms^{-1}	-0.828 kms^{-1}
13	-1.948 kms^{-1}	-2.650 kms^{-1}	-2.429 kms^{-1}	-2.271 kms^{-1}
14	-3.220 kms^{-1}	-3.179 kms^{-1}	-3.702 kms^{-1}	-3.873 kms^{-1}
15	-4.105 kms^{-1}	-4.193 kms^{-1}	-4.571 kms^{-1}	-4.802 kms^{-1}
16	-4.361 kms^{-1}	-5.561 kms^{-1}	-4.837 kms^{-1}	-4.855 kms^{-1}
17	-4.137 kms^{-1}	-4.270 kms^{-1}	-4.614 kms^{-1}	-4.641 kms^{-1}
18	-4.644 kms^{-1}	-4.308 kms^{-1}	-4.793 kms^{-1}	-4.600 kms^{-1}
19	-4.386 kms^{-1}	-4.386 kms^{-1}	-4.129 kms^{-1}	-4.045 kms^{-1}
20	-2.791 kms^{-1}	-2.791 kms^{-1}	-2.413 kms^{-1}	-2.402 kms^{-1}
21	+0.448 kms^{-1}	+0.448 kms^{-1}	-0.645 kms^{-1}	-0.738 kms^{-1}
22	+1.915 kms^{-1}	+1.915 kms^{-1}	+1.391 kms^{-1}	+1.484 kms^{-1}
23	+2.845 kms^{-1}	+2.845 kms^{-1}	+3.162 kms^{-1}	+3.024 kms^{-1}
24	+4.082 kms^{-1}	+4.082 kms^{-1}	+4.339 kms^{-1}	+4.383 kms^{-1}
25	+4.221 kms^{-1}	+4.221 kms^{-1}	+4.802 kms^{-1}	+4.845 kms^{-1}

26	+3.878 kms^{-1}	+3.878 kms^{-1}	+4.247 kms^{-1}	+4.391 kms^{-1}
27	+2.613 kms^{-1}	+2.613 kms^{-1}	+2.497 kms^{-1}	+2.715 kms^{-1}
28	+0.781 kms^{-1}	+0.781 kms^{-1}	+0.019 kms^{-1}	+0.235 kms^{-1}
29	-1.424 kms^{-1}	-1.424 kms^{-1}	-2.458 kms^{-1}	-2.197 kms^{-1}
30	-3.007 kms^{-1}	-3.007 kms^{-1}	-4.099 kms^{-1}	-3.879 kms^{-1}
31	-3.898 kms^{-1}	-3.898 kms^{-1}	-4.776 kms^{-1}	-4.869 kms^{-1}
32	-3.893 kms^{-1}	-3.893 kms^{-1}	-4.230 kms^{-1}	-4.495 kms^{-1}
33	-2.970 kms^{-1}	-2.970 kms^{-1}	-3.045 kms^{-1}	-3.153 kms^{-1}
34	-1.677 kms^{-1}	-1.677 kms^{-1}	-1.105 kms^{-1}	-1.116 kms^{-1}
35	+0.821 kms^{-1}	+0.821 kms^{-1}	+0.937 kms^{-1}	+0.908 kms^{-1}
36	-2.114 kms^{-1}	-2.616 kms^{-1}	-2.253 kms^{-1}	-1.895 kms^{-1}
37	-0.336 kms^{-1}	+1.087 kms^{-1}	-0.362 kms^{-1}	-0.556 kms^{-1}
38	+1.383 kms^{-1}	+0.057 kms^{-1}	+1.590 kms^{-1}	+1.209 kms^{-1}
39	+2.907 kms^{-1}	+3.627 kms^{-1}	+3.173 kms^{-1}	+3.154 kms^{-1}
40	+4.204 kms^{-1}	+5.117 kms^{-1}	+4.328 kms^{-1}	+4.487 kms^{-1}
41	+4.489 kms^{-1}	+4.478 kms^{-1}	+4.512 kms^{-1}	+4.752 kms^{-1}
42	+3.633 kms^{-1}	+2.262 kms^{-1}	+3.676 kms^{-1}	+3.876 kms^{-1}
43	+1.862 kms^{-1}	+1.544 kms^{-1}	+1.870 kms^{-1}	+2.076 kms^{-1}
44	-0.553 kms^{-1}	+0.930 kms^{-1}	-0.637 kms^{-1}	-0.214 kms^{-1}
45	-2.856 kms^{-1}	-2.930 kms^{-1}	-3.124 kms^{-1}	-2.837 kms^{-1}

****

Table 6.4 Relative radial velocities of ρ Pup (II)

#	mean of Fe I	mean of Si I	mean of S I
1	-1.119 kms^{-1}	-0.855 kms^{-1}	-0.950 kms^{-1}
2	+0.211 kms^{-1}	+0.341 kms^{-1}	+0.462 kms^{-1}
3	+1.508 kms^{-1}	+1.715 kms^{-1}	+1.846 kms^{-1}
4	+2.694 kms^{-1}	+2.956 kms^{-1}	+3.056 kms^{-1}
5	+3.824 kms^{-1}	+3.968 kms^{-1}	+4.007 kms^{-1}
6	+4.600 kms^{-1}	+4.695 kms^{-1}	+4.793 kms^{-1}
7	+4.860 kms^{-1}	+4.976 kms^{-1}	+5.002 kms^{-1}
8	+4.655 kms^{-1}	+4.871 kms^{-1}	+4.767 kms^{-1}
9	+3.866 kms^{-1}	+4.107 kms^{-1}	+4.017 kms^{-1}
10	+2.793 kms^{-1}	+2.713 kms^{-1}	+2.803 kms^{-1}
11	+1.162 kms^{-1}	+1.309 kms^{-1}	+1.244 kms^{-1}
12	-0.571 kms^{-1}	-0.651 kms^{-1}	-0.603 kms^{-1}
13	-2.384 kms^{-1}	-2.234 kms^{-1}	-2.332 kms^{-1}
14	-3.674 kms^{-1}	-3.447 kms^{-1}	-3.663 kms^{-1}
15	-4.526 kms^{-1}	-4.310 kms^{-1}	-4.518 kms^{-1}
16	-4.761 kms^{-1}	-4.629 kms^{-1}	-4.799 kms^{-1}
17	-4.544 kms^{-1}	-4.256 kms^{-1}	-4.629 kms^{-1}
18	-4.772 kms^{-1}	-4.768 kms^{-1}	-4.686 kms^{-1}
19	-4.097 kms^{-1}	-3.964 kms^{-1}	-4.046 kms^{-1}
20	-2.379 kms^{-1}	-2.267 kms^{-1}	-2.211 kms^{-1}
21	-0.592 kms^{-1}	-0.378 kms^{-1}	-0.440 kms^{-1}
22	+1.456 kms^{-1}	+1.652 kms^{-1}	+1.585 kms^{-1}
23	+3.191 kms^{-1}	+3.322 kms^{-1}	+3.283 kms^{-1}
24	+4.362 kms^{-1}	+4.450 kms^{-1}	+4.460 kms^{-1}
25	+4.798 kms^{-1}	+4.746 kms^{-1}	+4.791 kms^{-1}

26	+4.228 kms^{-1}	+4.116 kms^{-1}	+4.319 kms^{-1}
27	+2.519 kms^{-1}	+2.548 kms^{-1}	+2.551 kms^{-1}
28	+0.058 kms^{-1}	+0.176 kms^{-1}	+0.141 kms^{-1}
29	-2.457 kms^{-1}	-2.367 kms^{-1}	-2.277 kms^{-1}
30	-4.094 kms^{-1}	-3.948 kms^{-1}	-3.972 kms^{-1}
31	-4.720 kms^{-1}	-4.464 kms^{-1}	-4.646 kms^{-1}
32	-4.196 kms^{-1}	-4.100 kms^{-1}	-4.138 kms^{-1}
33	-2.964 kms^{-1}	-2.767 kms^{-1}	-2.862 kms^{-1}
34	-1.041 kms^{-1}	-0.875 kms^{-1}	-0.917 kms^{-1}
35	+0.987 kms^{-1}	+1.086 kms^{-1}	+1.146 kms^{-1}
36	-2.220 kms^{-1}	-1.990 kms^{-1}	-1.955 kms^{-1}
37	-0.361 kms^{-1}	-0.178 kms^{-1}	-0.319 kms^{-1}
38	+1.534 kms^{-1}	+1.807 kms^{-1}	+1.639 kms^{-1}
39	+3.155 kms^{-1}	+3.398 kms^{-1}	+3.077 kms^{-1}
40	+4.262 kms^{-1}	+4.439 kms^{-1}	+4.151 kms^{-1}
41	+4.500 kms^{-1}	+4.512 kms^{-1}	+4.393 kms^{-1}
42	+3.689 kms^{-1}	+3.562 kms^{-1}	+3.647 kms^{-1}
43	+1.803 kms^{-1}	+1.887 kms^{-1}	+1.718 kms^{-1}
44	-0.701 kms^{-1}	-0.901 kms^{-1}	-0.895 kms^{-1}
45	-3.136 kms^{-1}	-3.096 kms^{-1}	-3.230 kms^{-1}

****

variations of the stellar lines. Line cancellations by the standard spectrum are imperfect and the resulting residuals would then affect the HF line-position determinations.

A period-searching procedure was applied to the Ca II velocities of all three nights. The Maximum Entropy technique requires evenly spaced data and hence would not be very appropriate for this set of data which spreads over several nights. The period-finding computer program used in this present analysis was initially used by Ninkov [1985] to determine the orbital period of Cygnus X-1. It is based on the algorithm and computer program given by Morbey [1978]. Basically, a number of trial periods are attempted, and in each case, a phase is calculated for each velocity point. The optimum period would the one which gives the best plot of velocity against phase according to some significance criteria. A period of 0.14095^{d} was measured for the Ca II velocities. In view of the short time coverage, this agrees quite well with the period of 0.14088141^{d} given by Ponsen [1963] and the value of 0.14088067^{d} determined by Thulasi Doss [1969].

The Ca II λ8662 velocities have a 2K value of $9.08 kms^{-1}$ while the value for the H I λ8750 velocities is $8.35 kms^{-1}$. The corresponding values for the Fe I, Si I, and S I velocities are 9.46, 9.23, and $9.41 kms^{-1}$, respectively. Meanwhile, the Mg I λ8719 line has a 2K value of $9.64 kms^{-1}$. These are all lower than the values of 11 and $11.5 kms^{-1}$ given by Danzinger and Kuhi [1966] and Campos and Smith [1980], respectively. However, Struve et al [1956] and

Figure 6.22 Errors in the HF dispersion fits

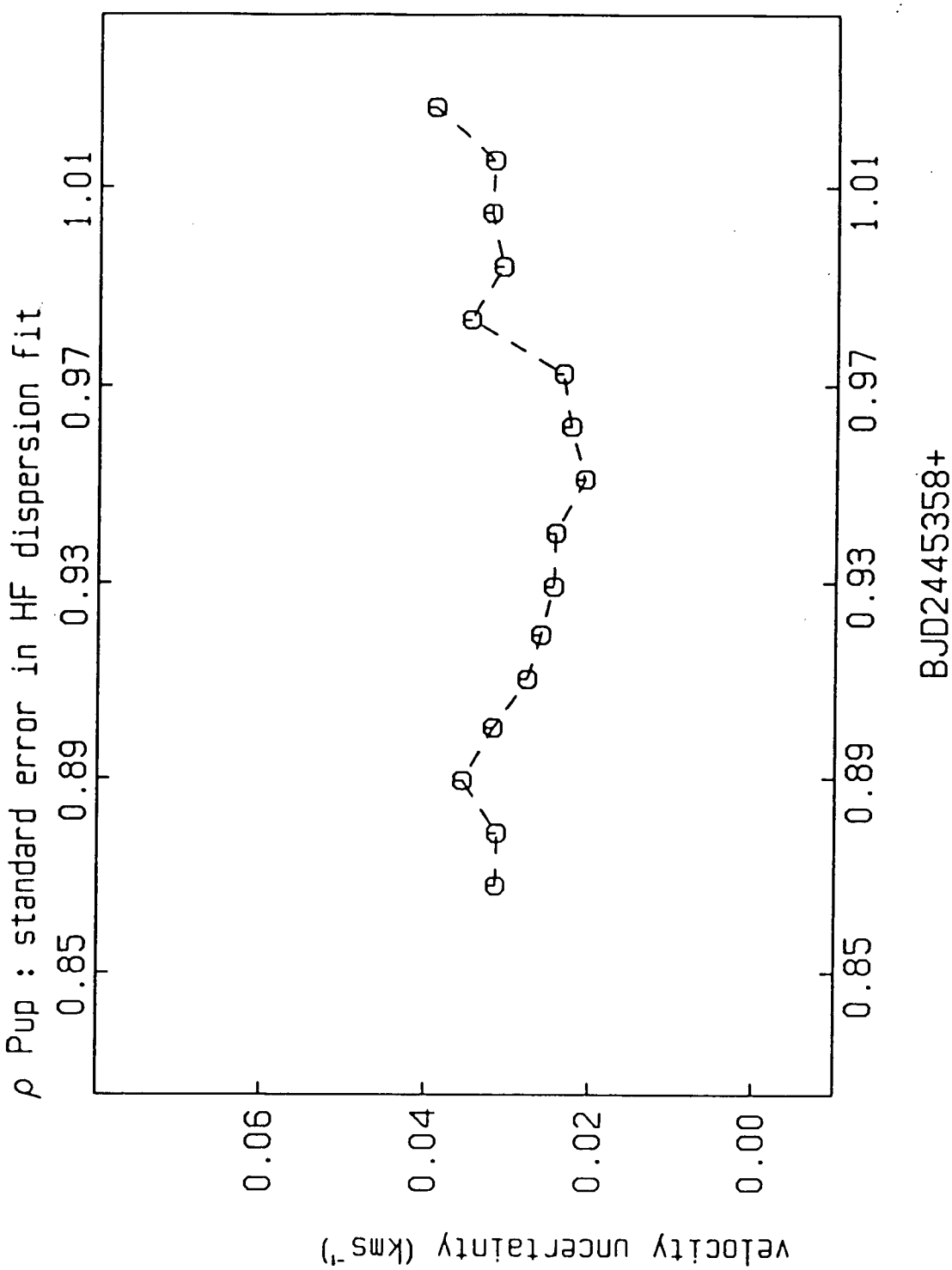

Figure 6.23 Velocity difference (Ca II curve - Fe I curve)

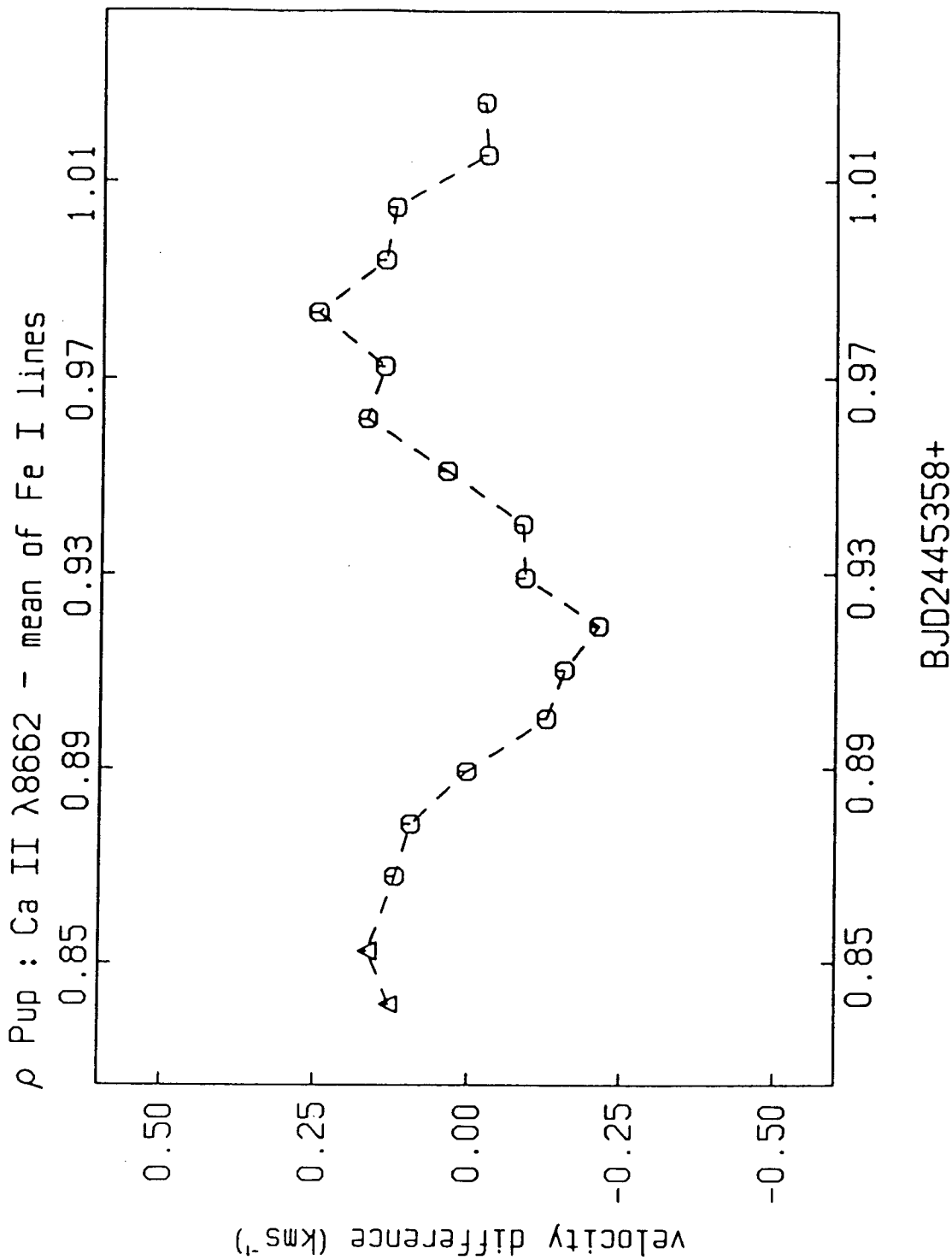

Bessell [1969] have measured the 2K values of 9.7, and 9.5kms^{-1}, respectively. The discrepancy could not have been the effect of phase smearing. The exposure time of each spectrum reported here was only about 6% of the period. Figure 6.23 shows the velocity difference plot between the Ca II and the mean Fe I velocities. The effect of the two different 2K values is very evident in the plot.

In spite of the amplitude differences, the Ca II λ8662 velocities are in phase with the velocity curves of all the other metallic lines. The H I λ8750 velocity curve, however, lags all the other curves by about 0.003^{d} or 2% of the period. This value is obtained by comparing the corresponding velocity minima. However, the H I λ8750 velocity maximum appears to be more in phase with those of the other velocity curves. This may cast doubt on the reality of the observed phase-lag phenomenon. But the observed effect is not the result of a few isolated velocity points. It is a rather large systematic trend of five consecutive velocity points. The H I velocities from the other nights are of poorer quality because of the lower s/n. And they cannot be used to check the reality or the repeatabilty of the observed phenomenon. In any case, the H I curve appears to have a different shape than those of the other lines. The phenomenon of the H I velocity curve lagging behind the other curves is similar to the classical van Hoof effect found in other variable stars. This is discussed further in Chapter eight.

6.7 DISCUSSION

Using the 2K value of the Fe I lines, a value of 93kms^{-1}mag^{-1} is obtained for the $2K/\Delta m_v$ parameter. This would agree with the value of 103±12kms^{-1}mag^{-1} obtained by Smith [1982b]. This rather large value for the $2K/\Delta m_v$ parameter would imply radial pulsation for ρ Pup. The same conclusion was obtained by Campos and Smith [1980] in their analysis of ρ Pup's line profiles.

There is a discrepancy in the published values of the log g parameter. This has been discussed in Kurtz [1976]. Using a mean value of 3.53 for log g and the other parameters from Table 6.1, one can calculate a Q value of 0.03 day for ρ Pup. This value would imply an identification of fundamental radial pulsation for ρ Pup. The values of 0.044 and 0.0395 day quoted by Breger and Bregman [1975] and Tsvetkov [1982b], respectively, were calculated using higher values for log g. Tsvetkov [1982b] who compared the M_{bol} of ρ Pup against theoretical mode-dependent values, has also arrived at the same conclusion of fundamental radial pulsation.

Because of its brightness, sharp lines, and simple variablities, ρ Pup offers a rather unique opportunity to study the δ Scuti pulsation. The high s/n data has enable the identification of a few additional problems associated with the spectroscopic study of δ Scuti stars. Profile variations would impose limitations on the precision attainable in the velocity curve of δ Scuti variables. The profile variations affect both the stellar and HF

line-position determinations. These variations may not only be the result of pulsation-generated surface velocity fields. The temperature variations over the pulsation cycle would also cause line-profile variations and these are in phase with the light curve and not the velocities. These variations can also be very complicated as the reversal at the core of the Fe I λ8689 line has indicated.

Chapter 7

THE DELTA SCUTI VARIABLE o^1 ERI

7.1 INTRODUCTION

The star o^1 Eridani (38 Eri, HR1298) is a broad-line δ Scuti variable. Hoffleit and Jaschek [1982] quote a vsini value of 96kms^{-1} while a value of 98kms^{-1} is given by Baglin et al. [1973]. Parameters for o^1 Eri are summarised in Table 7.1. Other parameters can be found in Tsvetkov [1982b], Halprin and Moon [1983], Breger [1979], Baglin et al. [1972], Gupta [1978], Antonello et al. [1981], Breger and Bregman [1975], and Hoffleit and Jaschek [1982]. Very few studies have been done on o^1 Eri. This star was first reported to be a photometric variable by Jorgensen et al. [1971]. A light amplitude of about 0.02^m was found in the intermediate-band y and b photometry. Jorgensen and Norgaard-Nielsen [1975] reobserved the star with uvby photometry. They found that the light curves cannot be represented by a simple periodic oscillation. The light amplitude is about 0.05^m and the dominant period is determined to be 0.0815^d (1.96 hours). There may be a second period of 0.1291^d. No study of the spectroscopic variations of the star has been reported.

7.2 THE OBSERVATIONS

The star o^1 Eri was observed spectroscopically with the HF absorption cell at the Canada-France-Hawaii 3.6m telescope on the 25th of January 1983 UT. A time series of

Table 7.1 Parameters for o^1 Eri

****

	Reference
HD number : 26574	
SAO number : 131019	
DM number : -7 764	
R.A. (1950) : $4^h\ 9^m\ 25.321^s$	
Dec. (1950) : -6° 57' 59.675"	
Annual parallax : +0.033"	
Proper motion in R.A. : +0.004"/yr	
Proper motion in Dec. : +0.083"/yr	
l_{II} : 199.32°	
b_{II} : -38.39°	
Spectral type : F2 II-III	Breger [1979]
Radial velocity = 11 kms^{-1}	Eggen [1979]
Vsini = 98 kms^{-1}	Baglin et al. [1973]
M_V = +1.85	Eggen [1979]
T_{eff} = 7300K	Breger and Bregman [1975]
log g = 3.9 (cgs)	Breger and Bergman [1975]
Broad band photometry :	Iriate et al. [1965]
V = 4.05^m	
B - V = $+0.33^m$	
U - V = $+0.47^m$	
V - R = $+0.32^m$	
V - I = $+0.48^m$	
Intermediate band photometry :	Eggen [1979]
β = 2.730^m	

$b - y = 0.197^m$

$m_1 = 0.192^m$

$c_1 = 0.789^m$

$\delta m_1 = -0.013^m$

****

spectra were obtained under the same conditions and with the same instrumental setups as for the data on 20 CVn and ρ Pup discussed earlier. Similar observing procedures were used. Stellar and lamp spectra with and without the imposed HF lines were obtained. These are shown in Figure 7.1. The mean stellar+HF spectrum with either the stellar or HF lines numerically removed are also shown. The exposure time for each spectrum was 650 seconds. This corresponds to about one-tenth the "cycle-count" period of 0.0815 day (1.96 hours). Each stellar+HF spectrum has a mean s/n of about 262 in each point at the continuum. The mid-exposure times of the spectra are summarised in Table 7.2. Spectrum #1 and #2 in Table 7.2 are the o^1 Eri spectra without the imposed HF lines. Approximate radial velocities can be measured from these spectra using the dispersion relation determined for spectrum #3. For this set of observations, the heliocentic times lag the barycentric times by about 4.4 seconds.

7.3 THE DATA REDUCTION

The data were processed and reduced using the identical procedure which were applied to the 20 CVn data. In fact, as with the 20 CVn reduction, the mean stellar spectrum of the

Figure 7.1 The o^1 Eri spectrum

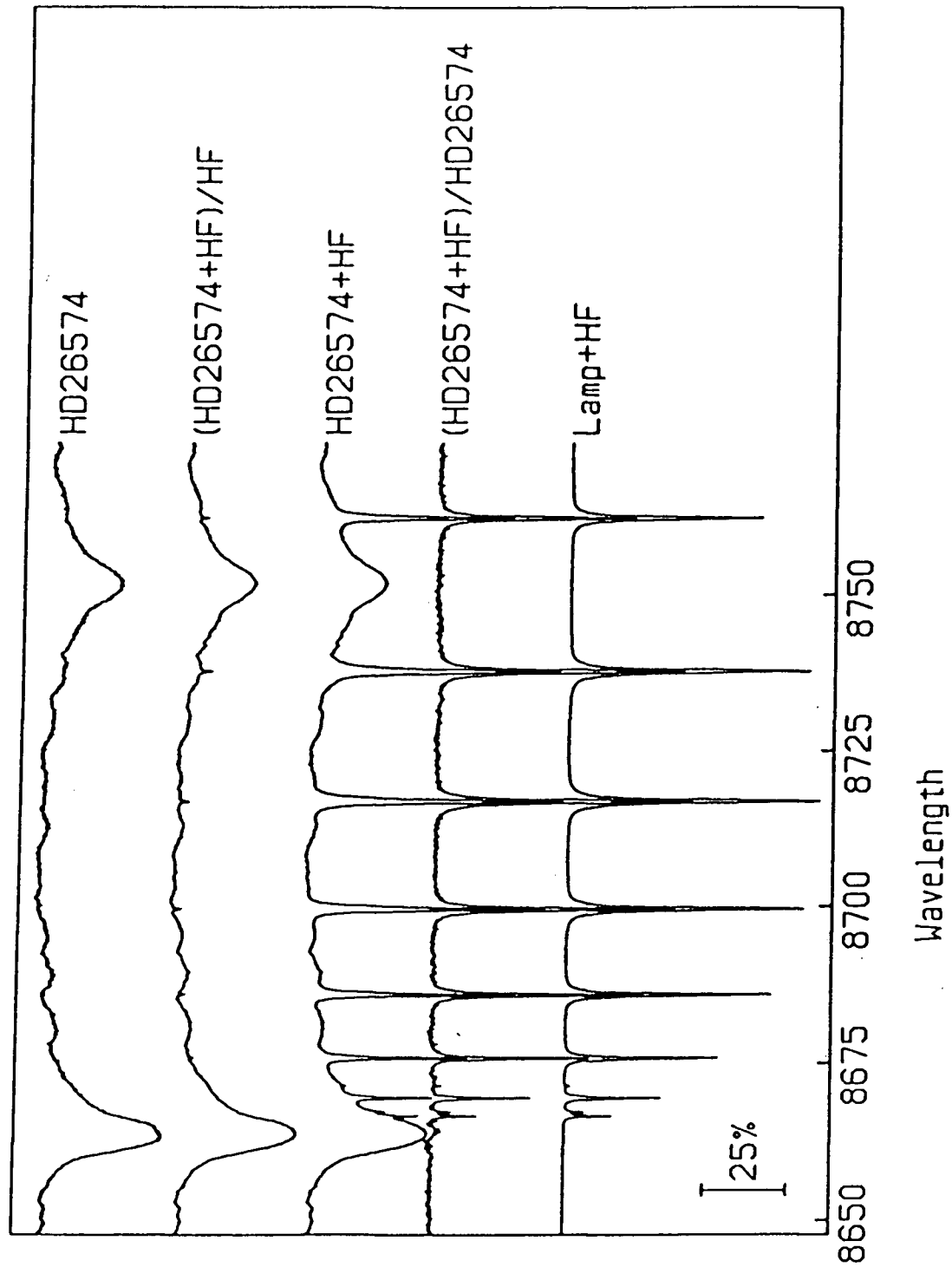

Table 7.2 Mid-exposure times for the o^1 Eri spectra

#	25 Jan 83 UT+	Barycentric JD	hour angle
1	(04:53:26.22)	2445359.7059216	1h 23m 45s East
2	(05:05:05.73)	2445359.7140171	1h 12m 03s East
3	(05:26:11.87)	2445359.7286704	0h 50m 54s East
4	(05:37:27.27)	2445359.7364868	0h 39m 36s East
5	(05:51:37.86)	2445359.7463308	0h 25m 23s East
6	(06:02:55.48)	2445359.7541730	0h 14m 04s East
7	(06:14:11.26)	2445359.7619939	0h 02m 46s East
8	(06:25:26.90)	2445359.7698132	0h 08m 31s West
9	(06:36:42.96)	2445359.7776373	0h 19m 49s West
10	(06:47:59.41)	2445359.7854660	0h 31m 08s West
11	(06:59:17.50)	2445359.7933136	0h 42m 27s West
12	(07:10:33.25)	2445359.8011341	0h 53m 45s West

time series has been chosen to be the radial-velocity standard spectrum. This spectrum has the HF lines numerically removed and it provides both the line-shape and position references in the application of the Fahlman-Glaspey difference technique. In addition to having a higher s/n, the mean spectrum averaged over one cycle will be a more appropriate standard spectrum if there are stellar pulsation related line-profile variations. As in the case of 20 CVn, any line broadening caused by the velocity phase-smearing effect in forming the mean spectrum will be small. It can be corrected in a second iteration of the reduction procedure.

Figure 7.2 The Ca II λ8662 velocity curve of o^1 Eri

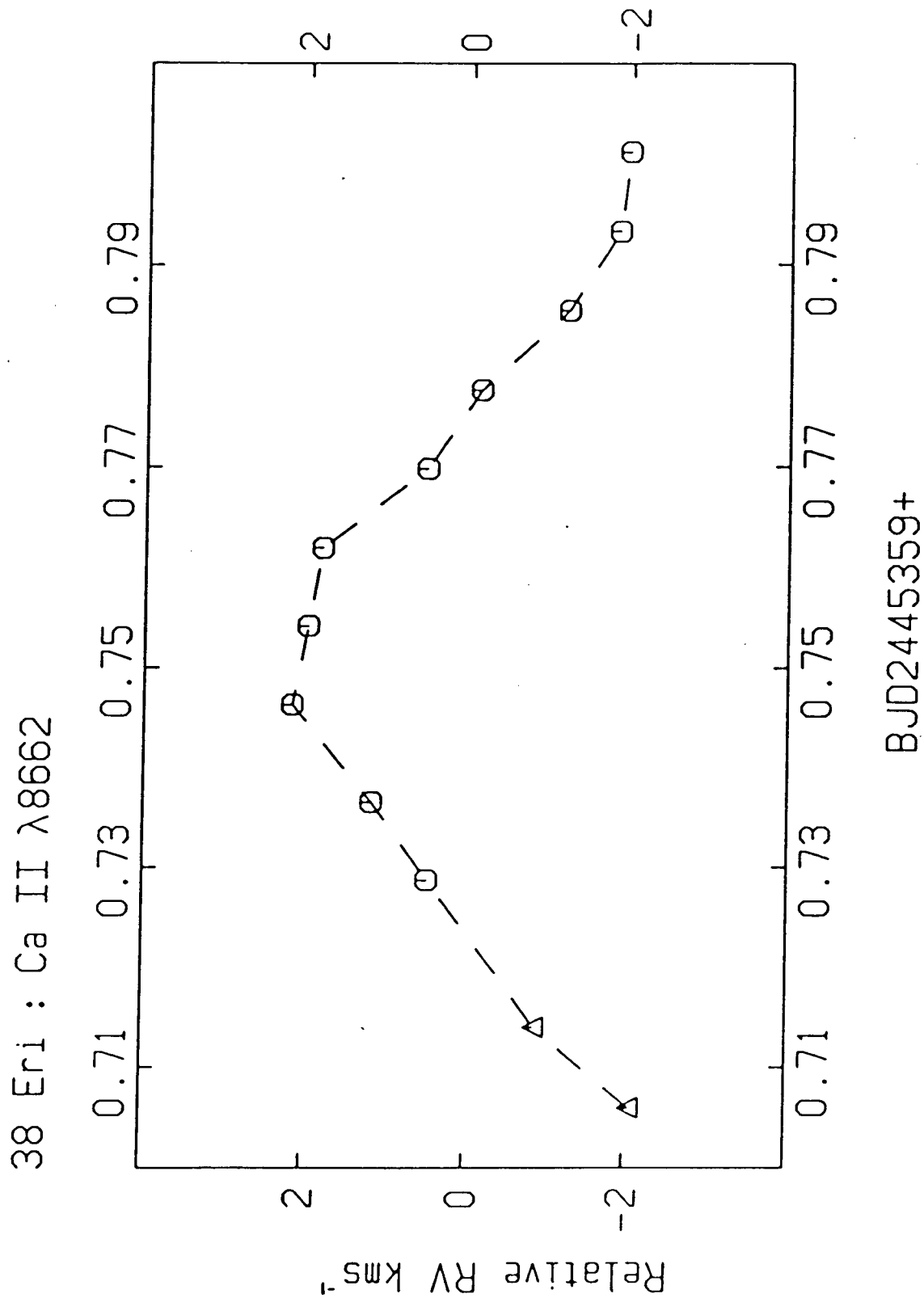

Figure 7.3 The H I λ8750 velocity curve of o^1 Eri

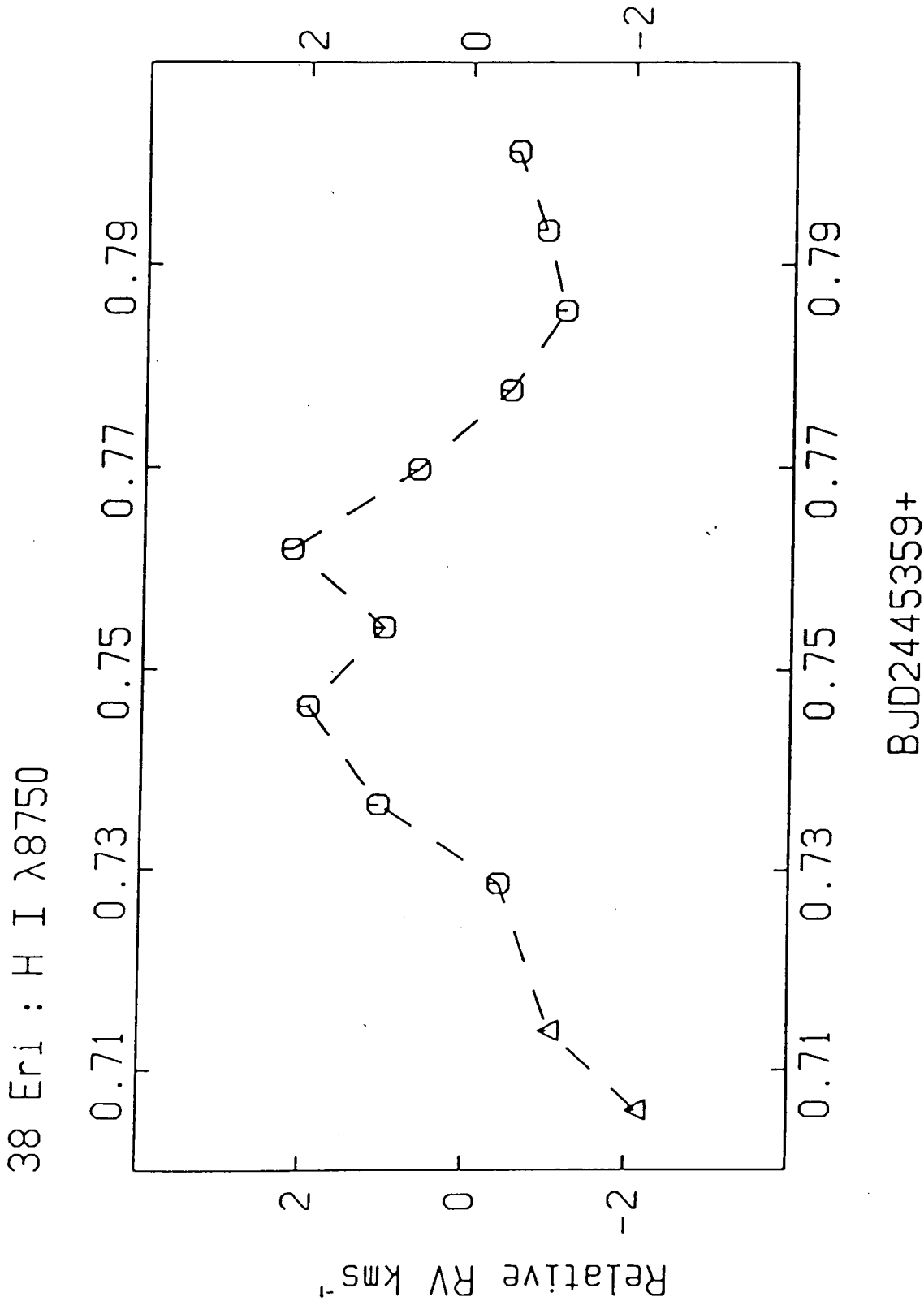

Figure 7.4 The velocity curve of o^1 Eri from weak lines

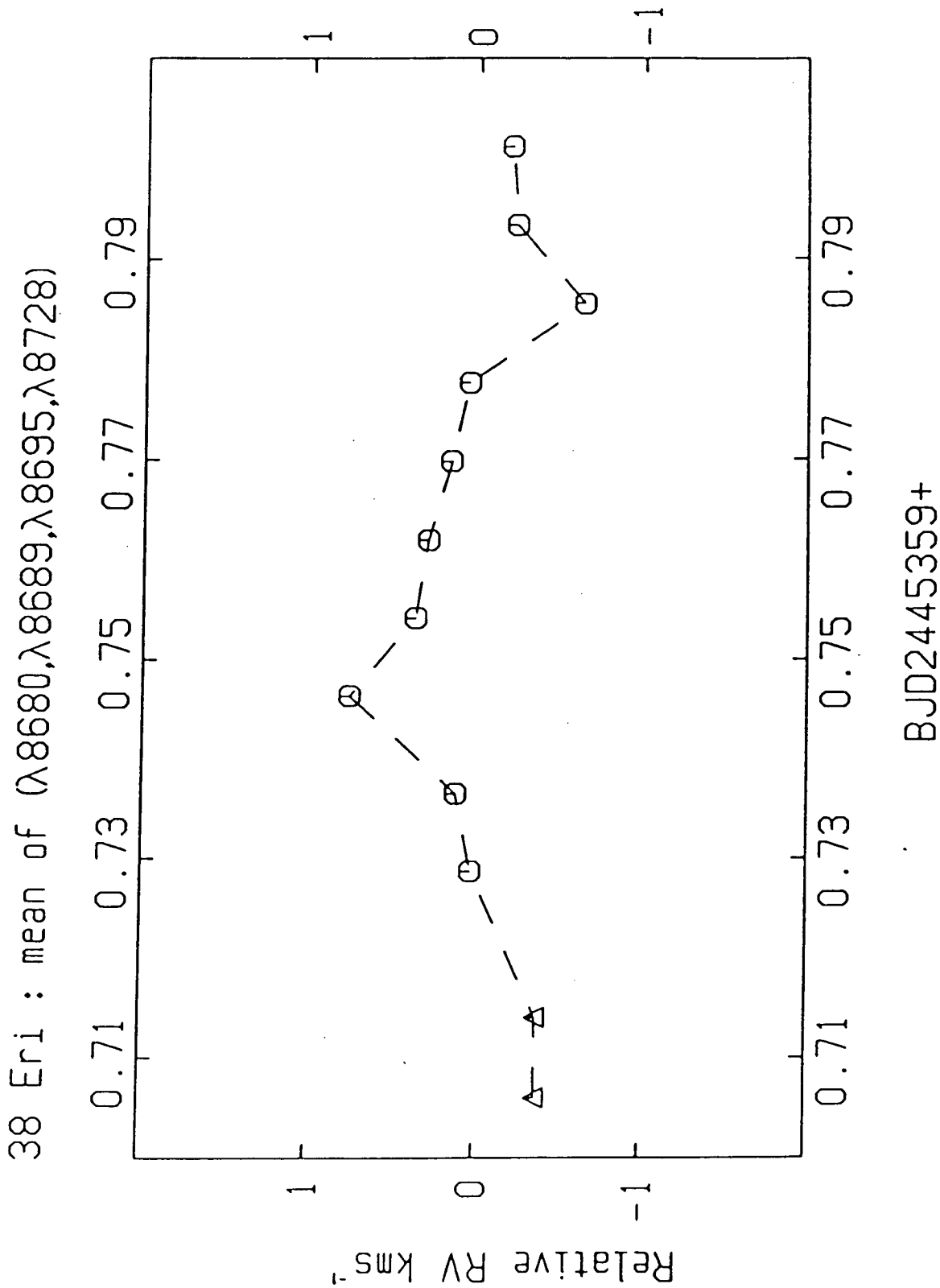

7.4 THE RADIAL VELOCITIES

The same criteria used for the 20 CVn reduction were used here to choose the line limits for both the stellar and HF lines. A typical set of stellar line limits is about 80 pixels in width. The unmodified difference function from Equation 4.4 was used for the stellar lines in the application of the Fahlman-Glaspey technique to measure line shifts. Individual relative radial-velocity curves were obtained for the stellar lines Ca II λ8662 and H I λ8750. These are presented in Figures 7.2 and 7.3, respectively. The s/n of the spectra are too low to lead to reasonable velocity curves for the other weaker stellar lines. In fact, even for the mean velocity curve of the lines S I λ8680, λ8695, Fe I λ8689, and Si I λ8728 given in Figure 7.4, one can barely discern the cyclic variations. This is partially caused by the low 2K velocity amplitudes for these weaker lines. Table 7.3 lists all the velocities shown in Figures 7.2 through 7.4. The mean systemic velocity is $11.947 kms^{-1}$. This has been calculated as the mean velocity of all the lines averaged over the observed cycle. It is approximately equal to the value of $11 kms^{-1}$ quoted by Eggen [1979].

The mean standard error in the HF dispersion fits of the spectra is $\pm 63 ms^{-1}$. This agrees very well with the values from the 20 CVn and ρ Pup data sets which have similar s/n. The Ca II curve in Figure 7.2 has an average one-standard-deviation uncertainty of $\pm 1.34 kms^{-1}$ in each stellar line-position measurement. This is the formal error estimate from the Fahlman-Glaspey technique. The large value

Table 7.3 Relative radial velocities of o^1 Eri

#	Ca II λ8662	H I λ8750	mean weak lines
1	-2.068 kms^{-1}	-2.136 kms^{-1}	-0.369 kms^{-1}
2	-0.855 kms^{-1}	-1.060 kms^{-1}	-0.369 kms^{-1}
3	+0.475 kms^{-1}	-0.434 kms^{-1}	+0.028 kms^{-1}
4	+1.168 kms^{-1}	+1.060 kms^{-1}	+0.123 kms^{-1}
5	+2.162 kms^{-1}	+1.942 kms^{-1}	+0.757 kms^{-1}
6	+1.968 kms^{-1}	+1.015 kms^{-1}	+0.370 kms^{-1}
7	+1.797 kms^{-1}	+2.163 kms^{-1}	+0.298 kms^{-1}
8	+0.517 kms^{-1}	+0.620 kms^{-1}	+0.164 kms^{-1}
9	-0.129 kms^{-1}	-0.504 kms^{-1}	+0.058 kms^{-1}
10	-1.212 kms^{-1}	-1.172 kms^{-1}	-0.638 kms^{-1}
11	-1.849 kms^{-1}	-0.923 kms^{-1}	-0.225 kms^{-1}
12	-1.974 kms^{-1}	-0.571 kms^{-1}	-0.196 kms^{-1}

here may signify the existence of line-profile variations. The corresponding values for the curves in Figures 7.3 and 7.4 are $\pm 1.56 kms^{-1}$ and $\pm 1.79 kms^{-1}$, respectively.

Periodogram and Maximum Likelihood power-spectrum analyses give a mean period of 0.088^d from the Ca II curve in Figure 7.2, or a mean frequency of 11.39 day^{-1}. This is different from the photometric value of 0.0815^d given by Norgaard-Nielsen [1975]. In view of the short duration of the time series here, the discrepancy between the two values may not be significant. The effect of beating by the secondary period may cause an apparently different primary period to be observed over the short time window.

Both the Ca II and H I curves have a 2K amplitude of $4.3 kms^{-1}$. The weak-line curve in Figure 7.4 has a 2K value of $1.2 kms^{-1}$ if one ignores the effect of the velocity points at BJD2445359.746 and BJD2445359.785. The reality of these two velocity points may be somewhat uncertain in view of the rather large error in the velocities. Nevertheless, they may be the genuine effect of line-profile variations. The differences in the amplitudes between the various velocity curves could not have been caused by the uncertainties in the choice of the various line limits. A difference of even several pixels in the line limits is too small to alter the result of such broad lines. Moreover, the error in the choice of the line limits should be small for the mean velocity curve.

The reality of the velocity dip at BJD2445359.754 in the H I curve is more probable. This dip of about $1.1 kms^{-1}$ is a relatively large effect. A much smaller dip may be present in the Ca II curve. A similar type of phenomenon has been reported in the radial-velocity curves of other δ Scuti stars. The "bump" in the radial-velocity curve is generally in the form of a velocity dip near the velocity maximum or a local velocity peak near the velocity minimum. This was first reported in the velocity curve of 14 Aur by Chevalier et al. [1968]. The "bumps" have also been observed in the radial-velocity curves of HR432 and HR515 by Valtier et al. [1979] and in γ Boo by Auvergne et al. [1979]. It has been pointed out by Auvergne et al. [1979] that the velocity bumps are associated with the splitting of the line

profiles. The splitting of the line profile in Cepheids is commonly known as the "Cheshire-Cat" lines phenomenon. The line splitting and the velocity "bumps" have been predicted for Cepheid variables by detailed hydrodynamic models (Karp [1975ab]). The line splitting is caused by the propagation of shock waves in the stellar atmosphere. As the shock wave moves outward in the atmosphere, it will accelerate because of the decreasing density. A temperature rise will result. In the region where the weak lines are formed, the gas requires only a very short time to return to equilibrium. However, in the region higher in the atmosphere where the cores of the strong lines are formed, it would take a much longer time for the gas to return to equilibrium. Within this time, the shock may travel a considerable distance and produce a thick layer of heated gas. Hence, line splitting can be observed when the temperature rise is strong enough at small continuum optical depths. Theoretically predicted velocity "bumps" may be seen in Figure 13 of Karp [1975b]. The theoretical calculations by Karp [1975ab], however, are for a Cepheid with a period of 12 days. No similar calculation has yet been done for the δ Scuti stars. The observed bump is not as pronounced as those observed by Auvergne et al. [1979] in γ Boo. This could be caused by phase-smearing effect in the observed curve.

Figure 7.5 The Ca II λ8662 line profiles

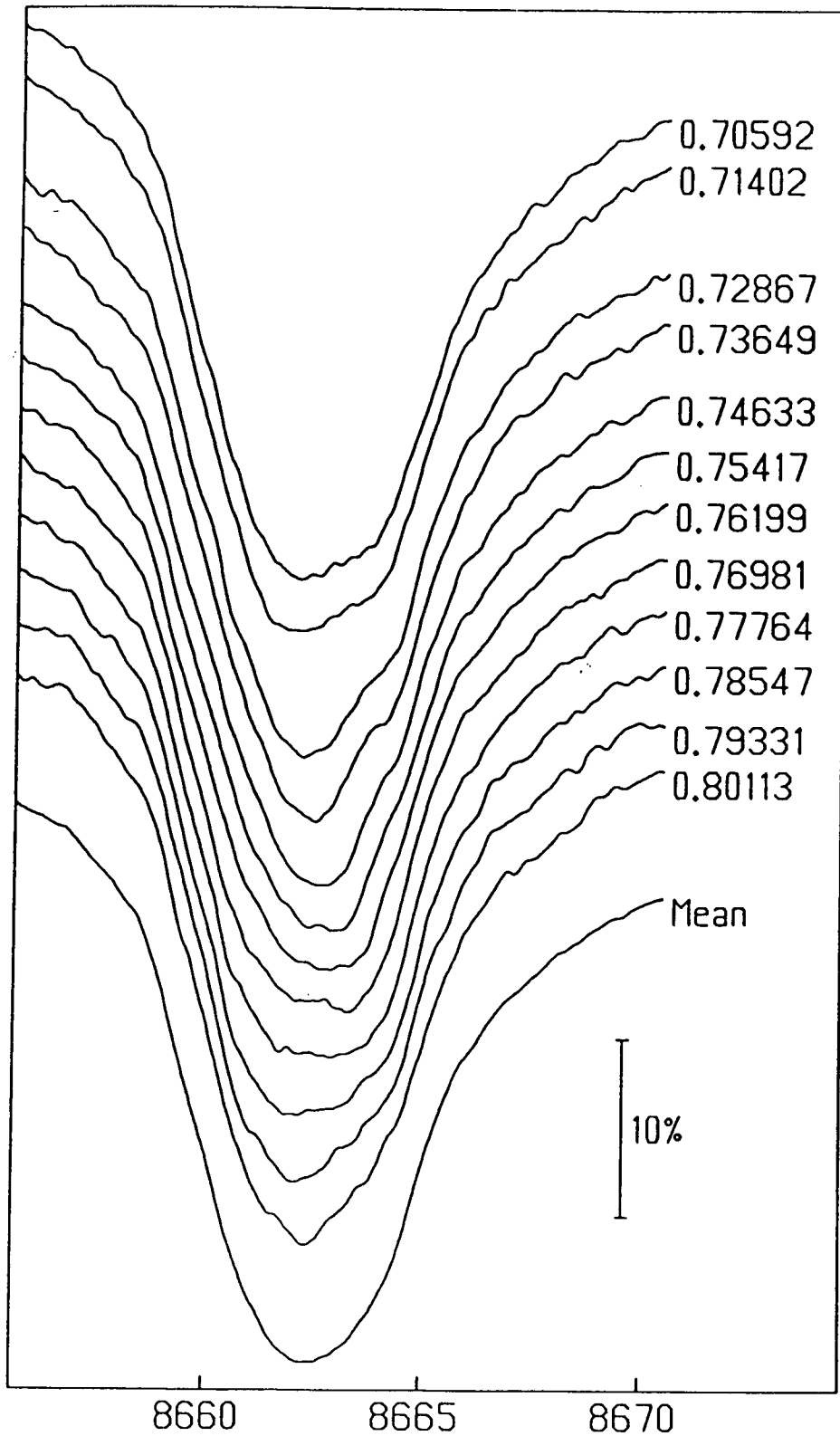

Figure 7.6 The residuals of the Ca II λ8662 line profiles

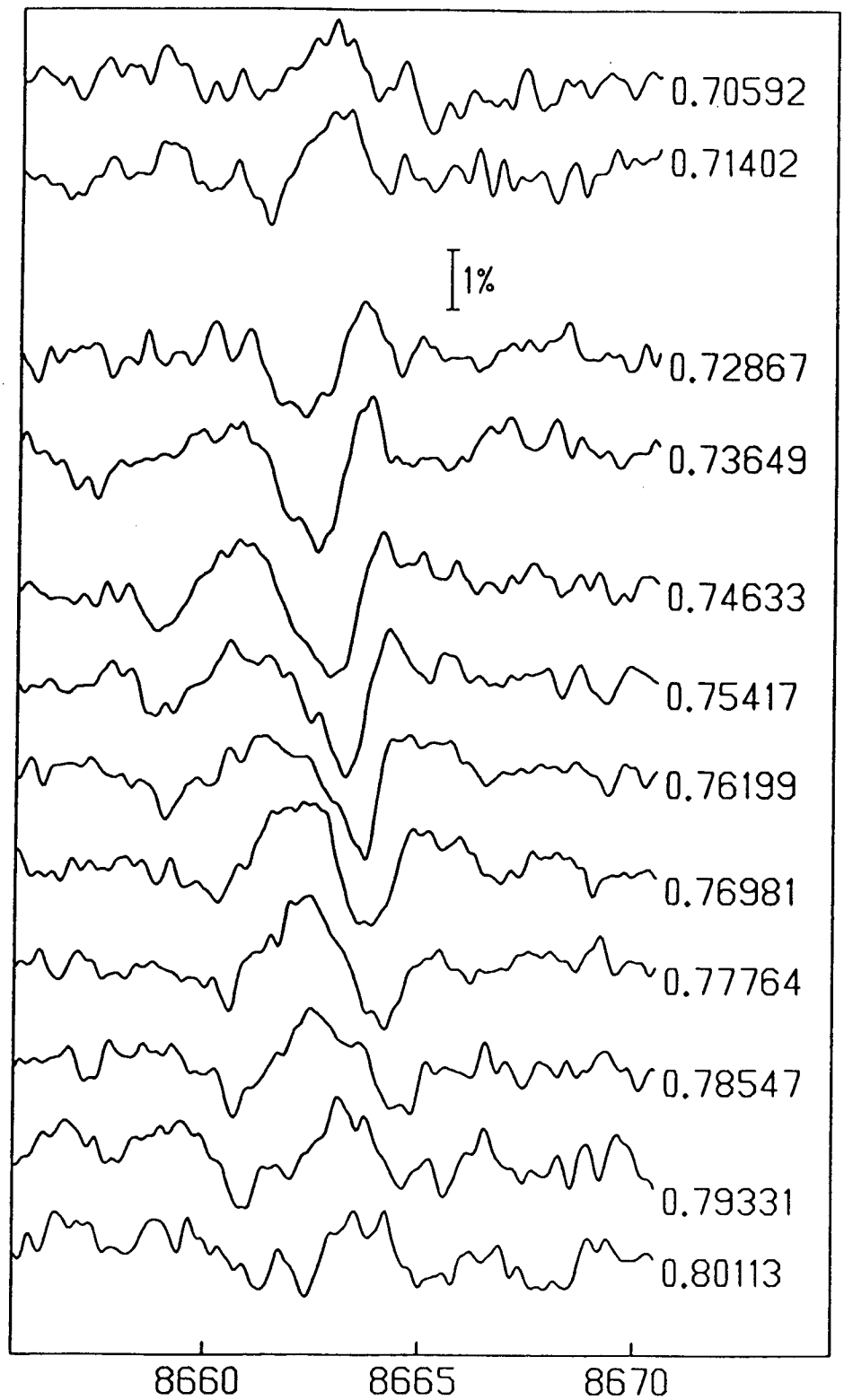

7.5 THE LINE-PROFILE VARIATIONS

Figure 7.5 shows the region of the Ca II line for each spectrum after correcting for the measured velocity shifts. The spectra have been smoothed by a Gaussian transfer function which has a σ of ±0.1Å. The mid-exposure time in fraction of days from BJD2445359 is indicated for each spectrum. Line-profile variations are evident from this "stacked" plot of the spectra. Some of the profiles have flatter line cores than others. Some have symmetric line profiles while others have the profiles skewed towards either the short or the long wavelengths. Figure 7.6 shows the residuals after subtracting a mean line profile from each spectrum. Since the eleven observed spectra cover about one cyclic variation in the radial velocities, the mean spectrum chosen for the subtraction is the average of all the observed spectra. The nature of the line-profile variations is evident in Figure 7.6. The systematic variations are at the level of about 1% to 2% of the continuum. The dominant variations can be characterised as the result of temporal movement of an absorption feature across the line profile. This feature is rather weak in the first two spectra as it has yet to enter the rotationally broadened line core. The feature can best be seen as it moves from the short wavelength side of the line core in spectrum #3 to the long wavelength side of the line core in spectrum #9. The strength of this feature grows as it moves towards the line centre and fades as it moves away from the line centre. It is strongest in spectrum #5. After spectrum

#9, the feature fades as it moves off the line core. One can also see another feature starting to enter the line core as the first feature was moving off the line core. The feature shown in the "stacked" residual plot is not the true representation of the profile variations. Because of the short time series, the feature would also contribute significantly towards the mean spectrum that was used for the subtraction. Hence the shapes and positions of the feature shown in Figure 7.6 can not be interpreted as identical to those of the true variations. A better representative of the line profile without the imposed variations would be a mean spectrum averaged over several cycles.

The type of line-profile variations exhibited by o^1 Eri is very similar to those found in the Oe star ζ Oph (Walker et al. [1979,1981b], Ninkov et al. [1983], Vogt and Penrod [1983]) and the β Cephei star α Vir (Walker et al. [1981a,1982], Fraser et al. [1983], Smith [1985]). The profile variations in these stars are generally considered to be caused by nonradial pulsations. Hence the profile variations observed in o^1 Eri strongly suggests the presence of nonradial pulsation modes in the star. One of the usual ways to identify the pulsation mode for a set of data such as this is to fit the observed profiles and their residuals to theoretically generated counterparts. The rather short time series and the small number of spectra available here, however, imply that a unique mode identification may be difficult if not impossible. The large number of parameters

necessary in the fit would enable a variety of modes or combination of modes to fit the small data set, all equally as well. In any case, mode identification by line profiles alone is treacherous (Smith [1981]). This conclusion does not even take into account any doubt about the appropriateness and correctness of the model.

7.6 DISCUSSION

With some simple assumptions, one can make a guess at the pulsation mode suggested by the observed variations. This is accomplished by interpreting the observed feature in Figure 7.6 to be caused by a pole-to-pole azimuthal strip of a nonradially travelling pressure wave on the stellar surface. If this is the case, then one can reason that since at most two such features are visible in the profile at any one time, there are probably at most three or four such travelling waves on the stellar surface. This would imply l=3 or 4. Of course, l could also be 2 or 1. This depends on the reality of the weaker second feature or any unseen third or fourth feature. A variety of assumptions have to be made in order to allow this interpretation of the observed profile variations. The first assumption is that the observed variations are caused by a single nonradial mode. Moreover, there has to be a large inclination angle between the star's rotation axis and the line of sight i.e $i \simeq 90°$. Tesseral modes are also assumed to be unimportant i.e. $l = |m|$. Some of these assumptions are quite realistic. Tesseral modes and low i values would cause only small line-profile

distortions (Smith [1981]). This is not the case here.

The pulsation constant Q was calculated to be 0.025 day by Breger and Bregman [1975] using the parameters in Table 7.1. From this value, they identified the dominant pulsation mode in o^1 Eri to be the first overtone radial pulsation. Tsvetkov [1982b] obtained a Q value of 0.0241 day. And he identified the pulsation mode to be the first overtone radial pulsation. This identification was only partially based on the Q value. Tsvetkov [1982b] also compared the observed M_{bol} value against the theoretical mode dependent values. The first overtone radial pulsation provided the best agreement. Using the 2K value of $4.3 kms^{-1}$ observed here for the Ca II and H I lines, one obtains a value of $86 kms^{-1}mag^{-1}$ for the $2K/\Delta m_v$ parameter. Using the criterion given by Smith [1982b], this large value would suggest radial pulsation for the star. However, if one uses the 2K value of the Fe I lines in the calculation, as is the case in Smith [1982b], the value for $2K/\Delta m_v$ becomes $26 kms^{-1}mag^{-1}$. This low value implies nonradial pulsation for the star.

The present data set is too limited to provide a concrete conclusion on the nature of o^1 Eri's pulsation. A more extensive data set is required for that purpose. A much longer time series with shorter exposure times and higher s/n would be desirable. This can still be accomplished at CFHT. The sky condition was rather poor at the time this data set was taken. As with the other observations reported earlier, there was a strong 60-knot wind coupled with poor seeing. Furthermore, the readout noise of the Reticon at CFH

has since been reduced. An improved through-put for the CFH red Coudé train has also been realised.

Chapter 8

THE DELTA SCUTI VARIABLE β CAS

8.1 INTRODUCTION

The star β Cassiopeiae (HR21, ADS 107A) is a broad-line δ Scuti variable. Baglin et al. [1972] give it a vsini value of 72kms^{-1} while Abt [1965] and Hoffleit and Jaschek [1982] quote a value of 70kms^{-1}. Parameters for β Cas are summarised in Table 8.1. Additional parameters are summarised in Tsvetkov [1982b], Gupta [1978], Halprin and Moon [1983], Breger [1979], Leung [1970], Baglin et al. [1972], Breger and Bregman [1975], and Hoffleit and Jaschek [1982]. In spite of its brightness, very few studies have been done on β Cas. It was first reported to be a photometric variable by Millis [1966]. The photometric observations indicated a period of 0.104 day and a V amplitude of 0.04 magnitude. Meanwhile, Hoffleit and Jaschek [1982] have quoted a period of 0.10430 day and a V amplitude of 0.06 magnitude for β Cas. Mellor [1917] has suggested a 27 days period for the variability of β Cas's radial velocity. This was based on a scatter of ±2.12kms^{-1} in the star's radial velocity. A review of the early radial-velocity measurements on β Cas has been given by Abt [1965] who also has monitored the star's radial velocity. Abt [1965] concluded that there is no evidence in the radial velocities to indicate any binary motion for β Cas. The much fainter optical companion at 22" away is probably independent. The velocity scatter may have been caused by

Table 8.1 Parameters for β Cas

****

	Reference
HD number : 432	
SAO number : 21133	
DM number : +58 3	
R.A. (1950) : $0^h\ 6^m\ 29.742^s$	
Dec. (1950) : 58° 52' 26.497"	
Annual parallax : +0.072"	
Proper motion in R.A. : +0.526"/yr	
Proper motion in Dec. : -0.177"/yr	
l_{II} : 117.52°	
b_{II} : -3.27°	
Spectral type : F2 III-IV	Morgan and Abt [1972]
Radial velocity = 11.8 kms^{-1}	Eggen [1979]
Vsini = 72 kms^{-1}	Baglin et al. [1973]
M_V = +1.35	Eggen [1979]
T_{eff} = 7100K	Breger and Bregman [1975]
log g = 3.7 (cgs)	Breger and Bergman [1975]
Broad band photometry :	Iriate et al. [1965]
V = 2.28^m	
B - V = $+0.34^m$	
U - V = $+0.45^m$	
V - R = $+0.31^m$	
V - I = $+0.52^m$	
Intermediate band photometry :	Eggen [1979]
β = 2.709^m	

$b - y = 0.216^m$

$m_1 = 0.177^m$

$c_1 = 0.785^m$

$\delta m_1 = -0.003^m$

****

irregular variability typical for an early F star.

8.2 THE OBSERVATIONS

The star β Cas was observed spectroscopically with the HF absorption cell at the Canada-France-Hawaii 3.6m telescope on the 21st of October 1980 UT. This set of data was among the first observations made with three instruments of the observatory. These are the four-grating-mosaic F/7.4 Coudé spectrograph, the UBC-built CFHT 1872-Reticon, and the CFHT HF-absorption-cell system. Only aluminum Coudé mirrors were available at the time. Hence the transmission efficiency of the Coudé train at λ8700 was only about 20% of what it could have been. Nevertheless, the time series of spectra were obtained under essentially similar conditions and instrumental setup as the earlier discussed data set on o^1 Eri. Similar observing procedure were also used. Stellar and lamp spectra with and without the imposed HF lines were obtained. These are shown in Figure 8.1. The mean stellar+HF spectrum with either the stellar or HF lines numerically removed are also shown.

The exposure time for each spectrum was 850 seconds. This corresponds to about one-tenth the "cycle-count" period

Figure 8.1 The β Cas spectrum

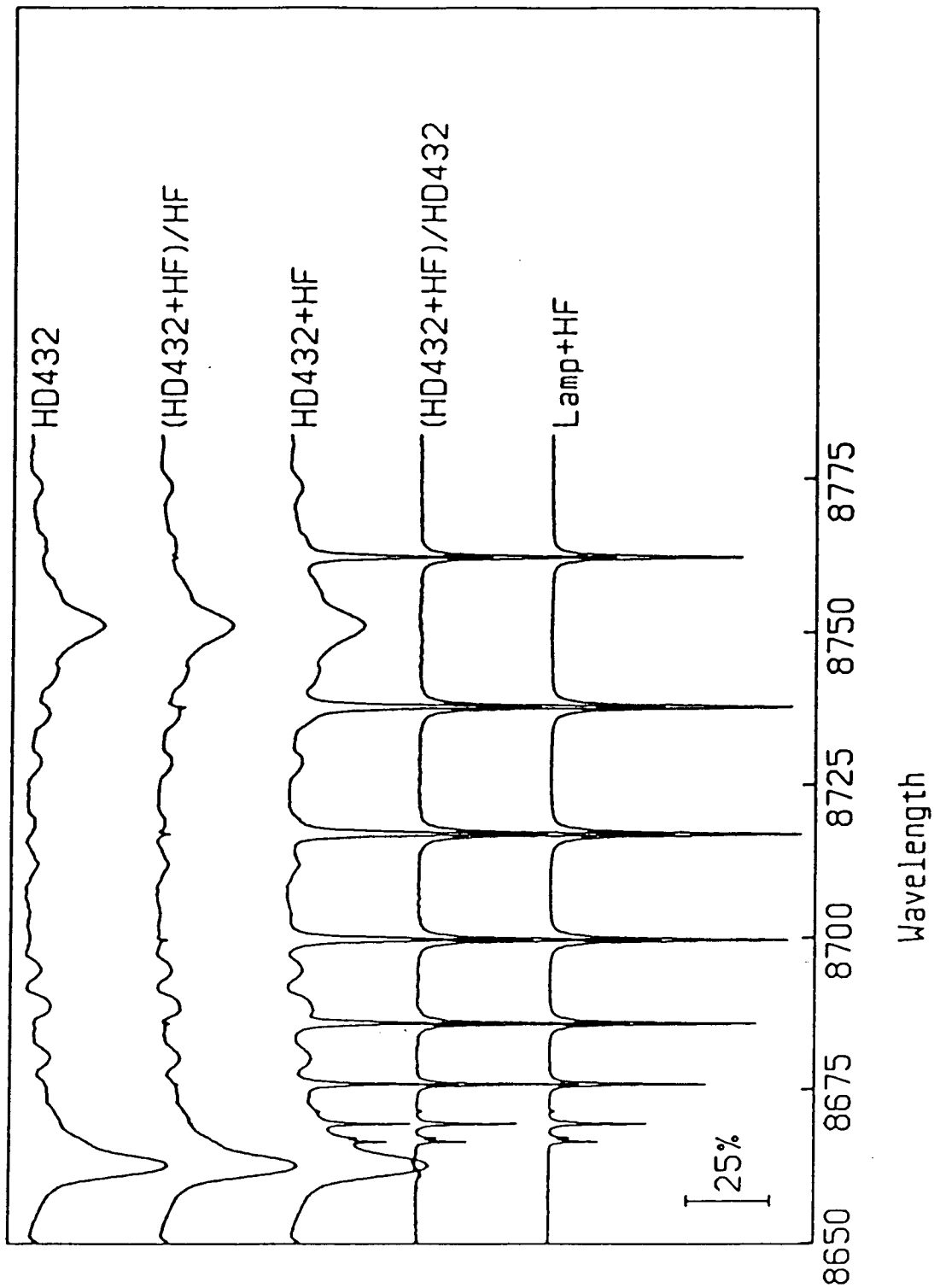

of 0.104 day (2.5 hours). The twenty spectra in the time series covered about two "cycle-count" periods. Each stellar+HF spectrum has a mean s/n of about 344 in each point at the continuum. The mid-exposure times of the spectra are summarised in Table 8.2. Spectrum #1, #13, and #19 are the β Cas spectra without the imposed HF lines. Approximate radial velocities can be measured from these spectra using the dispersion relations determined for the other spectra. For this set of data, the heliocentric times lag the barycentric times by about 2.4 seconds.

8.3 THE DATA REDUCTION

The data were processed and reduced using procedures which were similar to those applied to the o^1 Eri data. The only differences between the two data reductions include the fact that step-lamp spectra were not available for the β Cas data. Hence, the gain correction in this case relies upon the multiplicative four-line normalisation procedure. After flat-fielding by the lamp spectrum, an eight-line additive normalisation process was used to remove an eight-line pattern. This pattern was probably caused by a less than ideal match in the Reticon's response between the stellar and lamp spectra. There is a rather significant difference in the signal level between the lamp and stellar spectra. Moreover, they were taken at different times during the observing night. The eight-line normalisation was not necessary for the lamp+HF spectra. All other data processing and reduction procedure were identical between the o^1 Eri

Table 8.2 Mid-exposure times for the β Cas spectra

#	21 Oct 80 UT+	Barycentric JD	hour angle
1	(05:43:45)	2444533.7423178	2h 47m 00s East
2	(06:24:00)	2444533.7702693	2h 06m 38s East
3	(06:39:55)	2444533.7813227	1h 50m 41s East
4	(06:55:20)	2444533.7920287	1h 35m 13s East
5	(07:10:45)	2444533.8027348	1h 19m 46s East
6	(07:26:05)	2444533.8133830	1h 04m 23s East
7	(07:41:30)	2444533.8240891	0h 48m 56s East
8	(07:56:55)	2444533.8347952	0h 33m 28s East
9	(08:12:20)	2444533.8455013	0h 18m 00s East
10	(08:27:45)	2444533.8562074	0h 02m 33s East
11	(08:43:15)	2444533.8669714	0h 13m 00s West
12	(08:58:40)	2444533.8776774	0h 36m 38s West
13	(09:15:30)	2444533.8893673	0h 45m 20s West
14	(09:33:30)	2444533.9018674	1h 03m 23s West
15	(09:48:55)	2444533.9125735	1h 18m 50s West
16	(10:04:20)	2444533.9232796	1h 34m 18s West
17	(10:19:45)	2444533.9339857	1h 49m 45s West
18	(10:35:10)	2444533.9446917	2h 05m 13s West
19	(10:51:56)	2444533.9563353	2h 22m 02s West
20	(11:11:10)	2444533.9696919	2h 41m 19s West

and β Cas data set. In fact, identical to the o^1 Eri reduction, the mean stellar spectrum of the time series has been chosen to be the radial-velocity standard spectrum. This spectrum has the HF lines numerically removed and would provide both the line-shape and position references in the application of the Fahlman-Glaspey technique. In addition to having a higher s/n, the mean spectrum averaged over two cycles would be a more appropriate standard spectrum if there are stellar pulsation related line-profile variations.

8.4 THE RADIAL VELOCITIES

The same criteria which were used for the o^1 Eri reduction were again used here to choose the line limits for both the stellar and HF lines. A typical set of stellar line limits is about 50 pixels in width. The unmodified difference function from Equation 4.4 was again used in the application of the Fahlman-Glaspey technique to measure relative stellar line shifts. Individual relative radial-velocity curves were obtained for the stellar lines Ca II λ8662, H I λ8750, Fe I λ8689, S I λ8680, λ8695, and Si I λ8728, λ8742. Figures 8.2, 8.3, and 8.4 show the relative radial-velocity curve for the Ca II, H I, and Fe I lines, respectively. As in the case with the o^1 Eri data set, a mean velocity curve was formed from those of the weaker lines i.e. all lines except the Ca II and H I lines. This mean curve is shown in Figure 8.5. Table 8.3 lists all the velocities shown in Figures 8.2 through 8.5. The mean systemic velocity of β Cas is 11.9kms^{-1}. This was calculated

Figure 8.2 The Ca II λ8662 velocity curve of β Cas

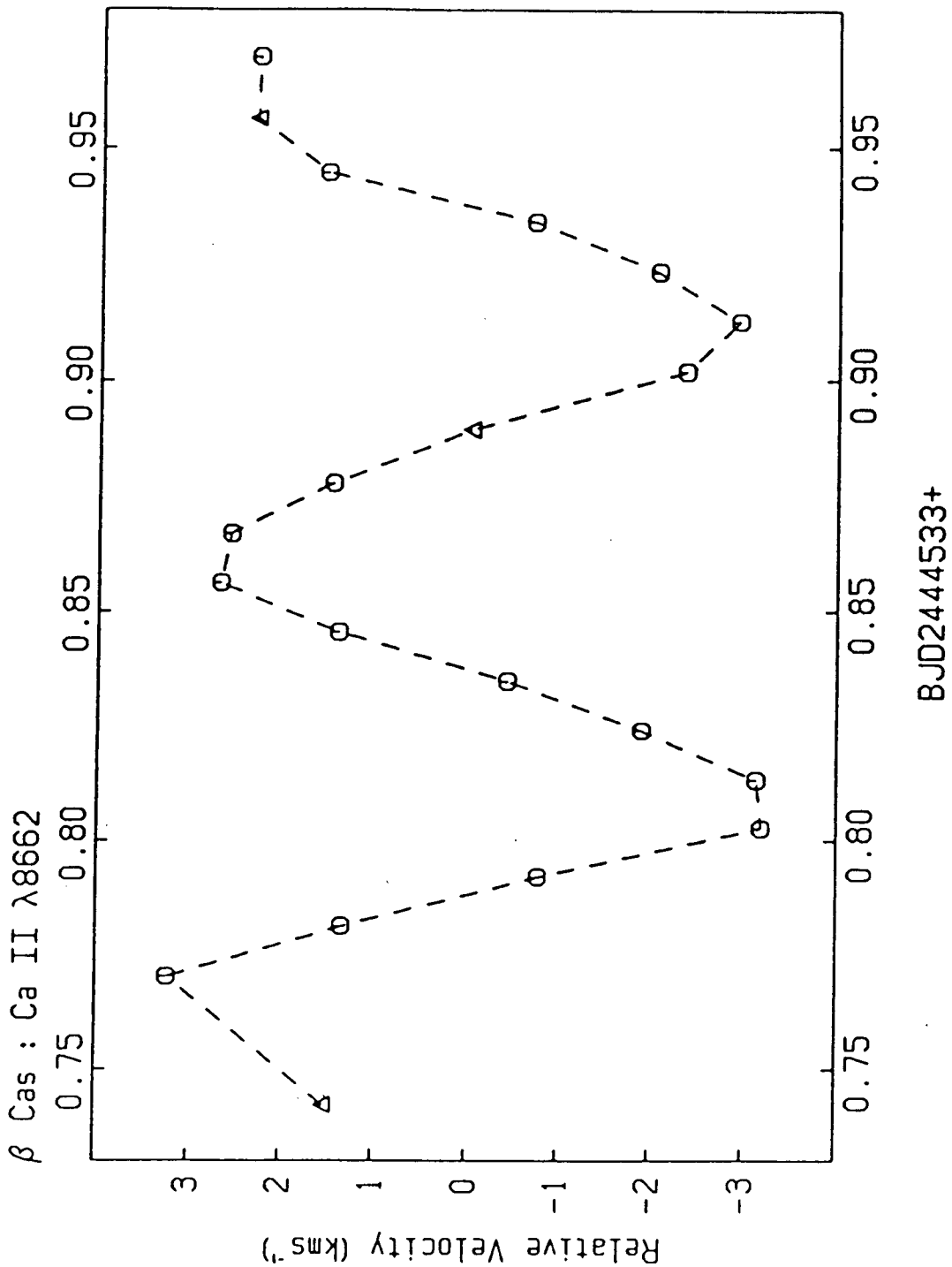

Figure 8.3 The H I λ8750 velocity curve of β Cas

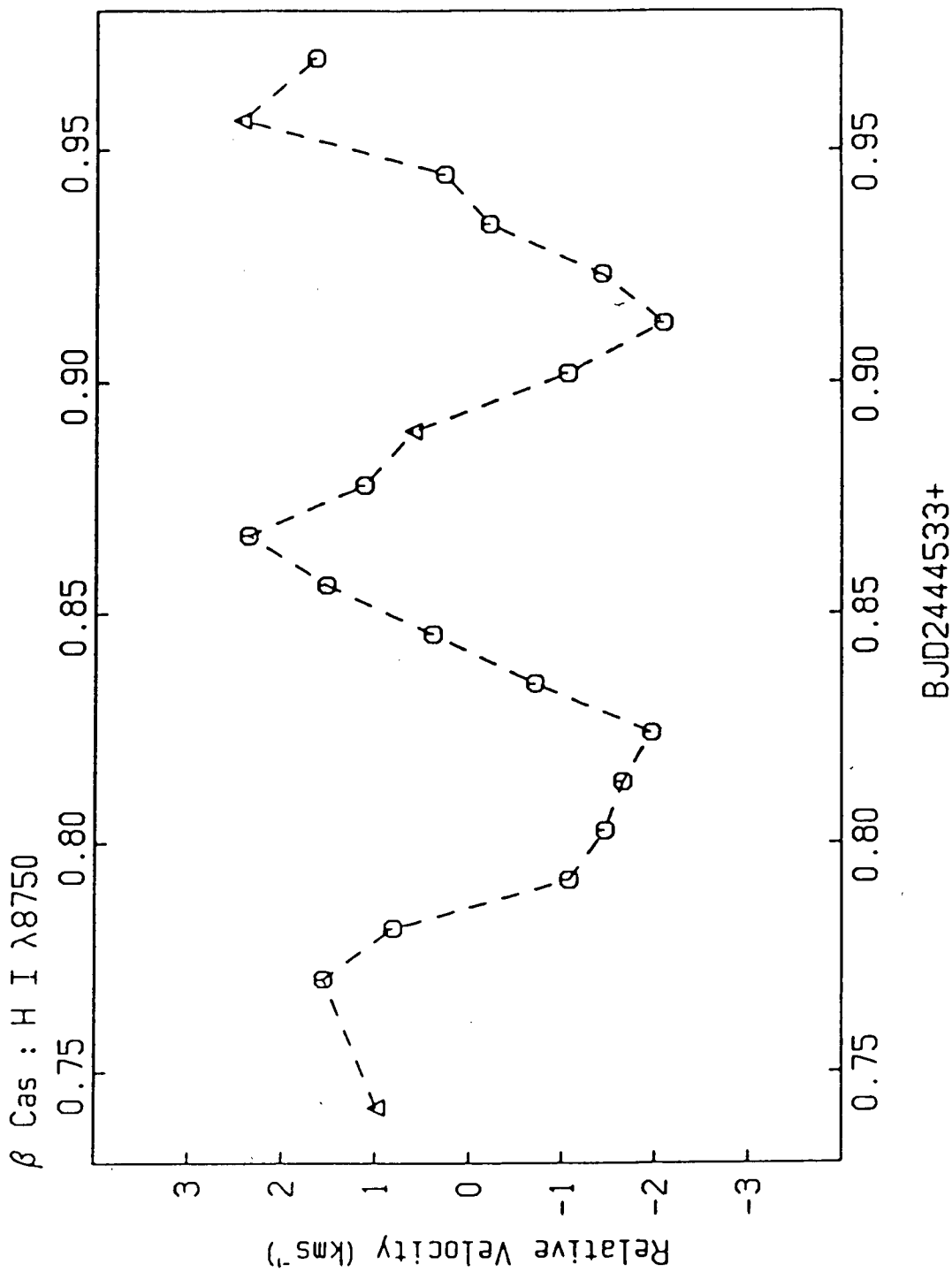

Figure 8.4 The Fe I λ8689 velocity curve of β Cas

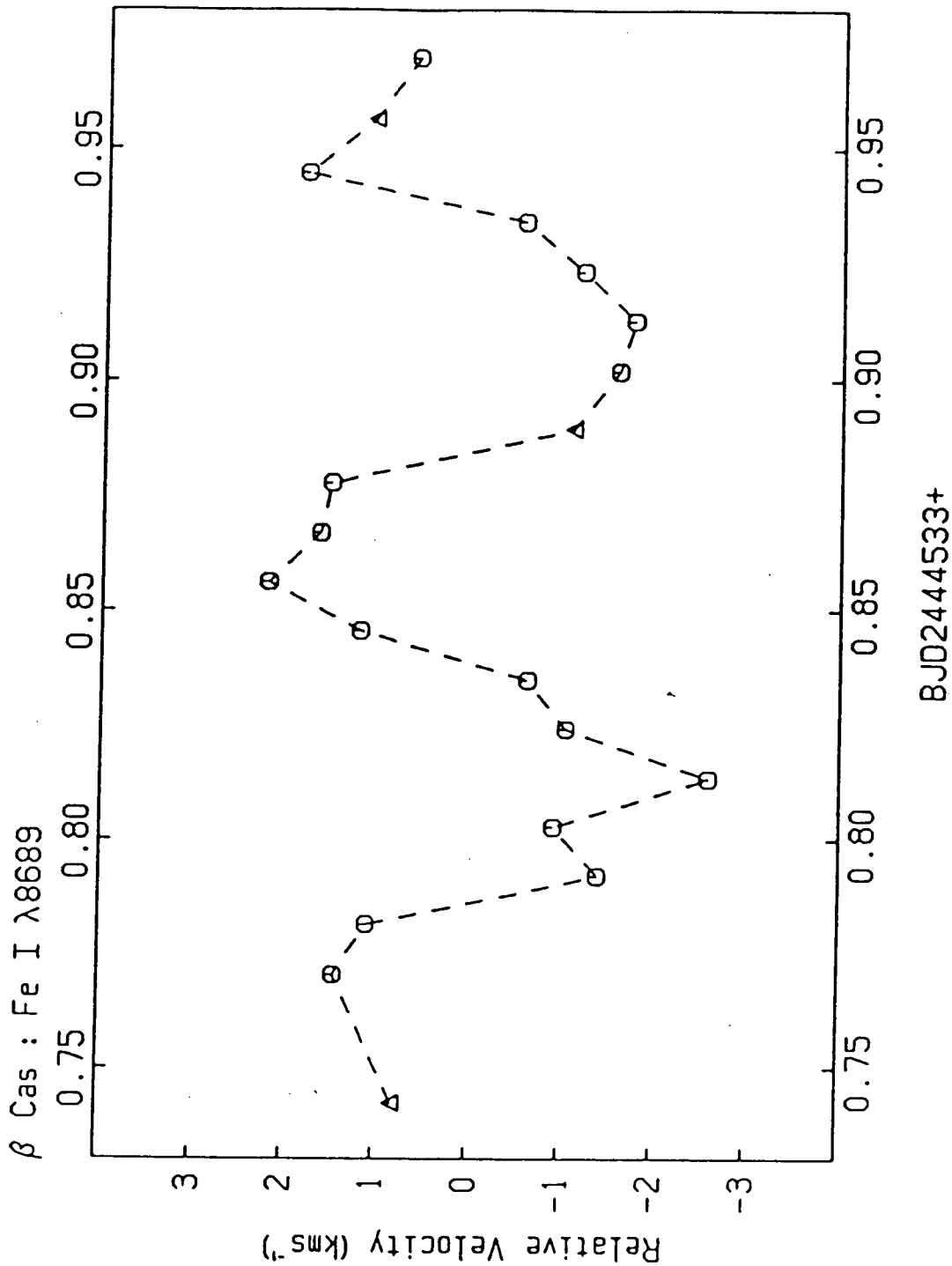

Figure 8.5 The velocity curve of β Cas from weak lines

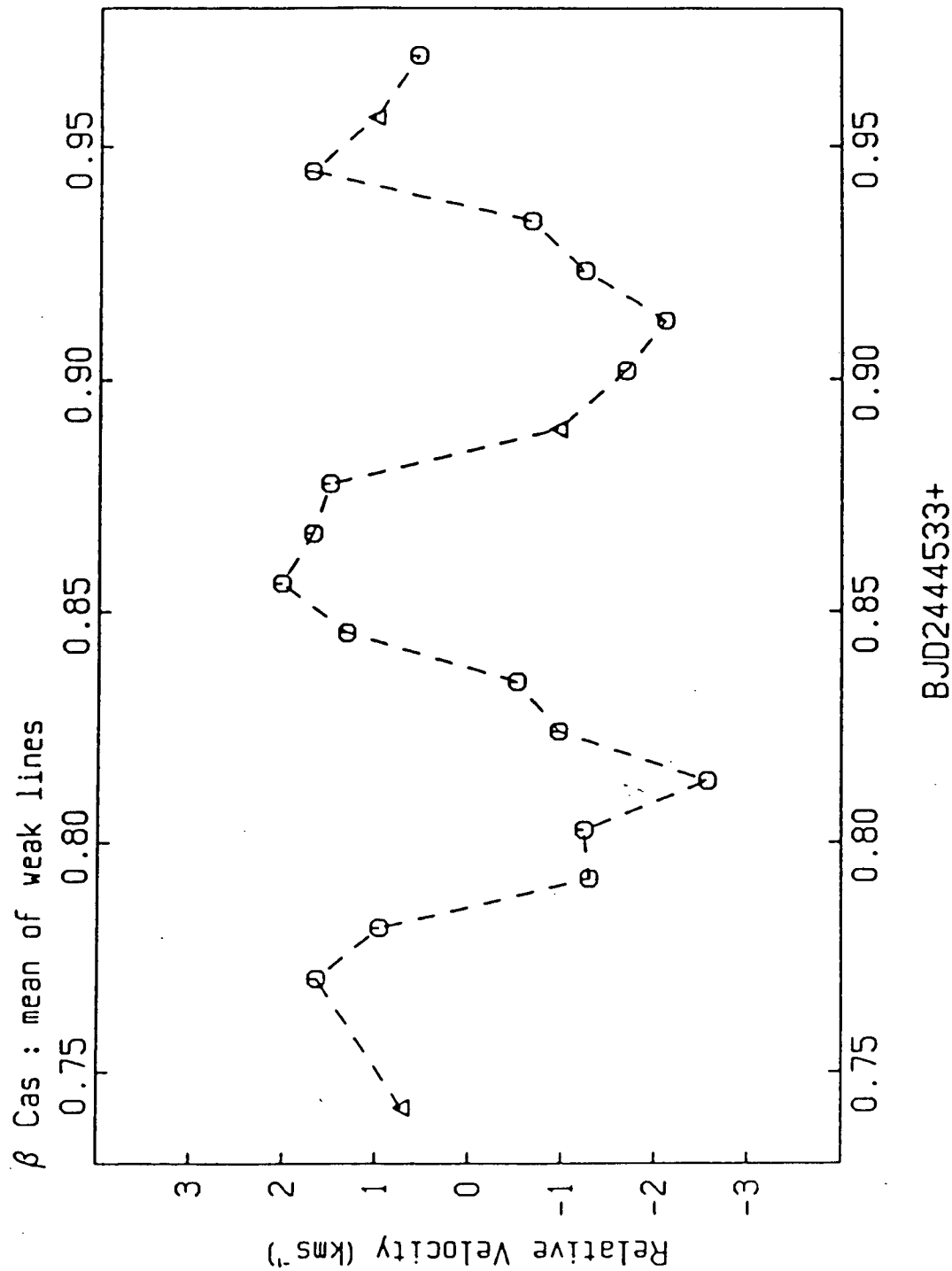

Table 8.3 Relative radial velocities of β Cas

#	Ca II λ8662	H I λ8750	Fe I λ8689	mean weak lines
1	+1.524 kms^{-1}	+0.989 kms^{-1}	+0.794 kms^{-1}	+0.715 kms^{-1}
2	+3.236 kms^{-1}	+1.558 kms^{-1}	+1.449 kms^{-1}	+1.641 kms^{-1}
3	+1.342 kms^{-1}	+0.818 kms^{-1}	+1.093 kms^{-1}	+0.960 kms^{-1}
4	-0.774 kms^{-1}	-1.072 kms^{-1}	-1.403 kms^{-1}	-1.293 kms^{-1}
5	-3.192 kms^{-1}	-1.460 kms^{-1}	-0.916 kms^{-1}	-1.236 kms^{-1}
6	-3.139 kms^{-1}	-1.650 kms^{-1}	-2.590 kms^{-1}	-2.563 kms^{-1}
7	-1.903 kms^{-1}	-1.957 kms^{-1}	-1.041 kms^{-1}	-0.962 kms^{-1}
8	-0.426 kms^{-1}	-0.708 kms^{-1}	-0.613 kms^{-1}	-0.505 kms^{-1}
9	+1.391 kms^{-1}	+0.397 kms^{-1}	+1.190 kms^{-1}	+1.323 kms^{-1}
10	+2.684 kms^{-1}	+1.530 kms^{-1}	+2.201 kms^{-1}	+2.025 kms^{-1}
11	+2.572 kms^{-1}	+2.365 kms^{-1}	+1.646 kms^{-1}	+1.691 kms^{-1}
12	+1.462 kms^{-1}	+1.126 kms^{-1}	+1.527 kms^{-1}	+1.508 kms^{-1}
13	-0.017 kms^{-1}	+0.611 kms^{-1}	-1.094 kms^{-1}	-0.947 kms^{-1}
14	-2.363 kms^{-1}	-1.056 kms^{-1}	-1.580 kms^{-1}	-1.673 kms^{-1}
15	-2.934 kms^{-1}	-2.083 kms^{-1}	-1.741 kms^{-1}	-2.095 kms^{-1}
16	-2.059 kms^{-1}	-1.422 kms^{-1}	-1.182 kms^{-1}	-1.230 kms^{-1}
17	-0.707 kms^{-1}	-0.210 kms^{-1}	-0.541 kms^{-1}	-0.655 kms^{-1}
18	+1.541 kms^{-1}	+0.281 kms^{-1}	+1.826 kms^{-1}	+1.705 kms^{-1}
19	+2.321 kms^{-1}	+2.440 kms^{-1}	+1.093 kms^{-1}	+1.019 kms^{-1}
20	+2.295 kms^{-1}	+1.652 kms^{-1}	+0.620 kms^{-1}	+0.560 kms^{-1}

as the mean velocity of the Ca II λ8662 line averaged over one observed cyclic variation which is represented by spectrum #3 through #13. This value agrees with that of 11.8kms^{-1} quoted by Eggen [1979] and the other values given in Abt [1965].

The mean error introduced by the uncertainties in the HF line-position measurements is about ±60ms^{-1}. This agrees with those of the other data sets. The mean one-standard-deviation uncertainty for each Ca II λ8662 line-position measurement is about ±0.65kms^{-1}. This is the formal error estimate derived by the Fahlman-Glaspey technique. The large value may signify the presence of line-profile variations. The corresponding values for the H I λ8750 and Fe I λ8689 lines are ±1.2kms^{-1} and ±3kms^{-1}, respectively.

Periodogram, Maximum Likelihood, and Maximum Entropy power-spectrum analyses give a mean period of 0.101^{d} from the Ca II curve in Figure 8.2, or a mean frequency of 9.94 day^{-1}. This agrees with the photometric period of 0.104^{d} given by Millis [1966]. In view of the short duration of the time series both here and in Millis [1966], the small discrepancy is not significant. The effect of beating by a possible second period may cause an apparently different primary period to be observed over the short time window. The Ca II curve in Figure 8.2 does show a slight tendency to decrease in amplitude over the two observed cycles.

The 2K amplitude of both the H I λ8750 and the mean weak-line velocity curves is about 4.5kms^{-1}. The 2K

amplitude of the Ca II λ8662 velocity curve, however, decreased from a value of about 7kms^{-1} in the first cycle to a value of about 6kms^{-1} in the second cycle. This phenomenon is usually explained as the effect of beating by another period. The effect is very small over the two observed cycles. It might not even have been observed if the precision in the Ca II velocity curve was any lower. This may explain why it is not seen in the other velocity curves which have both lower amplitudes and precision.

The difference in the velocity amplitudes between the various velocity curves cannot be solely caused by the uncertainties in the choice of the various spectral-line limits. A difference of even several pixels in the line limits is too small to alter the result from such broad lines. Moreover, the effect should be small for the mean velocity curve. The phenomenon is probably related to the differences in the depth and range of depths in the stellar photosphere over which the lines are formed. The Ca II λ8662 has the lowest excitation potential and hence would presumably be formed closer to the top of the photosphere than the other lines. The H I λ8750 line has the highest excitation potential and hence would presumably be formed lower in the photosphere than the other lines. It is also formed over a larger range of photospheric depths than the others.

In spite of the amplitude difference, the Ca II λ8662 velocity is in phase with the mean velocity curve of the weak metallic lines. The H I λ8750 velocity curve, however,

lags both the Ca II curve and mean weak-line curve by about 0.002^d or 2% of the principal photometric period. This phenomenon is probably related to the van Hoof effect found in β Cephei variables. It is usually in the form of the hydrogen-line velocity curves lagging behind the metallic-line velocity curves by several percent in phase. Van Hoof [1957] has pointed out that the effect is not solely caused by the fact that the pulsation pressure wave reaches different line formation depths at different times. Hot rising components of the atmospheric turbulence would also displace the centres of higher excitation lines to the violet. Different phase shifts between velocity curves which are derived from stellar lines of different ionisation states and excitation potentials have also been reported in the peculiar large-amplitude δ Scuti variable SX Phe (Haefner et al [1976]).

8.5 THE LINE-PROFILE VARIATIONS

The likelihood of line-profile variations has already been indicated by the large formal error estimates for the stellar line-position measurements. Figure 8.6 shows the uncertainties in the Ca II λ8662 line-position measurements for each spectrum. Comparing Figures 8.2 and 8.6, one cannote that the peaks in the uncertainty curve coincide with every velocity maxima and minima. Furthermore, the minima in the uncertainty curve coincide with every rising or decreasing branch of the velocity curve. This is different than the phenomenon reported earlier in ρ Pup. In

Figure 8.6 Uncertainties in the Ca II λ8662 line positions

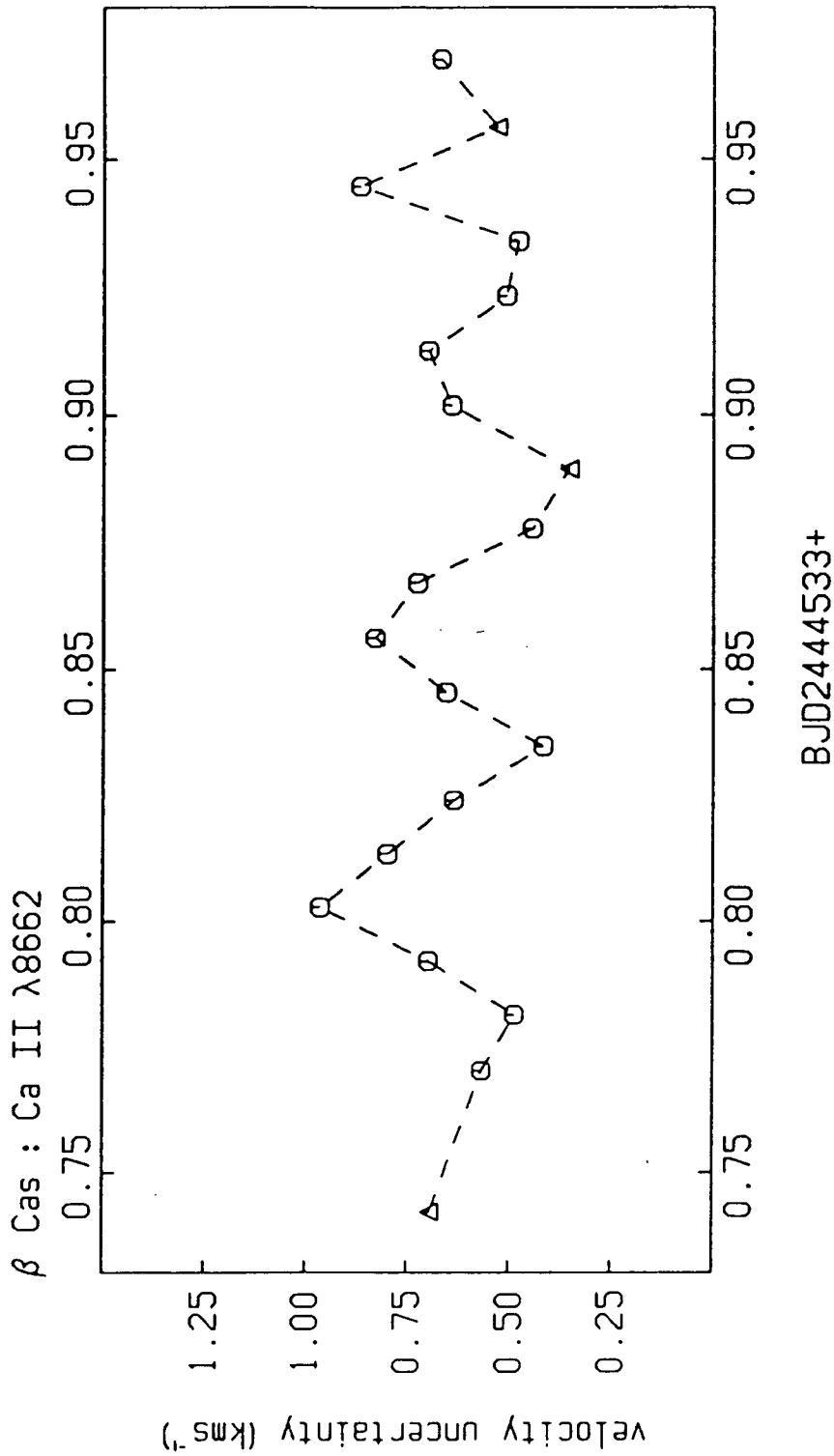

that case, the line-profile variations are in the form of line-depth variations which are in phase with the light curve.

Figure 8.7a shows the region of the Ca II λ8662 line profile for each spectrum. The line profile in this stacked plot have been aligned with respect to each other by correcting for the measured velocity shifts. The spectra have also been smoothed by a Gaussian transfer function which has a σ of ±0.1Å. The mid-exposure time in fraction of days from BJD2444533 is also indicated for each spectrum. Figure 8.7b shows the residuals after subtracting a mean line profile from each spectrum. It can be seen from this stacked residual plot that the variations are at the 1% level of the continuum. The variations can be characterised by phase dependent linewidth and line-depth variations. The spectra near BJD244453.78 show no obvious line-profile difference with respect to the mean profile. However, the profiles near BJD244453.81 are broader than the mean profile and the line cores are not as deep. The profiles near BJD244453.84 show again only random noise in the residuals. The profiles near BJD244453.86, however, are narrower than the mean profile and the line cores are deeper. The same phase dependent pattern repeats with no profile variations in the spectra near both BJD244453.88 and BJD244453.94 while the profiles near BJD244453.91 are broader and shallower than the mean profile. One can also notice that the profiles near BJD244453.96 are starting to show the characteristics of narrower linewidths and deeper line cores.

Figure 8.7 The Ca II λ8662 line profiles and their residuals

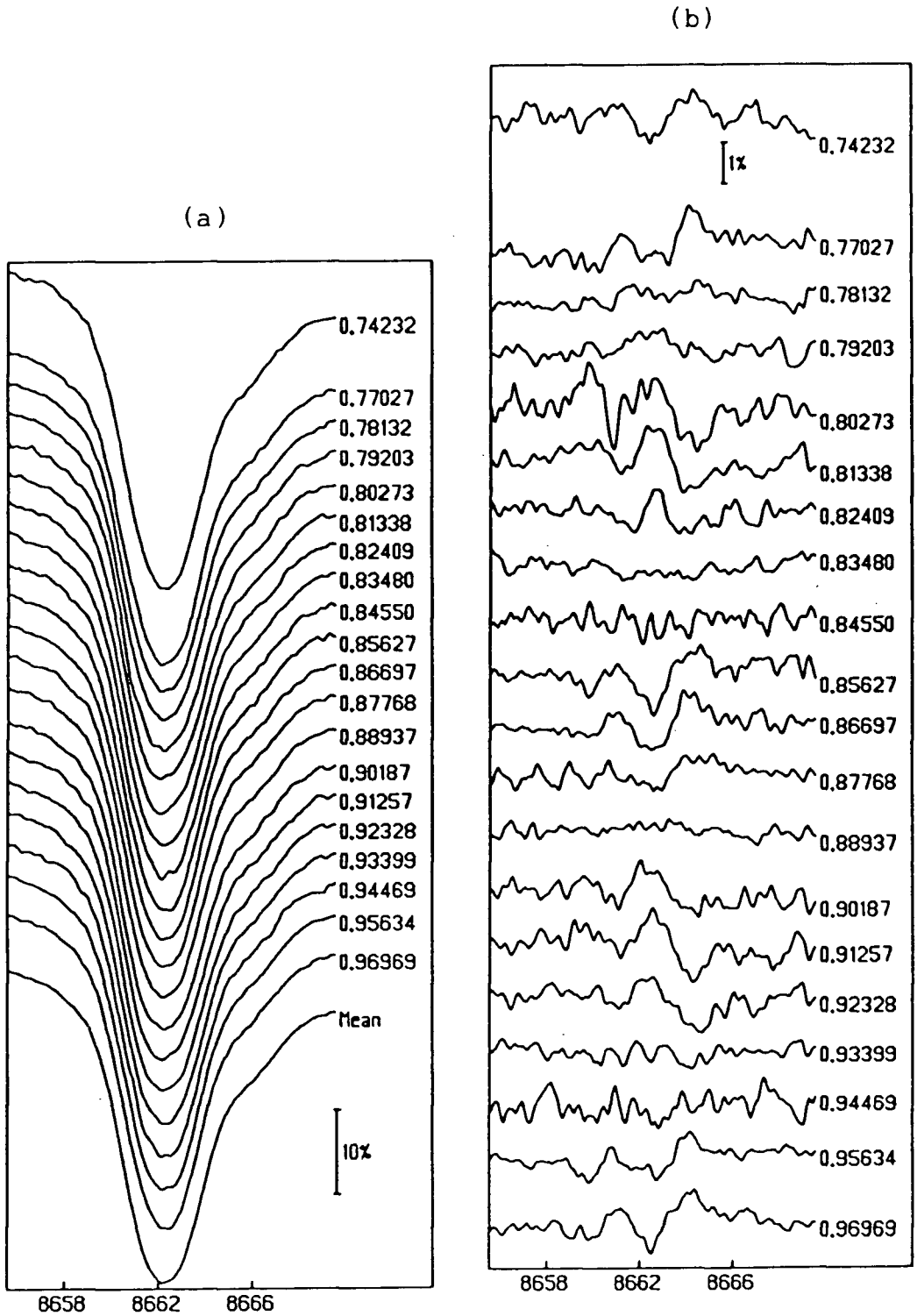

The observed sequence of line-profile variations could certainly explain the pattern displayed in the line-position uncertainty curve of Figure 8.6. Comparing the Ca II λ8662 velocity curve in Figure 8.2 against its uncertainty curve in Figure 8.6 as well as the sequence of line-profile variations, one can observe that the spectra which have near-zero relative radial velocities were also the ones which have similar linewidths and line depths as the mean line profile. Furthermore, the spectra which are near the minimum radial velocity have broader linewidths and shallower line depths while the spectra which are near the maximum radial velocity are the ones with narrow linewidths and deeper line depths.

Similar characteristics of the observed line-profile variations and their correlation with the radial-velocity curve have been reported in Cepheid variables. Van Hoof and Deurinck [1952] have generated theoretical pulsation-distorted line profiles which agree with the observations for the Cepheid η Aql. These theoretical line profiles display the identical type of velocity correlated variations as the ones observed here in β Cas. Naturally, the amplitudes of both the velocity and line-profile variations are many times larger in η Aql than in β Cas. Nevertheless, the theoretical line profiles do show the same type of variations with the narrower and deeper lines near velocity maxima while broader and shallower lines occur near velocity minima. In this particular model given by van Hoof and Deurinck [1952], the line-profile variations are the

direct result of surface-velocity-field variations generated by a pure radial pulsation mode. This suggests that the observed line-profile variations in β Cas may also be explained by radial pulsation.

8.6 DISCUSSION

If one uses the same method that was applied to guess the pulsation mode of the o^1 Eri data, the observed line-profile variations would imply a pulsation of l = 2, 1, or 0. This is based upon the fact that over the two observed cycles, no absorption feature was seen to move across the broadened line profile as was the case in o^1 Eri. Since similar types of line-profile variations have been predicted for radial pulsation (van Hoof and Deurinck [1952]), an l=0 mode or radial pulsation for β Cas would be more probable. There may also be a secondary mode if the beating-like effect observed in the Ca II λ8662 velocity curve is real.

Using the 2K value of $7 kms^{-1}$ observed here for the Ca II line, one obtains a value of $175 kms^{-1}mag^{-1}$ for the $2K/\Delta m_v$ parameter. If one uses the 2K value of $4.5 kms^{-1}$ observed for the other metallic and H I lines in the calculation, as was the case in Smith [1982b], a value of $113 kms^{-1}mag^{-1}$ is obtained for the $2K/\Delta m_v$ parameter. Both these values would strongly suggest radial pulsation for the star.

The pulsation constant Q was calculated to be 0.023 day by Breger and Bregman [1975] using the parameters in Table 8.1. From this value, they identified the dominant pulsation

mode in β Cas to be the first overtone radial pulsation. Tsvetkov [1982b] obtained a Q value of 0.0198 day and this would imply a pulsation mode belonging to the second radial overtone. Tsvetkov [1982b] compared the observed M_{bol} value against the theoretical mode-dependent values. The second overtone radial pulsation also provided the best agreement.

All the previously described tests which include line-profile analysis, the $2K/\Delta m_v$ parameter, and the Q value have implied an identification of radial pulsation for β Cas. Moreover, the low Q value of β Cas would rule out the fundamental mode and suggest overtone pulsation. The present data set is too limited to provide a concrete conclusion on the nature of β Cas's pulsation. This is especially the case if one wants to study in more detail, the phase lag between the different velocity curves as well as the possible existence of a secondary mode. A higher quality data set is also required for a detailed line-profile analysis. A much longer time series with shorter exposure times and higher s/n would be desirable. This can be easily accomplished at CFHT with the reduced Reticon readout noise and much the improved through-put of the red optics. In fact, observing β Cas with a time resolution of one-tenth the "cycle-count" period is possible even at the DAO 1.22m telescope if the sky condition is favorable. In this case, one can have longer time coverage than is possible at CFHT.

BIBLIOGRAPHY

Abt,H.A.: 1965, Ap.J.Suppl., 11, 429

Adams,R.M., and Katz,J.J.: 1956, J. Optical Society of America, 46, 895

Aikawa,T.: 1984, M.N.R.A.S., 206, 833

Akitt,D.P., and Yardley,J.,T.: 1970, I.E.E.E. Journal of Quantum Electronics, QE-6, 113

Albritton,D.L., Schmeltekopf,A.L., and Zare,R.N.: 1976, in "Molecular Spectroscopy: Modern Research", K.N.Rao (ed.), (London: Academic Press), 2, p1

Allen,C.W.: 1973, "Astrophysical Quantities", (London: Athlone Press)

Andreasen,G.K.: 1983, A.A., 121, 250

Andreasen,G.K., Hejlesen,P.M., and Petersen,J.O.: 1980, Space Science Reviews, 27, 381

Andreasen,G.K., Hejlesen,P.M., and Petersen,J.O.: 1983, A.A., 121, 241

Antonello,E.: 1982, in "Binary and Multiple Stars as Tracers of Stellar Evolution", Z.Kopal and J.Rahe (eds.), (Dordrecht: D.Reidel Publishing Company), p33

Antonello,E., and Conconi,P.: 1982, Astrophysics and Space Science, 88, 185

Antonello,E., Fracassini,M., and Pastori,L.: 1981, Astrophysics and Space Science, 78, 435

Antonello,E., and Pastori,L.: 1981, P.A.S.P., 93, 237

Atherton,P.D., Hicks,T.R., Reay,N.K., and Wells,M.: 1978, in "High Resolution Spectrometry", M.Hack (ed.), p573, Trieste

Auvergne,M, Le Contel,J.M, and Baglin,A.: 1979, A.A., 76, 15

Baglin,A., Breger,M., Chevalier,C., Hauck,B., Le Contel,J.M., Sareyan,J.P., and Valtier,J.C.: 1973, A.A., 23, 221

Balona,L.A.: 1981, M.N.R.A.S., 196, 159

Balona,L.A., Dean,J.F., and Stobie,R.S.: 1981, M.N.R.A.S., 194, 125

Balona,L.A., and Stobie,R.S.: 1979a, M.N.R.A.S., 187, 217

Balona,L.A., and Stobie,R.S.: 1979b, M.N.R.A.S., 189, 649

Balona,L.A., and Stobie,R.S.: 1980a, Space Science Reviews, 27, 371

Balona,L.A., and Stobie,R.S.: 1980b, M.N.R.A.S., 190, 931

Balona,L.A., and Stobie,R.S.: 1983, S.Afr.Astron.Obs.Circ., No. 7, p19

Bappu,M.K.V.: 1959, M.N.R.A.S., 119, 400

Baranger,M.: 1958a, Physical Review, 111, 481

Baranger,M.: 1958b, Physical Review, 111, 494

Baranne,A, Mayor,M., and Poncet,J.L.: 1979, Vistas in Astronomy, 23, 279

Barbiano Di Belgioso,A., Fracassini,M., Pasinetti,L.E., and Stroppa,P.: 1983, Astrophysics and Space Science, 94, 97

Barker,E.S., and Cochrane,W.D.: 1980, Bull.A.A.S., 12, 717

Barranco,M., Buchler,J.R., and Regev,O.: 1982, Astrophysics and Space Science, 84, 463

Beavers,W.I., and Eitter,J.J.: 1977, P.A.S.P., 89, 733

Beavers,W.I., Eitter,J.J., Ketelsen,D.A., and Oesper,D.A.: 1979, P.A.S.P., 91, 698

Benedict,W.S., and Herman,R.M.: 1963, J. Quantitative Spectroscopy and Radiative Transfer, 3, 265

Ben-Reuven,A., Friedmann,H., and Jaffe,J.H.: 1963, J. Chemical Physics, 38, 3021

Bessell,M.S.: 1969, Ap.J.Suppl., 18, 167

Betz,A.L., Johnson,M.A., McLaren,R.A., and Sutton,E.C.: 1976, Ap.J., 208, L141

Bezzerides,B.: 1967a, J. Quantitative Spectroscopy and Radiative Transfer, 7, 353

Bezzerides,B.: 1967b, Physical Review, 159, 3

Bidelman,W.P.: 1951, Ap.J., 113, 304

Blamont,J.E., and Roddier,F.: 1961, Phys.Rev.Lett., 7, 437

Blaney,T.G.: 1975, Space Science Reviews, 17, 691

Boggs,J.E.: 1972, in "Molecular Spectroscopy: Modern

Research", K.N.Rao and C.W.Mathews (eds.), (London: Academic Press), 1, p49

Bossi,M., Guerrero,G., Mantegazza,L., and Scardia,M.: 1983, A.A.Suppl., 53, 399

Bouanich,J.P.: 1977, J. Quantitative Spectroscopy and Radiative Transfer, 17, 639

Bouanich,J.P.: 1978a, J. Quantitative Spectroscopy and Radiative Transfer, 19, 381

Bouanich,J.P.: 1978b, J. Quantitative Spectroscopy and Radiative Transfer, 20, 419

Boulet,C., Isnard,P., and Levy,A.: 1973, J. Quantitative Spectroscopy and Radiative Transfer, 13, 911

Boulet,C., and Robert,D.: 1978, Chemical Physics Letters, 60, 162

Boulet,C., Robert,D., and Galatry,L.: 1977, J. Chemical Physics, 65, 5302

Brealey,G.A., Fletcher,J.M., Grundman,W., and Richardson,E.H.: 1980, Proc.S.P.I.E., 240, 225

Breene,R.G.Jr.: 1981, "Theories of Spectral Line Shape", (Toronto: John Wiley & Sons,Inc.)

Breger,M.: 1969, A.J., 74, 166

Breger,M.: 1970, Ap.J., 162, 597

Breger,M.: 1977, P.A.S.P., 89, 55

Breger,M.: 1979, P.A.S.P., 91, 5

Breger,M.: 1980a, Ap.J., 235, 153

Breger,M.: 1980b, Highlights of Astronomy, P.A.Wayman (ed.), 5, 463

Breger,M.: 1980c, Space Science Reviews, 27, 361

Breger,M.: 1982, P.A.S.P., 94, 845

Breger,M., and Bregman,J.N.: 1975, Ap.J., 200, 343

Breger,M., Hutchins,J., and Kuhi,L.V.: 1976, Ap.J., 210, 163

Breger,M., and Stockenhuber,H.: 1983, Hvar Observatory Bull., 7, 283

Brookes,J.R., Isaak,G.R., and van der Raay,H.B.: 1976, Nature, 259, 92

Brookes,J.R., Isaak,G.R., McLeod,C.P., van der Raay,H.B., and Roca Cortes,T.: 1978, M.N.R.A.S., 184, 759

Bryce,H.G.: 1964, in "Fluorine Chemistry", J.H.Simons (ed.), (London: Academic Press), 5, 440

Buchler,J.R., and Goupil,M.: 1984, Ap.J., 279, 394

Buckingham,A.D.: 1967, Advan.Chem.Phys., 12, 107

Buffa,G., and Tarrini,O.: 1983, J. Molecular Spectroscopy, 101, 271

Burki,G., and Mayor,M.: 1980, Information Bulletin on Variable Stars No. 1851

Burki,G., and Mayor,M.: 1981, A.A., 97, 4

Buscombe,W.: 1957, Observatory, 77, 144

Campbell,B.: 1977, P.A.S.P., 89, 728

Campbell,B.: 1983, P.A.S.P., 95, 577

Campbell,B.: 1984, private communication

Campbell,B., and Walker,G.A.H.: 1979, P.A.S.P., 91, 540

Campbell,B., and Walker,G.A.H.: 1985, Proc. I.A.U. Coll. No. 88, "Stellar Radial Velocities", Schenectady,N.Y., 24-27 Oct. 1984, A.G. Davis Philip and David W. Latham (eds.), (L. Davis Press), p5

Campbell,B., Walker,G.A.H., Pritchet,C., and Long,B.: 1985, Dominion Astrophysical Observatory preprint, Nov. 1985

Campbell,B., Walker,G.A.H., Johnson,R., Lester,T., Yang,S., and Auman,J.: 1981, Proc.S.P.I.E., 290, 215

Campbell,W.W., and Moore,J.H.: 1928, Lick Obs.Pub., 16, 124

Campos,A., and Smith,M.A.: 1980, Ap.J., 238, 667

Cattani,M.: 1972, Phys.Lett. A, 38, 147

Chevalier,C., Perrin,M.N., and Le Contel,J.M.: 1968, Ap.J.Lett., 2, 175

Christy,R.F.: 1966, Ann.Rev.Astron.Astrophys., 4, 353

Chun,Y.W., Lee,Y.S., and Nha,I.,-S.: 1983, Information Bulletin on Variable Stars, No. 2406

Clement,M.J.: 1984, Ap.J., 276, 724

Clough,S.A., Davies,R.W., and Tipping,R.H.: 1983, in "Spectral Line Shape", K.Burnett (ed.), (Berlin: Walter de Gruyter), 2, p553

Cochran,A.L., and Barnes III,T.G.: 1981, Ap.J.Suppl., 45, 73

Cochrane,W.D.: 1984, Proc. I.A.U. Coll. No. 88, "Stellar Radial Velocities", Schenetady,N.Y., 24-27 Oct. 1984

Cochrane,W.D., Harlan,J.S., and Smith,W.H.: 1982, Proc.S.P.I.E., 331, 315

Connes,P.: 1970, Annual Review of Astronomy and Astrophysics, L.Goldberg (ed.), 8, 209

Connes,P.: 1983 (in preparation)

Connes,P.: 1984, Proc. I.A.U. Coll. No. 88, "Stellar Radial Velocities", Schenectady,N.Y., 24-27 Oct. 1984

Cousins,A.W.J.: 1951, Observatory, 71, 199

Cox,J.P.: 1976, Ann.Rev.Astron.Astrophys., 14, 247

Cox,J.P.: 1980, "Theory of Stellar Pulsation", (Princeton: Princeton University Press)

Cox,J.P.: 1984a, P.A.S.P., 96, 577

Cox,A.N.: 1984b, in "Observational Tests of the Stellar Evolution Theory", IAU Symp. 105, A.Maeder and A.Rensini (eds.), (Dordrecht: D.Reidel Publishing Company), p421

Cox,A.N., King,D.S., and Hodson,S.W.: 1979a, Ap.J., 228, 870

Cox,A.N., King,D.S., and Hodson,S.W.: 1979b, Ap.J., 231, 798

Cox,A.N., and Hodson,S.W.: 1980, in "Lecture Notes in Physics", 125, (Springer Verlag), p41

Crawford,D.L.: 1975, A.J., 80, 955

Crawford,D.L.: 1979, A.J., 84, 1858

Danos,M., and Geschwind,S.: 1953, Physical Review, 91, 1159

Danziger,I.J., and Dickens,R.J.: 1966, Information Bulletin on Variable Stars, No. 150

Danziger,I.J., and Dickens,R.J.: 1967, Ap.J., 149, 55

Danziger,I.J., and Kuhi,V.: 1966, Ap.J., 146, 743

Davies,R.W.: 1975, Physical Review A, 12, 927

Davies,R.W., and Oli,B.A.: 1978, J. Quantitative Spectroscopy and Radiative Transfer, 20, 95

De Leeuw,F.H., and Dymanus,A.: 1973, J. Molecular Spectroscopy, 40, 418

Deutsch,T.F.: 1967a, Applied Physics Letters, 10, 153

Deutsch,T.F.: 1967b, Applied Physics Letters, 11, 18

Di Giacomo,A., and Tarrini,O.: 1970, Il Nuovo Cimento B, 68, 165

Di Lonardo,G., and Douglas,A.E.: 1973, Canadian Journal of Physics, 51, 434

Dickens,R.J., French,V.A., Owst,P.W., Penny,A.J., and Powell,A.L.T.: 1971, M.N.R.A.S., 153, 1

Doppler,C.: 1842, Abhandlungen d. Le Bohmischen Gesell. d. Wiss, 2, 467

Douglas,A.E., and Greening,F.R.: 1979, Canadian Journal of Physics, 57, 1650

Dravins,D.: 1975, A.A., 43, 45

Dravins,D.: 1982, Ann.Rev.Astron.Astrophys., 20, 61

Dravins,D., Lind,J., and Sarg,K.: 1977, A.A., 54, 392

Dziembowski,W.: 1977, Acta Astronomica, 27, 203

Dziembowski,W.: 1980, in "Lecture Notes in Physics", 125, (Springer Verlag), p22

Duncan,D.K., and Preston,G.W.: 1979, Bull.A.A.S., Vol 11, No. 4, part 1, p728

Dunham,J.L.: 1932, Physical Review, 41, 721

Edlen,B.: 1966, Metrologia, 2, 12

Eggen,O.J.: 1956, P.A.S.P., 68, 238

Eggen,O.J.: 1957, A.J., 62, 14

Eggen,O.J.: 1976, P.A.S.P., 88, 402

Eggen,O.J.: 1979, Ap.J.Suppl., 41, 413

Fahlman,G.G.: 1982, private communication

Fahlman,G.G.: 1984, unpublished

Fahlman,G.G., and Glaspey,J.W.: 1973, in "Astronomical

Observations with Television-Type Sensors", J.W.Glaspey and G.A.H.Walker (eds.), (Vancouver: University of British Columbia), p347

Fano,U.: 1963, Physical Review, 131, 259

Fishburne,E.S., and Rao,K.N.: 1966, J. Molecular Spectroscopy, 19, 290

Fitch,W.S.: 1976, in "Multiple Periodic Variable Stars", IAU Coll. 29, W.S.Fitch (ed.), (Budapest: Akademia i Kiado), p167

Fitch,W.S: 1980, in "Lecture Notes in Physics", 125, (Springer Verlag), p7

Fitch,W.S., and Wisniewski,W.Z.: 1979, Ap.J., 231, 808

Fitch,W.S.: 1981, Ap.J., 249, 218

Fizeau: 1870, Ann. de Chimie et de Physique, 19, 217

Fletcher,J.M., Harris,H.C., McClure,R.D., and Scarfe,C.D.: 1982, P.A.S.P., 94, 1017

Foley,H.M.: 1946, Physical Review, 69, 616

Forrest,A.K.: 1983, Proc.S.P.I.E., 445, 543

Forrest,A.K., and Ring,J.: 1978, in "High Resolution Spectrometry", M.Hack (ed.), p462, Trieste

Fossat,E., and Roddier,F.: 1971, Solar Physics, 18, 204

Fracassini,M., and Pasinetti,L.E.: 1982, A.A., 107, 326

Fracassini,M., Pasinetti,L.E., Castelli,F., Antonello,E., and Pastori,L.: 1983, Astrophysics and Space Science, 97, 323

Fraser,G., Yang,S., and Walker,G.A.H.: 1983, Hvar Observatory Bulletin, 7, 231

Frolov,M.S.: 1975, in "Pulsating Stars", B.V.Kukarkin (ed.), (New York: J.Wiley and Sons), p201

Frolov,M.S., and Irkaev,B.N.: 1984a, Information Bulletin on Variable stars, No. 2462

Frolov,M.S., and Irkaev,B.N.: 1984b, Information Bulletin on Variable stars, No. 2502

Frost,B.S.: 1976, J.Phys.B:Atom.Molec.Phys., 9, 1001

Frost,B.S., and MacGillivray,W.R.: 1977, J.Phys.B:Atom.Molec.Phys., 10, 3649

Garbuzov,G.A., and Mitskevich,A.S.: 1984, Sov.Astron.Lett., 10, 92

Geary,J.C.: 1976, in "Proceedings of IAU Coll. 40", M.Duchesne and G.Lelievre (eds.), (France: Paris-Meudon Observatory), paper 28

Geary,J.C.: 1979, Proc.S.P.I.E., 172, 82

Giraud,M., Robert,D., and Galatry,L.: 1973, J. Chemical Physics, 59, 2204

Giver,L.P., Gentry,B., Schwemmer,G., and Wikerson,T.D.: 1982, J. Quantitative Spectroscopy and Radiative Transfer, 27, 423

Gordon,R.G.: 1966, J. Chemical Physics, 44, 3083

Gordon,M.A.: 1976, in "Methods of Experimental Physics : Astrophysics", M.L.Meeks (ed.), (New York: Academic Press), 12C, p277

Gray,D.F.: 1983, P.A.S.P., 95, 252

Grec,G., Fossat,E., and Vernim,J.: 1976, A.A., 50, 221

Grec,G., Fossat,E., and Pomerantz,M.: 1980, Nature, 288, 541

Greenstein,J.L.: 1948, Ap.J., 107, 151

Griffin,R., and Griffin,R.: 1973, M.N.R.A.S., 162, 243

Guelachvili,G.: 1976, Optics Communications, 19, 150

Guelachvili,G., and Smith,M.A.H.: 1978, J. Quantitative Spectroscopy and Radiative Transfer, 20, 35

Gupta,S.K.: 1978, Astrophysics and Space Science, 59, 85

Gurnette,B.L., and Wooley,R.R.: 1974, "Explanatory Supplement to the Astronomical Ephemeris", (London: H.M. Stationery Office)

Haefner,R., Metz,K., and Schoembs,R.: 1976, A.A., 49, 107

Hall,D.N.B., Ridgway,S., Bell,E.A., and Yarborough,J.M.: 1979, Proc.S.P.I.E., 172, 121

Hall,D.N.B., and Hinkle,K.H.: 1981, in "Solar Instrumentation: What's Next?", R.B.Dunn (ed.), (Sunspot,N.M: Sacramento Peak Observatory), p246

Halprin,L., Moon,T.T.: 1983, Astrophysics and Space Science, 91, 43

Harris,D.L.III: 1963, in "Basic Astronomical Data",

K.A.Strand (ed.), (Chicago: University of Chicago Press), p263

Hauck,B., Foy,R., and Proust,D.: 1985, A.A., 149, 167

Heacox,W.D.: 1980, in "Lecture Notes in Physics", 125, (Springer Verlag), p55

Heacox,W.D.: 1983, P.A.S.P., 95, 591

Heacox,W.D.: 1984, Proc. I.A.U. Coll. No. 88, "Stellar Radial Velocities", Schenectady,N.Y., 24-27 Oct. 1984

Herget,W.F., Gailar,N.M., Lovell,R.J., and Nielsen,A.H.: 1960, J. Optical Society of America, 50, 1264

Herman,R.M.: 1963, Physical Review, 132, 262

Herman,R.M., Rothery,R.W., and Rubin,R.J.: 1958, J. Molecular Spectroscopy, 2, 170

Herman,R.M., and Tipping,R.H.: 1970, J. Quantitative Spectroscopy and Radiative Transfer, 10, 897

Herman,R.M., and Wallis,R.F.: 1955, J. Chemical Physics, 23, 637

Herzberg,G.: 1950, "Molecular Spectra and Molecular Structure I. Spectra of Diatomic Molecules", (London: Van Nostrand Reinhold Company), 2nd edition

Herndon,J.A., Deeds,W.E., Gailar,N.M., Herget,W.F., Lovell,R.J., and Nielsen,A.H.: 1962, J. Optical Society of America, 52, 1108

Hewitt,P.L.: 1976, J. Quantitative Spectroscopy and Radiative Transfer, 16, 499

Hill,S.J.: 1977, Bull.A.A.S., 9, 304

Himes,J.L., and Wiggins,T.A.: 1971, J. Molecular Spectroscopy, 40, 418

Hinchen,J.J.: 1974, J. Optical Society of America, 64, 1162

Hinchen,J.J., and Hobbs,R.H.: 1979, J. Optical Society of America, 69, 1546

Hoffleit,D., and Jaschek,C.: 1982, "The Bright Star Catalogue", (New Haven: Yale University Observatory)

Hough,J.J.T.: 1977, Applied Optics, 16, 2297

Huang,S.S., and Struve,O.: 1955, Ap.J., 122, 103

Huber,K.P., and Herzberg,G.: 1979, in "Molecular Spectra and Molecular Structure IV. Constants of Diatomic Molecules", (London: Van Nostrand Reinhold Company), p304

Huong,P.V., and Couzi,M.: 1969, Journal de Chemie Physique, 66, 1309

Imbert,M.: 1980, A.A., 86, 259

Imes,E.S.: 1919, Ap.J., 50, 250

Iriate,B., Johnson,H.L., Mitchell,R.I., and Wisniewski,E.K.: 1965, Sky and Telescope, July, 21

Irwin,A.W., and Campbell,B.: 1983 (in preparation)

Ishikawa,M.: 1975, Publ.Astr.Soc.Japan, 27, 1

Jaffe,J.H., Rosenberg,A., Hirshfeld,M.A., and Gailar,N.M.: 1965, J. Chemical Physics, 43, 1525

Janzen,J., and Bartell,L.S.: 1969, J. Chemical Physics, 50, 3611

Jarecki,J.: 1977, J. Chemical Physics, 65, 5318

Jarecki,J., and Herman,R.M.: 1975, J. Quantitative Spectroscopy and Radiative Transfer, 15, 707

Jarry,R.L., and Davis,W.Jr.: 1953, J. Physical Chemistry, 57, 600

Johns,J.W.C., and Barrow,R.F.: 1959, Proceedings of the Royal Society of London, Series A, 251, 504

Johnson,H.R., Marenin,I.R., and Price,S.D.: 1972, J. Quantitative Spectroscopy and Radiative Transfer, 12, 189

Johnson,R.: 1984a, private communication

Johnson,R.: 1984b, private communication

Jorgensen,H.E., Johansen,K.T., and Olsen,E.H.: 1971, A.A., 12, 223

Jorgensen,H.E., and Norgaard-Nielsen,H.U.: 1975, A.A.Suppl., 19, 235

Karp,A.H.: 1975a, Ap.J., 199, 448

Karp,A.H.: 1975b, Ap.J., 201, 641

Keeler: 1894, Lick Observatory Publications, 3, 195

Kholopov,P.N.: 1984, Sov.Sci.Rev. E Astrophys. Space Phys., 3, 97

Kirkpatrick,D.E., and Salant,E.O.: 1935, Physical Review, 48, 945

Kolb,A.C., and Griem,H.: 1958, Physical Review, 111, 514

Korb,C.L., Hunt,R.H., and Plyler,E.K.: 1968, J. Chemical Physics, 48, 4252

Kubiak,M.: 1978, Acta Astronomica, 28, 153

Kuhi,L.V., and Danziger,I.J.: 1967, Ap.J., 149, 47

Kuipers,G.A.: 1958, J. Molecular Spectroscopy, 40, 418

Kuipers,G.A., Smith,D.F., and Nielsen,A.H.: 1956, J. Chemical Physics, 25, 275

Kurtz,D.W.: 1976, Ap.J.Suppl., 32, 651

Kurtz,D.W.: 1978, Ap.J., 221, 869

Kurtz,D.W.: 1979, M.N.R.A.S., 189, 1

Kurtz,D.W.: 1980, Space Science Reviews, 27, 935

Kurtz,D.W.: 1981, M.N.R.A.S., 194, 737

Kurtz,D.W.: 1984, M.N.R.A.S., 204, 253

Kwok,M.A., Giedt,R.R., and Gross,R.W.F.: 1970, Applied Physics Letters, 16, 386

Lam,K.S.: 1977, J. Quantitative Spectroscopy and Radiative Transfer, 17, 351

Leavitt,R.P.: 1980, J. Chemical Physics, 73, 5432

Leavitt,R.P., and Korff,D.: 1981, J. Chemical Physics, 74, 2180

Ledoux,P., and Walraven,Th.: 1958, Handb.Phys., 51, 353

Leung,K.C.: 1970, A.J., 75, 643

Leung,K.C., and Wehlau,W.: 1967, Ap.J., 149, 39

Levy,A., Piollet-Mariel,E., and Boulet,C.: 1973, J. Quantitative Spectroscopy and Radiative Transfer, 13, 673

Lie,G.C.: 1974, J. Chemical Physics, 60, 2991

Livingston,W.C.: 1976, in "Proceedings of IAU Coll. 40",

M.Duchesne and G.Lelievre (eds.), (France: Paris-Meudon Observatory), paper 22

Livingston,W.C., Harvey,J., Slaughter,C., and Trumbo,D.: 1976, Applied Optics, 15, 40

Lorentz,H.A.: 1906, Proc.R.Acad.(Amsterdam), 8, 591

Lowry,H.S.III and Fisher,C.J.: 1982, J. Quantitative Spectroscopy and Radiative Transfer, 27, 585

Mack,J.E., McNutt,D.P., Roesler,F.L., and Chabbal,R.: 1963, Applied Optics, 2, 873

Mandin,J.Y., Flaud,J.M., Camy-Peyret,C., and Guelachvili,G.: 1980, J. Quantitative Spectroscopy and Radiative Transfer, 23, 351

Mann,D.E., Thrush,B.A., Lide,D.R.Jr., Ball,J.J., and Aquista,N.: 1961, J. Chemical Physics, 34, 420

Margenau,H.: 1935, Physical Review, 48, 755

Mason,A.A., and Nielsen,A.H.: 1967, J. Optical Society of America, 57, 1464

McMillan,R.S.: 1984, Proc. I.A.U. Coll. No. 88, "Stellar Radial Velocities", Schenectady,N.Y., 24-27 Oct. 1984

McNamara,D.H., and Augason,G.: 1962, Ap.J., 135, 64

Mellor,L.L.: 1917, Publ.Obs.Univ.Mich., 3, 61

Meredith,R.E.: 1972a, J. Quantitative Spectroscopy and Radiative Transfer, 12, 455

Meredith,R.E.: 1972b, J. Quantitative Spectroscopy and Radiative Transfer, 12, 485

Meredith,R.E., and Smith,F.G.: 1973, J. Quantitative Spectroscopy and Radiative Transfer, 13, 89

Meredith,R.E., and Smith,F.G.: 1974, J. Chemical Physics, 60, 3388

Messer,J.K., Khoobehi,B., and Roberts,J.A.: 1982, J. Chemical Physics, 76, 2914

Michelson,A.A.: 1895, Ap.J., 11, 251

Millis,R.L.: 1966, Information Bulletin on Variable Stars, No. 137

Mizushima,M.: 1951, Physical Review, 83, 94

Monnanteuil,N., and Colmont,J.M.: 1983, J. Quantitative Spectroscopy and Radiative Transfer, 29, 131

Moore,C.: 1984, in "UBC Curve : Curve Fitting Routines", (Vancouver: Computing Centre, The University of British Columbia), p130

Moore,C.E., Minnaert,M.G.J., and Houtgast,J.: 1966, "The Solar Spectrum 2935A to 8770A", National Bureau of Standards Monograph 61, (Washington: U.S. Government Printing Office)

Morbey,C.L.: 1978, Publications of the Dominion Astrophysics Observatory, 15, 105

Morgan,W.W., and Abt,H.A.: 1972, A.J., 77, 35

Muenter,J.S., and Klemperer,W.: 1970, J. Chemical Physics, 52, 6033

Murphy,J.S., and Boggs,J.E.: 1967a, J. Chemical Physics, 47, 691

Murphy,J.S., and Boggs,J.E.: 1967b, J. Chemical Physics, 47, 4152

Murphy,J.S., and Boggs,J.E.: 1968, J. Chemical Physics, 49, 3333

Naude,S.M., and Verleger,H.: 1950, Proc.Phys.Soc. (London), A63, 470

Neese,C., Detweiler,H.L., and Yoss,K.M.: 1985, P.A.S.P., 95, 78

Neilson,W.B., and Gordon,R.G.: 1973, J. Chemical Physics, 58, 4131

Niay,P., Bernage,P., Coquante,C., and Fayt,A.: 1977, Canadian Journal of Physics, 55, 1829

Niay,P., Coquante,C., and Bernage,P.: 1979, Canadian Journal of Physics, 57, 592

Ninkov,Z.: 1982, private communication

Ninkov,Z.: 1985, Ph.D. Thesis, University of British Columbia

Ninkov,Z., Yang,S., and Walker,G.A.H.: 1983, Hvar Observatory Bulletin, 7, 167

Nishimura,S.: 1969, Astrophysics and Space Science, 3, 77

Nishimura,S., Watanabe,E., and Yutani,M.: 1983, Proc.S.P.I.E., 445, 183

Odell,A., and Tapia,S.: 1981, Proceeding of the "Workshop on Pulsating B Stars", C.Sterken et al. (eds.), (Nice: Nice Observatory), p329

Ogilvie,J.F., and Koo,D.: 1976, J. Molecular Spectroscopy, 61, 332

Ogilvie,J.F., Rodwell,W.R., and Tipping,R.H.: 1980, J. Chemical Physics, 73, 5221

Ogilvie,J.F., and Tipping,R.H.,: 1983, International Reviews in Physical Chemistry, 3, 3

Osaki,Y.: 1971, Publ.Astr.Soc.Japan, 23, 485

Overend,J.: 1982, in "Vibrational Intensities in Infrared and Raman Spectroscopy", W.B.Person and G.Zerbi (eds.), (New York: Elsevier Scientific Publishing Company), p14

Papaloizou,J., and Pringle,J.E.: 1978, M.N.R.A.S., 182, 423

Parsons,S.B.: 1972, Ap.J., 174, 57

Pearce,J.A.: 1955, Trans.I.A.U., 9, 441

Peery,B.F.Jr.: 1978, in "High Resolution Spectrometry", M.Hack (ed.), p530, Trieste

Pena,J.H., and Gonzalez,S.: 1981, A.J., 86,1679

Pena,J.H., Peniche,R., and Warman,J.: 1981, P.A.S.P., 93, 234

Penfold,J.E.: 1971, P.A.S.P., 83, 497

Percival,J.E., and Nordsieck,K.H.: 1980, P.A.S.P., 92, 362

Percy,J.R.: 1970, P.A.S.P., 82, 126

Percy,J.R.: 1980, Highlights of Astronomy, P.A.Wayman (ed.), 5, 467

Perdang,J., and Blacher,S.: 1982, A.A., 112, 35

Petersen,J.O.: 1976, in "Multiple Periodic Variable Stars", IAU Coll. 29, W.S.Fitch (ed.), (Budapest: Akademia i Kiado), p195

Petrie,R.M., and Fletcher,J.M.: 1967, in "Determination of Radial Velocities and Their Applications", IAU Symp. 30, A.H.Batten and J.F.Heard (eds.), (London: Academic Press Inc.), p43

Phelps,F.M.III: 1982, "M.I.T. Wavelength Tables : Wavelengths by Element", 2, (Cambridge: The MIT

Press)

Philip,A.G.D., and Relyea,L.J.: 1979, A.J., 84, 1743

Pierce,A.K., and Beckinridge,J.B.: 1973, "Kitt Peak Table of Photographic Solar Spectrum Wavelengths", Kitt Peak Obs. Contrib. 559

Pine,A.S.: 1980, J. Molecular Physics, 82, 435

Ponsen,J.: 1963, Bull.Astr.Inst.Netherlands, 17, 44

Prevot,L.: 1967, in "Determination of Radial Velocities and Their Applications", IAU Symp. 30, A.H.Batten and J.F.Heard (eds.), (London: Academic Press Inc.), p37

Pritchet,C.J., Mochnacki,S., and Yang,S.: 1982, P.A.S.P., 94, 733

Pugh,L.A., and Rao,K.N.: 1976, in "Molecular Spectroscopy: Modern Research", K.N.Rao (ed.), (London: Academic Press), 2, p165

Rabitz,H.A.: 1974, Ann.Rev.Chem., 25, 155

Rank,D.H, Rao,B.S., and Wiggins,T.A.: 1965, J. Molecular Spectroscopy, 17, 122

Rao,K.N., and Mantz,A.W.: 1972, in "Molecular Spectroscopy: Modern Research", K.N.Rao and C.W.Mathews (eds.), (London: Academic Press), 1, p141

Reay,N.K., Hicks,T.R., and Atherton,P.D.: 1983a, Proc.S.P.I.E., 445, 13

Reay,N.K., Ring,J., and Pietraszewski,K.A.R.B.: 1983b, Proc.S.P.I.E., 445, 21

Reese,H.M.: 1903, Lick Obs.Bull., 2, 29

Ridgway,S.T., and Brault,J.W.: 1984, Annual Review of Astronomy and Astrophysics, G.Burbidge (ed.), 22, 291

Robert,D., Giraud,M., and Galatry,L.: 1969, J. Chemical Physics, 51, 2192

Roney,P.L.: 1975a, J. Quantitative Spectroscopy and Radiative Transfer, 15, 181

Roney,P.L.: 1975b, J. Quantitative Spectroscopy and Radiative Transfer, 15, 361

Ross,D.W.: 1966, Annals of Physics, 36, 458

Rothschild,W.G.: 1964, J. Optical Society of America, 54, 20

Saez,M., Auvergne,M., Valtier,J.C., Baglin,A., and Morel,P.: 1981, A.A., 101, 259

Saio,H.: 1982, Ap.J., 256, 717

Sandeman,I.: 1940, Proceedings of the Royal Society of Edinburgh, 60, 210

Sengupta,U.K., Das,P.K., and Rao,K.N.: 1979, J. Molecular Spectroscopy, 74, 322

Serkowski,K.: 1972, P.A.S.P., 84, 649

Serkowski,K.: 1976, Icarus, 27, 13

Serkowski,K.: 1977, Astr.Quart., 1, 5

Serkowski,K.: 1978, in "High Resolution Spectrometry" , M.Hack (ed.), p245, Trieste

Serkowski,K., Frecker,J.E., Heacox,W.D., KenKnight,C.E., and Roland,E.H.: 1979a, Ap.J., 228, 630

Serkowski,K., Frecker,J.E., Heacox,W.D., and Roland,E.H.: 1979b, Proc.S.P.I.E., 172, 130

Severny,A.B., Kotov,V.A., and Tsap,T.T.: 1976, Nature, 259, 87

Sharma,R.D.: 1971, Chemical Physics Letters, 8, 428

Sharma,R.D., and Caledonia,G.E.: 1971, J. Chemical Physics, 54, 434

Shaw,J.: 1976, A.J., 81, 661

Shaw,B.M., and Lovell,R.J.: 1969, J. Optical Society of America, 59, 1598

Shobbrook,R.R., and Stobie,R.S.: 1974, M.N.R.A.S., 169, 643

Sileo,R.N., and Cool,T.A.: 1976, J. Chemical Physics, 65, 117

Simons,J.H.: 1950, in "Fluorine Chemistry", J.H.Simons (ed.), (New York: Academic Press), 1, 225

Simons,J.H.: 1964, in "Fluorine Chemistry", J.H.Simons (ed.), (London: Academic Press), 5, 2

Slovak,M.H.: 1978, Ap.J., 223, 192

Smith,D.F.: 1958, J. Chemical Physics, 28, 1040

Smith,D.F.: 1959, J. Molecular Spectroscopy, 3, 473

Smith,E.W., Cooper,J., Chappell,W.R., and Dillon,T.: 1971a, J. Quantitative Spectroscopy and Radiative Transfer, 11, 1537

Smith,E.W., Cooper,J., Chappell,W.R., and Dillon,T.: 1971b, J. Quantitative Spectroscopy and Radiative Transfer, 11, 1567

Smith,E.W., Giraud,M., and Cooper,J.: 1976, J. Chemical Physics, 65, 1256

Smith,F.G., and Meredith.R.E.: 1974, J. Quantitative Spectroscopy and Radiative Transfer, 14, 385

Smith,M.A.: 1977, Ap.J., 215, 574

Smith,M.A.: 1981, Proceeding of the "Workshop on Pulsating B Stars", (Nice: Nice Observatory), p317

Smith,M.A.: 1982a, Ap.J., 253, 727

Smith,M.A.: 1982b, Ap.J., 254, 242

Smith,M.A.: 1983, Ap.J., 265, 325

Smith,M.A.: 1985, in press

Smith,P.H., McMillan,R.S., Frecker,J.E., Castillo,N.D., Perry,M.L., and Merline,W.J.: 1983, P.A.S.P., 95, 595

Snider,J.L.: 1970, Solar Physics, 12, 352

Spellicy,R.L., Meredith,R.E., and Smith,F.G.: 1972, J. Chemical Physics, 57, 5119

Spencer Jones,H.: 1928, Ann. Cape Obs., 10, Part 8, 174

St. John,C.E., Moore,C.E., Ware,L.M., Adams,E.F., and Babcock,H.D.: 1928, "Revision of Rowland's Preliminary Table of Solar Spectrum Wavelengths", Carnegie Institution of Washington Publication No. 396, Papers Mt. Wilson Obs. III

Stamford,P.A., and Watson,R.D.: 1980, Acta Astronomica, 30: 193

Stamford,P.A., and Watson,R.D.: 1981, Astrophysics and Space Science, 77, 131

Stellingwerf,R.F.: 1979, Ap.J., 227, 935

Stellingwerf,R.F.: 1980, in "Lecture Notes in Physics", 125, (Springer Verlag), p50

Stock,J., and Tapia,S.: 1971, A.A., 10, 147

Stothers,R.: 1981, M.N.R.A.S., 197, 351

Struve,O.: 1955, Sky and Telescope, 14, 461

Struve,O., Sahade,J., and Zebergs,V.: 1956, Ap.J., 124, 504

Stumpff,P.: 1977, A.A., 56, 13

Stumpff,P.: 1979, A.A., 78, 229

Stumpff,P.: 1980, A.A.Suppl.Ser., 41, 1

Talley,R.M., Kaylor,H.M., and Nielsen,A.H.: 1950, Physical Review, 77, 529

Talmi,Y., and Simpson,R.W.: 1980, Applied Optics, 19, 1401

Tassoul,J.L.: 1978, in "Theory of Rotating Stars", (Princeton: Princeton University Press), p116

Thulassi Doss,A.: 1969, Kodaikanal Observatory Bulletins, No. 191

Timothy,J.G.: 1983, P.A.S.P., 95, 810

Tippets,R., and Wilcken,S.K.: 1970, P.A.S.P., 82, 1156

Tipping,R.H.: 1973, J. Chemical Physics, 59, 6443

Tipping,R.H.: 1976, J. Molecular Spectroscopy, 61, 272

Tipping,R.H., and Forbes,A.: 1971, J. Molecular Spectroscopy, 39, 65

Tipping,R.H., and Herman,R.M.: 1970a, J. Molecular Spectroscopy, 36, 404

Tipping,R.H., and Herman,R.M.: 1970b, J. Quantitative Spectroscopy and Radiative Transfer, 10, 881

Tipping,R.H., and Ogilvie,J.F.: 1982, J. Molecular Spectroscopy, 96, 442

Toth,R.A., Hunt,R.H., and Plyer,E.K.: 1969, J. Molecular Spectroscopy, 23, 74

Toth,R.A., Hunt,R.H., and Plyer,E.K.: 1970, J. Molecular Spectroscopy, 35, 110

Townes,C.H., and Schawlow,A.L.: 1975, in "Microwave Spectroscopy", (New York: Dover Publications), p349

Traub,W.A., Mariska,J.T., and Carleton,N.P.: 1978, Ap.J., 223, 583

Traub,W.A., and Carleton,N.P.: 1979, Ap.J., 227, 329

Trodahl,H.J., and Sullivan,D.J.: 1977, M.N.R.A.S., 179, 209

Trodahl,H.J., Sullivan,D.J., and Beaglehole,D.: 1973, P.A.S.P., 85, 608

Tsao,C.J., and Curnutte,B.: 1962, J. Quantitative Spectroscopy and Radiative Transfer, 2, 41

Tsvetkov,Ts.G.: 1982a, Soviet Astronomy, 26, 576

Tsvetkov,Ys.G.: 1982b, Soviet Astronomy, 26, 666

Tsvetkov,Ts.G.: 1984, Information Bulletin on Variable Stars, No. 2523

Tull,R.G.: 1969, Applied Optics, 8, 1635

Unno,W., Osaki,Y., Ando,H., and Ahibahashi,H.: 1979, "Nonradial Oscillations of stars", (Tokyo: University of Tokyo Press)

Valtier,J.C.: 1972, A.A., 16, 38

Valtier,J.C., Baglin,A., and Auvergne,M.: 1979, A.A., 73, 329

Valtier,J.C., Le Contel,J.M., Ducatel,D., Auvergne,M., and Sareyan,J.P.: 1979, Acta Astronomica, 29, 233

van Citters,G.W.: 1974, M.N.R.A.S., 168, 469

van Citters,G.W.: 1976, A.J., 81, 766

van Hoof,A.: 1957, P.A.S.P., 69, 308

van Hoof,A., and Deurinck,R.: 1952, Ap.J., 115, 166

Van Vleck,J.H., and Weisskopf,V.F.: 1945, Reviews of Modern Physics, 17, 227

Varanasi,P.: 1971, J. Quantitative Spectroscopy and Radiative Transfer, 11, 1711

Varanasi,P., Sarangi,S.K., and Tejwani,G.D.T.: 1971, J. Quantitative Spectroscopy and Radiative Transfer, 12, 857

Vauclair,G.: 1976, A.A., 50, 435

Vauclair,S., and Vauclair,G.: 1982, Ann.Rev.Astron.Astrophys., 20, 37

Verma,R.P., Daniel,R.R., Ghosh,S.K., Iyengar,K.V.K., Rengarajan,T.N., Tandon,S.N., Sanwal,N.B., and Rahman,A.: 1983, Astrophysics and Space Science, 92, 173

Veto,B.: 1983, Communications from the Konkoly Observatory, No. 83, p249

Veto,B., and Kovacs,G.: 1983, Information Bulletin on Variable Stars, No. 2030

Vogt,S.S.: 1981, Proc.S.P.I.E., 290, 70

Vogt,S.S., and Penrod,G.D.: 1983, Ap.J., 275, 661

Vogt,S.S., Tull,R.G., and Kelton,P.: 1978, Applied Optics, 17, 574

Vohden,R.A., and Boksenberg,A.: 1984, "The Astronomical Almanac", (Washington: U.S. Government Printing Office)

Walker,G.A.H.: 1982, private communication

Walker,G.A.H., Amor,J., Yang,S., and Campbell,B.: 1984, in "Calibration of Fundamental Stellar Quantities", IAU Symp. No. 111, D.S. Hayes, L.E. Pasinetti, and A.G.D. Philip (eds.), (Dordrecht: Reidel), p587

Walker,G.A.H., Buchholz,V., Fahlman,G.G., Glaspey,J., Lane-Wright,D., Mochnacki,S., and Condal,A.: 1976, in "Proceedings of IAU Coll. 40", M.Duchesne and G.Lelievre (eds.), (France: Paris-Meudon Observatory), paper 24

Walker,G.A.H., Johnson,R., and Yang,S.: 1985, 8th Symp. on Photoelectronic Image Devices Proc. in "Advances in Electronics and Electron Physics", B.L.Morgan (ed.), (London: Academic Press), 64A, p213

Walker,G.A.H., Moyles,K., Yang,S., and Fahlman,G.G.: 1981a, Proceeding of the "Workshop on Pulsating B Stars", C.Sterken et al. (eds.), (Nice: Nice Observatory), p141

Walker,G.A.H., Moyles,K., Yang,S., and Fahlman,G.G.: 1982, P.A.S.P., 94, 143

Walker,G.A.H., Yang,S., and Fahlman,G.G.: 1979, Ap.J., 233: 199

Walker,G.A.H., Yang,S., and Fahlman,G.G.: 1981b, Proceeding of the "Workshop on Pulsating B Stars", C.Sterken et al. (eds.), (Nice: Nice Observatory), p261

Watson,R.D.: 1983, Astronomy and Space Science, 92, 293

Webb,D.U., and Rao,K.N.: 1966, Applied Optics, 5, 1461

Webb,D.U., and Rao,K.N.: 1968, J. Molecular Spectroscopy, 28, 121

Wehlau,W.H., Chen,S.N., and Symonds,G.: 1966, Information Bulletin on Variable Stars, No. 143

Weiler,E.J., and Oegerle,W.R.: 1979, Ap.J.Suppl., 39, 537

Wells,M., Atherton,P.D., Hicks,T.R., and Reay,N.K.: 1978, in "High Resolution Spectrometry", M.Hack (ed.), p586, Trieste

Werner,H.J., and Rosmus,P.: 1980, J. Chemical Physics, 73, 2319

White,M.H., Lampe,D.R., Blaha,F.C., and Mack,I.A.: 1974, I.E.E.E. Journal of Solid-state Circuits, SC-9, 1

Wickliffe,M., and Rollefson,R.: 1979, J. Chemical Physics, 70, 1371

Wiggins,T.A., Griffen,N.C., Arlin,E.M., and Kersteller,D.L.: 1970, J. Molecular Spectroscopy, 36, 77

Wolff,S.C.: 1983, in "The A-Stars: Problems and Perspectives", NASA SP-463, 93

Woolley,H,W.: 1962, J. Chemical Physics, 37, 1307

Yang,S.: 1980, M.Sc. thesis, University of British Columbia

Yang,S., and Walker,G.A.H.: 1983, Hvar Observatory Bulletin, 7, 309

Yang,S., Walker,G.A.H., Fahlman,G.G., and Campbell,B.: 1982, P.A.S.P., 94, 317

Young,A.T.: 1978, J. Optical Society of America, 68, 246

Young,A.T., Schorn,R.A., Young,L.D.G., Crisp,D., and Barker,E.S.: 1979, Icarus, 38, 435

Zaidi,H.R.: 1968, Physical Review, 173, 123

Zaidi,H.R.: 1972, Canadian Journal of Physics, 50, 2

INDEX